Symmetry Methods for Understanding Structures of Inorganic Functional Materials

JAMES WILLIAM LEWIS

How to cite:

LEWIS, JAMES WILLIAM (2018) Symmetry Methods for Understanding Structures of Inorganic Functional Materials. Doctoral thesis, Durham University.

Abstract

“Symmetry Methods for Understanding Structures of Inorganic Functional Materials”

James W. Lewis May 2018

The aim of this thesis is to develop and apply new techniques for structural characterisation of inorganic functional materials undergoing a phase transition. We develop robust, reliable and fast techniques that are demonstrated for existing known structures and used for new structure determinations. We hope they will be used well into the future as new structure characterisation needs arise.

Chapter 1 explains the concepts of symmetry and phase transitions in crystalline materials. It introduces experimental characterisation methods and the challenges for robust structure determination from polycrystalline samples.

Chapter 2 develops new structure determination techniques including Genetic Algorithms, exhaustive searches of subgroup trees and inclusion and exclusion type searches. WO_3 is used as a test example to illustrate the techniques and give detailed analysis of the advantages and disadvantages of the different methodologies.

Chapter 3 reports new structure determinations for α- and β-$Bi_2Sn_2O_7$. The β-$Bi_2Sn_2O_7$ structure is the first structural model that accounts fully for high resolution diffraction data while the α-$Bi_2Sn_2O_7$ model is considerably simpler than previously thought. Both structures are robustly determined using our new exhaustive search algorithms.

Chapter 4 discusses application of our algorithms to the known but highly complex ZrP_2O_7 structure. The structure is solved with our methods using displacive symmetry-adapted distortion modes. The new method of applying rotational distortion modes to rigid bodies allows us to simplify the structural description. An extremely complex search is undertaken which identifies the important rotational distortions.

Chapter 5 describes the development of new routines to model the effect of stacking faults in layered materials on powder diffraction data, allowing unprecedented model complexity and speed in Rietveld refinement. The new stacking routines are applied to $La_2O_2Cu_{0.667}Cd_{0.667}Se_2$ and $La_2O_2Cu_{0.667}Mn_{0.667}Se_2$ layered oxychalcogenides, allowing the observed powder diffraction data to be fitted to extract both structural and microstructural information. The chapter also tests our new search algorithms on another oxychalcogenide,

$(Ce_{0.78}La_{0.22})_2O_2MnSe_2$ with a known low temperature magnetic structure. The important magnetic modes are extracted using our search algorithms allowing the magnetic structure to be determined. The techniques are then applied to the previously unknown magnetic structure of $Ce_2O_2Fe_{0.75}Zn_{0.25}Se_2$ in order to extract important magnetic modes and try to determine the magnetic ordering in the low temperature phase.

Chapter 6 summarises the work in this thesis and explains how the new techniques may continue to be used in the future.

Symmetry Methods for Understanding Structures of Inorganic Functional Materials

James W Lewis M.Chem (Dunelm)

Hatfield College

Durham University

Supervisor: Prof. John S. O. Evans

A thesis submitted in partial fulfilment of the requirements

for the degree of Doctor of Philosophy

Department of Chemistry

Durham University

2018

Table of Contents

Abbreviations

AFM	Antiferromagnetic
ANSTO	Australian Nuclear Science and Technology Organisation
CIF	Crystallographic information file
DFT	Density functional theory
DOF	Degrees of freedom
ESRF	European Synchrotron Radiation Facility
FM	Ferromagnetic
FWHM	Full width half maximum
GA	Genetic algorithm
GEM	General Materials Diffractometer
GOF	Goodness of fit
HRPD	High Resolution Powder Diffractometer
HT	High temperature
.inp	TOPAS Academic input file
Irrep	Irreducible representation
LT	Low temperature
NMR	Nuclear magnetic resonance
OPD	Order parameter direction
PND	Powder neutron diffraction
PXRD	Powder X-ray diffraction
RT	Room temperature
SHG	Second harmonic generation
TA	TOPAS Academic
TOF	Time-of-flight

Declaration and Statement of Copyright

The work described in this thesis is entirely my own, except where I have acknowledged help from, or collaboration with, a named person, or given reference to a published source or thesis.

The research presented was performed in the Department of Chemistry, Durham University, between October 2014 and April 2018, the result of which have not been submitted for a degree in this or any other university.

Acknowledgements

I want to thank my supervisor, John Evans for accepting me into his research group. I consider myself as very fortunate to have had the opportunity to take on the research in this project. The level of understanding and skills needed were outside my capabilities when I began. With John's invaluable support, help and guidance throughout I have been able to develop the required skills and understanding that I hope will serve me well in the future. It's fair to say that none of the research achievements in this thesis would have been possible without John.

I also want to thank Branton Campbell of Brigham Young University, Utah. Branton has invested a lot of time and effort into helping to develop, test and integrate the tools used in this thesis with his existing software and innovations. Branton and I spent several months working together at the beginning of my PhD during his visiting professorship in Durham. He devoted countless hours working through the complexities of my early coding efforts with me. We have also spent many more communicating ideas and solving problems since his return to Utah. It is with his help that I developed an understanding and exploitation of the distortion mode basis that underpins much of this research.

I have also received invaluable help and support on a daily basis from my friends and colleagues in the Evans group past and present: Luiza Rosa de Araujo, Chris Ainsworth, Huiyu Liu, Matthew Chambers, Melissa Monzerrat Rodriguez, Chloe Fuller, Josie Auckett and Joe Peet. Aside the academic support, I have great memories from my time in the group and have made great friends. They have ensured that the experience of the past three and a half years has been extremely enjoyable and positive in both a personal sense due to the incredible community spirit within the group. I certainly won't forget it.

I would also like to thank the European and Physical Sciences Research Council (EPSRC) for their support in funding this work.

My final thanks go to my fiancée and partner of more than seven years Helena Kelly. I greatly value her intelligence, perseverance and commitment. She has worked hard for everything she has with no advantages and puts everybody else before herself. Her love and commitment makes every day brighter and the world better. She is richest in the world's two most valuable commodities: laughter and loyalty. I look forward to the day we marry.

Chapter 1 Introduction: Symmetry and Characterisation Methods

1.1 Introduction

This chapter gives an overview of structure-property relationships, their importance in materials chemistry and phase transitions. It covers the underpinning theory and characterisation techniques used in this work. Literature concerning the specific materials investigated can be found when those materials are introduced in individual chapters.

The overarching aim of the work in this thesis is to develop and apply new techniques for structure characterisation. By better understanding the structure of materials we can design and tune the resultant properties and applications. Providing new tools to aid this understanding is the motivation for this work.

1.2 Symmetry in Crystalline Materials

Crystalline materials exhibit translational ordering over long range and as such can be defined by a finite set of atomic positions within a unit cell. The atomic positions within each unit cell are tessellated to describe the entire crystal. Individual atomic positions may be further related to each other by symmetry. This means that the long range structure of the crystal may also be reproduced from a subset of atomic positions called the asymmetric unit and a set of symmetry operations that generate all atomic sites from those in the asymmetric unit.

The symmetry elements that are present in the crystalline arrangement of atoms can be subdivided into two types: point symmetry elements that involve no translational component; and space symmetry elements that involve a translational component. The collection of point symmetry elements present defines one of 32 possible point groups and the addition of space symmetry elements defines one of 230 possible space groups (for commensurate structures). These are tabulated in the International Tables for Crystallography Volume A[1].

Typically, for a new material, the space group is determined from diffraction (the principal method in this thesis) by determining whether the observed peaks are consistent with a proposed symmetry. The symmetry of materials imposes specific constraints upon where diffraction intensity may be observed known as systematic absences. If the systematic absences of the proposed symmetry do not exceed those observed, then the proposed symmetry may be accepted even where it is too low. However, it is always possible to create a structural model of crystalline materials without symmetry (or, more formally, use $P1$ symmetry) as this does not prevent the correct placement of atoms. While the "no symmetry" approach is attractive in terms of simplicity, it may be highly inefficient computationally. In structure solution, symmetry-based constraints that limit possible solutions to those that are realistic are extremely helpful in reducing complexity and therefore increasing the likelihood of identifying the correct model. An understanding of the true symmetry is also important for understanding structure-property relationships. A key advantage of the methods developed in this thesis is that they provide a way of dealing robustly with the true symmetry while retaining the simplicity of the "no symmetry" approach.

1.2.1 Group Theory

In our context, the word "group" refers to the fact that symmetry operations form a mathematical group that imposes the following four rules on them[2] (where A, A^{-1}, B and C are symmetry operations within the group and E is the identity, which is also within the group):

1. The group must have closure; this means that the result of multiplication of any two operations (or indeed the square of one operation) in the group must be another element in the group, e.g. $A \times B = C$.
2. The group must have an identity; this is an operation that when multiplied by any other operation returns that same operation, e.g. $A \times E = A$.
3. The operations must have associativity; this means the result of their multiplication must not depend on the order in which they are assessed, e.g. $(A \times B) \times C = A \times (B \times C)$.
4. There must be an inverse of every operation in the group; this inverse is defined by the fact that each operation should return the identity when multiplied by its own inverse, e.g. $A \times A^{-1} = E$.

Each symmetry operation within the group can be represented by a matrix so that when atomic positions in the asymmetric unit are multiplied by the matrix other symmetry equivalent atomic positions are obtained. Symmetry operations within a group may be combined into a larger block matrix representing the full group. If the matrix is not reducible by block factorisation then it is called an irreducible representation (irrep).

As the diffraction techniques used to probe symmetry in crystalline materials collect information on the reciprocal (rather than direct) lattice (Von Laue[3]), this is where symmetry operations are best considered. The direct and reciprocal lattices are related by a Fourier transform. The space containing all inequivalent positions can be defined as the volume within the locus of points that are closer to a single basis lattice point than any other. In direct space this is the Wigner-Seitz[4] cell but in reciprocal space it is a Brillouin zone[5] and each point within it is called a k-point. The Wigner-Seitz cell and Brillouin zone for a primitive cubic lattice are depicted in 2D in Figure 1.1.

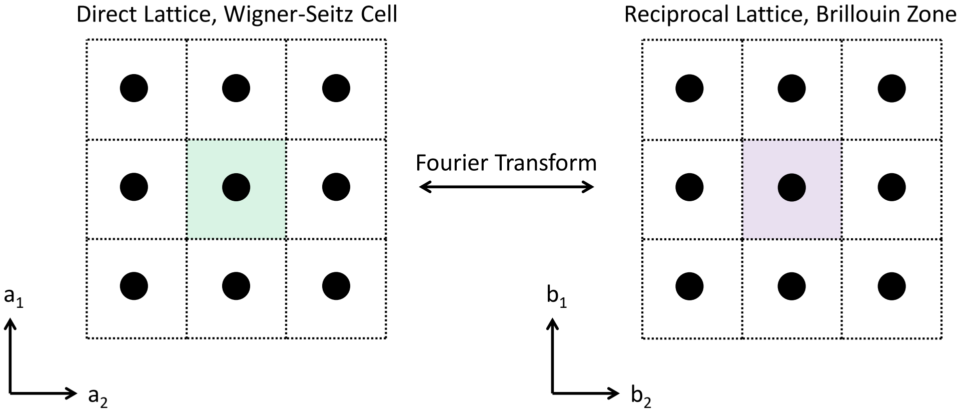

Figure 1.1: 2D depiction of (left) direct lattice Wigner-Seitz cell (green shading) and (right) reciprocal lattice (first) Brillouin Zone (purple shading) for a primitive cubic lattice.

Although the space within the Brillouin zone is finite, the number of k-points is infinite because there is a continuum of possible positions. Adopting the language of Campbell et al[6], there are, however, a limited number of high symmetry ("special") k-points where symmetry elements are located. Each receives a unique label. Considering such "special" k-points allows simpler irrep matrices to be constructed by reducing the effect of some symmetry operations to the identity or to only the translational component in the case of space symmetry operations. An example of the labelling of "special" k-points for a primitive cubic lattice is given in Figure 1.2. A primitive cubic lattice has symmetry elements at these points as a minimum. There are also "non-special" k-points that lie on the line or plane of symmetry connecting "special" k-points. There is an infinite number on any given line or plane so they receive the same non-unique label. All others are called "general" k-points and are always non-uniquely labelled "GP". As a result, irreps associated with "special" k-point labels are unique while irreps associated with "non-special" and "general" k-points are not and require the point in the reciprocal lattice to be specified.

The link between k-points and symmetry is highly technical but one could consider trying to break symmetry in space group $P\bar{1}$ as a simple example. There is just two symmetry elements: the identity, E; and an inversion centre, i. There are only "special" points where an inversion centre is located in reciprocal space and "general" points everywhere else. There are no "non-special" points. Clearly identity symmetry can never be broken and so the irrep matrix for E is the identity for all irreps at all k-points.

Out of all the "special" points only one distortion, at the Γ point (irrep label Γ_1^-), breaks the inversion symmetry. Here the available distortions involve displacing all symmetry equivalent atoms directly along either x, y or z crystallographic axes by the same degree and as such are described by a single parameter (a). More details are given on this parameterisation in Section 1.4.1. The 1D irrep matrix for Γ_1^- is (-1) for i. This means the symmetry is reduced to $P1$ as the inversion centre requires positions defined by (-a). All other distortions, at the Γ point and all other "special" points, only allow distortions that retain inversion symmetry and have irrep matrix (1) for i. The symmetry remains $P\bar{1}$ as the positions described by (a) are consistent with the inversion centre. One simple example involves doubling the size of the unit cell in one crystallographic direction and displacing atoms by the same degree but in the opposite direction in adjacent parent cells. Irrep labels X_1^+, Y_1^+ and Z_1^+ describe this for doubling along x, y and z respectively.

For the "general" point (non-unique irrep label GP1), there is an infinite number of positions to choose from but in all cases two parameters are available to describe the distortion (a, b). The first parameter describes distortions that retain i symmetry while the second describes distortions that break i symmetry and so the irrep matrix is $\begin{pmatrix} 1 & 0 \\ 0 & -1 \end{pmatrix}$ for i. Symmetry is reduced to $P1$ for any non-zero b as the inversion centre requires positions described by (a, -b). In the vast majority of real cases the "general" point allows far more complex distortions than required and so simpler "special" points with fewer parameters should be used. As we discuss below, using high symmetry k-points is particularly useful way to model the breaking of symmetry through phase transitions.

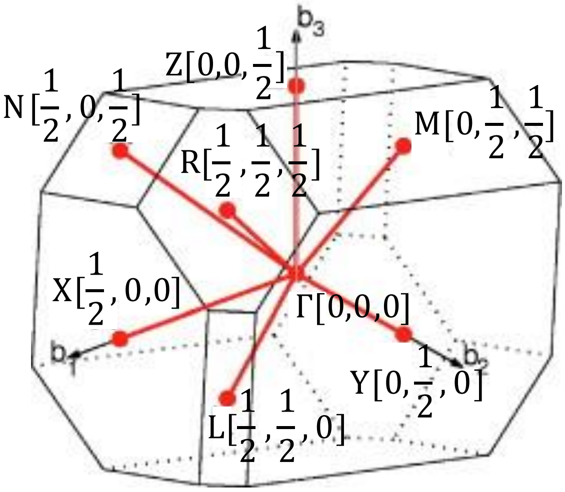

Figure 1.2: "Special" k-points in an example triclinic lattice. The box represents the Brillouin zone and Γ, R, L, M, N, X, Y and Z labels represent "special" high symmetry k-points. Other points in the Brillouin zone are "general" k-points. Square brackets indicate the position in the Brillouin zone. Adapted from Setyawan and Curtarolo[7].

1.3 Phase Transitions

In this thesis we mainly discuss phase transitions caused by a change in temperature leading to a structural (or magnetic) change in crystalline solids. These are usually phase transitions from a parent high temperature structure to a child low temperature structure where the parent "aristotype" can be described as a simplified version of the child (i.e. it has a superset of its symmetry elements) and the child "subgroup" can be described as a distorted version of the parent (i.e. it has a subset of its symmetry elements).

Structural changes occur when the free energy of an alternative structure is lower and there is sufficient energy in the system to overcome kinetic barriers to reach it. In many systems, when the temperature is reduced the relative importance of the entropy term in the Gibbs Free Energy, G (Equation 1.1) is reduced and so a more ordered phase (with more favourable enthalpy, H and less favourable entropy, S than the parent phase) may become energetically favoured.

$$\Delta G = \Delta H - T\Delta S$$

Equation 1.1

For crystalline materials, Landau theory[8,9] can be used to approximate the free energy of phases close to a phase transition. It can be used for both first-order (where there is a discontinuity in the first derivative of the free energy) and second-order (where there is no discontinuity in the first derivative of the free energy) phase transitions. However, for first-order phase transitions a region with more than one real solution is generated.

To begin, one must be able to construct an order parameter, ψ that describes the structural change at the phase transition. It is generally defined such that it has a value of zero for the high temperature disordered phase and some non-zero value that describes the ordering that occurs in the low temperature phase. As a mean-field theory, Landau theory assumes the state of the system can be described by a uniform order parameter and does not account for any localised deviations. In this thesis we will consider three types of order parameter: atomic displacements, rigid body rotations and magnetic ordering and discuss these parameters in more detail in 1.4.2.

A key underpinning tenet of the theory is that symmetry changes in a discontinuous fashion. We can consider a phase transition where atoms displace from high symmetry parent sites as an example. When atoms are moved from high symmetry sites, symmetry elements are immediately removed from the structure regardless of the degree of perturbation. There is no gradual change in symmetry - it is either present or it is not. In reality, the movement of atoms through the phase transition is continuous. The order parameter measures the scale of distortions as it may adopt a value on a continuous scale that reflects the degree of displacement of atoms. An order parameter relates the continuous nature of distortions to the discrete process of symmetry breaking as a result of the phase transition.

Landau theory models free energy as a function of the order parameter and temperature. The Landau free energy, F, approximates the Gibbs free energy per unit volume and, for second order phase transitions, can be expressed as a Taylor series expansion (Equation 1.2) in ψ. The odd order terms are usually omitted because F is normally a symmetric function of ψ. In order to determine the energetically favourable state of the system as temperature varies, one must minimise this expression.

$$F = F_0 + A\psi^2 + \frac{1}{2}B\psi^4 + \cdots$$

Equation 1.2

The coefficients A and B are functions of temperature (and pressure) and F_0 represents the energy of the disordered, high temperature phase (i.e. the phase described by $\psi = 0$). Although higher order terms exist, because the order parameter will be small near to the phase transition, these terms can generally be omitted. Within that limit then the minimum of F is found when $dF/d\psi = 0$ as in Equation 1.3.

$$\frac{dF}{d\psi} = 2A\psi + 2B\psi^3 = 0$$

Equation 1.3

The function only has a minimum if $B > 0$ (the second derivative may only be positive if $B > 0$) and it only has a minimum for $\psi \neq 0$ where $A < 0$. That is to say that if $A > 0$ then the high temperature disordered phase has minimum energy and that the phase transition occurs at $A = 0$. Therefore, to a first approximation, the temperature dependence of A near the phase transition can be formulated as $A = A_0(T - T_c)$ where T and T_c represent the actual temperature and phase transition temperature respectively. By taking the first derivative of the free energy we can derive the minimum for F as given by Equation 1.4 (which is equal to zero only when $\psi = 0$ if $T > T_c$ or for $\psi = \pm\sqrt{\frac{A_0(T_c-T)}{B}}$ if $T < T_c$).

$$\frac{dF}{d\psi} = 2A_0(T - T_c)\psi + 2B\psi^3 = 0$$

Equation 1.4

In order to describe first-order phase transitions (where there is a discontinuity in F as temperature varies), one must introduce a 6th order term to the Taylor series and have $B < 0$ and $C > 0$ to leave the first derivative as given in Equation 1.5.

$$\frac{dF}{d\psi} = 2A_0(T - T_c)\psi + 2B\psi^3 + 2C\psi^5 = 0$$

Equation 1.5

The equation has a trivial solution of $\psi = 0$ if $T > T_c$ and $\pm\sqrt{\frac{-B+\sqrt{B^2-4A_0(T-T_c)C}}{2C}}$ for $T < T_c$. However these latter solutions are also real for $(\frac{B^2}{4A_0C} + T_c) > T > T_c$. This creates a T region for which $\psi = 0$ and $\pm\sqrt{\frac{-B+\sqrt{B^2-4A_0(T-T_c)C}}{2C}}$ are both possible solutions to Equation 1.5 and so a single minimum for F is not described uniquely by Landau theory. Instead the latter solutions represent local minima in the $(\frac{B^2}{4A_0C} + T_c) > T > T_c$ region. A graphical representation of solutions for first and second order phase transitions is shown in Figure 1.3.

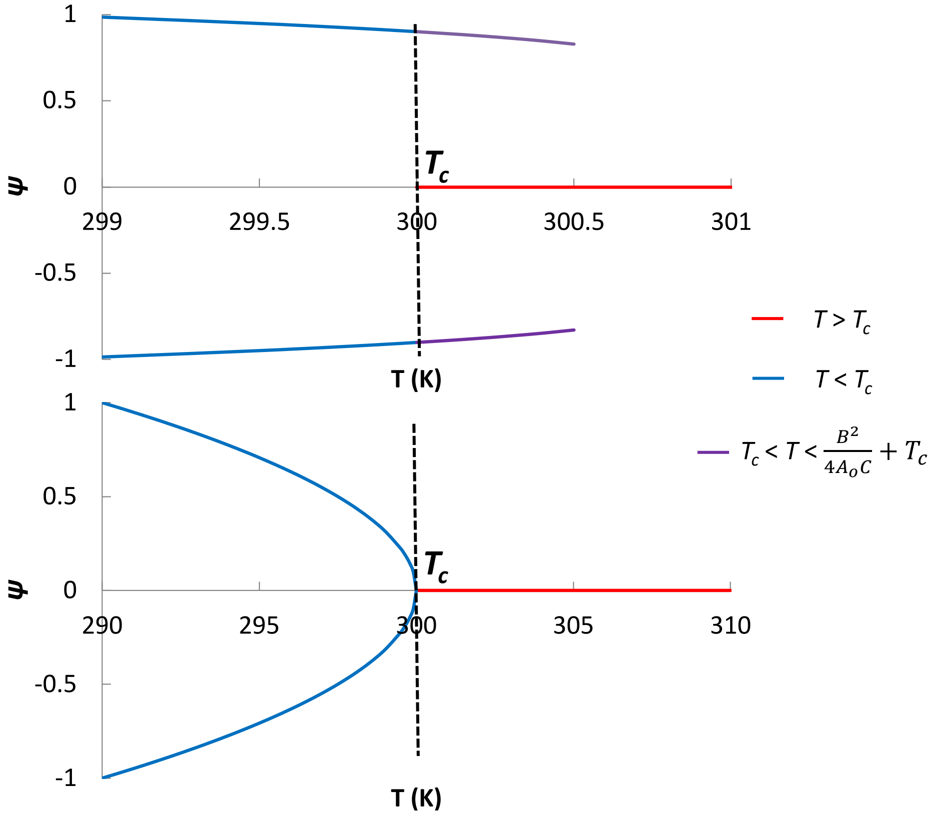

Figure 1.3: Dependence of order parameter on temperature for (top) first order phase transition with T_c = 300 K, A_o = 0.1, B = -0.5, C = 0.8 and (bottom) second order phase transition with T_c = 300 K, A_o = 0.1, B = 1. Values of A_o, B, and C are chosen to normalise the order parameters to between 0 and 1 over the ranges shown. First order picture shows narrower range for a clearer view of $T_c < T < \frac{B^2}{4A_oC} + T_c$ region.

The role of the order parameters is to break some of the symmetry of the high temperature disordered parent structure. This raises the fact that ordering almost always decreases symmetry and increases the complexity (number of independent parameters) of the model. Order and disorder refer to entropy and we do not need to go beyond the Gibbs Equation (Equation 1.1) to see that higher temperatures favour a higher entropy (more disordered) structure and vice versa. Landau theory deals specifically with the relationship to symmetry by introducing the continuous order parameter to the energetic calculation. For this reason it is useful close to a phase transition which involves disorder-order and a group-subgroup relationship.

1.4 Structure Description with Symmetry-Adapted Distortion Modes

The principal structural probe used in this thesis is powder diffraction (see 1.5.1 and 1.5.2). To understand the symmetry of materials from this we must develop a structural model and ensure that the model accounts for the observations in the powder diffraction data. This section discusses the parameters of that model using a symmetry-adapted distortion mode basis, how to create the model and how to refine it.

1.4.1 Distortion Mode Basis

When a material undergoes a phase transition on cooling and loses some symmetry elements but gains no symmetry elements (i.e. the child, low temperature phase has a subset of the symmetry of the high temperature parent) then it is called a subgroup of the parent phase. Subgroups can be subdivided into three categories[10]: *klassengleiche* where there are fewer translations but the crystal class is retained, *translationengleiche* where the translations are retained but the crystal class is lower symmetry and, *allgemein* where there is both fewer translations and a lower symmetry crystal class (this is sometimes considered a sub-category of *klassengleiche*).

In traditional structural work, an independent model of the child structure would be developed in Cartesian coordinate space which places the relevant symmetry constraints on atomic positions or magnetic moments independently of the parent. However, in the case of a group-subgroup transition, there is an alternative model where the child structure can be described by the structure of the parent with some additional symmetry-adapted distortion modes that break some of the symmetry constraints. This distortion mode basis, described by Campbell et al.[6], has significant benefits over the traditional Cartesian basis. Rather than considering the changes in fractional coordinates along individual *xyz* axes, distortion modes move atoms in a new “carrier space” defined by an order parameter direction (OPD). The OPD reflects how distortion modes can break the symmetry of the parent model for irreps at a particular k-point. The maximum symmetry breaking for a given irrep is to allow all associated distortion modes to act independently and have a non-zero value. This is called the irrep kernel. An irrep kernel therefore has a space group associated with it reflecting how much of the whole symmetry of the crystal is broken. It should also be noted that a distortion may break the symmetry relationship between “arms” of k-points. For example the X point of the primitive cubic cell has three arms at [½, 0, 0], [0, ½, 0] and [0, 0, ½] that are all symmetry equivalent. The arms are collectively referred to as the “star” of the k-point. A given distortion may affect all or only some of these arms depending on the symmetry constraints of the distorted structure.

For example $R_4^+(a,b,c)$ (three independent modes with amplitudes a, b and c) is an irrep kernel at the R-point of a cubic perovskite (which has only one arm) which reduces symmetry from $Pm\bar{3}m$ to $P\bar{1}$. The carrier space is designed so that, for the kernel, each independent mode corresponds to exactly one basis vector of the irrep. This complies with the requirement of Landau theory that order parameters must act with the same symmetry 'character' as the affected irrep. Where the distortion is not the maximum irrep kernel but an intermediate, the OPD places constraints upon the distortion modes so that they conform to an intermediate distorted structure symmetry. In this case a single independent mode may correspond to a linear combination of basis vectors of the irrep. An example is shown in Figure 1.4, where a single independent mode, $R_4^+(a,a,0)$ with amplitude a is permitted and this only reduces the cubic perovskite parent symmetry to $Imma$ rather than $P\bar{1}$.

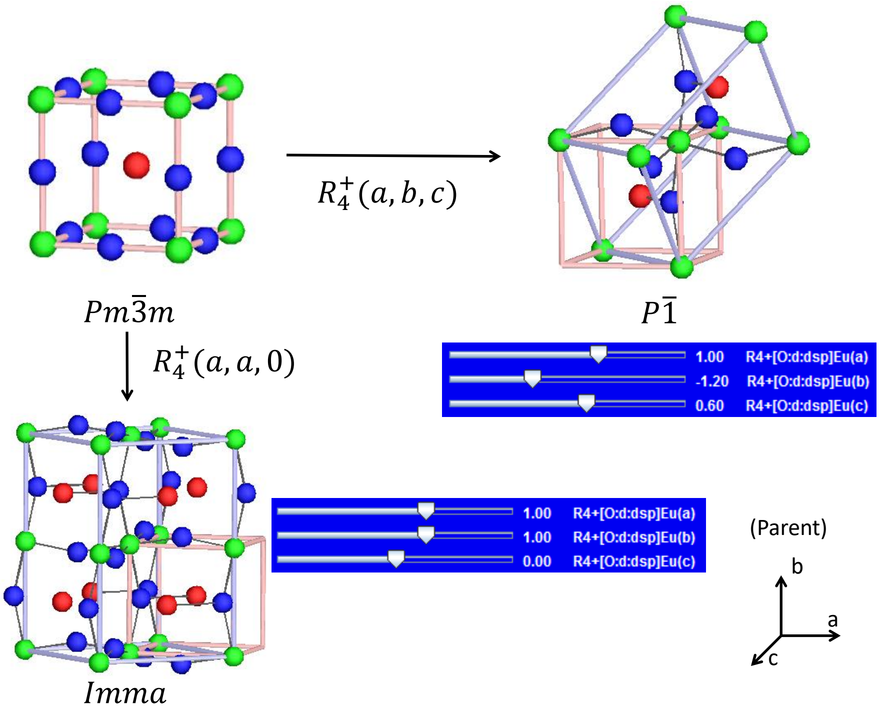

Figure 1.4: Distortion of (top left) cubic perovskite parent by a single independent distortion mode - $R_4^+(a,a,0)$ to create *Imma* child (bottom) or by irrep kernel - $R_4^+(a,b,c)$ to create $P\bar{1}$ child (right). Large pale blue cells shows the $\sqrt{2}\times2\times\sqrt{2}$ and $\sqrt{2}\times\sqrt{2}\times\sqrt{2}$ supercells required for the respective distorted structures. The small pink cell is the parent unit cell.

Where distortions occur only at the Γ point, which always lies at the centre of the Brillouin zone, the group-subgroup relationship must be *translationengleiche* because the translational relationship of the primitive unit cell with surrounding cells cannot be affected. Meanwhile, if k-points are elsewhere in the Brillouin zone (such as the R-point in the above example) the group-subgroup relationship must be *klassengleiche* or *allgemein* because the changes through the phase transition must break the translational relationship with the adjacent unit cell. In both the examples in Figure 1.4 the group-subgroup relationships are *allgemein* but, for example, an $X_1^+(a,a,a)$ distortion would lead to a *klassengleiche* relationship with the child retaining space group $Pm\bar{3}m$ but with a $2 \times 2 \times 2$ supercell as all three arms of the star of X are involved in an equivalent distortion.

Whilst examples of displacive symmetry-adapted distortion modes are given above, we also apply both magnetic and rotational modes in this thesis. Representations of the magnetic and rotational descriptions are shown in Figure 1.5.

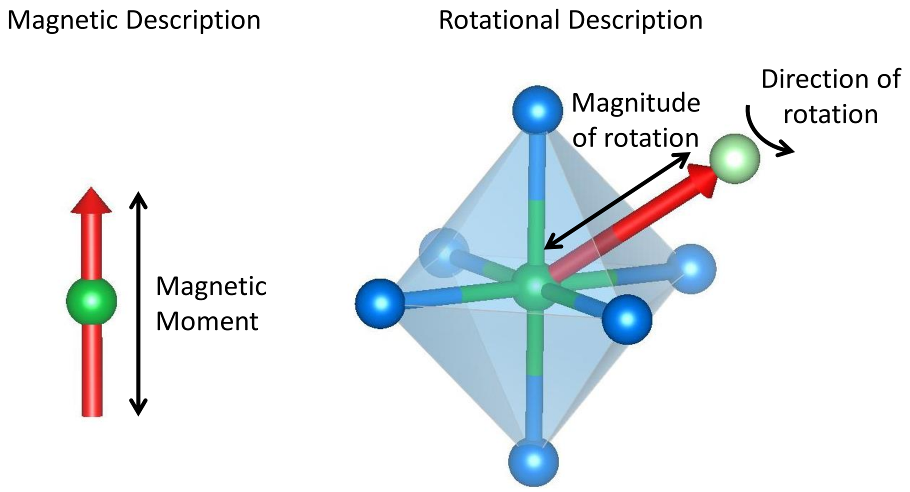

Magnetic Description

Rotational Description

Figure 1.5: Representation of the use of vectors (red arrows) to describe magnetic and rotational distortions. Left picture shows the magnetic description of the moment of a single atom. Right picture shows the rotational description of rigid polyhedra. The light green atom represents a dummy position used to define the direction of rotation about the pivot (dark green).

In the case of magnetic distortion modes that describe magnetic ordering in materials, the irrep matrices represent symmetry operations applicable to the magnetic moments. They are prefixed with the letter “m” in order to differentiate them from irreps that describe the symmetry of atomic positions. Magnetic distortion modes act to break some of this symmetry depending on the constraints of the magnetic space group (Shubnikov group) of the distorted mode. Magnetic moments can be described using “axial vectors” (or pseudo vectors) that act as ordinary vectors but allow a sign flip upon reflection to account for the reversal of charge in the opposite direction to the vector. As with displacive modes, these vectors may be decomposed into conventional orthogonal components (m_x, m_y, m_z). Typically magnetic ordering involves limited symmetry breaking that can be described by distortion modes of a single irrep and so far fewer mode amplitudes are needed than in a conventional (m_x, m_y, m_z) type description of each moment.

In the case of rotational modes, we define rigid polyhedra with fixed bond lengths and angles so that internal distortions are excluded. These rigid bodies are bound to a dummy position (formally described by a fixed bond from the central position or "pivot" of the polyhedra to a dummy atom with zero occupancy) allowing a vector about which each rigid body may rotate depending on symmetry constraints of the distorted model. The rigid bodies may also translate which we allow using displacive modes applied to the pivot of the polyhedra which carries all "passenger" atoms of the rigid body with it. Both the rotational and translational modes acting on rigid bodies can be decomposed into the conventional 3 orthogonal components. Although a combination of displacive distortion modes can always be used to achieve the same description as any rotational distortion mode, in cases where the distortion mainly consists of rotations of rigid polyhedra, rotation modes offer a much simpler description than can be achieved by displacive distortion modes.

The distortion mode basis has the advantage of providing an "on/off" measurement of symmetry breaking. In the traditional xyz description it might not be immediately obvious, if atoms are close to high symmetry sites, whether the symmetry is truly broken. This is useful because it is far easier to design an algorithm that works with "on/off" parameters than with continuous parameters. The distortion mode basis also provides the advantage of direct quantification of a distortion magnitude. This is because it uses an order parameter, where zero amplitude means zero distortion and the amplitude scales with the magnitude of the distortion. This is in contrast to the traditional basis, where information on the scale of the distortion must be obtained indirectly by using the difference between positions or moments of parent and child structures. The distortion mode basis may also provide a simpler (fewer parameters) model if the modes more naturally model the distortions of the structure than atomic coordinates in Cartesian coordinate space. Given that distortion modes act directly on irrep basis vectors this is likely when the child structure has a subset of the parent symmetry (i.e. is a subgroup). The fewer order parameters that are used, then the easier it is to identify the global minimum energy arrangement.

1.4.2 Generating Subgroups - ISODISTORT

ISODISTORT[6] (part of the ISOTROPY suite[11]) is a freely available online tool for generating symmetry-adapted distortion-mode descriptions of distorted systems. When a parent loses symmetry via distortion, ISODISTORT is able to describe the child structure using parent atomic sites plus symmetry-allowed distortion modes that distort the structure as specified by the user. In this thesis we apply displacive, rotational and magnetic modes to model distorted structures, although occupational and strain modes are also available in ISODISTORT. When a symmetry breaking distortion is applied, ISODISTORT returns a list of distortion modes applied to the irreps at selected k-points where the symmetry constraints are relaxed in the distorted model compared to the parent. An order parameter direction (OPD) gives the constraints upon these modes enforced by the symmetry constraints of the distorted model. ISODISTORT provides 4 methods by which the user can specify the distortion and obtain a distorted structure:

1. By searching for distortions over all “special” k-points; where the k-point is unique and constrained by the user-choice of crystal system, space group and lattice distortion before selecting from possible irreps and OPDs.
2. By searching over specific k-points; specifying the variables if “non-special” or “general” k-points are chosen and superposing multiple k-points if required before choosing the irreps and OPDs.
3. By searching for k-points or combinations of k-points that distort the structure to a user-specified space group and lattice before choosing from a list of allowed irreps and OPDs. ISODISTORT algorithms search for the simplest possible combination of “special” k-points.
4. By loading a pre-existing child structure from a CIF file and allowing ISODISTORT to automatically match sites with the parent; specifying the basis and origin of the distorted lattice and selecting the distortion from allowed irreps and OPDs. ISODISTORT algorithms search for the simplest possible combination of “special” k-points.

The amplitudes of modes generated by ISODISTORT can be moderated by a normalisation factor (normfactor) such that the sum of the squares of the resulting displacement, rotation or magnetic moments of all atoms is 1 (Å, radian or μ_B depending on the mode type). The normfactor can be obtained as defined by Equation 1.6 where for all unique atoms, i, that are affected by the mode: m_i is the multiplicity, $\boldsymbol{v_i}$ is the vector along which the mode acts and B' is the matrix of column vectors defining the child supercell before any strain is applied.

$$normfactor = \frac{1}{\sqrt{\sum_i m_i \left(\|B'.\boldsymbol{v_i}\|\right)^2}}$$

Equation 1.6

In order to return the strain independent displacement, rotation or magnetic moment of a given atom resulting from a given distortion mode, Equation 1.7 may be used where A is the mode amplitude and B is the strained supercell column matrix (this can be eliminated where there is no strain).

$$d/r/\mu = A \times normfactor \times \|B.\boldsymbol{v}\|$$

Equation 1.7

Once a distorted structure model is obtained from ISODISTORT, even if irrep kernels were selected, there is still no reason why the maximum possible symmetry breaking allowed by the model must be used when fitting a set of experimental diffraction data. For example, some mode amplitudes could be zero or some could be related in amplitude. In this case the actual symmetry of the model may be higher than that implied by the space group (or magnetic space group). This is important because it allows the use of a lower symmetry distorted model than the one that actually occurs at the phase transition, and the use of search algorithms to decide which distortion modes are really needed. This is helpful for robust symmetry determination because it is possible to start structural refinements with a $P1$ model and then extract the space group by deciding which modes are actually necessary to describe the experimental data. The best choice is usually the model that uses the fewest distortion modes but still fits the data. Figure 1.6 summarises this idea.

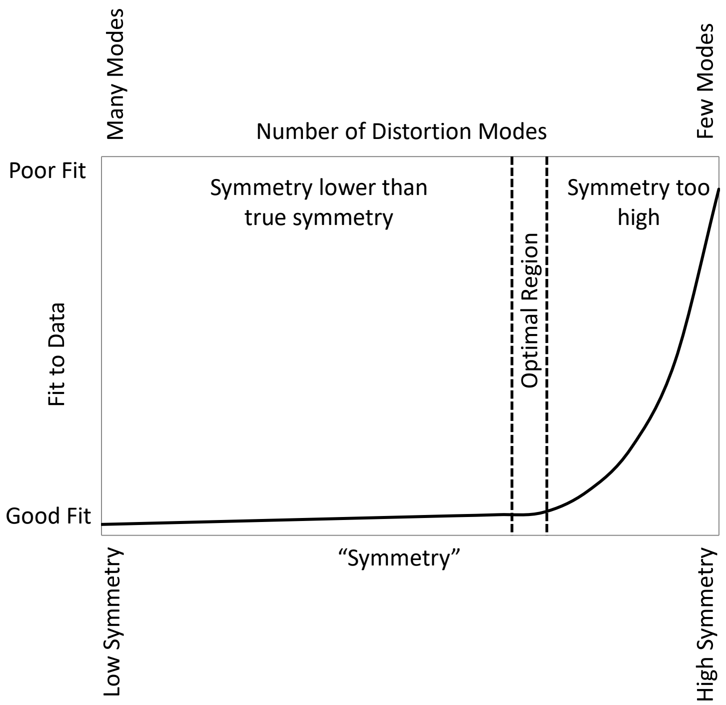

Figure 1.6: Graph showing balance in achieving fit to diffraction data while using the lowest number of distortion modes and highest symmetry possible. The best model is in the optimal region where the most possible symmetry constraints have been applied without compromising the fit.

Once the necessary modes have been identified, the ISOTROPY suite provides another tool, FINDSYM[12] that allows us to determine the true symmetry of our model based on the position of atoms, or alignment of magnetic moments that are obtained once the amplitudes of the refined modes have distorted the parent structure. The routine allows a tolerance (an allowed distance or moment variation from a higher symmetry arrangement) that we specify whenever FINDSYM is used in this thesis.

As well as generating an individual child distorted model, ISODISTORT is also able to create a "subgroup tree" which lists structural models for all possible subsets of the distortions available to the child structure. This creates an additional way to determine the true symmetry of the sample – by trialling each subgroup model. Again the aim of this approach is to identify the candidate with fewest distortion modes that fits the experimental data. It is a similar approach to trialling distortion modes of a *P1* model but avoids the FINDSYM step by working directly with possible space groups. Details and examples of both these approaches are found in Chapter 2. In every case where structures are generated using ISODISTORT during this thesis, there is an Appendix giving step by step instructions of how this was done.

1.5 Diffraction Methods

Diffraction is a very powerful structural probe for studying crystalline materials, and almost all the structural information discussed in this thesis is derived from diffraction data. For many materials it is not possible to obtain single crystals for diffraction and so this thesis focuses on the information that can be extracted from powder diffraction techniques. This section discusses the fundamental theory of diffraction and how to extract structural information from it.

1.5.1 Powder X-ray Diffraction (PXRD)

Powder X-ray Diffraction (PXRD) is a powerful probe of polycrystalline structures that relies on the interference of X-rays scattered by electrons. In PXRD experiments the scan is usually performed by illuminating the sample in a monochromatic X-ray beam over a range of incident angles, θ, and detecting the X-rays diffracted at angle 2θ (Figure 1.7). We will be concerned with elastic scattering of X-rays (where the energy of X-rays is unchanged by diffraction) to create Bragg peaks in the diffraction pattern which probe the long range order of the structure. We won't seek to derive any structural information from inelastic (Compton) scattering of X-rays or diffuse (disordered) scatter. Bragg's law (Equation 1.8) relates the wavelength of the X-ray radiation, λ, to the d-spacing between parallel Miller planes, d_{hkl}, and the incident angle of X-rays.

$$\lambda = 2d_{hkl}sin\theta$$

Equation 1.8

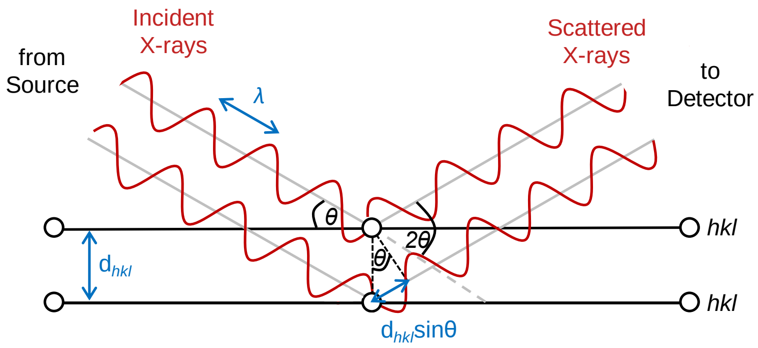

Figure 1.7: Schematic illustrating Bragg's Law and the derivation of interplanar *d*-spacing from diffraction of monochromatic X-rays. Adapted from Ainsworth[13].

Due to the interference of X-rays, whether X-ray intensity can be observed at a particular angle 2θ is determined by the unit cell and space group. The relationship between the unit cell parameters and d-spacing is given generally for an orthorhombic unit cell by Equation 1.9, although it is more complex or simple for other crystal classes.

$$\frac{1}{d^2} = \frac{h^2}{a^2} + \frac{k^2}{b^2} + \frac{l^2}{c^2}$$

Equation 1.9

The structure factor F_{hkl}, gives the intensity observed for a given hkl reflection due to the contribution of all atoms j, where f_j is the scattering factor of the atom and x_j, y_j and z_j are the fractional coordinates of the atom (Equation 1.10).

$$F_{hkl} = \sum_j f_j \exp\left[2\pi i\left(hx_j + ky_j + lz_j\right)\right]$$

Equation 1.10

The scattering factor depends on the number of electrons of the atoms in question and the distribution of intensity amongst different reflections probes the relative position of atoms to each other. There are also additional effects on the observed diffraction pattern resulting from the nature of the sample and the instrument. Some effects that lead to a change in intensity or position of peaks include (but are not limited to): thermal vibrations, where the observation of time-averaged atomic positions reduces observed intensity in a 2θ-dependent fashion; preferred orientation, where polycrystalline grains prefer to lie in a particular non-random orientation relative to the X-ray beam so redistributing intensity in a hkl dependent fashion; and sample height variation, where the position of the sample relative to the X-ray beam shifts the position of observed peaks uniformly. Other effects change the shape of observed peaks including: microstrain broadening, where the stress of the sample creates a 2θ-dependent broadening of peaks; size broadening; where small polycrystalline grains leads to broadening of peaks, and asymmetry; where attempting to detect X-rays diffracted in a cone with a flat detector leads to a 2θ angle dependent uneven distribution of peak intensity about the maximum.

All PXRD data analysed in this thesis was collected on D8 Bruker Advance laboratory diffractometers or on synchrotron sources at: Diamond Light Source, Harwell Science and Innovation Campus, Didcot, UK; at the European Synchrotron Radiation Facility (ESRF), Grenoble, France; at the National Synchrotron Light Source, Brookhaven National Laboratory, New York, US; or at the ANSTO Australian Synchrotron, Sydney, Australia prior to the start of this work. A detailed comparison of X-ray generation at lab and synchrotron sources is not provided here. However, synchrotron sources offer very intense monochromatic radiation and therefore high resolution diffraction data that may, for example, resolve subtle peak splitting not visible using a lab source. They also offer versatility in the wavelength of X-rays required unlike the D8 lab source which supplies Cu Kα_1 radiation at $\lambda = 1.540598$ Å. However, lab X-ray sources are far more readily available and are often sufficient for many standard characterisation needs.

1.5.2 TOF Neutron Diffraction

Time-of-flight (TOF) neutron diffraction data is also used throughout this thesis. All TOF neutron data analysed in this thesis was collected on HRPD or GEM at ISIS, Didcot, UK. Neutron scattering is highly complementary to X-ray diffraction data. Since X-ray scattering power is proportional to the number of electrons an atom has, it is very difficult to distinguish between atoms with a similar number of electrons and isoelectronic species are completely indistinguishable. Furthermore, it is difficult to accurately refine the position of atoms with a small number of electrons. Conversely, neutron scattering lengths vary independently of atomic number (they depend on the nuclear interaction distance of the isotope in question) and, unlike X-ray scattering, vary by isotope. This means that most atoms that cannot be distinguished by X-rays can be distinguished from neutron diffraction data; conversely, where neutron scattering lengths coincide, those atoms can usually be distinguished by X-ray diffraction data.

In the TOF neutron diffraction experiment, pulsed neutron bursts with a distribution of neutron velocities are directed at the sample. After diffraction by the sample, these neutrons reach the detector banks (which are positioned at a known fixed distance and angle from the sample) and the time of flight for the neutron can be measured. The wavelength of the neutron, λ, can be determined using the de Broglie relationship (Equation 1.11, where h is Planck's constant, m_n is the mass of a neutron, L is the flight path length and t is the flight time). Defining the neutron velocity as $v_n = L/t$, we can substitute into the Bragg equation and solve for d_{hkl} as in Equation 1.12. Due to the distribution of velocities, a range of d-spacing can be probed from a single fixed detector bank. Lower angle detector banks typically probe longer d-spacing ranges but have lower resolution.

$$\frac{h}{\lambda} = \frac{m_n L}{t}$$

Equation 1.11

$$\frac{h}{m_n v_n} = 2d_{hkl} sin\theta$$

Equation 1.12

1.5.3 Rietveld Refinement

The Rietveld method[14] is a least squares minimisation of the squares of the difference between calculated and observed diffraction patterns. It specifically minimises S_Y as defined by Equation 1.13, where for each point of diffraction data, m: w_m is the weight (Equation 1.14), $Y_{o,m}$ is the observed intensity with standard error $\sigma(Y_{o,m})$ and $Y_{c,m}$ is the calculated intensity.

$$S_Y = \sum_m w_m (Y_{o,m} - Y_{c,m})^2$$

Equation 1.13

$$w_m = \frac{1}{\sigma(Y_{o,m})^2}$$

Equation 1.14

The calculated pattern is generated from a proposed structure and peak shape description so the calculated pattern can be changed by incrementally adjusting the parameters of the model. The parameters used to create the calculated diffraction pattern include: structural parameters, such as unit cell parameters and atomic positions (either directly with Cartesian fractional coordinates or via the distortion mode basis); and additional parameters used to model other experimental and instrumental effects that affect peak shape and position. A good model for the structure, experimental and instrumental effects is needed to generate a calculated pattern that closely fits the observed data. In order to measure the quality of the fit to the observed data we typically quote a weighted Residual-factor (R_{wp}) as measured by Equation 1.15. R_{wp} is usually useful and sufficient when comparing fits to the same diffraction pattern over the same d-spacing range with a lower R_{wp} indicating a higher quality of fit. This is typically how R_{wp} will be used in this thesis. However R_{wp}, which is weighted to the inverse of the standard error squared, may sometimes give too little weight to small but important observed Bragg peaks and can therefore be insensitive to small improvements. Conversely, by including areas of the fit that contain no Bragg reflections it may give too much weight to merely fitting the background (i.e. a relatively low R_{wp} could be obtained for a diffraction pattern consisting mainly of background intensity even if the few Bragg peaks are poorly fitted). R'_{wp} is an alternative measure that is calculated in the same way as R_{wp} but with the background function subtracted to eliminate this problem. In cases in this thesis where an overall R_{wp} is quoted for combined refinements it is such that the contribution of each data set is approximately equal and the overall R_{wp} is the mean of the R_{wp} of the constituent fits.

$$R_{wp} = \sqrt{\frac{\sum_m w_m (Y_{o,m} - Y_{c,m})^2}{\sum_m w_m {Y_{o,m}}^2}}$$

Equation 1.15

We can also measure an unweighted R-factor, R_p, as defined by Equation 1.16 and R_{Bragg}, which measures the quality of fit only by "observed" and calculated intensities of reflections (Equation 1.17) where $I_{"o",k}$ and $I_{c,k}$ refer to the intensity of observed and calculated reflection k respectively. However, it should be noted that R_{Bragg} is biased by the model for peaks that overlap severely. In the extreme case of two completely overlapping peaks, R_{Bragg} takes no account of the unequal contributions of the different reflections to the overall intensity.

$$R_p = \sqrt{\frac{\sum_m |Y_{o,m} - Y_{c,m}|}{\sum_m Y_{o,m}}}$$

Equation 1.16

$$R_{Bragg} = \frac{\sum_m |I_{"o",k} - I_{c,k}|}{\sum_m I_{"o",k}}$$

Equation 1.17

As most fits presented in this thesis will compare the fit of multiple different models to the same diffraction data, R_{wp} will mainly suffice. To provide meaning to R_{wp} figures relative to the data (rather than relative to other fits to the data) we can measure the goodness of fit (GOF) or χ^2 as defined by Equation 1.18 where the R_{exp} is the expected minimum possible value of R_{wp} (Equation 1.19); depending on the number of data points (including constraints), M, and the number of parameters (including restraints), P.

$$GOF = \chi^2 = \frac{R_{wp}}{R_{exp}} = \sqrt{\frac{\sum_m w_m (Y_{o,m} - Y_{c,m})^2}{M-P}}$$

Equation 1.18

$$R_{exp} = \sqrt{\frac{\sum M-P}{\sum_m w_m {Y_{o,m}}^2}}$$

Equation 1.19

1.5.4 Pawley Refinement

It is also possible to fit powder diffraction data without including a structural sites model (i.e. using only a unit cell and a space group). This is called a Pawley[15] refinement, which generates allowed reflections on the basis of the unit cell and space group provided and then freely refines intensity of the generated reflections in order to fit the observed lineshape. This can be useful because it allows us to obtain a good model of the lineshape of observed peaks independently of the structural sites model. The Pawley refinement offers a simple check that the unit cell and space group provided do not result in systematic absences that are incompatible with the data.

1.5.5 TOPAS Academic

TOPAS Academic (TA)[16-18] is the Rietveld refinement software that is used throughout this thesis. TA reads in information for Rietveld refinement from text files in the form of extremely versatile input files (.inp files). The text editing software Jedit[19] is particularly useful because it can be easily configured to interact with TA and "knows" the keywords and formatting used in .inp files. The TA software contains countless innovations for both speed and ease of use across a range of refinement objectives, some of which are exploited and further-developed in this thesis. Refinements performed in this thesis were carried out using TA version 6 unless otherwise stated.

The basic objective of the Rietveld refinement is the minimisation of S_Y by incremental change of the available parameters. Due to the incremental nature of the change the process is prone to finding false or local minima; where the parameter set appears to be minimised because any incremental change will result in increased χ^2 but the global parameter space in fact contains a lower minima. The principal factors which dictate whether a refinement will find a false minimum are: the shape of the χ^2 cost function in the parameter space, the size of incremental changes to parameters, the constraints of the parameters, and the starting values of parameters. Of those, all can be manipulated: the χ^2 cost function by adding penalties (parameter restraints), and the others by changing parameters and adding limits in TA. However, the principal verification that a minimum is global must be by further (ideally full) exploration of the parameter space. For this reason it is helpful to randomise parameters to a new starting value once they have converged. The new set of starting parameters is then minimised by Rietveld refinement and again re-randomised in an iterative process called simulated annealing. A global minima is usually confirmed by identifying it repeatedly when starting from different parts of the parameter space. It is worth noting that when seeking to obtain a subgroup model by refinement of a parent structure as a starting point (which is the fundamental approach of the distortion mode basis), the parent structure is likely to represent a local minimum in the fit to diffraction data. This is because at least some diffraction peaks are likely to be insignificantly changed by the distortion (and so well fit by the parent). Therefore, simulated annealing where distortion mode amplitudes are reset to a random value close to zero but slightly perturbed from it is useful.

Most peak shape effects in powder patterns be approximated by using a simple pseudo-Voigt Thompson-Cox-Hastings[20] (TCHz) function. The six (u, v, w, x, y, z) parameter peak shape function describes Gaussian and Lorentzian components as defined by Equation 1.20 and Equation 1.21 respectively.

$$TCHz(Gauss) = \sqrt{u(tan^2\theta) + v(tan\theta) + w + \frac{z}{cos^2\theta}}$$

Equation 1.20

$$TCHz(Lorentz) = x(tan\theta) + \frac{y}{cos\theta}$$

Equation 1.21

Where anisotropic, hkl-dependent peak broadening is observed a Stephens[21] anisotropic peak shape may also be appropriate. In this case an additional hkl dependent anisotropic broadening term, $\Gamma_A(hkl)$, is included as defined by Equation 1.22 where σ is the variance of M_{hkl}. The individual components of M_{hkl} can vary by the refinement of A, B, C, D, E and F that allow a distribution of intensity about its centre with restrictions dependent on the crystal system. The Gaussian and Lorentzian terms are then defined by Equation 1.23 and Equation 1.24 respectively where ζ represents the relative scale between the two anisotropic broadening terms.

$$\Gamma_A(hkl) = \sqrt{\sigma^2 M_{hkl}}(\frac{tan\theta}{M_{hkl}}), M_{hkl} = \frac{1}{d^2_{hkl}} = Ah^2 + Bk^2 + Cl^2 + Dkl + Ehl + Fhk$$

Equation 1.22

$$TCHz + Stephens(Gauss) = \sqrt{u(tan^2\theta) + v(tan\theta) + w + \frac{z}{cos^2\theta} + (1-\zeta)^2\Gamma_A^2(hkl)}$$

Equation 1.23

$$TCHz + Stephens(Lorentz) = x(tan\theta) + \frac{y}{cos\theta} + \zeta\Gamma_A(hkl)$$

Equation 1.24

TA contains command line functionality allowing TA .inp files to be read in and refined using external programs and commands. There is also functionality allowing information to be included in .inp files directly from the command line or to be read in from externally created files and outputs collected in external text files. This makes the software ideal for running Rietveld refinements as part of a larger algorithmic process governed by external scripting. All external scripting in this thesis, unless otherwise specified, runs TA version 6 from command line with no graphics or console display. Chapter 2 introduces the methods we have developed and used in detail.

1.6 Thesis Overview

This thesis focuses on the development and use of structure determination tools and techniques. The distortion mode basis allows search algorithms to be simply and efficiently applied to structure solution of materials undergoing a phase transition involving group-subgroup relationships between parent and child. This allows a more direct exploration of the symmetry of materials leading to both robust and fast structure determination. This in turn allows us to explore the limits of information that can be extracted from powder X-ray and neutron diffraction using new innovations. We will show how we have developed a range of different algorithms with the suitability and speed of each depending on the nature of the search space. The new techniques are applied to a range of examples including both phases with a known structure and those previously unknown. The thesis studies phase transitions involving displacive, rotational and magnetic ordering.

In addition we develop new routines to model stacking faults in layered materials. We are able to develop routines offering a significant improvement in both speed and complexity of modelling. This allows new insights into the impact of stacking faults on a series of layered oxychalcogenides which will be generally applicable to other layered materials exhibiting similar faults.

Several times throughout this thesis we refer to computational time taken to perform specific tasks. Due to computer and TA software upgrades during the course of this work, two different set-ups are used (the set-up is specified wherever computational times are given) with significantly different baseline performance. Therefore as a benchmark we have given the time taken for each setup to perform a complex Rietveld refinement on a $Bi_2Sn_2O_7$ structure in Appendix 9.

1.7 References

(1) Hahn, T.; *International Tables for Crystallography Volume A.*, Reidel Publishing Co.: 1983.

(2) Cotton, F. A. *Chemical Applications of Group Theory*; John Wiley & Sons, 2008.

(3) Von Laue, M. *Ergebnisse der Exakten Naturwissenschaften* **1931**, *10*, 133.

(4) Wigner, E.; Seitz, F. *Physical Review* **1933**, *43*, 804.

(5) Brillouin, L. *J. Phys. Radium* **1930**, *1*, 377.

(6) Campbell, B. J.; Stokes, H. T.; Tanner, D. E.; Hatch, D. M. *Journal of Applied Crystallography* **2006**, *39*, 607.

(7) Setyawan, W.; Curtarolo, S. *Computational Materials Science* **2010**, *49*, 299.

(8) Landau, L. D. *Zh. Eksp. Teor. Fiz* **1937**, *7*.

(9) Müller, U. *Symmetry Relationships Between Crystal Structures: Applications of Crystallographic Group Theory in Crystal Chemistry*; OUP Oxford, 2013; Vol. 18.

(10) Hermann, C. *Zeitschrift für Kristallographie-Crystalline Materials* **1929**, *69*, 533.

(11) Stokes, H. T.; Hatch, D. M.; Campbell, B. J. *URL* http://www.iso.byu.edu **2007**.

(12) Stokes, H. T.; Hatch, D. M.; Campbell, B. J. *URL* http://stokes.byu.edu/iso/findsym.php **2007**.

(13) Ainsworth, C. M. *Synthesis, Structure and Properties of Metal Oxychalcogenides* **2016**, *PhD Thesis*.

(14) Rietveld, H. M. *Journal of Applied Crystallography* **1969**, *2*, 65.

(15) Pawley, G. *Journal of Applied Crystallography* **1981**, *14*, 357.

(16) Coelho, A. A. *Journal of Applied Crystallography* **2003**, *36*, 86.

(17) Coelho, A. A. *Bruker AXS, Karlsruhe, Germany* **2007**.

(18) Coelho, A. A.; Evans, J. S. O.; Evans, I. R.; Kern, A.; Parsons, S. *Powder Diffraction* **2011**, *26*, S22.

(19) Pestov, S. *URL* http://www.jedit.org **2008**.

(20) Thompson, P.; Cox, D.; Hastings, J. *Journal of Applied Crystallography* **1987**, *20*, 79.

(21) Stephens, P. W. *Journal of Applied Crystallography* **1999**, *32*, 281.

Chapter 2 Structure Solution by Exhaustive Symmetry Searches: Method Development and Testing on WO_3

2.1 Introduction

This chapter introduces techniques for structure solution of materials undergoing symmetry loss after phase transitions from powder diffraction data. It does this by testing search algorithms on known phases of WO_3. We start with a full analysis using an exhaustive subgroup search before showing how the same conclusions can be reached using a Genetic Algorithm approach or by simple inclusion/exclusion searches.

When a material is cooled through a phase transition there is usually an associated loss of symmetry. When the remaining symmetry elements of the new child phase are a subset of the symmetry elements of the parent, then the phases are said to have a group-subgroup relationship. In this situation it can be helpful to try to determine the structure of the new phase by determining which of the symmetry elements are lost from the parent phase rather than trying to establish the symmetry elements present in the child from scratch. This approach helps combat the problem of low information content when determining structures from powder data because a model containing too many symmetry elements will give a poor fit to diffraction data whereas a model with either the correct or a subset of the correct symmetry elements would still be able to fit the data.

The first requirement to implement this approach is to be able to describe the child as its parent plus a set of convenient parameters that destroy some of its symmetry. We can do this using symmetry-adapted distortion modes from ISODISTORT as discussed in 1.4.2.

The second requirement, specifically for our exhaustive search approach, is to create a comprehensive map of all the possible pathways for loss of parent symmetry. To do this we need a child structure which have sufficiently low symmetry (and generally lower symmetry than required) that it will fit all the features of diffraction data. We can then generate a subgroup tree using ISODISTORT as discussed in 1.4.2.

A full subgroup tree generated by ISODISTORT can be broken down into sub-trees based on the relative volume to the parent (which is the first member of the tree). That is to say that group-subgroup relationships within a sub-tree are strictly *translationengleiche*. Sub-trees appear in ascending order of the relative volume. The subgroup at the base of each of these sub-trees has the child space group but a different supercell to other subgroups that appear at the base of other sub-trees. The subgroups at the base of sub-trees are called “lattice subgroups”. The final lattice subgroup (and final subgroup in the entire tree) is the child subgroup. Figure 2.1a illustrates this arrangement. In section 2.6.2 we will show that, because the lattice subgroup of each sub-tree encompasses all of the degrees of freedom (DOF) within that sub-tree, they are useful for quickly eliminating possible structures from a subgroup tree.

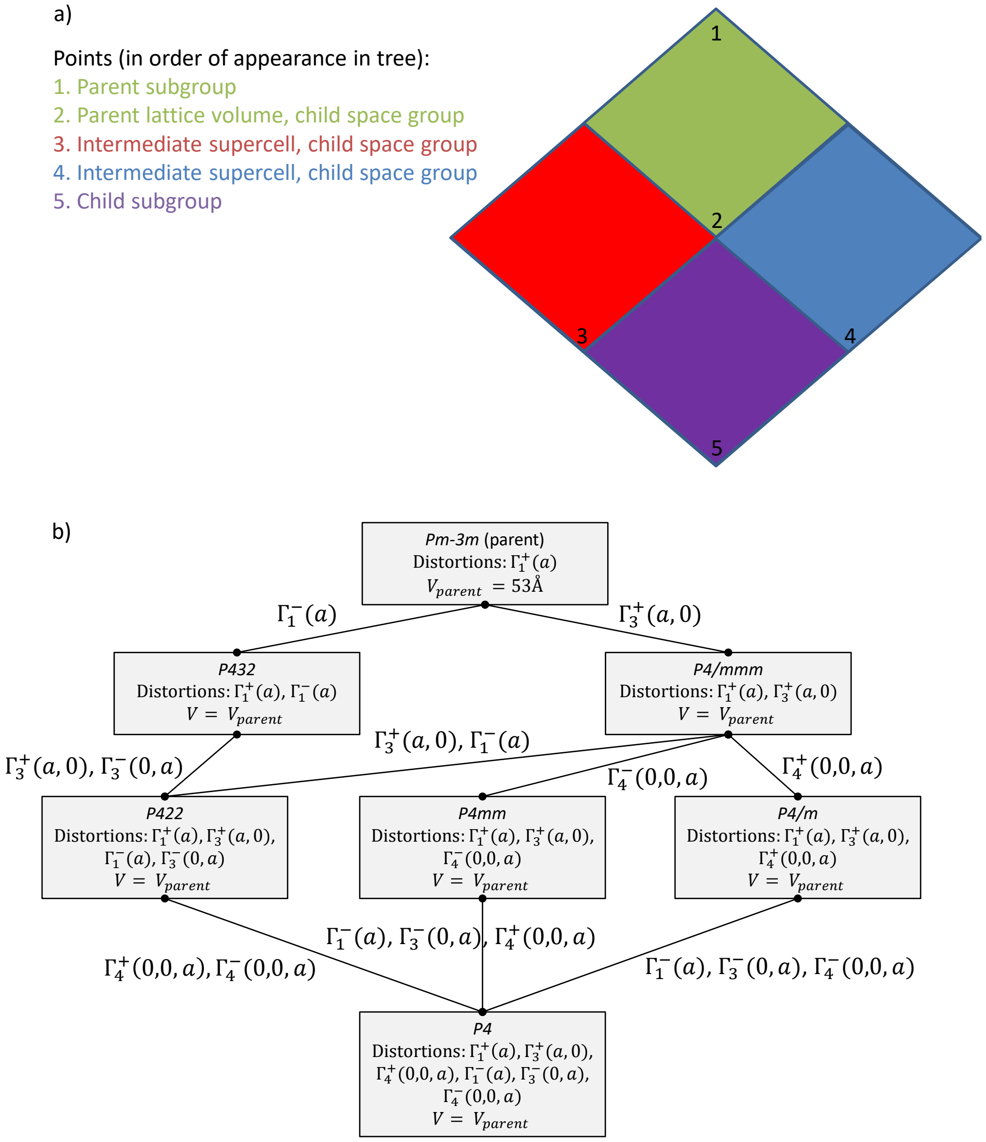

Figure 2.1: Simple example of a subgroup tree. Top panel (a) shows a subgroup tree containing several coloured sub-trees. ISODISTORT lists all the subgroups within a subtree before the next sub-tree. Bottom panel (b) shows a simple example of distortions within a sub-tree from the HT WO_3 distortion example we will use later (see 2.7).

2.2 Phase Transitions in WO_3

WO_3 is an excellent example of a material undergoing successive phase transitions involving distortions of a parent structure. Since the first description of room temperature WO_3 in the literature by Braekken[1], the structures of the multiple phases of WO_3 have been the subject of much debate. Each phase can be described as a distortion of a $Pm\bar{3}m$ parent phase which, even though it is never actually found for WO_3, is useful to imagine as the highest temperature structure. All the structures in the series are then subgroups of the parent structure which is perovskite-related but with the A site of the general ABX_3 perovskite vacant. Distortions throughout the series consist primarily of W atoms distorting off-centre within WO_6 corner-sharing octahedra of the parent structure and, for all but the highest temperature structure, concerted tilts of those octahedra. Figure 2.2 shows the progressive distortion of the series on cooling.

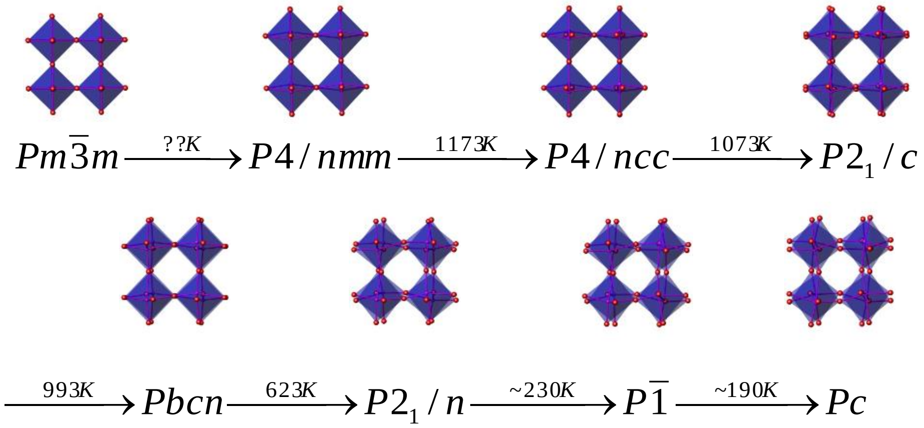

Figure 2.2: Distortions of WO_3 on cooling. All the phases can be described using the virtual cubic parent plus symmetry-adapted distortion modes. The distortions of the HT *P4/ncc* phase can be described with just two distortion modes, while the RT temperature phase needs seven for a good fit to diffraction data.

While the temperature stability ranges for each phase in the literature are still somewhat conflicting, it is clear that the hypothetical $Pm\bar{3}m$ parent (a_{parent} = 3.76Å) distorts to a (>1173K) $P4/nmm$ ($a \approx \sqrt{2}a_{parent}, c \approx a_{parent}$)[2] phase then to the following phases on progressive cooling: $P4/ncc$ (referred to as the high temperature structure in this chapter with $a \sim \sqrt{2}a_{parent}, c \sim 2a_{parent}$), $P2_1/c$ ($\sqrt{2}a_{parent} \times \sqrt{2}a_{parent} \times 2a_{parent}$, $\beta \sim 90.5^\circ$), $Pbcn$ ($2a_{parent} \times 2a_{parent} \times 2a_{parent}$), $P2_1/n$ (the room temperature structure with $2a_{parent} \times 2a_{parent} \times 2a_{parent}$, $\beta \sim 90.8^\circ$; the non-standard setting is used for comparative consistency), $P\bar{1}$ ($2a_{parent} \times 2a_{parent} \times 2a_{parent}$, $\alpha \sim 88.5^\circ$, $\beta \sim 90.5^\circ$, $\gamma \sim 90.5^\circ$) and Pc

($\sqrt{2}a_{parent} \times \sqrt{2}a_{parent} \times 2a_{parent}$, $\beta \sim 91.5^{\circ}$)[3-7]. The material has been of interest for colour switching,[8] anisotropic conductivity[9] and ferroelectricity.[10] There has also been interest in the tungsten bronze intercalates, M_xWO_3, due to ferroelectricity,[11] photochromic properties,[12] superconductivity,[13] and potential battery applications[14]. However in this chapter, we look at two test phases of WO_3 that illustrate the efficacy of different algorithmic search process in structure determination. Table 2.1 shows the important distortion mode contributions to each distorted structure.

Table 2.1: Important distortions of WO_3 phases. Column 3 indicates the supercell size relative to the cubic parent (*a* = 3.76 Å) excluding angles. Column 6 (*n*) indicates the number of distortion modes required for an adequate description of the distortion. These are indicated by bold letters in column 8. Column 7 (*p*) shows the number of traditional Cartesian xyz parameters required for the same description. This table is reproduced from Campbell et al.[15]

Temp (K)	*Space Group*	*Supercell /parent cell*	*Refs.*	*Glazer Tilt Symbol*	*n*	*p*	*Important irreps(OPDs)*
> 1173	*P4/nmm*	$\sqrt{2} \times \sqrt{2} \times 1$	16	$a^0a^0c^0$	1	2	$M_3^-(\boldsymbol{a},0,0)$
1063-1173	*P4/ncc*	$\sqrt{2} \times \sqrt{2} \times 2$	3,16	$a^0a^0c^-$	2	3	$M_3^-(\boldsymbol{a},0,0) + R_4^+(\boldsymbol{a},0,0)$
1033-1063	$P2_1/c$	$\sqrt{2} \times \sqrt{2} \times 2$	16	$a^-a^-c^-$	3	12	$M_3^-(\boldsymbol{a},0,0) + R_4^+(\boldsymbol{a},\boldsymbol{b},\boldsymbol{b});X_5^-(0,0,a,0,0,0)$
673-1033	*Pbcn*	$2 \times 2 \times 2$	3,16	$a^0b^+c^-$	4	12	$M_3^-(\boldsymbol{a},b,0) + R_4^+(\boldsymbol{a},0,0) + X_5^-(0,0,0,0,\boldsymbol{a},-\boldsymbol{a});M_3^+(0,0,\boldsymbol{a})$
290-673	$P2_1/n$	$2 \times 2 \times 2$	3,16	$a^-b^+c^-$	5	24	$M_3^-(\boldsymbol{a},b,0) + R_4^+(\boldsymbol{a},\boldsymbol{b},0) + X_5^-(0,0,a,a,\boldsymbol{b},-\boldsymbol{b});M_3^+(0,0,\boldsymbol{a})$
233-290	$P\bar{1}$	$2 \times 2 \times 2$	7,17	$a^-b^-c^-$	6	48	$M_3^-(\boldsymbol{a},b,0) + R_4^+(\boldsymbol{a},\boldsymbol{b},\boldsymbol{c}) + X_5^-(0,0,a,b,\boldsymbol{c},-\boldsymbol{d});M_3^+(0,0,a)$
< 233	*Pc*	$\sqrt{2} \times \sqrt{2} \times 2$	7,18	$a^-b^-c^-$	6	24	$M_3^-(\boldsymbol{a},0,0) + R_4^+(\boldsymbol{a},\boldsymbol{b},\boldsymbol{b}) + \Gamma_4^-(a,a,\boldsymbol{b});X_5^-(0,0,\boldsymbol{a},0,0,0)$

A simple example with which to begin is the distortion in the *P4/ncc* (1073K-1173K) phase. The tilting distortion can be described by a single $R_4^+(a,0,0)$ mode which rotates octahedra around the tetragonal axis (c axis of the parent). W displacements are also governed by just one $M_3^-(a,0,0)$ mode which displaces atoms parallel to the tetragonal axis.

A more complicated example is the room temperature phase. Campbell et al.[15] have been able to show that the room temperature structure can be described very well by applying just 7 distortion modes to the parent and reasonably well by just 5 distortion modes (considerably fewer than the 24 xyz coordinates that would be allowed to refine in the traditional description of this structure). In this chapter we work on the basis of the 7 mode fit. Two $M_3^-(a,b,0)$ modes and two $X_5^-(0,0,a,a,b,-b)$ modes contribute to the displacement of W from octahedral centres. The M_3^- modes correspond to an antiferroelectric distortion with W atoms moving out of phase with each other along all crystallographic axes while the X_5^- modes displace W atoms in the same direction along the b axis of the cubic parent.[19].

Meanwhile, two $R_4^+(a,b,0)$ distortion modes describe out-of-phase octahedral tilts for successive octahedra along the tilt axis while a single $M_3^+(0,0,a)$ mode describes in-phase octahedral tilting patterns leading to a Glazer tilt pattern of $a^-b^+c^-$.

2.3 Sample Preparation and Data Collection

The RT WO_3 diffraction data used in this chapter were collected prior to the start of this work. Samples for X-ray and TOF neutron powder diffraction analysis were prepared separately by Sarah Tallentire and Francesca Perselli respectively. In both cases, due to reagent grade WO_3 sometimes containing triclinic impurities, WO_3 (Alpha Aesar, 99.8 % purity) was ground in a mortar and pestle and annealed in a platinum crucible to 1273 K before being cooled at a rate of 0.25 K/min to 298 K. The samples were pale green/yellow and no evidence of impurity phases was found from lab X-ray data.

2.3.1 X-ray Data

X-ray powder diffraction data was collected on a Bruker AXS d8 Advance X-ray powder diffractometer by Sarah Tallentire. The sample was heated to 303 K by an Anton Paar HTK1200 furnace and data was collected for ~ 30 mins over a 10-140° 2θ range (d = 0.82 Å to 8.81 Å).

2.3.2 TOF Neutron Data

TOF neutron data was collected by John Evans. The sample powder was placed in a $10\ mm \times 25\ mm \times 18\ mm$ slab can on the High Resolution Powder Diffraction (HRPD) instrument at ISIS and data collected over a 30 minute period (16.6 µAh) at 300 K. The data presented here was collected on the back-scattering detector bank for TOF in the range 40-102.4 ms (d = 0.83 Å to 2.12 Å).

2.4 Choosing a Child Subgroup

The first step, universal to all our search processes, is to choose a child subgroup. The child must have a large enough cell and low enough symmetry that all the observable peaks in the diffraction data can be fitted (i.e. it must be a subgroup of the true structure). However, the child should be sufficiently simple that the searches don't become prohibitively large and complex.

For the RT phase, on which we will test all our search methods, we choose to limit the scale of the lattice distortion to supercells $2 \times 2 \times 2$ times the parent size. This matches the known lattice of the phase from the literature. We then choose space group *P1*. This illustrates that, in principle, nothing needs to be known or assumed about the space group symmetry of the phase in question (although this information can help limit the search) and ensures that our child structure meets the criteria above (it is a subgroup of the true structure).

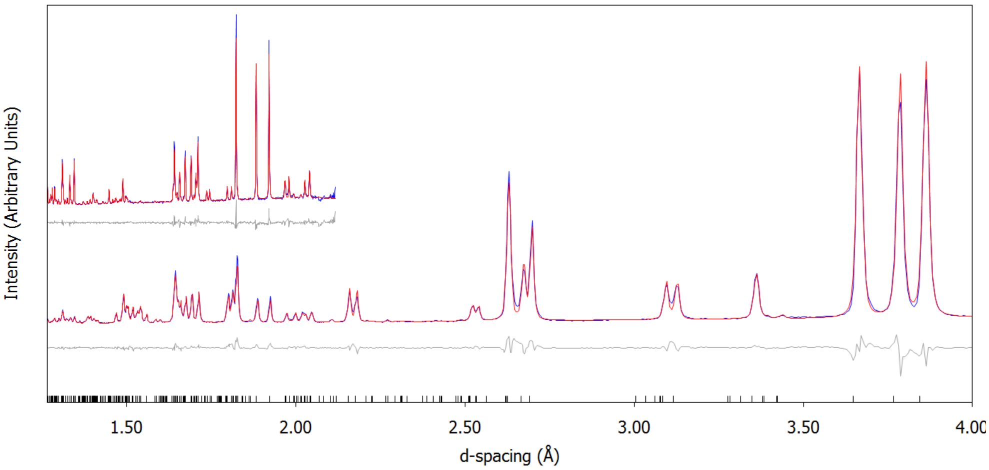

Figure 2.3: Rietveld fit to X-ray (bottom) and TOF neutron (top) data using the child subgroup. The model provides an excellent fit to all the features of both data sets. Space group *P1*, a = 7.29768(5) Å, b = 7.53516(5) Å, c = 7.68825(5) Å, α = 89.993(5)˚, β = 90.8579(9)˚, γ = 90.015(3)˚. R_{wp} (R_{Bragg}) for X-ray / TOF neutron are 7.76 % (3.46 %) / 5.70 % (2.75 %).

We can see from Figure 2.3 above that the child subgroup (*P1*, 2 × 2 × 2 supercell) does indeed provide an excellent fit to X-ray and neutron powder diffraction data as required. We can now use this fit to extract key, non-structural parameters for our search algorithms. This will save us having to redetermine these parameters when we repeatedly trial candidate structures and ensures differences arising in our fitness function are due to structural differences between candidates. Fixing these non-structural parameters also increases the probability of optimising the structural parameters that vary between candidates in a reasonable timeframe. A copy of this *P1* child subgroup fit containing all non-structural parameters extracted from it is available in e-Appendix 1.

For the HT phase (to which we only apply the exhaustive search) it seems more reasonable to limit the extent of the symmetry distortion to tetragonal cells by requiring at least retention of the parent 4-fold axis. The child space group is therefore *P4*. If the lattice distortion is again limited to the literature lattice then this simplifies the search significantly and illustrates how prior information can speed the process up. To further simplify the example and to give us a clear target for the exhaustive search, we use simulated X-ray data of the literature structure adding in noise and peakshape broadening effects similar to those found in real data.

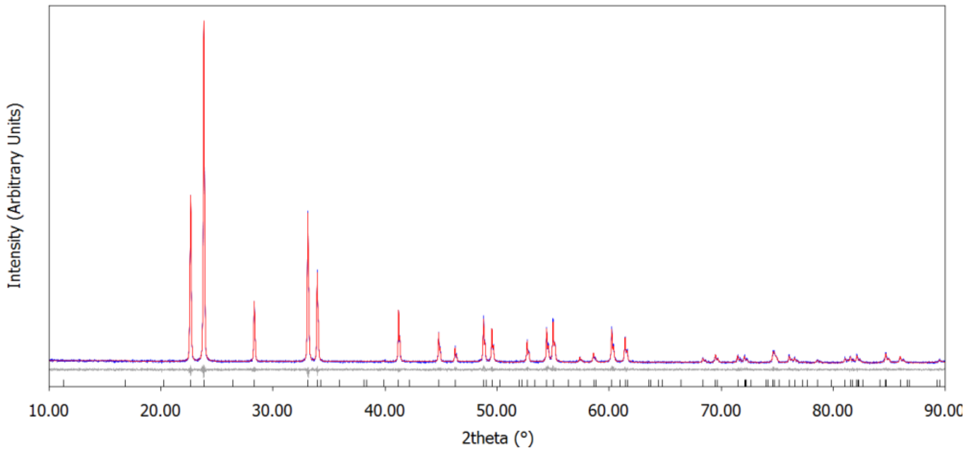

Figure 2.4: Rietveld fit to simulated X-ray data using the child subgroup. The model provides an excellent fit to all the features of the data because it is a subgroup of the simulated structure. Space group *P4, a* = 5.27591(3) Å, *c* = 7.84625(7) Å. R_{wp} (R_{Bragg}) = 10.88 % (1.67 %).

We can see from Figure 2.4 that the child subgroup again provides an excellent fit to simulated X-ray data as expected. In this case, as the data was simulated, we do not need to extract non-structural parameters from this fit because we know the parameters used to simulate the data and can simply reuse them throughout the exhaustive search process. A copy of our *P4* child fit to the simulated HT data can be found in e-Appendix 1.

2.5 Exhaustive Subgroup Search

Here we describe the steps needed to create and trial each subgroup in a subgroup tree against powder diffraction data sets at both RT and 1123 K. This allows us to exhaustively search through all the possible loss of symmetry pathways to identify the structure of each phase and show the result is consistent with the literature.

2.5.1 Set Up

For our RT child structure, ISODISTORT generates (see Appendix 1 for the method) 1427 candidate subgroups (including the parent structure) of which 10 (subgroups #2-4, #7, #217-219, #221, #223 and #225) have no active distortions. As it is clear that some supercell reflections are observed, there is no need for these to be considered in the search. This leaves 1416 candidates to test using our exhaustive method. We will show that even this relatively large subgroup tree can be explored on a reasonable timescale. For reference, subgroup #1357 is the literature structure assignment for RT WO_3. A full list of all subgroup candidates in the tree is given in e-Appendix 3.

For the HT phase, ISODISTORT generates (see Appendix 2 for the method) just 72 candidate subgroups between the parent and child (including the parent structure) of which 2 (subgroups #2 and #31) have no active distortions and are therefore not considered. This leaves 69 candidates to test using our exhaustive method. A full list of candidate subgroups can be found in e-Appendix 4. For reference, subgroup #58 is the literature structural model for HT WO_3.

2.5.2 Iterative Process

The general principle of all our search methods is to test a series of candidate structures by Rietveld refinement of the available structural parameters against diffraction data. At the end we use the quality of the Rietveld refinement, as measured by R_{wp}, and the number of parameters to choose an optimal candidate. Before this can happen, we must develop a refinement strategy that can be applied to all candidate subgroups in our tree which will allow the structural parameters to converge properly in each case. We have found that this is most reliable when each refinement is broken down into 2 steps; one focusing primarily on the optimisation of unit cell parameters and one focusing on the optimisation of distortion mode amplitudes. Python scripting (available in e-Appendix 2) controls the creation of .inp instruction files for Rietveld refinement in TA. The scripting first inserts information for each candidate structure into a predefined template .inp file that already contains refinement instructions, instrumental parameters and other non-structural information before sending it to TA and collecting the R_{wp} and structural information returned after refinement. Figure 2.5 summarises the overall process.

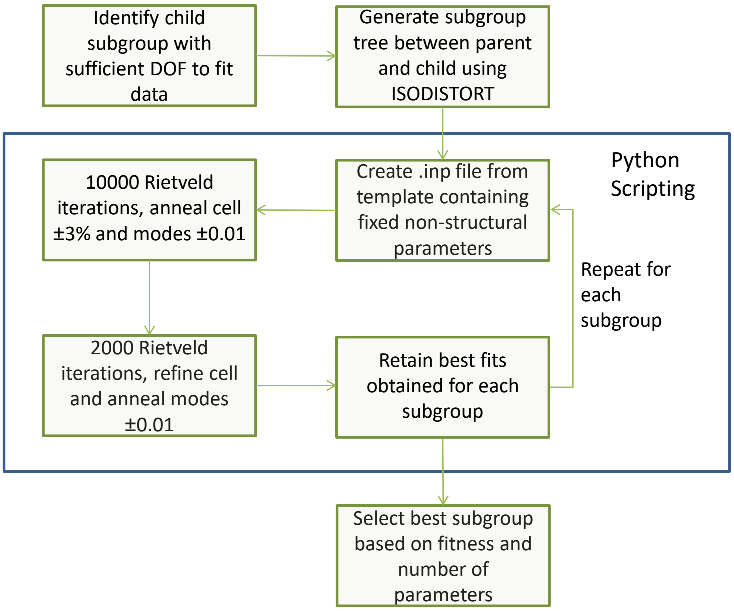

Figure 2.5: Schematic of exhaustive search process used for RT and HT WO$_3$.

To ensure that we find the best possible fit to the data that can be provided by each of the candidates, we perform a fixed number of Rietveld refinement iterations (a single step change in refineable parameters). We use a χ^2 convergence criteria of a ≤ 0.001 improvement for two consecutive iterations after which parameters are randomised on convergence to new values and refinement continues to convergence again. Each randomisation and re-convergence process is known as a Rietveld cycle. The best model found is saved at the end of each of the two protocols described below.

2.5.2.1 Lattice Refinement

In the first step the focus is to optimise the unit cell parameters of the candidate to account for the observed lattice distortion as well as possible. Distortion modes are included in this step because we cannot be sure that the optimal values of the cell parameters (in terms of R_{wp}) are not significantly different when they are excluded. In both HT and RT cases the scale of the distortion approaches but does not exceed a 3 % change in any given cell parameter relative to the cubic position. Therefore we find that a randomisation to a value within ±3 % of starting unit cell parameters (which are derived from the mean, undistorted cubic cell) on convergence (a 3 % annealing) is an effective choice. We also find it helpful to convolute an additional refineable parameter (ostensibly a peakshape parameter) with the unit cell parameters to aid their convergence. This allows calculated reflections to overlap with observed peaks from their cubic starting positions using an initially broad peakshape. A Gaussian strain parameter with FWHM initially approximately equal to the splitting in the

200/020/002 (RT) and 110/002 (HT) reflections is effective (see Figure 2.6). As the cell parameters optimise, the contribution of Gaussian strain broadening tends to zero, leaving only the fixed peakshape based on the child structure refinement. In this step we have found that 10000 iterations are sufficient to be confident of finding the right cell. We find this occurs for the child subgroup in 59/133 cycles and 122/180 cycles for RT and HT searches respectively. Given the child subgroup has more parameters than any other then we can be confident of efficient convergence in this step for all candidate subgroups.

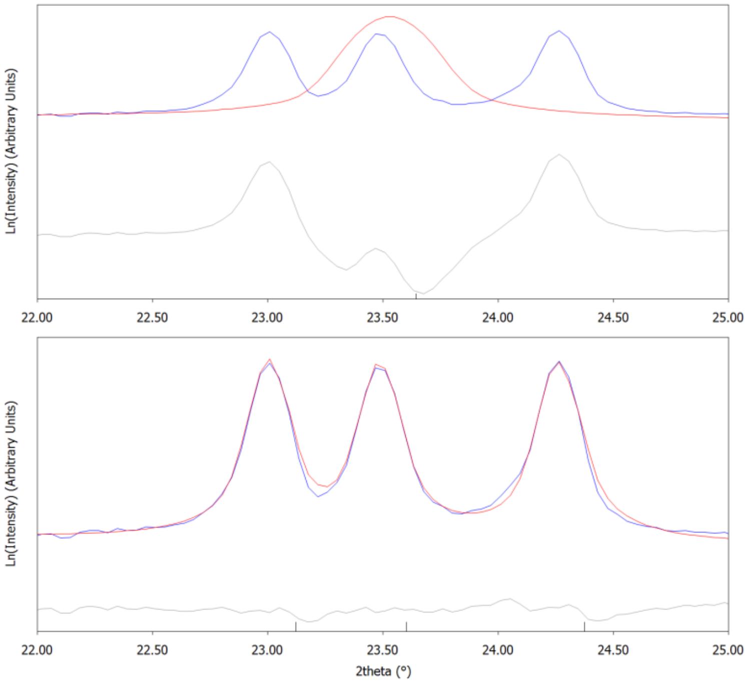

Figure 2.6: RT child subgroup fit to X-ray diffraction data, plotted on a logarithmic scale to emphasise peak tails. Top view shows initial cubic calculated model with calculated 200, 020 and 002 reflections at the same 2θ value with a broad peakshape. Bottom view shows fit after initial lattice refinement stage. Due to the broad initial peakshape, the reflections have at least partial overlap with the observed peak positions and cell parameters converge to monoclinic values quickly. The peakshape then narrows to fit the true profile.

2.5.2.2 Full Optimisation

In the second step the focus is on fully optimising all parameters from the values found in the first step. Once the cell parameters are close to their true values it is much more likely for a refinement to successfully converge than if the cell begins undistorted. Therefore, the cell parameters need only be refined (not annealed) to allow for small changes to fully optimise as distortion mode parameters vary. It is useful to anneal the distortion modes by resetting their value close to zero after each cycle. It also aids convergence to restrain the amplitude of modes to zero unless the diffraction data requires their inclusion by applying a "penalty" as a function of mode amplitudes throughout both steps. This, together with restricting atomic displacement to < ~ 0.5Å, prevents unphysical models being obtained and aids convergence. For the child subgroup we find that 2000 iterations for both RT and HT phases are sufficient to fully optimise parameters in 16/27 and 37/63 cycles respectively. Again we can then be confident of optimal convergence for all candidate subgroups. The repeatability of our experiments (see 2.6.1.3 and 2.7.1.2) gives further reassurance.

2.6 Room Temperature Structure Solution

2.6.1 Full Exhaustive Search Results

The simplest and most exhaustive approach we can take for RT WO_3 is to trial all 1416 candidate subgroups with active distortions in the tree between the $Pm\bar{3}m$ parent and our $2 \times 2 \times 2$ $P1$ child. It takes around 27 hours to complete the nearly 17 million Rietveld iterations on a desktop PC (6th generation i7, 3.4 GHz) using tc.exe from command line with no graphics plotted. Figure 2.7 below shows the R_{wp} achieved for each of the 1416 candidates in our tree against X-ray and TOF neutron powder diffraction data.

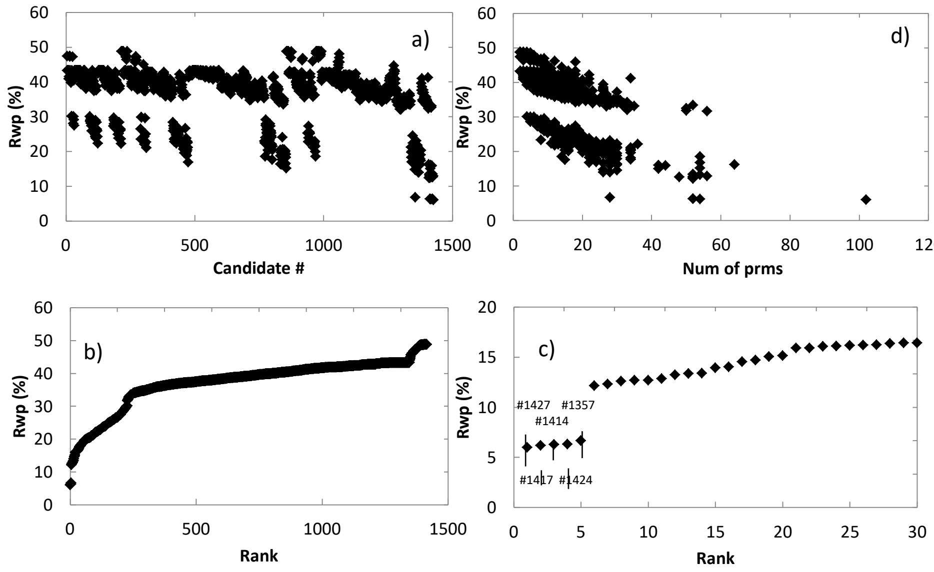

Figure 2.7: Combined R_{wp} obtained for each of 1416 candidate models after Rietveld refinement against lab X-ray and TOF neutron powder diffraction data of RT WO_3. Individual panels show: (a) R_{wp} as a function of tree candidate subgroup number; (b) R_{wp} of all candidates in ranked order; (c) R_{wp} of only best 30 candidates in ranked order with labels identifying the top five subgroups; and (d) R_{wp} of all candidates as a function of the number of structural parameters available to them.

We can see from Figure 2.7a that subgroups divide into three R_{wp} tiers of fitness depending on whether they have sufficient distortion modes available in each of the four ($X_5^-, R_4^+, M_3^-, M_3^+$) important distortion branches: very poor with $R_{wp} > 30$ % (typically lacking the important DOF of at least two of the four significant distortion irreps), poor with 30 % $> R_{wp} >$ 10 % (lacking the important DOF of at least one of the four significant distortion irreps), and good with $R_{wp} < 10$ % (all the important DOF are present). Looking at candidates in ranked order (Figure 2.7b and c; all candidates and best thirty respectively), they divide into several R_{wp} plateaus, the lowest of which (Figure 2.7c) contains five candidates. Finally, looking at the fitness of candidates by the number of structural parameters they have (Figure 2.7d), we can see that one of the five best candidates has far fewer parameters (28) than any other. This candidate is number #1357 in our tree with R_{wp} = 6.75 % and matches the literature $P2_1/n$ ($2a_{parent} \times 2a_{parent} \times 2a_{parent}$, β ~ 90.8°) structure. While this kind of simple analysis is very useful and the correct choice appears obvious in this case, we can also show additional evidence for choosing this structure, which is useful in more complex examples.

2.6.1.1 Visual Evidence

The simplest evidence we can give for candidate #1357 being the correct model is that it gives an excellent fit to our powder diffraction data (Figure 2.8). The quality of fit is visually identical to the child subgroup with far fewer parameters and all the key features of the data are accounted for. However, this does not prove that an even simpler structure would not also provide an excellent fit to the data. Due to the exhaustive nature of our search, if such a structure exists, it must be another candidate in our tree. The next best fit to the data provided by a candidate with fewer parameters than #1357 is candidate #1368 ($P2/n$, 26 parameters, R_{wp} = 14.04 %, rank 16) and its fit is shown in Figure 2.9. It is clear that this structure provides an inadequate fit to the diffraction data. Assuming that no structure with higher R_{wp} provides an adequate fit to our data, we can conclude that candidate #1357 is not missing any symmetry elements that are present in the RT structure of WO_3.

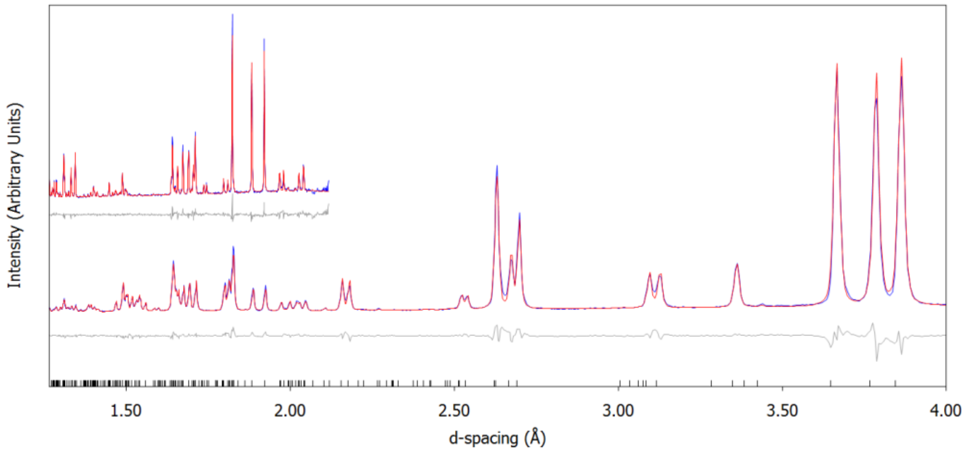

Figure 2.8: Rietveld fit to X-ray (bottom) and TOF neutron (top) data using candidate #1357. The quality of fit is comparable to that achieved by the child subgroup. Space group *P2₁/n*, *a* = 16.92183(14) Å, *b* = 7.53513(5) Å, *c* = 7.68837(5) Å, *β* = 154.4552(3)˚. R_{wp} (R_{Bragg}) for X-ray / TOF neutron is 7.75 % (3.51 %) / 6.59 % (3.16 %).

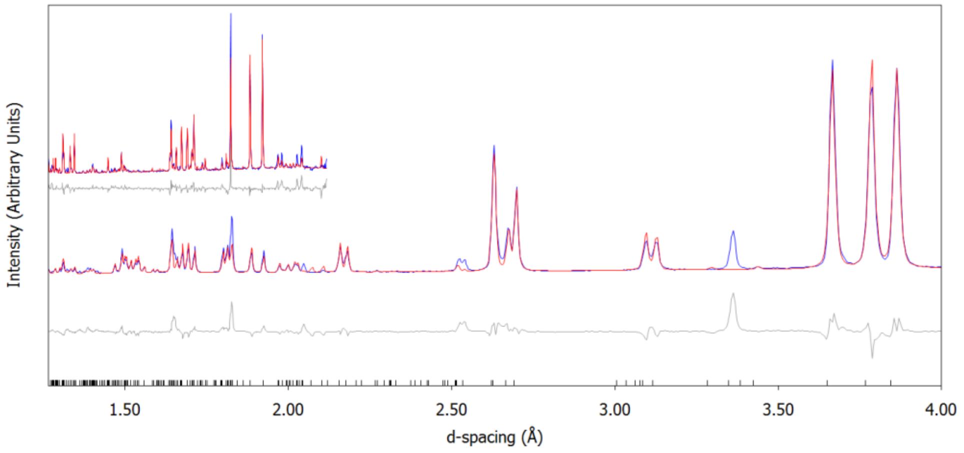

Figure 2.9: Rietveld fit to X-ray (bottom) and TOF neutron (top) data using candidate #1368. There are obvious deficiencies in the quality of the fit. Space group *P2/n*, *a* = 16.5992(3) Å, *b* = 7.53504(11) Å, *c* = 7.29787(11) Å, *β* = 152.4124(6)˚. R_{wp} (R_{Bragg}) for X-ray / TOF neutron is 18.26 % (10.41 %) / 13.30 % (8.40 %).

2.6.1.2 F-tests

The Hamilton R-ratio test[20] is a type of F-test designed to determine whether the fit of a model with more freedom (lower symmetry) is statistically better than a model with less freedom (higher symmetry) given the extra parameters of the less constrained model and the data set in question. While the test is most appropriate for structures derived from single crystal diffraction, we still find it can be of use with powder data.

A major difficulty with applying F-tests to powder data is in the counting of observations when there is peak overlap. Determining the number of observations is important because the principle of the test is that more observations allow the selection of a lower symmetry model with more certainty for a given improvement in fitness. For RT WO_3 we can show that even with a very conservative view of the number of observations (each peak cluster in the pattern counts as one observation, assuming overlapping reflections are completely indistinguishable and discounting the mode amplitude restraints in the model), candidate #1357 is still chosen in preference to the higher symmetry candidate #1368 using a 95 % certainty criteria. We can also show that, even when a very optimistic view of the number of observations is taken (every predicted reflection counts as one observation, imagining there is no peak overlap and counting each restraint in the model as an observation), candidate #1357 is chosen over a lower symmetry alternative with slightly better fitness (candidate #1427, the *P1* child subgroup, 96 parameters, R_{wp} = 6.00 %, rank 1) using a 95 % certainty criteria. Table 2.2 summarises these two F-tests. While a more realistic estimate of the number of observations clearly lies between these two extremes, candidate #1357 would be chosen for any such value. This gives confidence in our assignment.

Table 2.2: F-tests for selected candidates. Candidate X is the high symmetry model and candidate Y is the low symmetry model. A conservative observation count is used for candidate #1368 vs. #1357 while an optimistic count is used for #1357 vs. #1427.

Candidate #X vs. #Y	*1368 vs. 1357*	*1357 vs. 1427*
R_{wp} of X (%)	14.043	6.752
R_{wp} of Y (%)	6.752	6.004
observations (n)	33	444
parameters of X (q)	26	28
parameters of Y (p)	28	102
p-q	2	74
n-p	5	342
F value (X vs. Y)	8.314	1.224
95 % probability	1.9	1.59
Is Y proven?	Yes	No

2.6.1.3 Repeatability

In order to verify that we have obtained the best fit to the diffraction data for each candidate we have repeated our search process three times (51 million Rietveld iterations) and found an essentially identical fit for each of the 1416 subgroup candidates in all three runs. Figure 2.10 is a scatter plot showing the R_{wp} found for each candidate in each of the three runs.

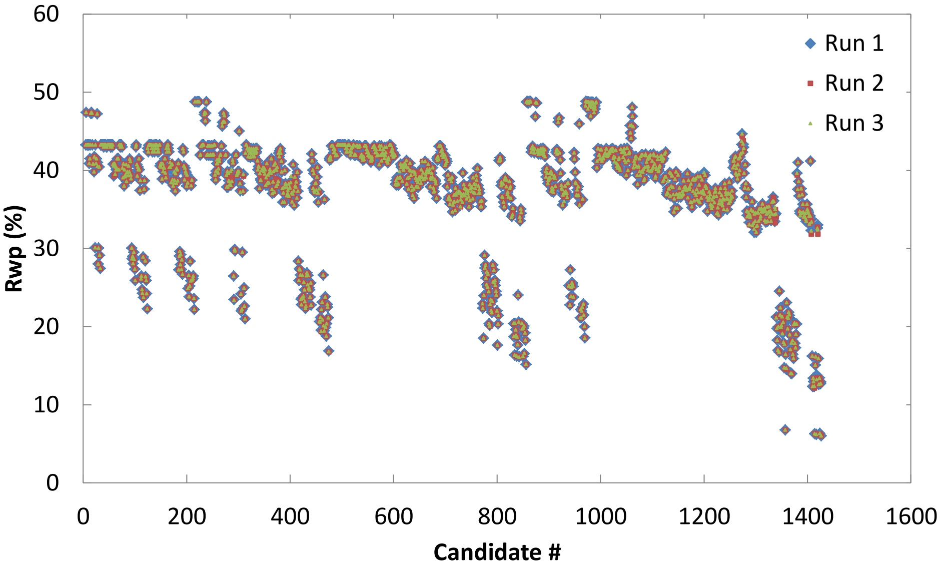

Figure 2.10: Overlay plot showing combined X-ray/TOF neutron R_{wp} found for each of the 1416 candidate subgroups on three repeats of the exhaustive search process. The small green triangles (run 3) lie on top of medium sized red squares (run 2) which lie on top of large blue diamonds (run 1). This shows that an essentially equivalent fit to our diffraction data is found in all three runs for all candidates.

We also show that our chosen penalty function, which restrains the sum of the mode amplitudes squared ($\sum a^2$ where a is the mode amplitude) to zero, is effective at producing repeat convergences to a similar R_{wp} minimum. Figure 2.11 shows the percentage of repeat convergences for both refinement steps for both our mode amplitude squared penalty and a softer logarithmic penalty on selected candidates with a very large number of distortion modes available.

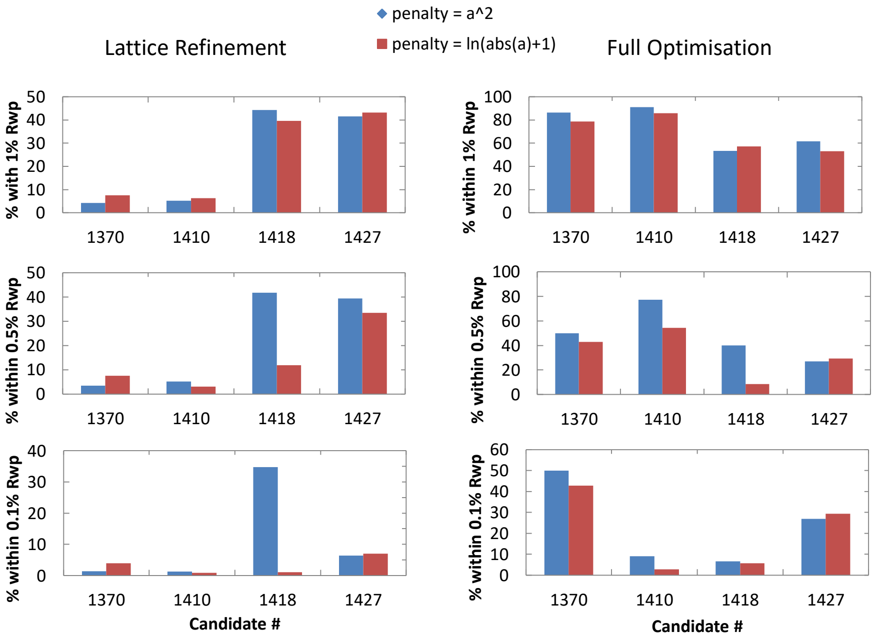

Figure 2.11: Percentage of convergences achieved within: (top row) 1 % R_{wp} of minimum, (middle row) 0.5 % R_{wp} of minimum and (bottom row) 0.1 % of minimum for four of the candidates with the highest number of parameters. Left column shows convergences in the lattice refinement step and right column shows convergences in full optimisation step. Generally an a^2 penalty gets either a higher or a similar percentage success rate than an $\ln(Abs(a)+1)$ penalty. Throughout our exhaustive runs each candidate achieves the same convergence within 1 % R_{wp} on at least 10 occasions (see e-Appendix 5). All R_{wp} values are combined X-ray / TOF neutron.

Using the 'within 1 % R_{wp}' criteria, we can also show that we have obtained an equivalent convergence in at least 10 separate Rietveld cycles for both steps of our annealing process for all 1416 candidates (see e-Appendix 5). Given we reset structural parameter values at the end of each cycle, this shows adequate internal consistency in our refinement process.

2.6.2 Lattice Subgroup Search

An alternative and potentially quicker approach to exhaustively trialling every candidate is to begin by searching only the lattice subgroups in the 1416 member tree. A lattice subgroup has all the symmetry elements of the parent removed and therefore has space group *P1*. The size of the lattice relative to the parent is therefore the only differentiator between them. As described in Section 2.1, our ISODISTORT tree is ordered such that it can be subdivided into several smaller trees each with a lattice subgroup at the base. In the WO$_3$ case there are 8 such lattice subgroups and their relationship is summarised in Figure 2.12 below. By searching only these candidates we can first identify the simplest lattice distortion that fits the data and then we only need to search amongst supergroups of that lattice subgroup.

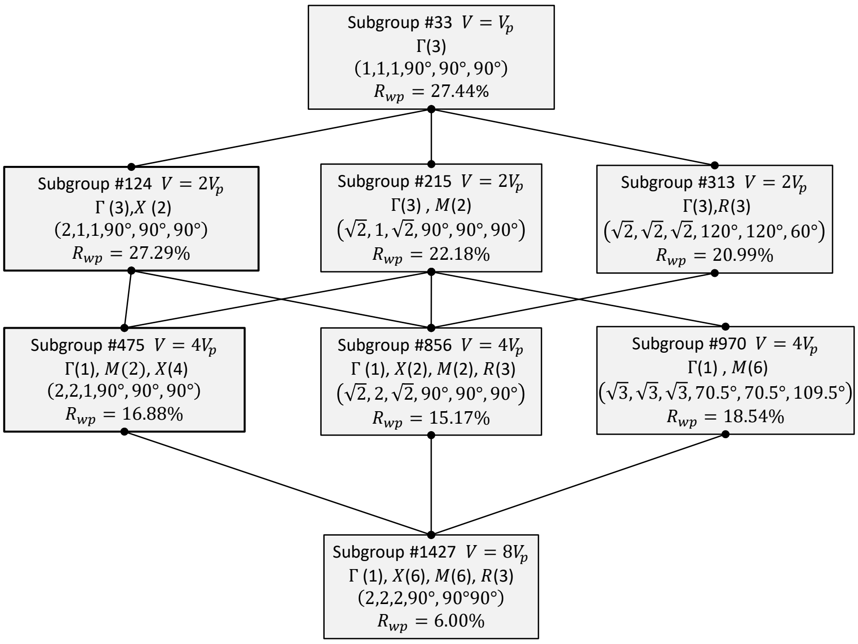

Figure 2.12: Lattice-sublattice relationships amongst the 8 lattice subgroup candidates extracted from the tree of 1427 candidates for WO_3. For each entry, the first line shows the subgroup candidate number and the cell volume (relative to that of the parent cell, V_p = 53 Å^3); the second line indicates the active k-vectors with the maximum number of DOF available to it; the third line shows the unit cell parameters (a/a_{parent}, b/a_{parent}, c/a_{parent}, α, β, γ), with edge lengths presented relative to the cubic parent (a_{parent} = 3.76 Å) and angles in degrees; the fourth line gives the combined R_{wp} resulting from the refinement against X-ray and TOF neutron powder diffraction data. A given lattice is linked to each of its minimal superlattices and maximal sublattices with a solid black line. Each lattice contains a subset of the DOF of its sublattices.

The initial search of the 8 lattice subgroup candidates takes only 18 minutes on a desktop PC (6th generation i7, 3.4 GHz) to complete the 96000 Rietveld iterations. Figure 2.13a, b and c show the R_{wp} of the 8 lattice subgroup candidates against candidate number, in ranked order and against number of parameters respectively. It's easy to see that the correct choice must be candidate #1427 (i.e. the child subgroup). No other lattice subgroup provides a reasonable quality of fit to our data. Although the child subgroup has the most parameters we know from this analysis that at least some of those additional parameters are important and reflect real symmetry broken from the parent.

This process then leaves us with 457 possible candidates to investigate (candidates #971-#1427 in the full tree). Given we have already trialled candidate #1427 this leaves 456 further space symmetry combinations to trial within this lattice subgroup. This takes a further 11 hours on a desktop PC (6th generation i7, 3.4 GHz) to complete the approximately 5.5 million Rietveld iterations.

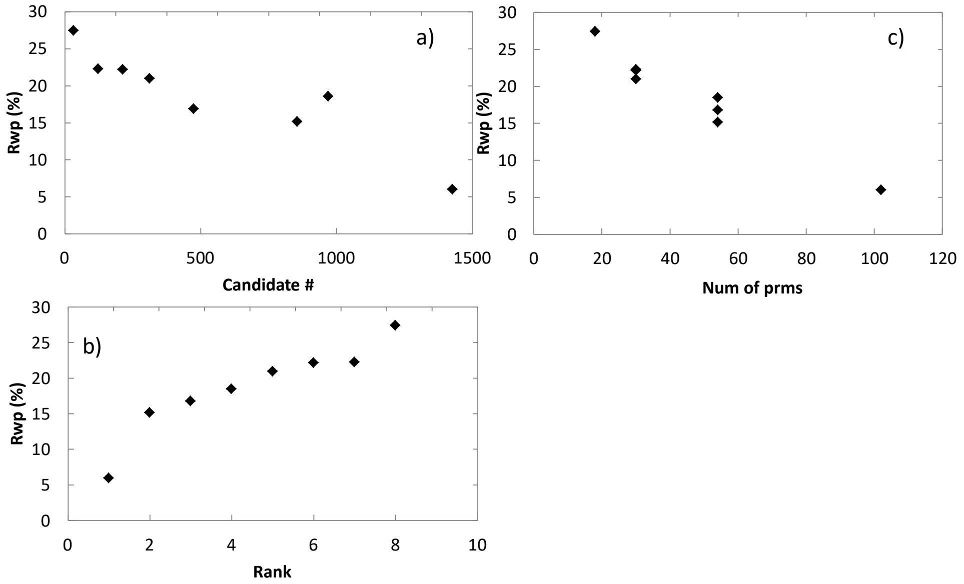

Figure 2.13: Combined R_{wp} obtained for each of 8 lattice subgroup candidates after Rietveld refinement against lab X-ray and TOF neutron powder diffraction data of RT WO_3. Individual panels show (a) R_{wp} as a function of tree candidate number (b) R_{wp} of all candidates in ranked order and (c) R_{wp} of all candidates as a function of the number of structural parameters available to them.

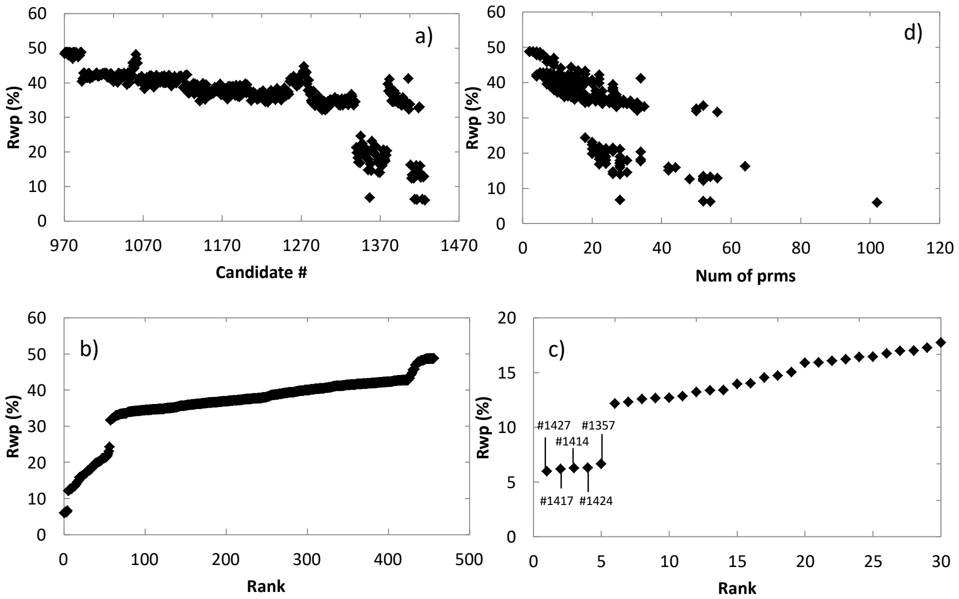

Figure 2.14: Combined R_{wp} obtained for each of 457 candidates (#971-#1427 in the original tree) after Rietveld refinement against lab X-ray and TOF neutron powder diffraction data of RT WO_3. Individual panels show (a) R_{wp} as a function of tree candidate number (b) R_{wp} of all candidates in ranked order (c) R_{wp} of only best 30 candidates in ranked order and (d) R_{wp} of all candidates as a function of the number of structural parameters available to them.

Figure 2.14 shows the fit obtained for just candidates #971-#1427. It is easy to see that the conclusion for which is the "best" model will be the same as reached in the full exhaustive search (candidate #1357 has the fewest parameters of the candidates on the lowest R_{wp} plateau). This conclusion is reached in less than half the time taken by trialling all candidate subgroups. The time savings would be even greater if the chosen lattice subgroup was not the child subgroup. This would have meant the remaining candidates having fewer parameters on average than those with the child lattice subgroup and so the Rietveld iterations would have been completed more quickly. Even so, a lattice subgroup search is an effective way to quickly trial the full solution space of the exhaustive search without trialling every candidate in a large tree that spans multiple lattice distortions.

2.7 850°C Structure Solution

Turning to HT WO_3, we selected a *P4* child subgroup. This means that our tree contains only structures with *P4* or higher space symmetry and therefore no *P1* lattice subgroups. While it would be possible to break our search down by initially searching only amongst space group *P4* candidates, given there are just 69 candidates to trial, we choose to just use a fully exhaustive approach in this instance. Furthermore, this example forms the basis of a step-by-step tutorial we have created for the exhaustive process, a link to which can be found in Appendix 4.

2.7.1 Full Exhaustive Search Results

It takes just 10 minutes to trial all 69 candidates with active distortions on a desktop PC (6th generation i7, 3.4 GHz), completing 483,000 Rietveld iterations in total. We can see from Figure 2.15a that candidates divide into three R_{wp} tiers of fitness depending on which of the two important distortion branches (R_4^+, M_3^-) are available to them: very poor with $R_{wp} > 40$ % (which have neither distortion available), poor with $30\ \% > R_{wp} > 20$ % (which always lack the M_3^- distortion), and good with $R_{wp} < 15$ % (which always have the M_3^- distortion available). Looking at candidates in ranked order (Figure 2.15b and c), the "good" grouping divides further into several R_{wp} plateaus. Only the best of these plateaus, containing 5 candidates with $R_{wp} < 10.9$ %, have both distortions available. All other candidates in the "good" grouping lack the R_4^+ distortion. The presence of M_3^- distortions leads to a much larger R_{wp} improvement because X-rays are more sensitive to W atomic shifts than the WO_6 rotations associated with R_4^+ distortions. Finally, looking at the fitness of candidates as a function of the number of structural parameters (Figure 2.15d), we can see that one of the 5 best candidates has fewer parameters (5) than the others. This candidate is #58 in our tree, with R_{wp} = 10.88 %. This matches the literature *P4/ncc* $(a = \sqrt{2}a_{parent}, c = 2a_{parent})$ structure. In this case, as we used simulated data, we should be able to clearly support our assignment with visual evidence alone.

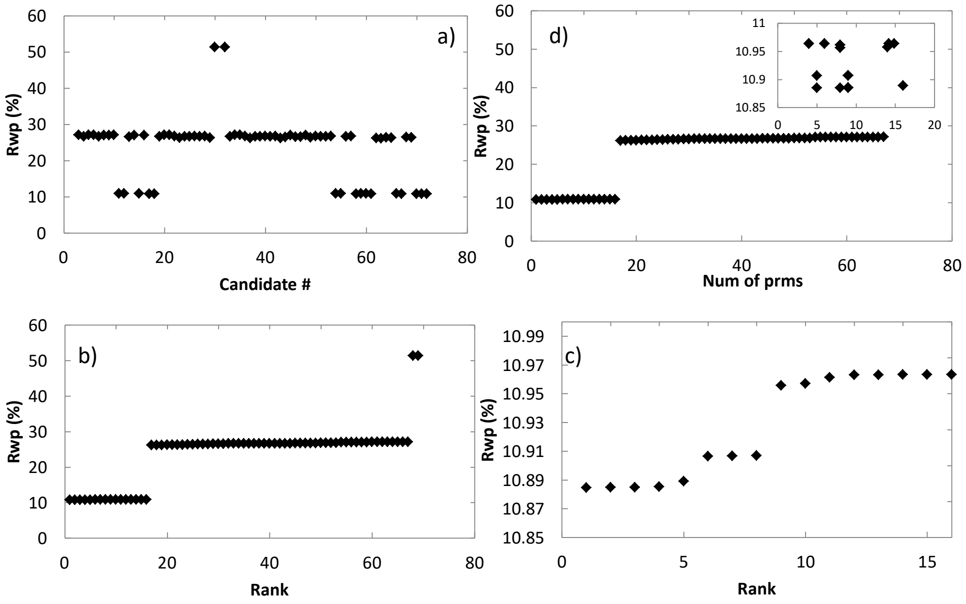

Figure 2.15: R_{wp} obtained for each of 69 candidates after Rietveld refinement against simulated X-ray powder diffraction data of HT WO_3. Individual panels show (a) R_{wp} as a function of tree candidate number (b) R_{wp} of all candidates in ranked order (c) R_{wp} of only best 16 candidates in ranked order and (d) R_{wp} of all candidates as a function of the number of structural parameters available to them.

2.7.1.1 Visual Evidence

We can start by inspecting the fit provided by candidate #58 (Figure 2.16). Unsurprisingly, given this is the simulated data, we have an excellent fit. We also note that the quality of fit (as measured by R_{wp}) is the same as achieved by the child subgroup to 2 decimal places. For real data we would expect to see the additional parameters of the child subgroup slightly improve the fit to the data by accounting for non-structural peakshape effects. The additional parameters of the child subgroup do not improve the fit here because an ideal peakshape was used in simulations. This allows us to immediately exclude a lower symmetry candidate choice because there is no candidate that provides a better fit to the simulated data than candidate #58, regardless of how many parameters it has.

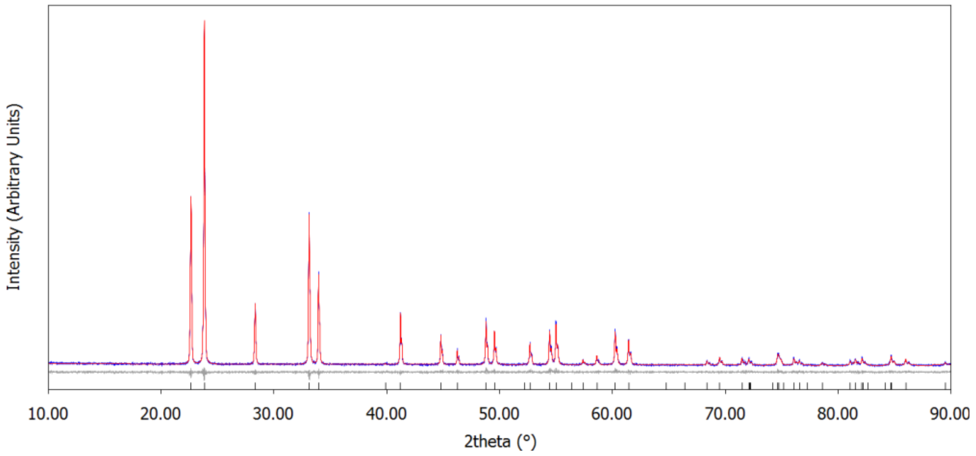

Figure 2.16: Rietveld fit to simulated X-ray data using candidate #58. The model fits all the features of the data excellently. Space group *P4/ncc*, *a* = 5.27591(3)Å, *c* = 7.84625(7)Å. R_{wp} (R_{Bragg}) = 10.88 % (1.68 %).

We must also exclude the existence of a higher symmetry candidate that can provide an equivalent fit to candidate #58 with fewer parameters. The highest ranked candidate with fewer parameters is candidate #11 (*P4/nmm*, 4 parameters, R_{wp} = 10.96 %, rank 14). While the R_{wp} is only fractionally worse than candidate #58, there are some deficiencies in the fit to the data (Figure 2.17). The most notable of these deficiencies, arising from the lack of R_4^+ distortions in candidate #11 to account for the octahedral tilts present in this phase, is at a 2θ angle of 39.9˚. The peaks arising (and the R_{wp} difference resulting) from this distortion are small because of the relative insensitivity of X-rays to O. Even plotted on a logarithmic scale (Figure 2.18) it is difficult to differentiate the 39.9˚ peak from the background. Only by removing the simulated noise is it clear the peak is a structural feature of the data. This illustrates the difficulty in extracting structural information from real powder data with low information content for some active distortions. If real X-ray diffraction data alone was used then the visual evidence may suggest that candidate #11 is the best choice. This illustrates the useful complementarity of X-ray and neutron data together.

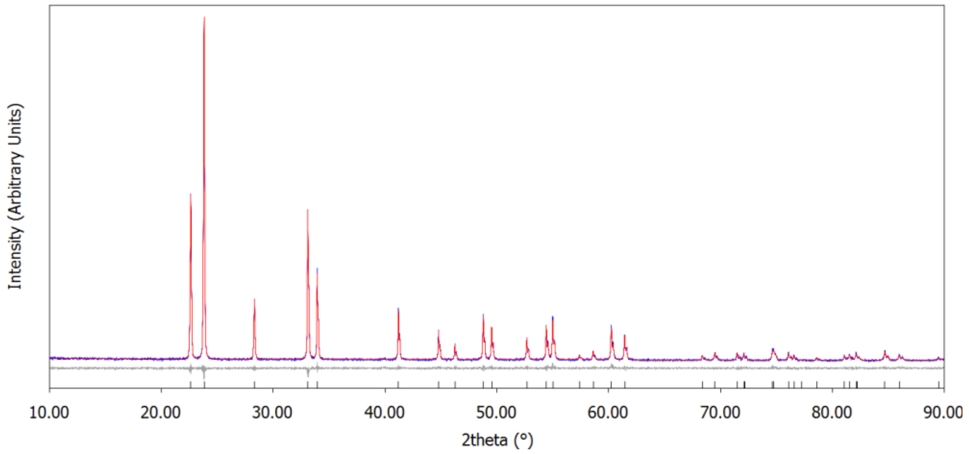

Figure 2.17: Rietveld fit to simulated X-ray data using candidate #11. The model has slight deficiencies for some very small peaks compared to candidate #58, most notably at 39.9˚ 2θ. Space group *P4/nmm*, *a* = 5.27590(3)Å, *c* = 3.92313(7)Å. R_{wp} (R_{Bragg}) = 10.96 % (2.08 %).

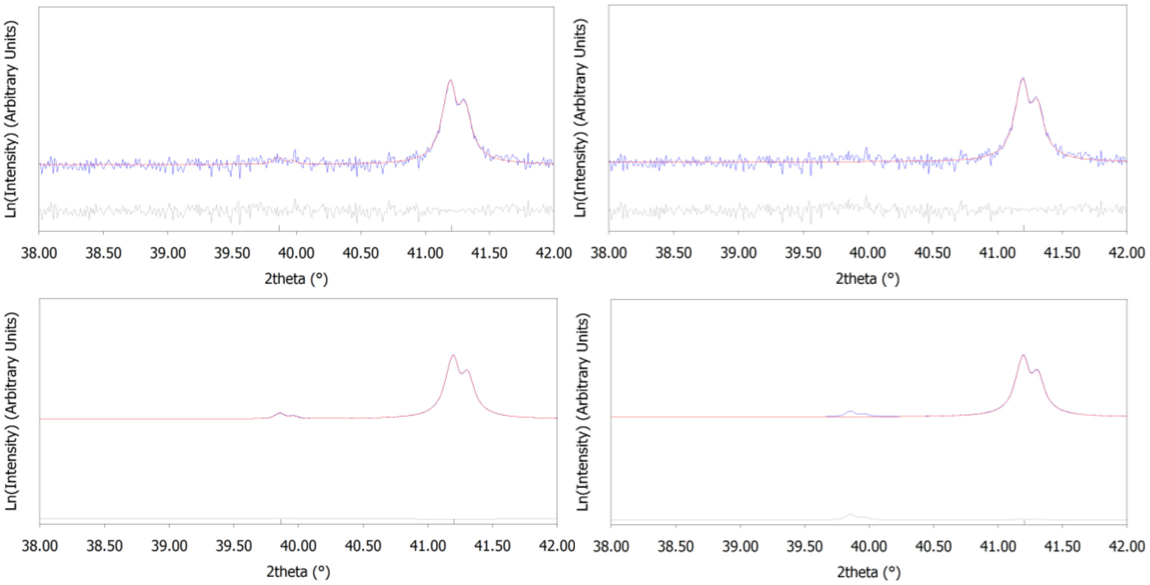

Figure 2.18: Zoomed fits to simulated HT WO_3 X-ray diffraction data on a logarithmic scale. Top row shows the fit to simulated data including noise while the bottom row shows the fit to the same simulated data without the noise. Left hand column shows the fit provided by candidate #58 while the right hand column shows the fit provided by candidate #11. The small peak at 39.9˚ is only accounted for by candidate #58 but it is only clear that the peak is real when noise is removed.

2.7.1.2 Repeatability

Again we can verify the above results are obtained from fully converged structures by repeating the search process three times and finding an equivalent fit for each of the 69 candidates in all three. Figure 2.19 shows the R_{wp} found for each candidate is very similar on each of the three runs.

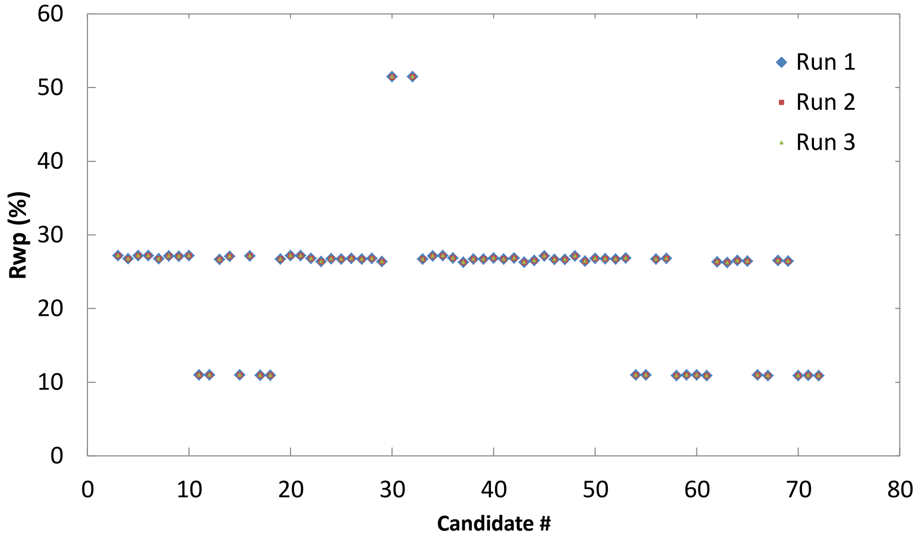

Figure 2.19: Overlay plot showing R_{wp} found for each of the 69 candidate subgroups on three repeats of the exhaustive search process. An equivalent fit to the simulated data is found in all three runs for all candidates. Small green triangles (run 3) overlay medium red squares (run 2) which overlay large blue diamonds (run 1).

We can also show that we have obtained an equivalent convergence on at least 9 separate Rietveld cycles for the first step of our annealing process for all 69 candidates and in at least 20 separate Rietveld cycles for the second (see e-Appendix 6). This again shows excellent internal consistency in our refinement process.

2.8 Structural Relationship

As the RT structure is a subgroup of the HT structure of WO_3, it is also possible to obtain an excellent fit to the HT simulated diffraction data using the RT model (Figure 2.20).

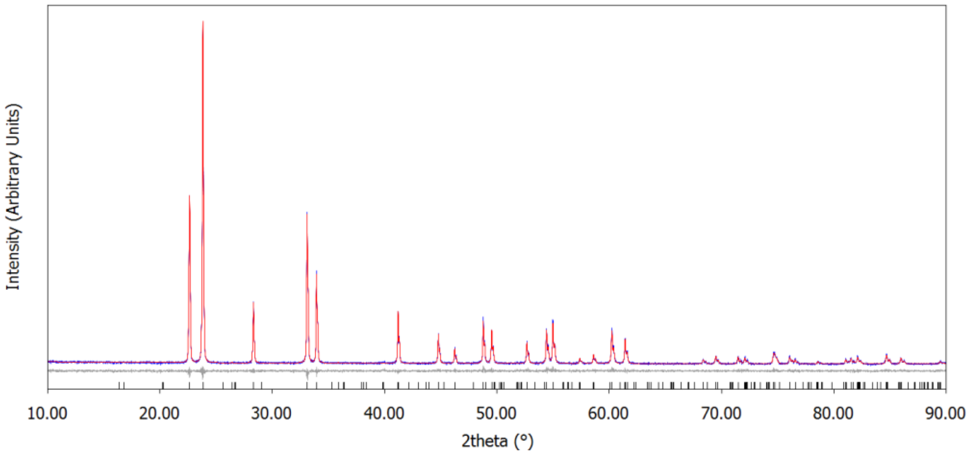

Figure 2.20: RT structure fit to HT simulated X-ray diffraction data. As the RT structure is a subgroup of the HT structure the fit is equivalent. Space Group $P2_1/n$, a = 17.3746(7) Å, b = 7.4603(7) Å, c = 7.84620(7) Å, β = 154.565(2)˚. R_{wp} (R_{Bragg}) = 10.88 % (1.68 %).

This allows us to make a direct comparison of the important distortion modes in the HT and RT structures by comparing the active modes in the RT model when fitting each data set. Figure 2.21 shows mode amplitudes obtained for each of these fits.

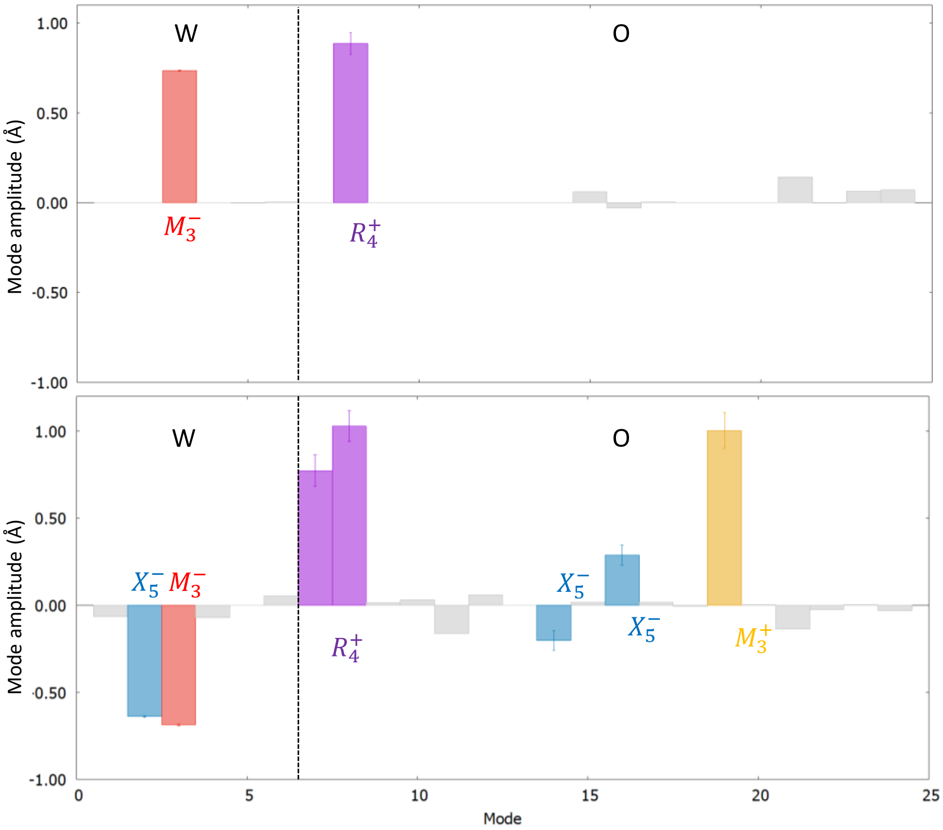

Figure 2.21: Mode amplitudes obtained from RT structure fit to: (top) HT simulated X-ray diffraction data and (bottom) RT X-ray and TOF neutron diffraction data. The mode amplitudes of the minimum set required to fit the data in each case are coloured and labelled by irrep. W and O modes are separated by a vertical line. The two phases have a

group-subgroup relationship as the RT structure retains both important modes of the HT structure while adding an additional 5 modes. Error bars are omitted from other (grey) modes for clarity.

As expected from the literature (see Table 2.1), there is a single important M_3^- mode and a single important R_4^+ mode required to account for the HT simulated data whereas the RT data requires an additional R_4^+ mode as well as an additional M_3^+ mode and three additional X_5^- modes. The RT structure retains the HT out-of-phase octahedral tilt about the c axis resulting from the $R_4^+(a,\boldsymbol{b},0)$ mode (which is retained with equal amplitude and sign) with additional out-of-phase rotation about the a axis and in-phase rotation about the b axis arising from the $R_4^+(\boldsymbol{a},b,0)$ mode and $M_3^+(0,0,\boldsymbol{a})$ mode respectively. Meanwhile, the sign of the $M_3^-(\boldsymbol{a},b,0)$ mode is reversed in the RT structure relative to HT and so the W retains its out-of-phase displacement parallel to the a axis but in the opposite direction relative to the octahedral tilt. The addition of the W $X_5^-(0,0,\boldsymbol{a},\boldsymbol{a},b,-b)$ mode corresponds to displacement of W parallel to the b axis which is in-phase with respect to the c direction and out-of-phase with respect to the a direction. The addition of the two O $X_5^-(0,0,\boldsymbol{a},\boldsymbol{a},b,-b)$ modes corresponds to a small out-of-phase displacement of O parallel to the b axis leading to a minor distortion octahedral bond angles.

Figure 2.21 also illustrates that even when the best possible candidate choice is made there is likely to be some redundant DOF. The RT structure has an additional 17 modes that are not required to fit the data, however no candidate exists which has fewer redundant DOF while retaining the important modes.

2.9 Exhaustive Search Conclusions

We have shown that exhaustive searches can be used for structural assignment by trialling every possible loss of symmetry pathway between a parent and child structure. The process is widely applicable because we can guarantee that the process trials the true structure with only minimal assumptions: i.e. that the structure in question has a group-subgroup relationship with a known parent structure, and that a child structure with some subset of the symmetry of the true structure can be identified (e.g. a *P1* model with a sufficiently large lattice).

In some ways the least important part of the process is the final candidate choice. The real value of the exhaustive search lies in mapping the relationship between each symmetry element retained by the candidate and the quality of fit. Here we have presented examples where the choice of candidate (symmetry to retain) is reasonably easy. We emphasise that a comprehensive map of the effect of every possible combination of loss of every symmetry element not present in the child structure is more valuable than which symmetry elements we choose to retain in our final structural assignment.

2.10 Genetic Algorithms for Structure Solution

Genetic Algorithms are a type of evolutionary algorithm that optimises parameters by artificially mimicking natural selection processes. The algorithm takes a population of individuals whose fitness is evaluated depending on how well their defined attributes meet specific criteria. Improvement in the population is driven by the selection of individuals with the best fitness to generate a new population. This new population undergoes a variation process creating new individuals which are evaluated before the best members are again selected, creating a new generation. Figure 2.22 shows a simple schematic of the process.

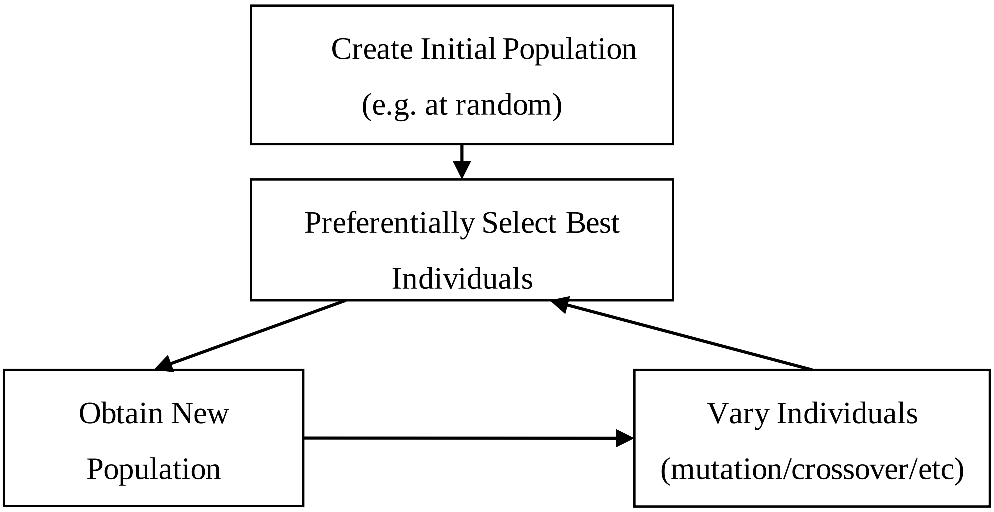

Figure 2.22: Simple schematic for Genetic Algorithm process

Genetic Algorithms in this form were first proposed by John Holland[21,22] in the 1970s. He used a "cognitive maze" to illustrate the concept whereby the GA attempts to find the set of directions that leads to the maze exit by measuring the proximity to the exit of individual solutions and selecting the closest individuals.

More recently, GA methods have been used for molecular structure problems including: protein folding[23,24] and structural sequencing[25,26], ligand docking arrangements[27-29] and RNA secondary structures[30,31]. This approach has been largely effective in these fields because the attributes being optimised lend themselves to a binary parameterisation. Even though there are often a large number of permutations, the GA has proved more efficient than brute-force, Monte-Carlo and simulated annealing algorithms in these cases because it is able to minimise the fitness function by trialling fewer individuals. In some cases the GA mimics real biological mutation effects and so it is unsurprisingly a powerful computational technique for modelling it. Until now, GAs have not been used to model symmetry changes on phase transition in crystalline materials. However, the distortion mode basis presents an opportunity to model phase transitions using a binary "on/off" parameter set and so we have developed GA methods with the aim of developing a quick and reliable structure solution method for such materials.

2.11 GAs for Phase Transitions

We will only be concerned with GAs where the individuals are candidate structures for fitting of powder diffraction data from a distorted material whose attributes are binary (on/off) symmetry-adapted distortion modes. Candidates in this example therefore consist of a string of the form "100101…" where a 1 indicates a mode is "on" and refines when the candidate is evaluated while a 0 indicates a mode is "off" and its amplitude is fixed to zero. We therefore limit the discussion of variation, evaluation and selection processes to details relevant to these candidates.

In the WO_3 case there are 96 available distortion modes to the *P1* child structure and so the candidate model is defined by a string of 96 1s and 0s. The parent $Pm\bar{3}m$ model is indicated by a string of 96 0s (indicating all modes are "off") and the *P1* child structure is indicated by a string of 96 1s (indicating all modes are "on"). The string "00000000000100010000000000000000000011000000000000000000000100000100000000 0010000000000000000000" indicates the 7 active modes of the correct $P2_1/n$ structure

We assess the fitness of each candidate dependent on the same criteria we identified for the exhaustive search process; the fit to diffraction data as measured by R_{wp} and, the number of active parameters in the candidate. We therefore assess the fitness of a candidate according to Equation 2.1 where $R_{wp}(min)$ is the lowest possible value of R_{wp} for the system (i.e. when all available modes are active), p is a fixed penalty applied for each active mode and n is the number of active modes.

$$fitness = \frac{R_{wp}}{R_{wp}(min)} + (p \times n)$$

Equation 2.1

We then allow the "survival of the fittest" principle of the GA to drive towards candidate structures that are both simple and consistent with diffraction data. Due to the correlation between the number of parameters available to a given candidate and its fit to diffraction data, there is again a need to make a judgment as to the trade-off between the two criteria. For our GA this is dictated by the value of the fixed penalty per mode, p. Large values of p increase the relative importance of producing a simple model whereas small values of p increase the relative importance of the fit to diffraction data. It is not possible to know in advance at which level of p we can achieve the ultimate goal of fitting all the structurally significant features of the diffraction data with as simple a model as possible. We therefore run a series of GA processes with varying p in order to build a map of the relationship between the two criteria from which we can identify the candidate that best achieves that goal. For RT WO_3 we have a value of $R_{wp}(min)$ ~ 6 % using all 96 distortion modes available to the child *P1* candidate model (see 2.4). This value simply acts as a normalisation of the R_{wp} contribution to the fitness function and makes it easier to gauge the relative contribution of the $p \times n$ penalty term. In general, if p is large then n is small because a given mode must offer a large improvement R_{wp} otherwise the large penalty will make it unfavourable. Conversely if p is small then n is large because a given mode requires a much smaller improvement in R_{wp} to be favourable.

2.11.1 Algorithm Development

The underlying GA process is governed by Python 2.7 scripts adapted from the open source Distributed Evolutionary Algorithms in Python (DEAP) package.[32] Below we discuss the relevant DEAP tools, how they were developed and additions made to them. Figure 2.23 shows a schematic overview of the process.

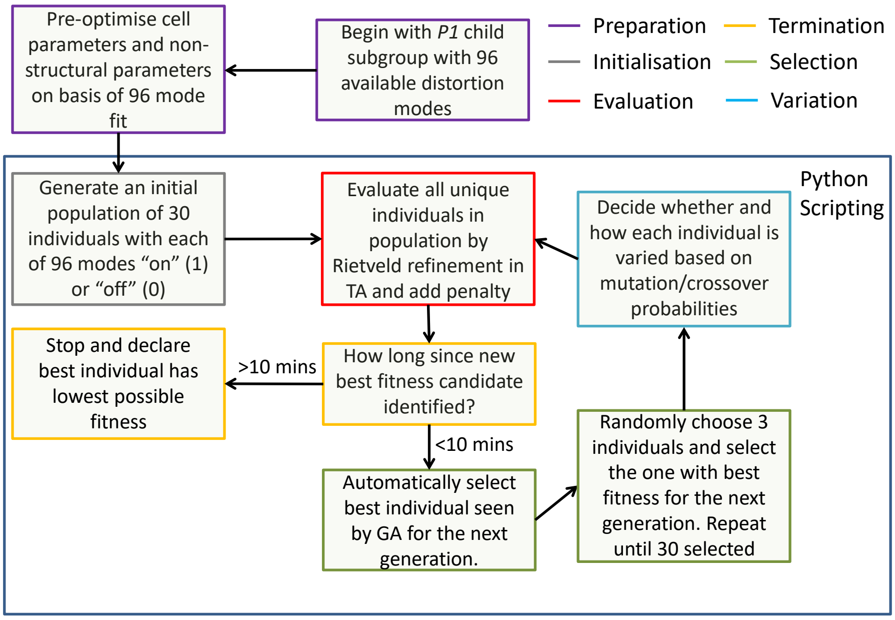

Figure 2.23: Schematic of GA process used to search candidate models for RT WO_3.

2.11.1.1 Evaluation of Candidate Models

Scripting for evaluation is the main area where we have added to the DEAP package. This is because unique tools are required to interact the GA processes with R_{wp} evaluations made in TA via a template .inp0 file (a precursor to a .inp file that is created by adding in the active distortion modes of the candidate). Additionally, as the time taken by a GA used in this way is almost entirely spent on R_{wp} evaluations (rather than on variation or selection processes, see 2.13), we also modified the handling of candidates for evaluation to ensure repeat candidates are never evaluated more than once. We have also introduced an adaptable approach to the number of Rietveld iterations performed for a candidate depending on its structural complexity to ensure convergence is achieved. The extensive, multi-step approach to candidate evaluation of the exhaustive search is not required here because the entire search takes place in the child $2a_{parent} \times 2a_{parent} \times 2a_{parent}$ lattice and *P1* space group. This allows us to pre-optimise the lattice and refine only the available distortion modes and a scale factor for each data set. This is in addition to the steps taken to pre-optimise instrumental, peakshape and thermal parameters already discussed in 2.4. A Rietveld refinement based on allowing 10 iterations per mode with a minimum of 100 iterations is able to consistently converge to the same minima for every candidate trialled by our GA. There is also no need for an internal penalty on mode amplitudes because the GA itself penalises the complexity of the candidate structure. All discussion of time taken by the GA in this chapter is based on

)

running on a typical desktop PC (3rd generation i5, 3.2 GHz) using tc.exe with no graphics plotted.

2.11.1.2 Variation of Candidate Models

Variation occurs via two broad processes; crossover and mutation (Figure 2.24). In the crossover process the on/off status of some modes are exchanged between two “parent” candidates (not to be confused with the parent structure which has no distortion modes) to create two new candidates each with a mixture of the active modes from the parents. We also introduced a new block crossover process based on mode irreps that allow parents to exchange active modes in irrep blocks rather than individually (bit crossover). The probability of a candidate varying by crossover, the probabilities of block and bit crossover events and the probability of a given mode or block being involved in the exchange are all controllable parameters of the GA. In the mutation process some of a single candidate’s modes “flip” status to produce a single new candidate. Both the probability of a candidate varying by mutation and the probability that a mode flips during the mutation process are controllable parameters. We discuss optimal values for some of these parameters in 2.13. We have also created links that turn distortion modes belonging to the same branch of the same OPD on or off together at the end of the variation process. This means that if e.g. the $X_5^-(a,b,c,d,e,f)$ c branch is on or off for W atoms it is automatically matched for O atoms. The determining factor in these cases is the lowest numbered mode belonging to the branch in question. This process gives a fuller picture of the real number of modes available if the given distortion is applied and can help to reach the optimal candidate quickly. We also mask (automatically turn off) the 3 distortion modes (1-3) that displace the W atom lying at the origin of the parent structure so as to avoid distortion modes simply translating the whole structure. Figure 2.24 gives an overview of the variation process.

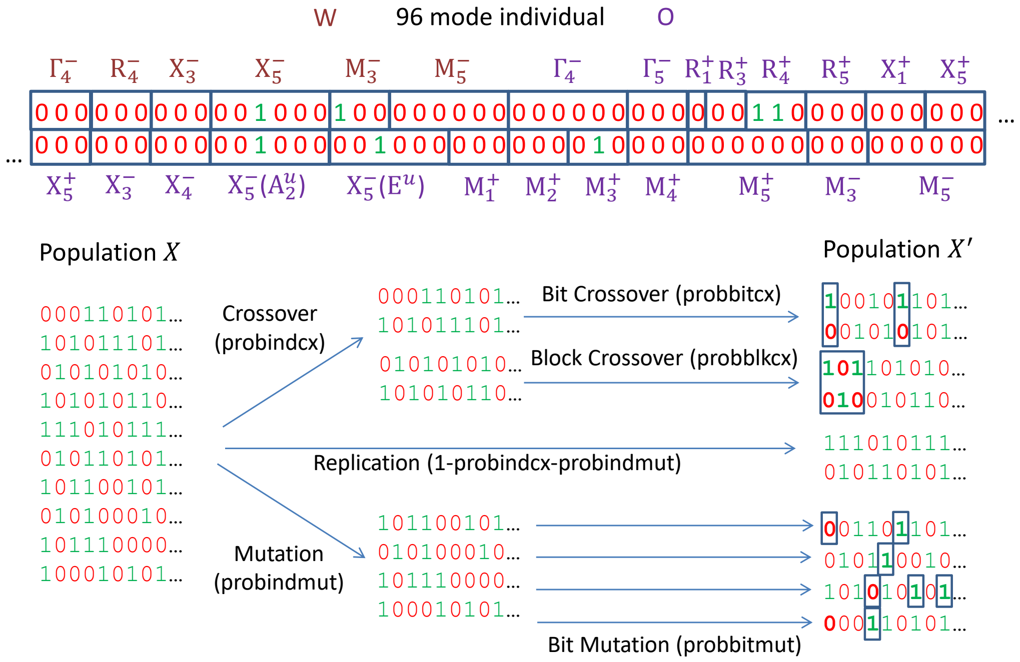

Figure 2.24: Top: Example candidate individual with distortion modes by block irrep. Bottom: Overview of available variation processes. Changes are highlighted in larger bold font. Probability labels: probindcx; the probability of a individual being selected for crossover, probindmut; the probability of an individual being selected for mutation, probbitcx; the probability of an individual selected for crossover exchanging a given mode with its partner, probblkcx; the probability of an individual exchanging a irrep block of modes with its partner, probbitmut; the probability of “flipping” a mode in a mutating individual. Crossover individuals are selected for bit and block crossover on a 50:50 basis.

2.11.1.3 Selection of Candidate Models

While the principle of selecting the individuals with the best fitness to derive a new population is simple, there is also a competing desire to retain a relatively diverse population to allow new, previously untested candidates to be produced by crossover. In order to achieve this we use a “selection tournament” scheme where the best individual is chosen from a randomly selected subset of the population. However the best candidate seen by the GA process is also always retained which ensures that if the GA variation processes destroy all copies of the best candidate seen, the candidate can be reintroduced to the population at the selection stage.

2.11.1.4 Termination Criteria

While a typical simple GA might be limited, and its success measured, by the number of generations required to find the optimal candidate this is not a useful statistic for our GA. The time taken by each generation is nearly entirely dependent on the number of new evaluations that must be made which in turn depends on the variation probabilities and chance. Furthermore, before running the GA, there is no absolute measure of what the optimal candidate is as, without prior knowledge of the system, there is no assurance that a candidate with even better fitness will not emerge if the GA is allowed to continue. Therefore we stop the algorithm when the optimal candidate has *probably* emerged. Throughout the results and analysis for this RT WO_3 GA we take this to be when no improvement in the best candidate is made for 10 minutes. The support for this criteria comes from the fact that (for a given p) the same candidate is repeatedly found over many GA runs but it is worth stating that whatever time criterion is chosen there is always *some* chance that the optimal candidate is not found by the GA. In all cases the time period chosen should reflect the complexity of the structure that is being solved and the analysis based on the evidence of repeat concordant results.

2.11.1.5 Output

We have also developed useful outputs for structure solution from the GA as well as interactive features that can be used to monitor and cycle through GA processes, adapt GA parameters as the algorithm runs or manually terminate the GA when a satisfactory result has been obtained. All discussion of time taken by GA runs is based on using the GA without interactivity. A tutorial explaining how to use the GA and some of its features on this WO_3 example can be found in Appendix 5 and includes a copy of the full GA script with line-by-line annotations and dependent modules.

2.12 Structure Solution

As we have already stated, just 7 of the 96 modes available to a 2×2×2 *P1* child subgroup are required to obtain a good fit to the data. Figure 2.25 shows the lowest fitness candidate obtained by a series of GA runs where the penalty per mode (p) in the fitness function was varied. Each candidate found for each value of p is found on multiple separate repeats of the GA process. We have also identified the true symmetry of each candidate found by analysing the symmetry loss caused by the active modes using FINDSYM[33]. We allowed a tolerance of 0.00001 Å for the cell parameters and 0.001 Å for atomic positions.

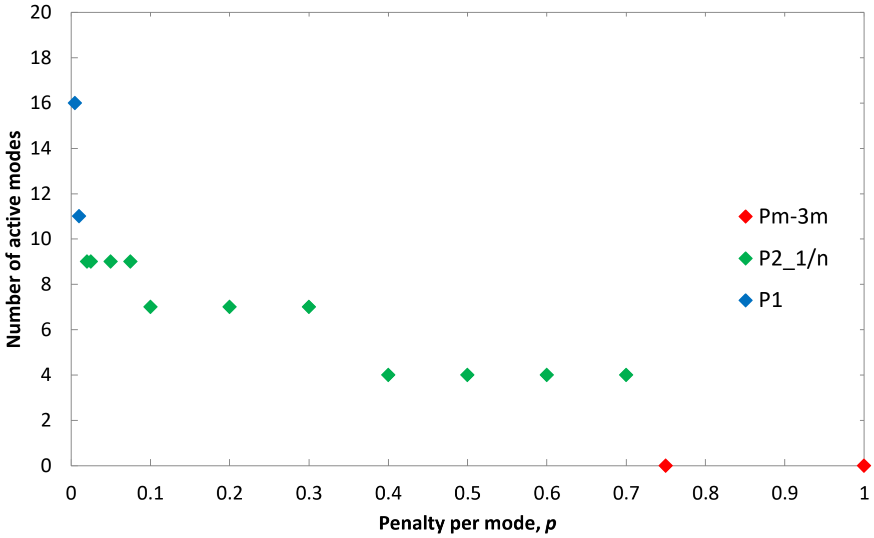

Figure 2.25: Number of active modes of best candidate found from GA with varying *p*. The true symmetry of the candidates is indicated by the colour.

At very high p values we see that no distortion modes provide sufficient improvement in the fit to the data to overcome the penalty. As p is reduced, modes 16, 37, 38 and 77 become active below $p = 0.75$. This is already sufficient to reduce the parent symmetry to the true $P2_1/n$ symmetry. As p is further reduced, there is a plateau before the next 3 important modes (12, 60 and 66) become active below $p = 0.3$. From this point there is another plateau until $p < 0.1$) at which point two further modes (47 and 88) that are not required for a good fit to the data, but are allowed by $P2_1/n$ symmetry, become active. Further reduction to $p < 0.02$ results in the addition of modes that reduce the symmetry to $P1$. A full list of the available distortion modes by mode number is in Appendix 6. It is interesting that modes do not get switched on individually but in groups. This indicates a degree of non-separability of the distortion modes. The decrease in $R_{wp}/R_{wp}(min)$ from activating groups of modes is greater than the sum of the individual decreases from separately activating the modes. Therefore the group of distortion modes of size n overcomes the penalty associated with the entire group, $p \times n$, before any mode in the group can overcome its individual penalty, p.

Figure 2.26 shows the R_{wp} achieved by these candidates. We can see that the first two groups of modes to become active lead to large improvements in R_{wp} of the candidate but subsequent modes lead to only very minor improvements. This matches the pre-existing knowledge that just these 7 modes are sufficient to provide a good fit to RT WO_3 diffraction data and replicates the conclusion of $P2_1/n$ symmetry.

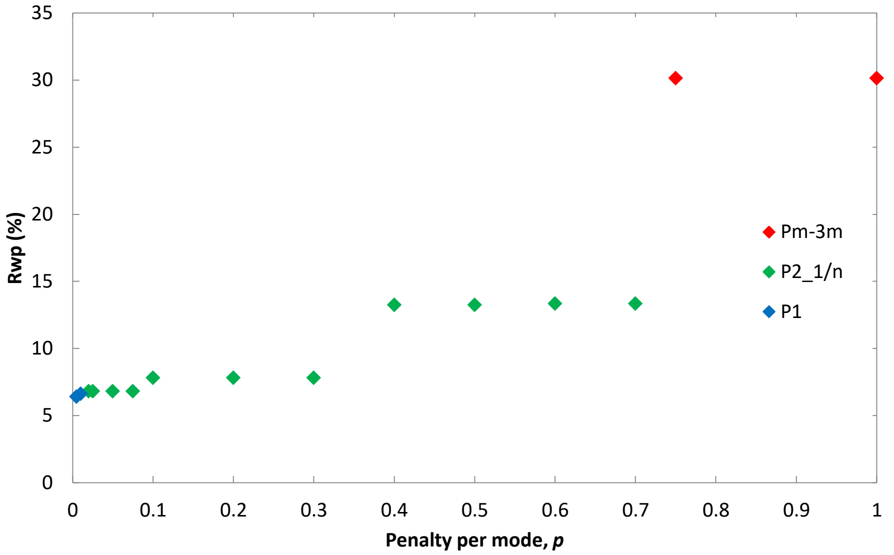

Figure 2.26: Combined X-ray / TOF neutron R_{wp} achieved by best candidates found by GA with varying *p*. The true symmetry of the candidates is indicated by the colour.

This then leads us to consider Figure 2.27 showing the R_{wp} achieved by candidates based on the number of modes available to them. The plot is analogous to Figure 2.7d in the exhaustive analysis but focuses only on the best possible candidates for each level of complexity (number of modes) as identified by the GA.

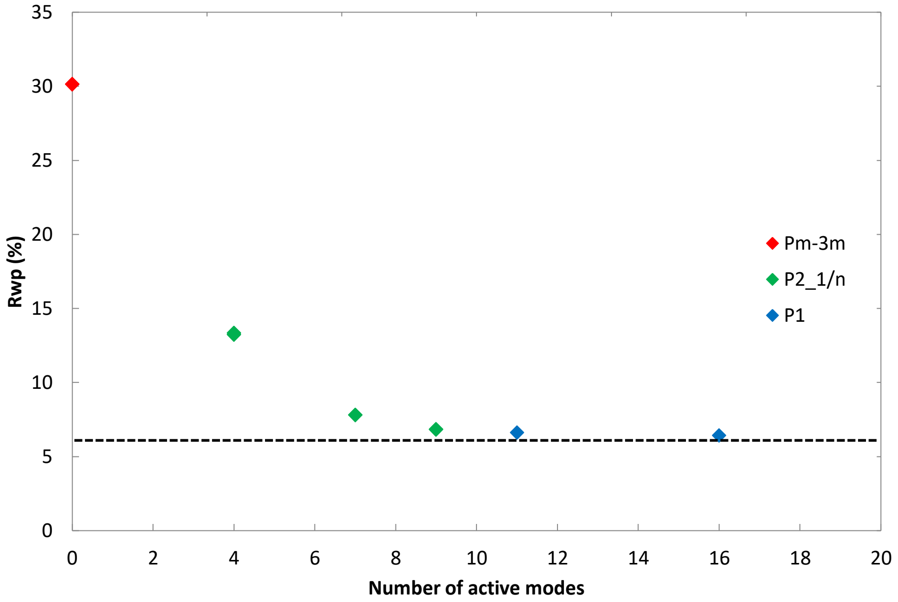

Figure 2.27: Combined X-ray / TOF neutron R_{wp} achieved by best candidates found by GA depending on the number of active modes. The true symmetry of the candidates indicated by the colour. The dotted line indicates the fit achieved by the 96 mode model (i.e. $R_{wp}(min)$).

The R_{wp} falls sharply initially but then quickly plateaus when modes that are not needed to fit the diffraction data become active. Using the same arguments as in our exhaustive search analysis we can say that the 7 mode candidate is the simplest model that provides a good fit to the diffraction data.

2.12.1 Visual Evidence

Figure 2.28 shows the fit of the 7 mode candidate. All of the structural features of the diffraction data are accounted for by this model and the fit is qualitatively as good as provided by using all 96 modes available (Figure 2.3).

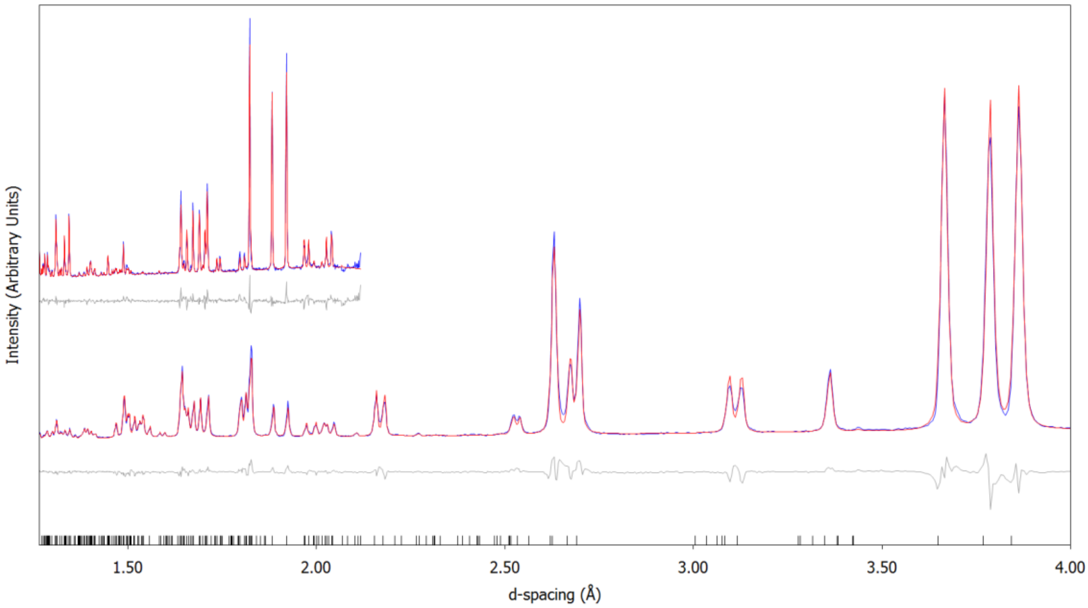

Figure 2.28: Rietveld fit to X-ray (bottom) TOF neutron (top) data using the 7 mode candidate. The model provides an excellent fit to all the features of both data sets. Space group *P1, a* = 7.297720 Å, *b* = 7.535185 Å, *c* = 7.688269 Å, *α* = 90˚, *β* = 90.85533˚, *γ* = 90˚. R_{wp} (R_{Bragg}) for X-ray / TOF neutron are 7.96 % (3.74 %) / 7.79 % (4.07 %).

Figure 2.29 shows the fit of the 4 mode candidate. There are substantial inadequacies in the fit to the data resulting from the lack of the important X_5^- W mode as well as two X_5^- O modes.

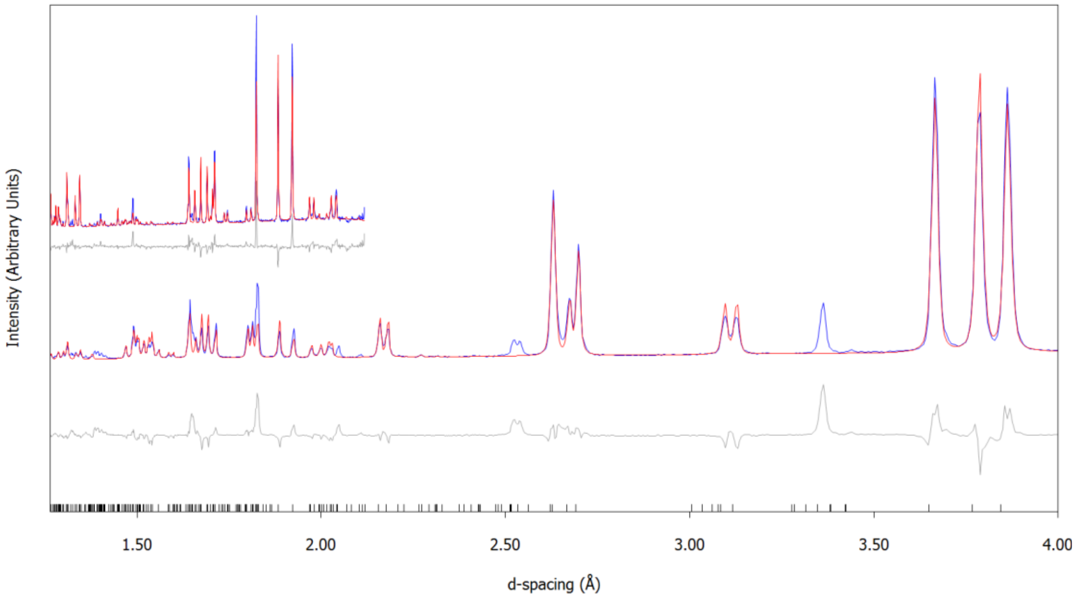

Figure 2.29: Rietveld fit to X-ray (bottom) TOF neutron (top) data using the 4 mode candidate. There are several unfitted features. Space group *P1, a* = 7.297720 Å, *b* = 7.535185 Å, *c* = 7.688269 Å, *α* = 90˚, *β* = 90.85533˚, *γ* = 90˚. R_{wp} (R_{Bragg}) for X-ray / TOF neutron are 20.76 % (11.90 %) / 11.72 % (10.10 %).

2.13 Algorithm Optimisation

While the principal outcome of the GA is to correctly identify the same 7 mode candidate for RT WO_3 as found previously, it is interesting to compare how quickly the optimal candidate can be identified. This is partially dependent on choices for the GA parameters as discussed below. We have performed some investigations into how the various parameters controlling the GA influence the route of structure solution. We are working on the principle that the GA process that requires the fewest sub-optimal evaluations prior to finding the optimal candidate will be the fastest. Figure 2.30 shows how the time taken to find the 7 mode target candidate depends on the number of evaluations made which is only indirectly related to the number of generations for which the GA runs. This is a consequence of the GA time being dominated by evaluations and our design that a given candidate needs to be evaluated only once no matter how many times it reoccurs.

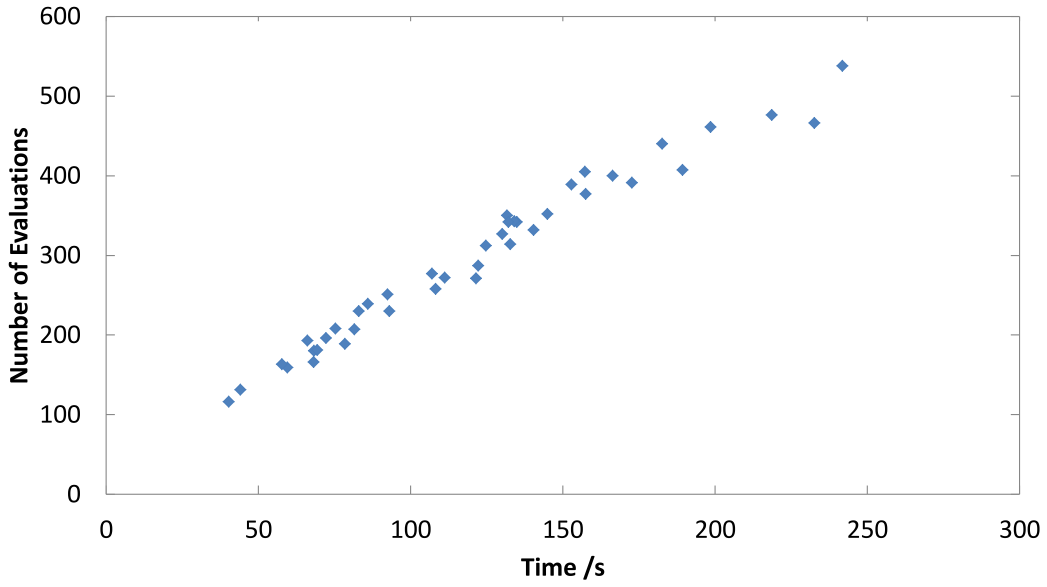

Figure 2.30: Time taken to find 7 mode target candidate by GA runs depending on number of evaluations for runs with p = 0.1, p = 0.2 and p = 0.3. The time taken is almost entirely dependent on the number of evaluations as all other processes take a negligible amount of time. Given each generation has a non-fixed number of new evaluations to make, it is not appropriate to measure the efficiency of the GA by the number of generations taken.

We don't suggest that these GA parameters are independent of each other or that the investigation is exhaustive; the intention is to illustrate the basic pathway the GA process takes to find the 7 mode target candidate. We define the time taken to identify the target candidate as the time at which it is first evaluated by the GA. This ignores the 10 minutes the GA spends after this unsuccessfully attempting to find a lower fitness candidate. All of the analysis below is based on averaging the time taken by at least 10 repeat GA processes. Standard errors assume a normal distribution.

The variation parameters discussed here are: probindcx; the probability of a candidate undergoing crossover, probindmut; the probability of a candidate undergoing mutation, and probbitmut; the probability of a mode being flipped during mutation. We also investigate the candidates in the initial population. We investigate using an algorithm where crossover and mutation may not both occur during a single variation process (i.e. probbitcx + probbitmut ≤ 1) and use a fixed population size of 30 throughout. We use p = 0.1 meaning the fitness of the 7 mode target candidate is given by Equation 2.2.

$$fitness = \frac{7.806}{6} + 0.1 \times 7 = 2.001$$

Equation 2.2

2.13.1 Starting Population

We considered three possibilities for the composition of the starting population: all modes are on (i.e. all $P1$ candidates), all modes are off (all $Pm\bar{3}m$ candidates), modes have a 50 % probability of being on (random symmetry candidates). The speed at which the optimal candidate is found is summarised in Table 2.3.

Table 2.3: Time taken to find optimal 7 mode candidate with varying starting populations. Other parameters: probindmut = 1, probindcx = 0, probbitmut = 0.02, probbitcx = 0, probblkcx = 0

Starting Population	*Time to find optimal candidate /s*
All modes off	550(50)
All mode on	1610(40)
50 % probability of each mode being on	990(30)

We find that starting with all modes off gives the fastest structure solution. There are several reasons for this. Firstly, using 7/96 available modes represents a sparse solution (i.e. one where a small fraction of the available modes are active). This simple mutation-only GA reveals the obvious advantage of starting with a sparse candidate when looking for a sparse solution. There are fewer candidate evaluations that need to be made between the starting candidates and the target 7 mode candidate and so time is saved. Additional time is also saved by trialling sparse solutions first as the Rietveld refinement process is able to converge more quickly with fewer parameters.

2.13.2 Probindmut / Proindcx

This test probed the best mixture of crossover and mutation events in order to quickly find our 7 mode target candidate. Figure 2.31 shows the speed at which the target candidate is found as the mutation to crossover ratio is varied.

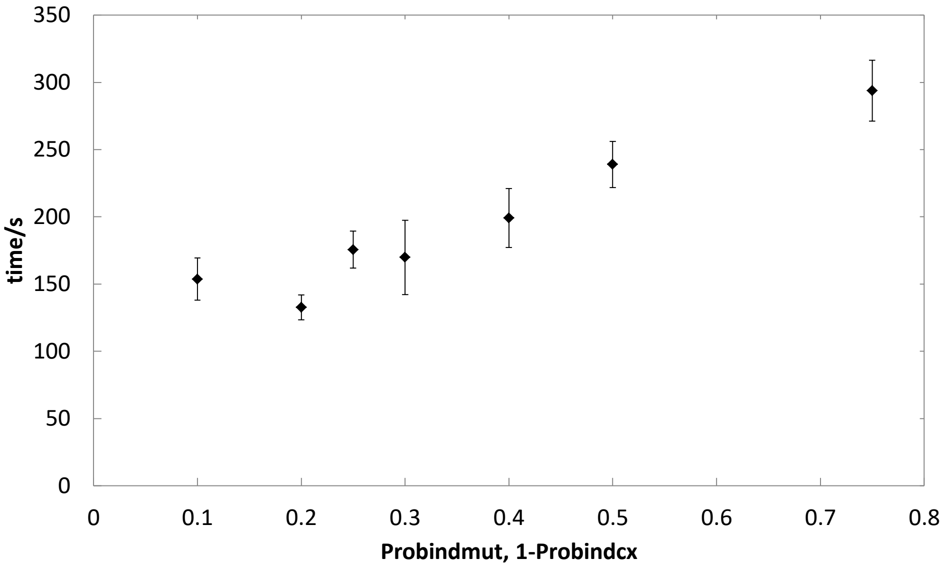

Figure 2.31: Time taken to find the optimal 7 mode candidate with varying probindmut:probindcx ratio. Error bars indicate standard error. Other parameters: probbitmut = 0.02, probitcx = 0.2, probblkcx = 0.2.

There appears to be a minor advantage when the mutation to crossover event ratio is in the region of 0.2:0.8. While this ratio does help find the target 7 mode candidate more quickly, the conclusion is not necessarily that crossover is more likely to create a candidate with better fitness than mutation. In fact, in this case, the role of crossover is predominately to spread any gains made by mutation over the whole population. Any further mutation of a candidate not matching the best candidate found by the GA at a given point greatly reduces the chance of identifying a new best candidate. To illustrate this we look at the pathway the GA takes to find the best candidate with probindmut = 0.2, probindcx = 0.8 (Figure 2.32).

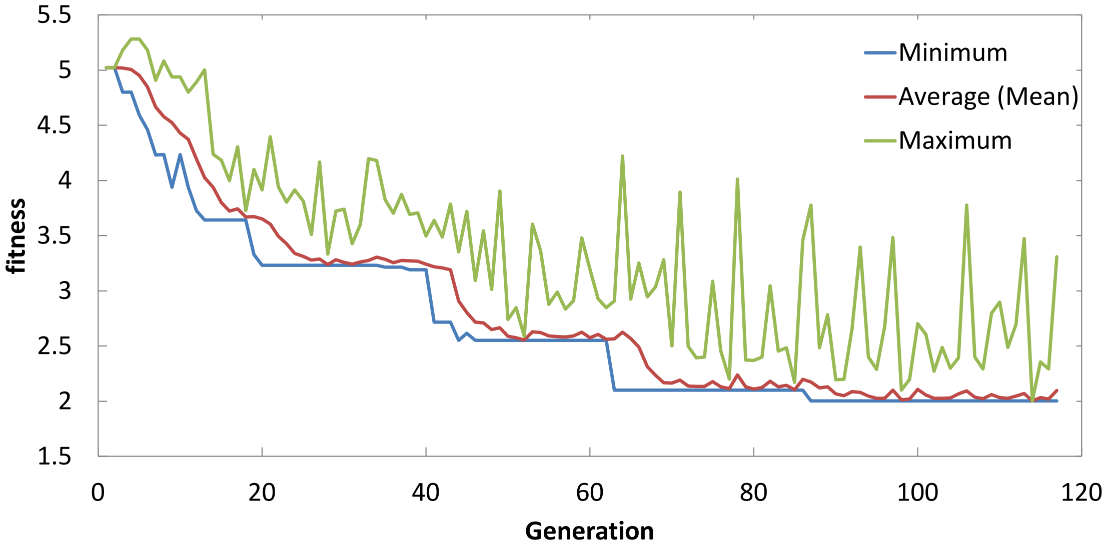

Figure 2.32: Fitness of candidates in first 120 generations of GA with probindmut = 0.2, probindcx = 0.8, probbitmut = 0.02, probitcx = 0.2, probblkcx = 0.2. Subsequent generations lead to no further improvement on best possible candidate.

The improvement of the best candidate in a population (labelled as minimum) improves in a step like fashion as the GA finds a good mutation. As soon as an improvement is made in fitness the algorithm removes the population diversity rapidly in the subsequent generations by spreading the improvement through crossover so that the average fitness (red) becomes very close to the minimum (blue). The fitness of the worst candidate in the population (maximum, green) spikes above the average as new candidates created by poor mutations of the best candidate are trialled and then rejected by the selection process. Plots showing the evolution of fitness for all 14 repeat runs of this experiment are available in Appendix 3 and all display a similar trend. On average over these runs the GA needs to make only 380(20) evaluations over 71(6) generations before finding the target 7 mode candidate.

Conversely with probindmut = 0.75 and probindcx = 0.25 (Figure 2.33), the average fitness remains significantly higher than the minimum as any improvements achieved by mutation spread more slowly through the population. The worst candidate remains significantly worse than the average because more poor mutations are made from the inferior (on average) population. The number of poor candidates in the population remains high because there is insufficient crossover to spread a good mutation widely and so some poor candidates are selected and then may mutate again. For many GA processes (where evaluations are time inexpensive compared to variation and selection) this diversity would be an advantage; this is shown by the fact that the 7 mode target candidate has been identified in far fewer generations than with probindmut = 0.2 and probindcx = 0.8. However, because the time taken by the GA is dominated by making new evaluations, this is a disadvantage – the GA (on average over 14 repeat runs) has needed to make 820(60) evaluations in just 47(4) generations before finding the target 7 mode candidate. This takes more time. Plots of all 14 repeat runs are available in Appendix 3 and all show a similar trend.

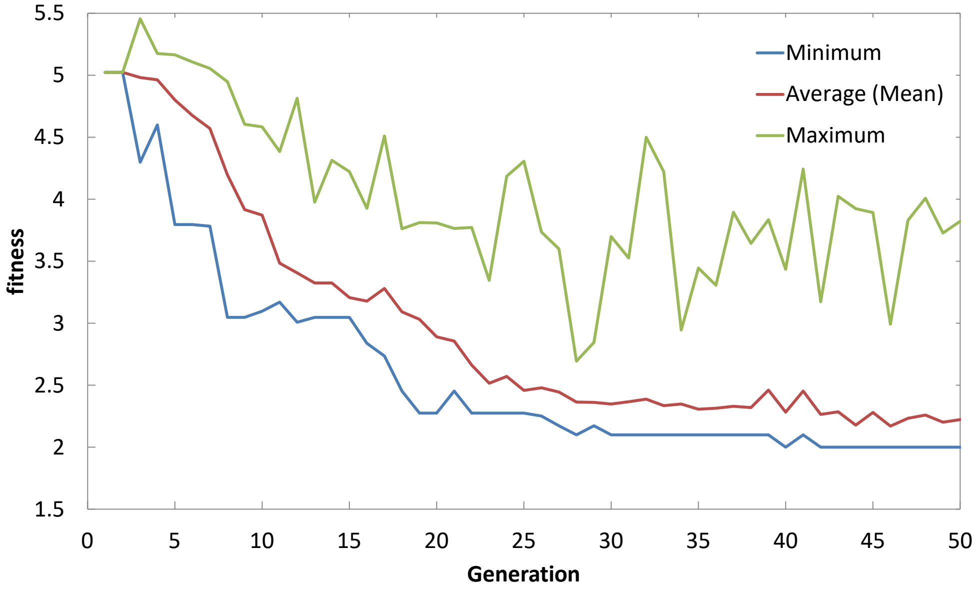

Figure 2.33: Fitness of candidates in first 50 generations of GA with probindmut = 0.75, probindcx = 0.25, probbitmut = 0.02, probitcx = 0.2, probblkcx = 0.2. Subsequent generations lead to no further improvement on best possible candidate.

2.13.3 Probbitmut

Given that we believe that improvements in the best candidate during the GA are driven by mutation, it is worth investigating the optimal rate at which to "flip" modes. Figure 2.34 summarises the results.

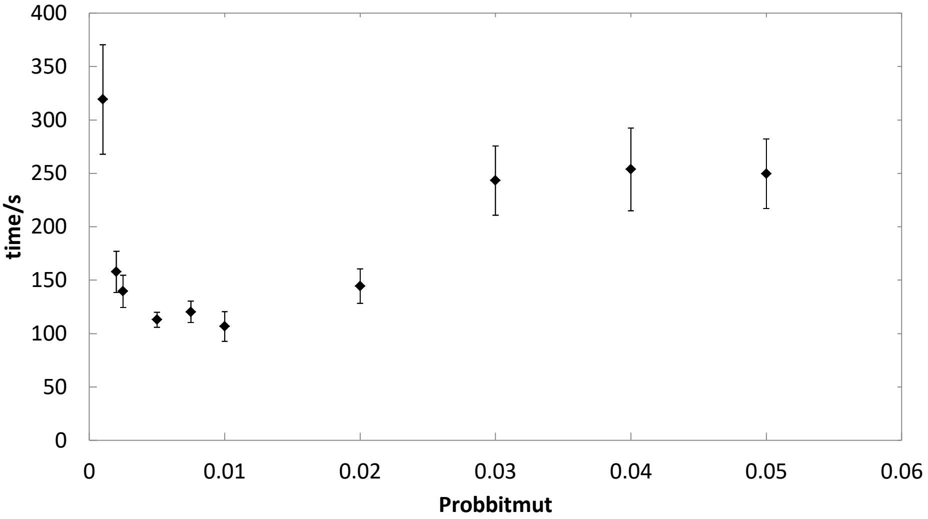

Figure 2.34: Time taken to find the optimal 7 mode candidate with varying probbitmut. Error bars indicate standard error. Other parameters: probindmut = 0.2, probindcx = 0.8, probitcx = 0.2, probblkcx = 0.2.

We notice that we find the optimal 7 mode candidate fastest when probbitmut ~ 0.01. Given there are 96 available modes this equates to changing ~ 1 mode per mutation event on average. This indicates that the fastest method is similar to a simple inclusion/exclusion approach where the highest chance of finding a new best candidate is to try random possibilities of adding or subtracting a single mode from the existing best model. Additionally, the time taken is not severely affected by reducing probbitmut from this point until it is less than 0.001 at which point the algorithm stagnates because it finds no new candidates. A small reduction in probbitmut leads to a very small time penalty because passing repeat candidates through the algorithm is time inexpensive. Meanwhile increases in probitmut initially result in a time penalty as the probability of being forced to evaluate a bad mutation rises because simultaneously making multiple correct changes to the current best candidate is unlikely.

2.14 GA Conclusions

The GA represents a fast and effective structure solution technique for RT WO_3. We effectively search only a small subset of the possible candidate structures of the exhaustive approach. The *P1* base structure for all candidates excludes the lattice from the search space and saves further time. The use of FINDSYM to identify the true space group symmetry after the important distortion modes are found allows this approach. The best optimised set of GA parameters we identified in our investigations found the 7 mode best candidate in just 98(12) seconds on average over 14 repeat runs. The record time during our investigations was 23 seconds. It is important to remember that time is a measure of effectiveness in this GA scenario; a poorly designed GA (for a given search space) would eventually find the candidate with best possible fitness but take far longer. Put differently, if a GA fails to identify the lowest possible fitness candidate then it is almost certainly because it has not been run for long enough. A GA that *cannot* find the lowest fitness candidate could only be designed by deliberately ensuring a mode is excluded from all candidates. In the fastest case the GA has favoured a pathway resembling a much simpler algorithm where the candidates are incrementally improved via mutation. This goes against the typical GA improvement pathway which mainly finds improved candidates via crossover within a diverse population.

However, the time taken to identify the best 7 mode candidate in a single, well optimised run is not the most useful statistic. If we consider the situation where we do not know which modes we need to identify, nor how many, then we need to consider both the time taken to run through a series of p values and the time allowed at the end of a given run to check if a lower fitness candidate is possible. There is also the need for repeat runs in order to be sure that sufficient time for improvement has been allowed. Furthermore, when approaching a search for the first time, it is unlikely to be immediately obvious what GA control parameters are optimal (although sensible assumptions can be made). With this consideration it is useful to note that the time taken to trial 15 values of p, allowing 10 minutes after the best candidate was found and allowing just 3 repeats of each run using a reasonably well optimised set of GA parameters takes just under 10 hours. This shows that the practical time saving of the GA approach compared to the fully exhaustive approach is not as dramatic as it first appears.

We also note that the mutation dominated improvement pathway found may not apply to all attempts to use a GA to search distortion modes for structure solution following phase transition. A consequence of the No Free Lunch Theorem[34] is that the optimal set of parameters for the GA is different for each different search space. Therefore the work here may only be partially transferable to other materials.

2.15 Inclusion/Exclusion Searches

Given the dominant effect of simple single mutations on the efficacy of the GA, it is interesting to test this algorithm explicitly. We therefore wrote an “inclusion” algorithm that takes a starting candidate with no active modes (i.e. the parent structure) and turns on each single available distortion mode one at a time. The distortion mode that leads to the greatest improvement in R_{wp} is then selected as “on”. The algorithm then sequentially tries each of the remaining modes one at a time before again selecting the mode associated with the greatest improvement in R_{wp}. It continues in this fashion until all distortion modes are active. We have also created the corresponding "exclusion" algorithm where modes are successively turned off one at a time. The distortion mode removed in each case is the one that leads to the smallest deterioration in R_{wp}. The approaches are similar to the alternating inclusion/exclusion approach of Kerman et al.[35] designed to eliminate so called 'phantom' modes. These are modes that appear to have a non-zero amplitude even when not required to obtain a good fit to the diffraction data, usually due to correlation with another mode. Our approach is simplified to include or exclude a single mode per cycle (rather than selecting modes above a fraction of the largest change as Kerman et al. did).

Candidate's fitness is evaluated purely on R_{wp} because the complexity (i.e. the number of active parameters) of the candidate is fixed for each inclusion or exclusion cycle. We have integrated the python 2.7 scripting required for these runs into the GA framework. Discussion of time taken by the algorithm is based on evaluation being made on a typical desktop PC (6th generation i7, 3.4 GHz) using tc.exe with no graphics. As with the GA, the time taken for the algorithm to produce candidate structures is negligible compared to the time required to evaluate them.

This inclusion algorithm relies on the separability of the important distortion modes required to model RT WO_3 because each mode is tested independently of other inactive modes. Conversely, the exclusion algorithm is very resilient to non-separable modes because each mode is considered alongside all other modes that have not previously been eliminated. We noted in 2.12 that modes became sufficiently important in groups as the GA penalty was lowered. In these algorithms, unlike the GA or Kerman et al. approach, there is intentionally no mechanism by which a 'mistake' (i.e. an unimportant mode turned on or important mode turned off) can be reversed. Therefore, these inclusion and exclusion algorithms also act as a measure of the degree of non-separability of individual important modes. Non-separable modes will appear to be less important to the fit to the data in the inclusion algorithm than the exclusion algorithm and so insight into separability may be obtained from a comparison of the results of the two algorithms.

2.15.1 Using Symmetry-Adapted Distortion Modes

Figure 2.35 shows the number of distortion modes active and the R_{wp} achieved after each iteration of this process for both inclusion and exclusion algorithms.

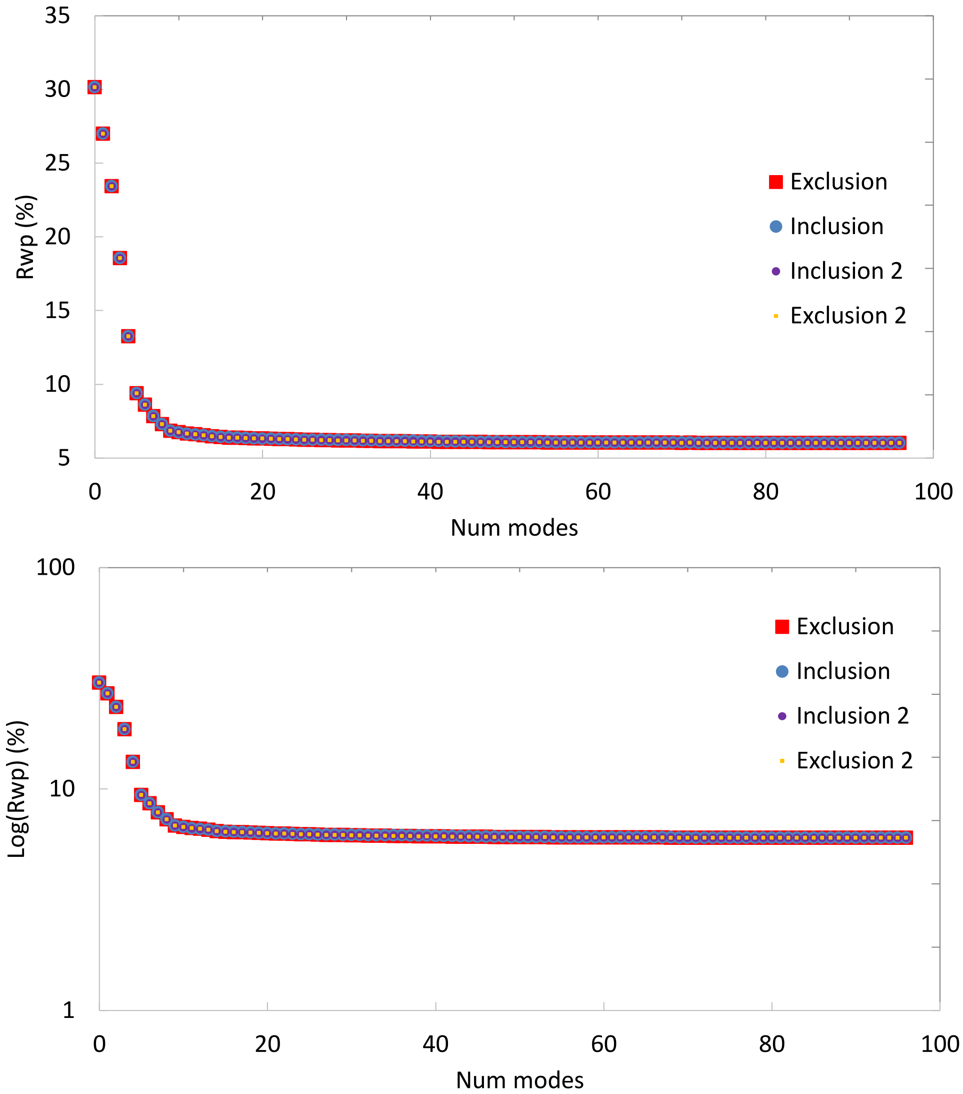

Figure 2.35: (Top) Combined X-ray / TOF neutron R_{wp} achieved by candidates in simple inclusion/exclusion searches using the distortion mode basis. Also plotted on a logarithmic scale (bottom) to show plateauing of R_{wp} for ≥ 7 modes. Modes are turned on/off one at a time based on the largest improvement/deterioration in R_{wp}. Inclusion (circles) and exclusion (squares) runs result in the same R_{wp} profile repeatedly.

The fit to the data improves rapidly as the first five modes are turned on (or deteriorates rapidly for the last five modes turned off), then more gradually for the next two modes after which activating or deactivating further modes results in only a negligible change in R_{wp}. This result matches the conclusions of previous work that most features of the diffraction data can be fitted with five modes with a further two modes giving a small but significant improvement. There is also very little hysteresis between the two algorithms indicating there is a high enough degree of mode separability in order to identify the same order of importance for all significant modes regardless of whether modes are considered alone or as a group. Figure 2.36 shows the successive change in R_{wp} of the 12 highest ranking modes in each search in the order they were turned on/off in each algorithm. Refer to Appendix 6 for a numbered list of distortion modes.

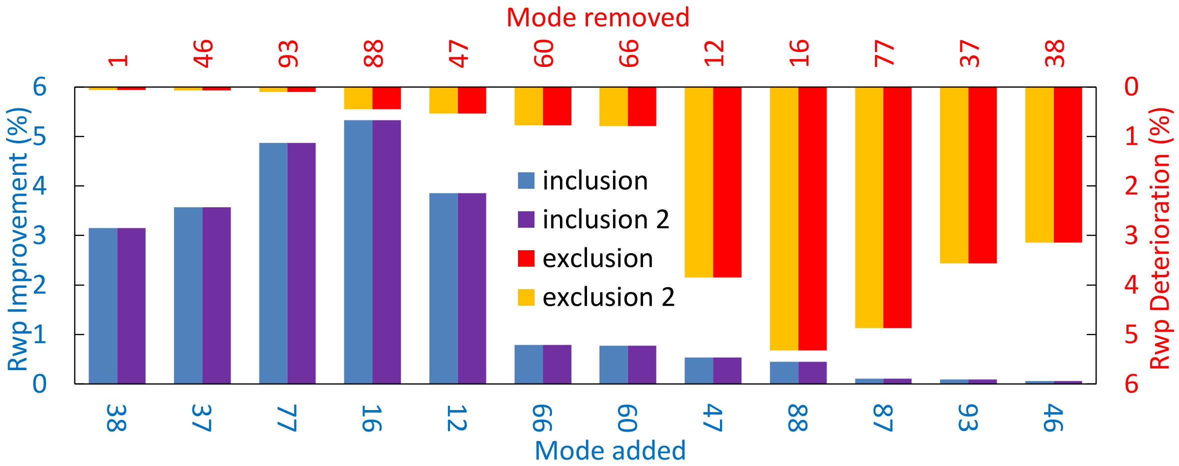

Figure 2.36: Blue/Purple (left and bottom axes): Improvement in combined X-ray / TOF neutron R_{wp} on successive inclusion of 12 highest ranking distortion modes. Red/Orange (right and top axes): Deterioration in R_{wp} on successive exclusion of 12 highest ranking distortion modes.

Both algorithms agree on the order of importance of the 9 highest ranking modes. It is only when the change in R_{wp} is very small that the algorithms disagree (the inclusion algorithm ranks mode 87 as 10th most important while exclusion ranks mode 93 as 10th most important). It is clear that there are some cooperative effects between modes because in both algorithms the improvement/deterioration in R_{wp} does not decrease/increase for every mode included/excluded. However, the effect is sufficiently uniform to retain the ranking order. As a simple example, consider only modes 38 and 37. In the first cycle of the inclusion algorithm mode 38 is turned on because the improvement in R_{wp} (-3.15 %) exceeds that of mode 37 (-2.91 %) and all others. In the subsequent cycle the improvement, in R_{wp} terms, from inclusion of mode 37 (-3.57 %) exceeds its earlier value and so modes 37 and 38 are, to some degree, non-separable in R_{wp} terms. Considering the penultimate cycle of the exclusion algorithm one might expect mode 37 (+3.57 %) to be retained due to its increased importance when mode 38 is also active. However, the importance of mode 38 has increased by even more (to R_{wp} +3.80 %) and so the order of switching off reverses the order of switching on in the inclusion algorithm. The value of the modes in R_{wp} terms is changed depending on whether the modes are considered individually (inclusion) or cooperatively (exclusion) but the relative importance, in R_{wp} terms, of each mode is broadly unaffected (mode 38 is 0.24 % more important individually or 0.23 % more important cooperatively).

As a result of this, the RT WO_3 example lends itself to simple and fast individual mode trialling such as these algorithms or the GA approach where improvement occurs largely by one mode at a time mutations. Exploration of a large number of permutations such as in the exhaustive approach is not required and takes longer.

2.15.2 Separability

The comparison of the inclusion and exclusion algorithms acts as a measure of separability for the parameter set. However the inclusion search does not consider parameters completely independently. It instead considers the first parameter turned on independently of all others, then subsequent parameters together with those that have already been turned on. Equally, exclusion searches only test parameters together with those that have not already been turned off. Therefore, a direct test of the separability of the 7 distortion modes of the best candidate is useful.

Therefore we perform a simple test where we attempt to match the 7 distortion mode model using each parameter individually. If the parameters are separable then the amplitude returned will be very close to that obtained when all 7 are active. Meanwhile, if amplitudes are considerably different from the values used in the best 7 mode model then it shows the true value of the distortion mode cannot be revealed unless the mode is trialled with others (i.e. the parameter is not very separable). Table 2.4 shows the result of this test.

Table 2.4: Mode amplitudes returned when attempting to match X-ray and TOF neutron diffraction data using only 1 of 7 important modes. The best 7 mode model returns combined X-ray / TOF neutron R_{wp} = 7.82 %.

Mode #	*Amplitudes of the best 7 mode model /Å*	*Amplitudes obtained using individual modes /Å*	*Combined R_{wp} obtained using individual modes (%)*
12	0.636(7)	±0.77(2)	28.20
16	-0.726(6)	±0.80(2)	27.53
37	1.063(7)	±1.07(3)	27.23
38	-0.794(7)	±1.11(3)	26.99
60	0.243(10)	±0.55(4)	29.80
66	-0.329(9)	±0.82(3)	28.57
77	-1.047(7)	±1.14(3)	27.53

The sign of the amplitude obtained is not defined because there are separate domains which cannot be unambiguously defined by a single mode amplitude. For example if mode 12 has positive sign then mode 16 will have negative sign, however, mode 12 may have negative sign and mode 16 positive sign. Either way the same structure resulting in the same R_{wp} would be found. Modes 12, 16, 37 and 77 return amplitudes close to the values of the 7 mode model. All modes return amplitudes larger than in the 7 mode model but modes 38, 60 and 66 do so significantly. This is because they attempt to model features of the diffraction pattern ordinarily accounted for by other modes. Put differently, the true value of the modes cannot be realised unless it is trialled together with others – they are not very separable. Looking back to Figure 2.36, we can now see that modes have turned on or off according to the order of individual improvement to the fit to the data (column 4 of Table 2.4). That is to say, as we have discussed, that any cooperation between modes does not result in a change to the individual order of importance in R_{wp} terms. However the apparent importance is not clearly proportional to the mode amplitude causing that improvement (column 3 of Table 2.4) which illustrates the need to be cautious about making assessments about the importance of modes based only on amplitudes.

With this information in mind, we can analyse in depth the exact pathway followed by inclusion and exclusion searches. Beginning with the inclusion search, Figure 2.37 shows how the important modes were included in the model.

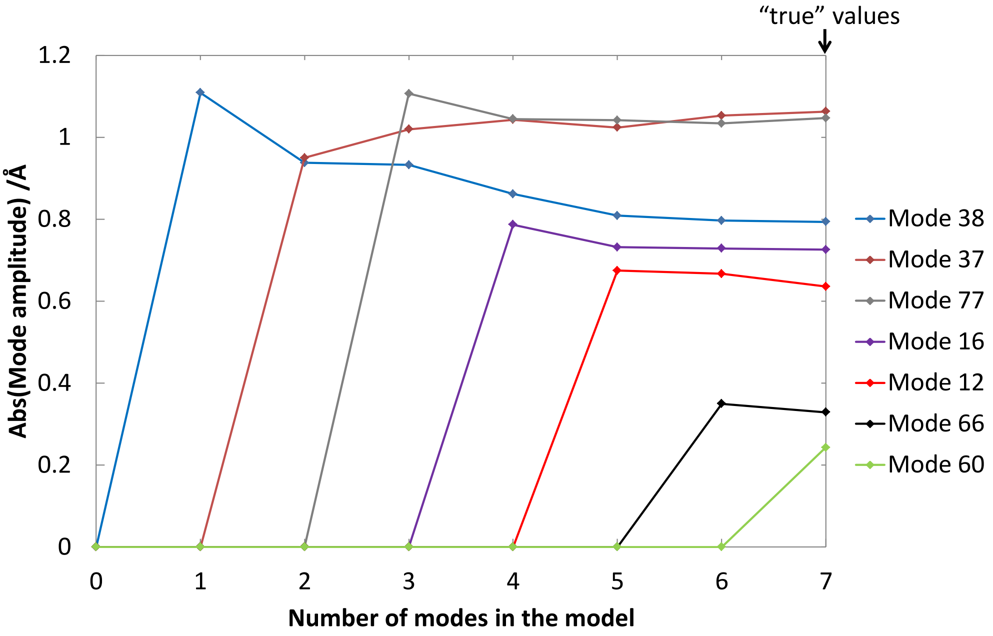

Figure 2.37: Absolute mode amplitudes obtained for 7 most important distortion modes during inclusion search. Absolute amplitudes are shown to eliminate the effect of switching domains. Amplitudes shown for 7 modes in the model represent the "true" value in the correct $P2_1/n$ model.

Initially, mode 38 is turned on but with significantly inflated amplitude representing a compromise obtained due to the absence of cooperative modes. Next mode 37 is turned on with amplitude slightly below that of its "true" value. This significantly reduces the discrepancy of mode 38 from its "true" value and at this point modes 37 and 38 share nearly the same amplitude. When mode 77 is turned on (with an amplitude close to its "true" value), the discrepancy of modes 37 and 38 are further reduced allowing more features of the diffraction pattern to be accounted for and so R_{wp} continues to improve sharply. Once mode 16 is turned on, all active mode amplitudes become very close to their "true" values and this corresponds to the sharpest R_{wp} improvement of all. This means that at this point the active modes are only accounting for features of the diffraction pattern that they will in the final 7 mode model. The remaining modes (12, 66 and 60) turn on at roughly their "true" amplitude and have very little impact on the other active modes as the R_{wp} improvement falls off. Mode 60 and 66 in particular make a relatively small impact in R_{wp} terms as only minor features are not already fit.

Turning to the exclusion search (Figure 2.38), the situation is very similar in reverse. Modes 60 and 66 can be turned off sequentially with a relatively small deterioration in R_{wp} because the fit to most diffraction features is not compromised (the amplitudes of the remaining modes are approximately unchanged). The loss of modes 12, 16 and 77 sequentially compromises the remaining modes leading to sharp R_{wp} deteriorations. Finally, turning off mode 37 sharply changes the amplitude of mode 38 which must then attempt to fit as many diffraction features as possible alone.

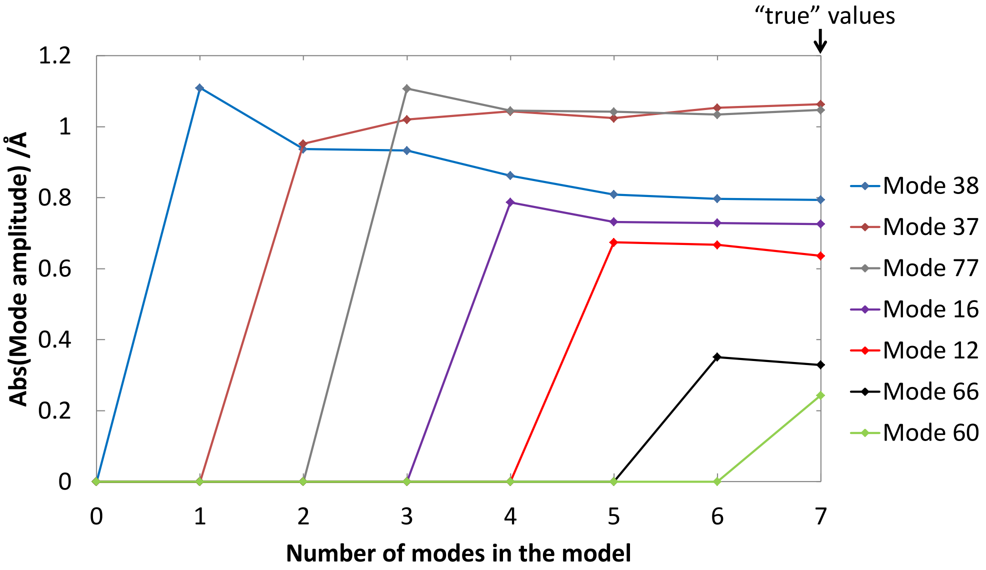

Figure 2.38: Absolute mode amplitudes obtained for 7 most important distortion modes during exclusion search. Absolute amplitudes are shown to eliminate the effect of switching domains. Amplitudes shown for 7 modes in the model represent the "true" value in the correct $P2_1/n$ model.

2.15.3 Using Cartesian Coordinates

These simple inclusion and exclusion searches also allow us to contrast our distortion mode basis with the traditional Cartesian coordinate approach. While the traditional basis does not lend itself to an on/off parameterisation, we can do this by parameterising the 96 xyz coordinates available to our *P1* structure as either included in the Rietveld refinement ("on") or fixed to the parent site values ("off"). A full table showing the numbering system for Cartesian coordinates is available in Appendix 7. Figure 2.39 shows the change in R_{wp} as these coordinates are included or excluded from a Rietveld refinement.

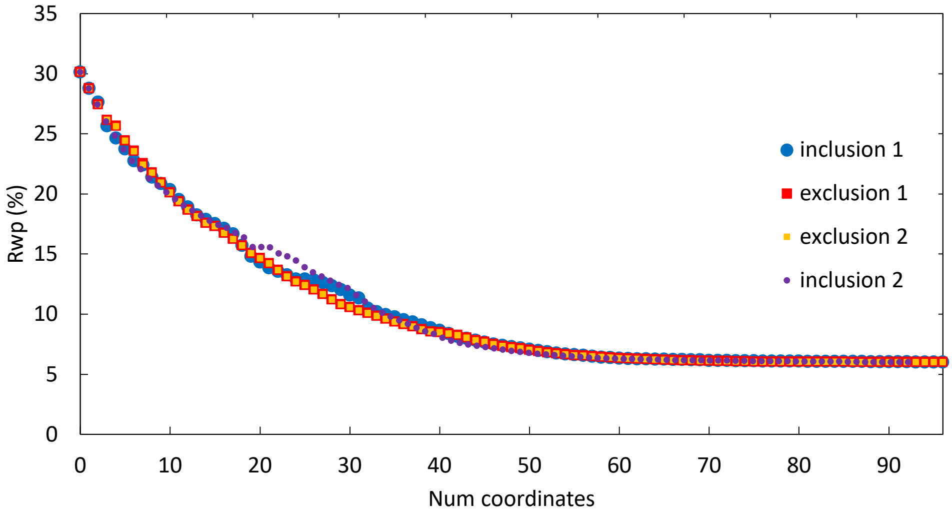

Figure 2.39: Combined X-ray / TOF neutron R_{wp} achieved by candidates in simple inclusion/exclusion searches using the traditional Cartesian basis. Coordinates are turned on/off based on the largest improvement/deterioration in R_{wp}.

While a very good fit to the diffraction data is found for just 7 active distortion modes, all inclusion and exclusion runs find that the same R_{wp} is not achieved until between 43 and 44 traditional *P1* coordinates are refining in the Cartesian basis. In all cases the true symmetry of the structure, as identified by FINDSYM with atomic tolerance of 0.001 Å, is *P1*. This illustrates an advantage of the distortion mode basis which identifies the true $P2_1/n$ symmetry with just 7 parameters. With a larger group of parameters required, each individual parameter depends more greatly on contributions of other parameters in order to apply the correct displacive distortion. This makes it more difficult to identify which parameters are important and so the searches may identify modes that are not needed and unnecessarily lower the symmetry if those parameters offer a greater improvement to the fit considered individually.

Furthermore, there is considerable variation in the R_{wp} vs. number of coordinates between inclusion and exclusion searches. Exclusion searches have a consistent profile with R_{wp}

increasing smoothly for each excluded parameter. Conversely, the inclusion search profile is inconsistent and non-smooth due to the inclusion of parameters whose relative value is affected by the presence or absence of other parameters. The most important parameters identified by the two approaches (Figure 2.40) show that exclusion searches agree on the most important parameters whereas inclusion searches follow differing pathways.

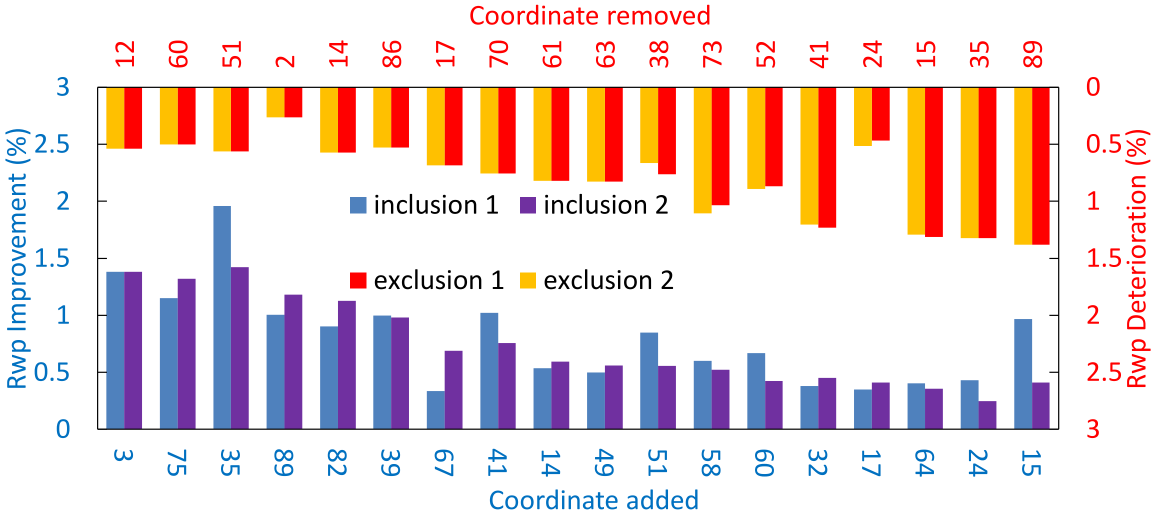

Figure 2.40: Blue/Purple (left and bottom axes): Improvement in combined X-ray / TOF neutron R_{wp} on successive inclusion of 18 highest ranking xyz coordinates. Red/Orange (right and top axes): Deterioration in combined X-ray / TOF neutron R_{wp} on successive exclusion of 18 highest ranking xyz coordinates.

The considerable difference between the inclusion and exclusion profiles when traditional Cartesian coordinates are used shows that the parameters are less separable than symmetry-adapted distortion modes. This is due to the need for far more parameters to obtain a good fit to diffraction data when Cartesian coordinates are used. Distortions mainly described by an individual or small group of distortion modes must now use a larger group of traditional coordinates and therefore the true value of that coordinate to the fit cannot be realised unless other important coordinates are also able to refine.

While we have discussed the important distortion modes earlier in this chapter, a summary of the Cartesian coordinates affected by these distortions is found in Table 2.5.

Table 2.5: Cartesian coordinates moved from parent positions by 7 distortion mode refinement. A full list of distortion modes by number can be found in Appendix 6. 72 of the 96 available coordinates in *P1* are affected.

Distortion Mode #	*Amplitude /Å*	*Cartesian coordinates affected (total DOF in P1)*
12	-0.647(7)	y for all W (8)
16	0.702(6)	z for all W (8)

37	1.062(9)	y for O1+O2, x for O3+O4 (16)
38	-0.782(8)	z for O3+O4, y for O5+O6 (16)
60	-0.205(12)	y for O3+O4 (8)
66	0.304(18)	y for O5+O6 (8)
77	-0.980(9)	z for O1+O2, x for O5+O6 (16)

Although just 7 distortion modes affect 72 of the 96 available Cartesian coordinates in *P1*, this does not necessarily mean that 72 Cartesian coordinates must refine in order to obtain the same fit to the diffraction data in R_{wp} terms (as is clear from Figure 2.39). Looking at the effect of distortion modes on Cartesian coordinates, some components have partially contrary effects; for example mode 38 has a component that moves O5 and O6 along the y axis (which also correctly positions O3 and O4 atoms along the z direction) but mode 66 is then needed to move O5 and O6 atoms part way back along the y axis in the opposite direction. This, at least, will change the relative importance of the Cartesian coordinates compared to distortion modes and, in the case of a completely contrary effects, may mean that the coordinate makes no significant contribution at all. When working directly with a much larger group of Cartesian coordinate parameters the web of dependencies inevitably becomes much more complex and therefore mistakes in the inclusion search much more likely.

2.16 Inclusion/Exclusion Searches Conclusions

These searches represent a baseline for solving distorted structures by way of an algorithm. Inclusion searches begin with an assumption of 100 % separability of parameters and flatten the search space to only those permutations that add a single DOF to the current model. Meanwhile the exclusion searches begin with an assumption of 0 % separability and flatten the search space to consider only permutations that remove a single DOF from the current model. Table 2.6 and Table 2.7 show the time taken (6th generation i7, 3.4 GHz) by simple inclusion and exclusion searches to find the best model for the distortion mode basis and Cartesian coordinate basis.

Table 2.6: Time taken by a simple inclusion search using distortion mode basis and Cartesian coordinates basis to find the best model for RT WO_3.

Inclusion Search Basis	*Time to find 7 mode or 43 coordinate model /s*	*Time to complete search /s*
Distortion Mode	124	7067
Cartesian	673	1854

Table 2.7:Time taken by a simple exclusion search using distortion mode basis and Cartesian coordinates basis to find the best model for RT WO_3.

Exclusion Search Basis	*Time to find 7 mode or 43 coordinate model /s*	*Time to complete search /s*
Distortion Mode	1453	1834
Cartesian	984	1846

When using the distortion mode basis, two considerations favour the inclusion search: the true model is sparse, just 7 of 96 available modes are needed so distortion modes are quite separable; and the inclusion approach begins with the simplest models and increases their complexity, so that the sparse solution is arrived at earlier in the process. The first of these two observations ensures that the inclusion search arrives at the correct model consistently and reliably while the second ensures it does so quickly. The fact that the average time taken to find the optimal 7 mode model is only slightly longer than when using the GA method, supports the conclusion that the GA pathway resembles the inclusion approach. The GAs small advantage results from the advanced methods used to link distortion modes together, thus reducing the number of required steps. However if we consider the series of runs required by the GA to establish the best candidate at various possible values of p in order to get a complete picture, then the simple inclusion run can be considered the more efficient search technique for the structure of RT WO_3 using a distortion mode basis.

In the Cartesian coordinate basis the situation is slightly different. The higher number of coordinates required means that there is a lower degree of separability and that a good fit requires roughly half the available parameters, which makes the exclusion search less unfavourable. In terms of speed, the inclusion search is still favoured because it is faster to trial 43 simple models prior to obtaining the correct model than 47 complex ones, although the advantage is not as large as in the distortion mode basis. However, the balance is tilted in favour of an exclusion search in terms of consistency because the non-separability leaves the inclusion run vulnerable to undervaluing important modes considered without others or overvaluing unimportant modes in the absence of important modes.

2.17 Conclusion

The primary aim of this chapter was to test three novel search techniques for structure solution of materials undergoing phase transitions where the distorted child symmetry is a subset of the parent's. In this case the distortion mode basis allows the application of new and rigorous algorithms to establish the true symmetry of the distorted structure. All of these approaches have proved to be effective in establishing the known structure of our WO_3 test systems. While our tests are on simple and previously established structures, the results represent a proof of concept for the techniques. They also illustrate some of the challenges in algorithm selection and optimisation that will arise for any system these algorithms are applied to. My personal preference would be to use a GA type approach in a case where I would expect a small number of modes to be important from a large pool (e.g. during a magnetic phase transition) but to rely on the slower but more predictable exhaustive tree search for a complex structural transition.

In later chapters we apply these ideas to different unknown and more challenging problems.

2.18 References

(1) Bräkken, H. *Zeitschrift für Kristallographie-Crystalline Materials* **1931**, *78*, 484.
(2) Kehl, W. L.; Hay, R. G.; Wahl, D. *Journal of Applied Physics* **1952**, *23*, 212.
(3) Vogt, T.; Woodward, P. M.; Hunter, B. A. *Journal of Solid State Chemistry* **1999**, *144*, 209.
(4) Tanisaki, S. *Journal of the Physical Society of Japan* **1960**, *15*, 566.
(5) Tanisaki, S. *Journal of the Physical Society of Japan* **1960**, *15*, 573.
(6) Locherer, K. R.; Swainson, I. P.; Salje, E. K. H. *Journal of Physics-Condensed Matter* **1999**, *11*, 4143.
(7) Woodward, P. M.; Sleight, A. W.; Vogt, T. *Journal of Physics and Chemistry of Solids* **1995**, *56*, 1305.
(8) Salje, E.; Viswanathan, K. *Acta Crystallographica Section A: Crystal Physics, Diffraction, Theoretical and General Crystallography* **1975**, *31*, 356.
(9) Gehlig, R.; Salje, E. *Philosophical Magazine Part B* **1983**, *47*, 229.
(10) Woodward, P. M.; Sleight, A. W.; Vogt, T. *Journal of Solid State chemistry* **1997**, *131*, 9.
(11) Hornebecq, V.; Reau, J.; Ravez, J. *Solid State Ionics* **2000**, *127*, 231.
(12) Fukuda, K.; Akatsuka, K.; Ebina, Y.; Ma, R.; Takada, K.; Nakai, I.; Sasaki, T. *Acs Nano* **2008**, *2*, 1689.
(13) Brusetti, R.; Haen, P.; Marcus, J. *Physical Review B* **2002**, *65*, 144528.
(14) Kumagai, N.; Kumagai, N.; Umetzu, Y.; Tanno, K.; Pereira-Ramos, J. *Solid State Ionics* **1996**, *86*, 1443.
(15) Campbell, B. J.; Evans, J. S. O.; Perselli, F.; Stokes, H. T. *IUCr Computing Comission Newsletter* **2007**, 81.
(16) Howard, C. J.; Luca, V.; Knight, K. S. *Journal of Physics: Condensed Matter* **2001**, *14*, 377.
(17) Diehl, R.; Brandt, G.; Salje, E. *Acta Crystallographica Section B: Structural Crystallography and Crystal Chemistry* **1978**, *34*, 1105.
(18) Salje, E. K.; Rehmann, S.; Pobell, F.; Morris, D.; Knight, K. S.; Herrmannsdörfer, T.; Dove, M. T. *Journal of Physics: Condensed Matter* **1997**, *9*, 6563.

(19) Campbell, B. J.; Evans, J. S. O.; Perselli, F.; Stokes, H. T. *From the Editor of Newsletter No. 8* **2007**, 81.

(20) Hamilton, W. *Acta Crystallographica Section A: Crystal Physics, Diffraction, Theoretical and General Crystallography* **1969**, *25*, 194.

(21) Holland, J. H. *SIAM Journal on Computing* **1973**, *2*, 88.

(22) Holland, J. H.; Reitman, J. S. *Acm Sigart Bulletin* **1977**, 49.

(23) Unger, R.; Moult, J. *Journal of Molecular Biology* **1993**, *231*, 75.

(24) Dandekar, T.; Argos, P. *Journal of Molecular Biology* **1994**, *236*, 844.

(25) Chacon, P.; Moran, F.; Diaz, J.; Pantos, E.; Andreu, J. *Biophysical Journal* **1998**, *74*, 2760.

(26) Desjarlais, J. R.; Handel, T. M. *Protein Science* **1995**, *4*, 2006.

(27) Morris, G. M.; Goodsell, D. S.; Halliday, R. S.; Huey, R.; Hart, W. E.; Belew, R. K.; Olson, A. J. *Journal of Computational Chemistry* **1998**, *19*, 1639.

(28) Jones, G.; Willett, P.; Glen, R. C.; Leach, A. R.; Taylor, R. *Journal of Molecular Biology* **1997**, *267*, 727.

(29) Jones, G.; Willett, P.; Glen, R. C. *Journal of Molecular Biology* **1995**, *245*, 43.

(30) Van Batenburg, F. H. D.; Gultyaev, A. P.; Pleij, C. W. A. *Journal of Theoretical Biology* **1995**, *174*, 269.

(31) Gultyaev, A. P.; Van Batenburg, F. H. D.; Pleij, C. W. A. *Journal of Molecular Biology* **1995**, *250*, 37.

(32) Fortin, F.-A.; Rainville, F.-M. D.; Gardner, M.-A.; Parizeau, M.; Gagné, C. *Journal of Machine Learning Research* **2012**, *13*, 2171.

(33) Stokes, H. T.; Hatch, D. M.; Campbell, B. J. *URL http://stokes.byu.edu/iso/findsym.php* **2007**.

(34) Wolpert, D. H.; Macready, W. G. *IEEE Transactions on Evolutionary Computation* **1997**, *1*, 67.

(35) Kerman, S.; Campbell, B. J.; Satyavarapu, K. K.; Stokes, H. T.; Perselli, F.; Evans, J. S. O. *Acta Crystallographica Section A: Foundations of Crystallography* **2012**, *68*, 222.

Chapter 3 $Bi_2Sn_2O_7$: Structure Solution by an Exhaustive Subgroup Tree Search

3.1 Introduction

In this chapter we will show how we have used an exhaustive search (as outlined in Chapter 2) to find new structural models for two phases of $Bi_2Sn_2O_7$. The work clears up a significant literature controversy over their structures and has been published in JACS (Lewis et al. 2016[1]).

3.2 Phase Transitions in $Bi_2Sn_2O_7$

$Bi_2Sn_2O_7$ belongs to the family of pyrochlore materials with general formula $A_2B_2O_6$O`. The structure can be best understood as interpenetrating frameworks of $SnO_6$ octahedra and $Bi_4$O` tetrahedra with Bi at the centre of a BiO_6 puckered hexagonal environment (Figure 3.1). Proposed applications of the material include photocatalysis,[2] carbon monoxide sensing,[3-6] isobutene oxidation catalysis[7-9] and methane coupling[10]. RT α-$Bi_2Sn_2O_7$ was discovered in 1956[11] and later found to undergo two phase transitions: to an intermediate temperature β phase between 390K and 900K, and to a high temperature γ phase on further heating[12]. Each structure remains related to that of simple pyrochlore but with peak splitting in powder diffraction data indicating different distortions for each phase.

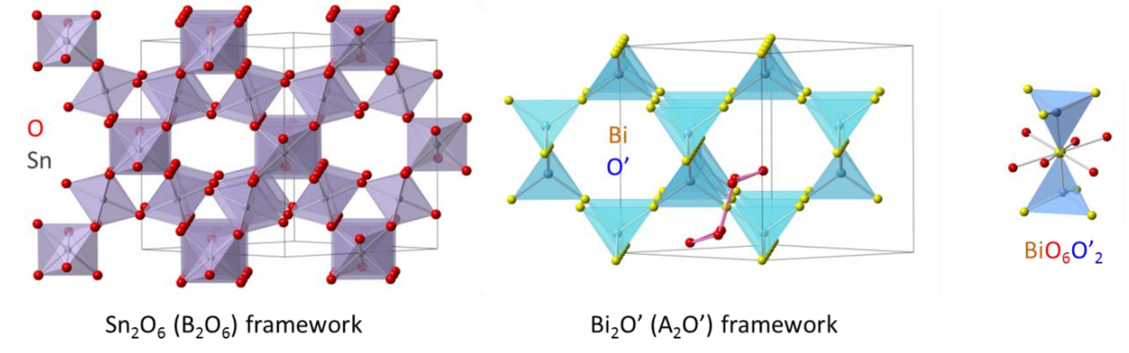

Figure 3.1: Pyrochlore structure of $Bi_2Sn_2O_7$ ($Bi_2Sn_2O_6$O`) emphasising (left) the corner-sharing $SnO_{6/2}$ octahedral framework and (middle) the interpenetrating $Bi_{4/2}$O` anticristobalite framework. Right hand view shows one puckered hexagonal O6 ring that completes the BiO_6O`$_2$ coordination environment of each Bi.

The γ-phase structure is a relatively straightforward cubic pyrochlore with cell parameter a_γ = 10.73Å and space group $Fd\overline{3}m$ with local distortions moving Bi(III) ions off ideal pyrochlore sites due to lone pair effects[13-16]. In contrast to the β and α phases, the structure has remained uncontroversial in the literature.

The β phase structure was first reported to be face-centred cubic with unit cell parameter a = 21.4 Å ($2a_\gamma$) while the α phase was reported to be body-centred tetragonal with unit cell parameters a = 15.14 Å ($\sqrt{2}a_\gamma$) and c = 21.4 Å ($2a_\gamma$)[12]. These assignments later proved to be incompatible with diffraction data observations by Evans et al[17]. This work adopted a semi-exhaustive type approach to solving the α structure albeit deliberately limited in scope by the following assumptions: α and β phases are both SHG active; the γ, β and α structures all have group-subgroup relationships; and the β phase has a cubic unit cell parameter twice that of the parent γ phase. Although the proposed α structure with 528 atomic DOF in its unit cell and space group Pc (which for convenience we now refer to as α_{old}) provides a good fit to diffraction data, diffraction data from the β phase later revealed peak splitting that rules out a cubic unit cell[18,19]. Figure 3.2 shows this peak splitting and the unit cell parameters derived for both phases. No β phase structure has since been proposed that accounts for this. This means that not only is a new structural model required for the β phase but also, without the assumptions of earlier work that eliminated potentially valid candidates, the α structure proposed could be improved by using a higher symmetry structure with fewer DOF than α_{old} (i.e. a supergroup of α_{old}). An exhaustive search seems ideal for investigating these possibilities.

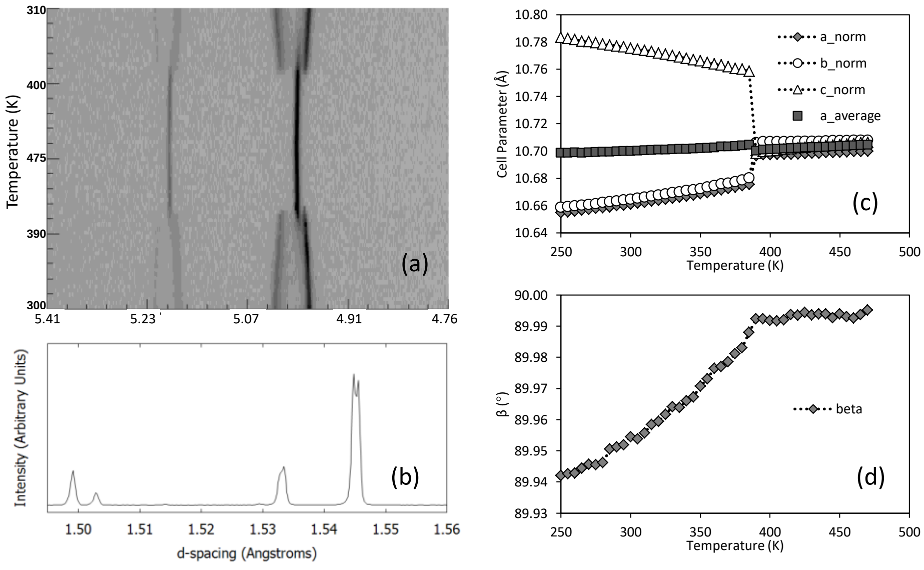

Figure 3.2: Peak splitting and cell parameters derived from synchrotron X-ray data showing a) α-β phase transition on heating and β-α phase transition on cooling, b) β-$Bi_2Sn_2O_7$ peak splitting observed at d ~ 1.545 Å, c) and d) cell parameters derived from

data collected on cooling. Cell edge parameters are normalised to show the change in cell parameter relative to a_γ.

3.3 Sample Preparation and Data Collection

Sample preparation and data collection were carried out prior to the start of this work by Julia Payne. $Bi_2Sn_2O_7$ was prepared by grinding together stoichiometric quantities of Bi_2O_3 (1.214 g, 2.61 mmol) and SnO_2 (0.786 g, 5.22 mmol) in a mortar and pestle and firing at 1373 K for 16 h. RT lab X-ray powder diffraction data confirmed a single $Bi_2Sn_2O_7$ phase was formed.

Prior to both synchrotron X-ray and neutron diffraction data collections, the sample was reheated to 1223 K. In the case of synchrotron X-ray data, the sample was loaded into a 0.3 mm capillary and measured at the Diamond I11 beamline between 2 and 140° 2θ at 293 K (α-$Bi_2Sn_2O_7$) over a 2 h period. The sample was also measured over the same range at 470 K (β-$Bi_2Sn_2O_7$) over a 4 h period. In both cases an X-ray wavelength of 0.82644 Å and high resolution multianalyser crystal (MAC) detectors were used. TOF neutron powder diffraction data were collected on the HRPD instrument at ISIS over a TOF range of 30–130 ms at both 298 K (α) and 473 K (β). In each case, data was collected for 8 h (250 μAh).

For speed we analyse a truncated d-spacing range of 1.2-13.5 Å (3.5-40° 2θ) for synchrotron X-ray data and 1.2-2.5 Å (58.3-125 ms) for TOF neutron data in our exhaustive search analysis. Rietveld refinements of the final structural models over the full ranges collected can be found in Section 3.4.3.5.

3.4 Exhaustive Search Process

In this section we give details of the steps to setup the exhaustive search process by creating a comprehensive subgroup tree and efficiently finding the quality of fit obtainable to both our α and β-phase diffraction data for each candidate structure. We then use this to propose definitive structural models for both β and α -$Bi_2Sn_2O_7$.

3.4.1 Set Up

The crucial limitations of the work by Evans et al.[17] were the assumptions of group-subgroup relationships between the γ, β and α structures due to the retention of the pyrochlore structure at all temperatures measured, and that the β structure had a cubic unit cell based on Pawley fits to diffraction data without the later-observed peak splitting. In this work we create structural models without these assumptions. In order to produce a subgroup tree in which we can be confident that models for both β and α phases will exist, we must ensure that our child subgroup fits data from both phases. A child space group choice that achieves this is $P1$. With regard to the metric of the child, previous work has indicated that a unit cell of $\sqrt{2}a_\gamma \times \sqrt{2}a_\gamma \times 2a_\gamma$ is large enough to fit all observed peaks and this therefore seems a good choice to ensure the child lattice encompasses the true lattice of both phases, while allowing the search to be conducted in a reasonable timescale. Figure 3.3 shows that this child structure does indeed achieve an excellent fit to both data sets.

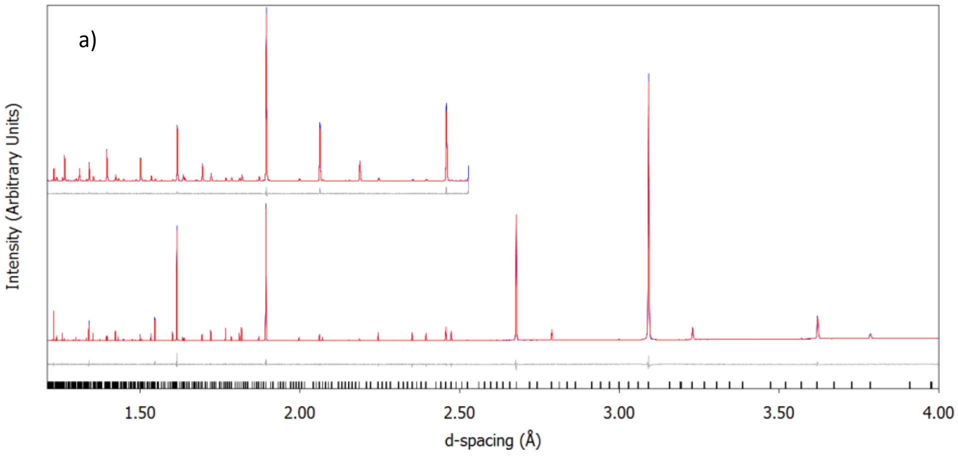

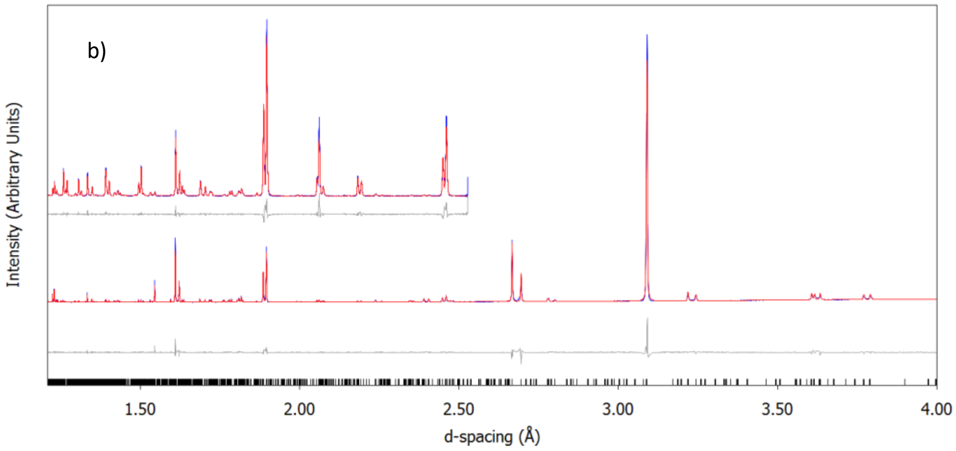

Figure 3.3: Fits after Rietveld refinements of child subgroup model to synchrotron X-ray (lower pattern) and HRPD neutron (offset pattern) for (a) β-$Bi_2Sn_2O_7$ – synchrotron X-ray / TOF neutron R_{wp} (R_{bragg}) = 4.49 % (1.99 %) / 4.17 % (1.82 %) and (b) α-$Bi_2Sn_2O_7$ – synchrotron X-ray / TOF neutron R_{wp} (R_{Bragg}) = 8.87 % (4.23 %) / 7.02 % (3.81 %).

3.4.1.1 Fixed Parameters

From the child subgroup fit we can extract some non-structural parameters to avoid the need to redetermine them during the iterative search process. This will speed up the search process and increase the probability of successful convergence as there are fewer parameters to optimise. This fit, containing all of the experimental, peakshape and thermal parameters extracted from the *P1* child fit which were fixed for the exhaustive search process, is available in e-Appendix 7.

3.4.1.2 Creating the Subgroup Tree using ISODISTORT

We can obtain a tree of all possible subsets of the distortions available to our child using ISODISTORT[20]. Full step-by-step instructions on how to do this can be found in Appendix 8. In this case the tree consists of 547 subgroups (including the parent γ and child structures). Because our child subgroup provides an excellent fit to both data sets, we can be confident that the structure with the fewest possible parameters that can fit these data sets will be amongst these 547 candidates. Of the 547, candidates #1 (the parent), #3 and #4 have no active distortions and so, given supercell peaks are clearly observed, can be discounted. A comprehensive list of the candidates can be found in e-Appendix 8 and a picture representation of candidates in the tree and the very complex relationships between them is in Figure 3.4.

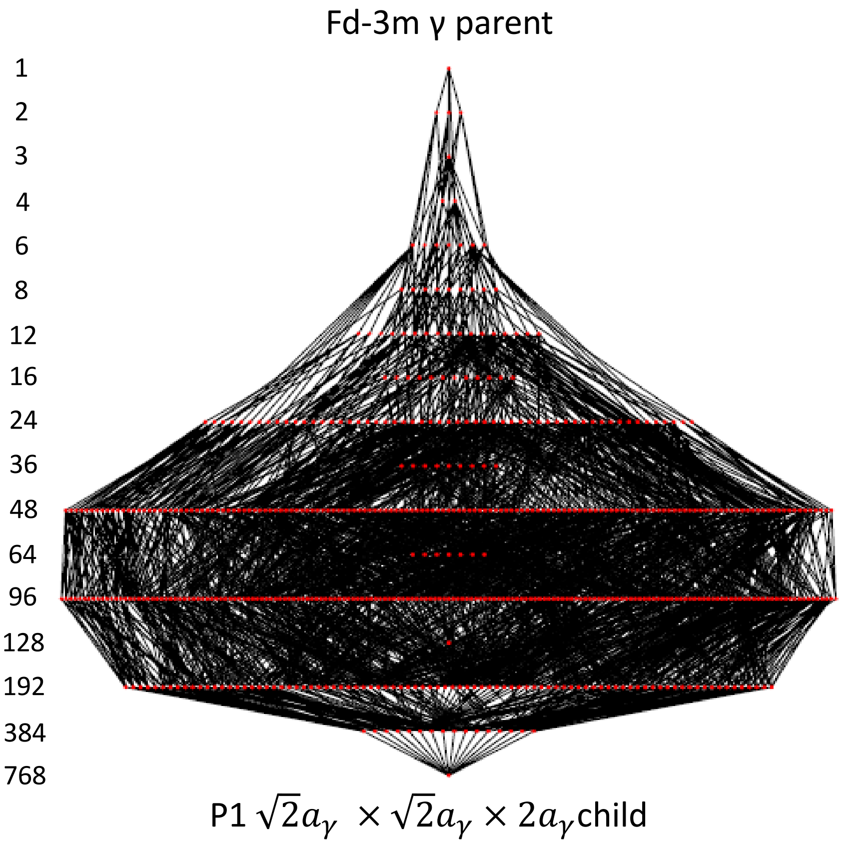

Figure 3.4: Representation of the 547 candidate tree. Each red dot represents one candidate. Symmetry decreases on progression down the tree from the γ-parent to our *P1* child. The numbers to the left of each 'tier' of the tree indicate the order of candidates

in that tier relative to the parent (e.g. the parent subgroup has 768 times as many symmetry elements as the child).

3.4.2 Iterative Process

For the remaining 544 candidates, a refinement scheme that ensures they all achieve the best possible convergence of their allowed structural parameters within a reasonable timescale is required. As in the case of the WO_3 examples, it is helpful to divide optimisation of the structural parameters into two stages: a lattice refinement (that focuses on optimising unit cell parameters), and a full optimisation step that focuses on distortion mode optimisation.

3.4.2.1 Lattice Refinement

It is clear from the peak splitting observed in our powder diffraction patterns that the initial lattice refinement step here requires considerably less distortion of the unit cell parameters than required in the WO_3 examples in Chapter 2. Table 3.1 shows the scale of lattice distortion required using the child subgroup fit for both phases. As the scale of the lattice distortion is smaller, we find we can effectively optimise unit cell parameters using a much smaller randomisation at the end of each Rietveld cycle of ±1 %. Furthermore, we find there is no need to convolute an additional “peakshape” parameter to artificially broaden peaks (as in Chapter 2) because calculated peaks achieve sufficient peak overlap (Figure 3.5) from cubic starting points without it. We have also shown (Appendix 10) that distortion modes can be excluded from the refinement altogether at this stage and the resulting fit to both data sets remains equivalent for all candidates. While this speeds up the overall search process by a factor of ~ 3, for consistency we present results here which include distortion modes in the refinement at this stage (i.e. following exactly the Chapter 2 protocol).

Table 3.1: Starting cubic and refined unit cell parameters for child subgroup for β and α - $Bi_2Sn_2O_7$ data sets. Percentage changes are relative to $(\sqrt[3]{(V_\beta/4)} \times 2\,\text{Å}, \sqrt[3]{(V_\beta/4)} \times \sqrt{2}\,\text{Å}, \sqrt[3]{(V_\beta/4)} \times \sqrt{2}\,\text{Å}, 90^\circ, 90^\circ, 90^\circ)$ and $\left(\sqrt[3]{\left(\frac{V_\alpha}{4}\right)} \times 2\,\text{Å}, \sqrt[3]{\left(\frac{V_\alpha}{4}\right)} \times \sqrt{2}\,\text{Å}, \sqrt[3]{\left(\frac{V_\alpha}{4}\right)} \times \sqrt{2}\,\text{Å}, 90^\circ, 90^\circ, 90^\circ\right)$ for β and α -$Bi_2Sn_2O_7$ respectively.

Unit Cell Parameter	*800˚C starting cell*	*Refined value (β-phase)*	*% Change from cubic*	*Refined value (α-phase)*	*% Change from cubic*
a	21.445 Å	21.40942(10) Å	0.000	21.55036(15) Å	0.703
b	15.1639 Å	15.1390(2) Å	0.001	15.0775(2) Å	0.360
c	15.1639 Å	15.1386(2) Å	0.001	15.0806(2) Å	0.340
α	90˚	89.9831(3)˚	0.019	89.995(7)˚	0.006
β	90˚	89.9677(8)˚	0.036	90.004(5)˚	0.004
γ	90˚	90.0268(7)˚	0.030	89.958(1)˚	0.047

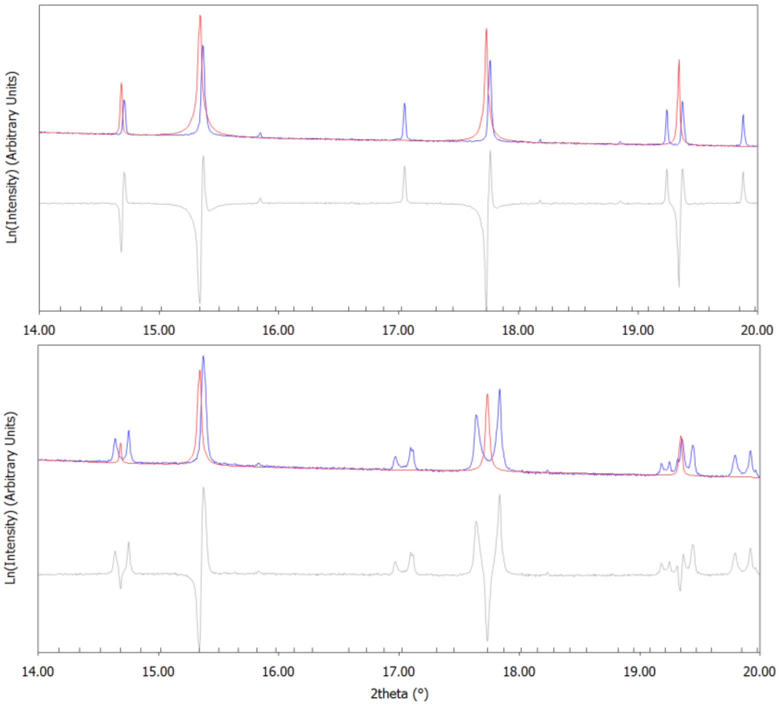

Figure 3.5: Initial peak overlap of calculated cubic structure to (top) β-$Bi_2Sn_2O_7$ synchrotron X-ray data and (bottom) α- $Bi_2Sn_2O_7$ synchrotron X-ray data. Both are shown on a logarithmic scale to emphasise peak tails.

3.4.2.2 Full Optimisation

This step follows the protocol laid out in Chapter 2, refining distortion modes and resetting to values close to zero on convergence. We can confirm, by the agreement of multiple convergence cycles and the overall R_{wp} dependence through our tree, that the global minimum is found for all examples. E-Appendixes 9 and 10 show we can be confident of finding the global minima for all candidates as we find the same convergence minima ≥ 34 and ≥ 26 times for all 544 candidates for β and α -$Bi_2Sn_2O_7$ searches respectively.

3.4.3 Full Exhaustive Search Results

Figure 3.6 and Figure 3.10 show the R_{wp} of the model against the data set obtained for all 544 candidates for β- (470 K) and α-$Bi_2Sn_2O_7$ (293 K) respectively. This fully exhaustive search gives the most comprehensive understanding of the relationship between each distortion available in the tree and the fit to the data. It does, however, take around 232 hours to complete the > 3.8 million Rietveld iterations on an ordinary desktop computer (6th generation i7, 3.4Ghz) using tc.exe from command line with no graphics.

3.4.3.1 β-$Bi_2Sn_2O_7$

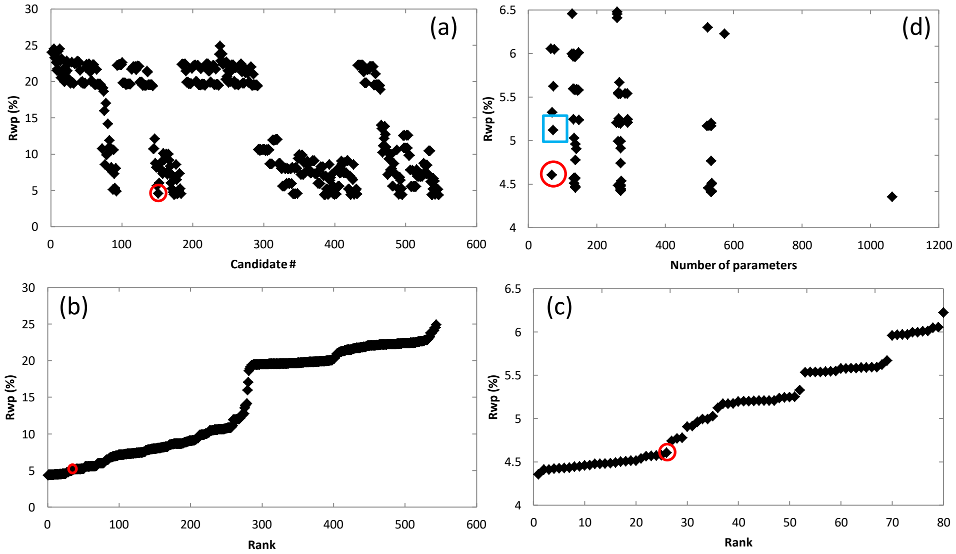

Figure 3.6: Combined R_{wp} obtained for each of 544 candidates after Rietveld refinement using synchrotron X-ray and HRPD neutron powder diffraction data of β- $Bi_2Sn_2O_7$. Individual panels show (a) R_{wp} as a function of tree candidate number (b) R_{wp} of all candidates in ranked order (c) R_{wp} of only best 80 candidates in ranked order and (d) R_{wp} of all candidates as a function of the number of structural parameters available. β-$Bi_2Sn_2O_7$ structural model chosen is shown in red circles in all plots. Blue square shows α-$Bi_2Sn_2O_7$ model chosen (see Section 3.4.3.3).

Firstly, turning to β-$Bi_2Sn_2O_7$ data, a simple analysis of Figure 3.6 allows us to choose the first reliable structural model for β-$Bi_2Sn_2O_7$. Firstly, from Figure 3.6a we see that candidates divide roughly into two categories: those with R_{wp} > 15 %, and those with R_{wp} < 15 %. From Figure 3.6b we can see candidates further divide into several distinct R_{wp} plateaus depending on how many of the key distortions required to fit the diffraction peaks are available to them.

Amongst the best 80 candidates (Figure 3.6c), 26 have all the required distortions and lie on the lowest R_{wp} plateau with R_{wp} < 4.7 %. Finally, Figure 3.6d shows R_{wp} against the number of parameters available to the best candidates. Of those on the lowest plateau, candidate #152 has fewer parameters (69) than any other, has R_{wp} = 4.61 % and is ranked 26th overall. It has a $a_\gamma/\sqrt{2}\times 2a_\gamma \times \sqrt{2}a_\gamma$ unit cell and orthorhombic space group *Aba2* (see Table 3.2 for a list of basic structural parameters of the top 30 ranked models). Other candidates amongst the 26 on the lowest R_{wp} plateau have all the parameters of candidate #152 plus additional parameters that provide no significant improvement in fitness – all 25 other candidates on the lowest R_{wp} plateau are subgroups of #152. We emphasise that this does not mean all parameters of candidate #152 are necessary to fit the data; merely that candidate #152 has the fewest unnecessary parameters. It is also not a requirement of any candidate on the lowest R_{wp} plateau to be a subgroup of #152 (they may differ in those parameters that are unnecessary to fit the data). Those candidates with R_{wp} > 4.7 % all lack at least one key distortion and so provide an inferior fit to the data. A detailed discussion of the important distortion modes in both β- and α-$Bi_2Sn_2O_7$ can be found in section 3.5.2.

Table 3.2: Structural parameters and combined X-ray / TOF neutron R_{wp} for the top 30 ranked candidates for β-$Bi_2Sn_2O_7$. The basis given in column 1 and V_{frac} in column 13 are relative to the parent.

Basis - origin	Rank	Candidate #	Rwp min/%	prms	a/Å	b/Å	c/Å	al/°	be/°	ga/°	Volume/Å^3	V_{frac}
1 P1, basis={(0,0,2),(-1,-1,0),(1,-1,0)}, origin=(0,0,0)	1	547	4.357	1064	21.409	15.139	15.139	89.983	89.968	90.027	4906.677	4.0
7 Pc, basis={(0,0,2),(-1,-1,0),(1,-1,0)}, origin=(-3/8,-3/8,0)	2	538	4.410	534	21.413	15.143	15.132	90.000	90.004	90.000	4906.690	4.0
7 Pc, basis={(-1,1,0),(-1,-1,0),(0,0,2)}, origin=(-3/8,-3/8,0)	3	537	4.412	534	15.132	15.143	21.413	90.000	90.005	90.000	4906.689	4.0
1 P1, basis={(-1,-1,0),(-1,1,0),(1,0,-1)}, origin=(0,0,0)	4	496	4.420	536	15.140	15.140	15.143	120.013	120.016	90.005	2453.330	2.0
7 Pc, basis={(0,0,-2),(-1/2,-1/2,0),(-1,1,0)}, origin=(-1/8,-1/8,0)	5	387	4.425	270	21.413	7.572	15.132	90.000	90.006	90.000	2453.347	2.0
7 Pc, basis={(-1,1,0),(1/2,1/2,0),(0,0,-2)}, origin=(1/8,1/8,0)	6	386	4.427	270	15.132	7.572	21.413	90.000	90.006	90.000	2453.346	2.0
7 Pc, basis={(-1/2,-1/2,1),(-1,1,0),(-1,-1,0)}, origin=(0,0,0)	7	423	4.434	270	13.110	15.143	15.132	90.000	54.753	90.000	2453.348	2.0
7 Pc, basis={(-1,1,0),(0,0,-2),(-1/2,-1/2,0)}, origin=(0,0,0)	8	391	4.445	270	15.132	21.412	7.572	90.000	90.011	90.000	2453.346	2.0
9 Cc, basis={(1,-2,-1),(-1,0,-1),(1,0,-1)}, origin=(0,-1/4,-1/4)	9	491	4.448	270	26.221	15.143	15.132	90.000	54.749	90.000	4906.691	4.0
3 P2, basis={(-1,1,0),(-1,-1,0),(0,0,2)}, origin=(-1/8,1/8,1/4)	10	542	4.457	526	15.143	15.132	21.413	90.000	89.993	90.000	4906.697	4.0
7 Pc, basis={(-1/2,1,-1/2),(1/2,0,-1/2),(-1,0,-1)}, origin=(0,0,0)	11	174	4.462	138	13.110	7.572	15.132	90.000	54.753	90.000	1226.674	1.0
5 C2, basis={(0,0,-2),(-1,-1,0),(-1,1,0)}, origin=(-1/2,-1/4,-3/4)	12	428	4.475	266	21.413	15.132	15.143	90.000	89.997	90.000	4906.700	4.0
9 Cc, basis={(-1,0,-1),(0,-2,0),(-1/2,0,1/2)}, origin=(-1/8,-1/4,-1/8)	13	175	4.477	138	15.132	21.413	7.572	90.000	89.989	90.000	2453.346	2.0
4 P2_1, basis={(-1/2,-1/2,0),(-1,1,0),(0,0,-2)}, origin=(0,0,0)	14	400	4.479	270	7.572	15.132	21.413	90.000	89.998	90.000	2453.350	2.0
3 P2, basis={(-1/2,-1/2,0),(-1,1,0),(0,0,-2)}, origin=(0,0,0)	15	399	4.485	262	7.572	15.132	21.413	90.000	89.995	90.000	2453.349	2.0
7 Pc, basis={(1/2,1/2,0),(0,0,-2),(-3/2,1/2,0)}, origin=(0,0,0)	16	392	4.489	270	7.572	21.412	16.923	90.000	116.593	90.000	2453.342	2.0
5 C2, basis={(1,-2,-1),(-1,0,-1),(1,0,-1)}, origin=(1/4,-1/4,-1/2)	17	494	4.501	266	26.227	15.132	15.143	90.000	54.729	90.000	4906.698	4.0
1 P1, basis={(0,0,-2),(-1,1,0),(1/2,1/2,0)}, origin=(0,0,0)	18	403	4.505	536	21.409	15.138	7.570	89.983	90.028	89.969	2453.335	2.0
5 C2, basis={(0,-2,0),(-1,0,-1),(1/2,0,-1/2)}, origin=(0,-1/4,-1/4)	19	179	4.512	134	21.413	15.132	7.572	90.000	89.995	90.000	2453.349	2.0
1 P1, basis={(-1/2,-1/2,-1),(-1,1,0),(1/2,1/2,-1)}, origin=(0,0,0)	20	432	4.512	536	13.107	15.139	13.114	90.014	70.524	90.034	2453.335	2.0
1 P1, basis={(-1/2,-1,-1/2),(-1/2,1,-1/2),(1/2,0,-1/2)}, origin=(0,0,0)	21	184	4.537	272	13.107	13.113	7.570	89.984	90.035	109.473	1226.668	1.0
29 Pca2_1, basis={(1/2,1/2,0),(0,0,-2),(-1,1,0)}, origin=(0,0,0)	22	343	4.564	137	7.572	21.413	15.132	90.000	90.000	90.000	2453.353	2.0
30 Pnc2, basis={(0,0,-2),(-1/2,-1/2,0),(-1,1,0)}, origin=(0,0,0)	23	345	4.567	133	21.413	7.572	15.132	90.000	90.000	90.000	2453.352	2.0
32 Pba2, basis={(0,0,-2),(-1/2,-1/2,0),(-1,1,0)}, origin=(0,0,-1/2)	24	342	4.570	133	21.413	7.572	15.132	90.000	90.000	90.000	2453.352	2.0
33 Pna2_1, basis={(0,0,-2),(-1/2,-1/2,0),(-1,1,0)}, origin=(0,0,-1/2)	25	348	4.575	137	21.413	7.572	15.132	90.000	90.000	90.000	2453.352	2.0
41 Aba2, basis={(1/2,0,-1/2),(0,2,0),(1,0,1)}, origin=(-1/4,-3/4,-1/2)	26	152	4.605	69	7.572	21.413	15.132	90.000	90.000	90.000	2453.352	2.0
7 Pc, basis={(-1/2,-1/2,-1),(-1,1,0),(1/2,1/2,-1)}, origin=(-1/8,1/8,0)	27	424	4.742	270	13.110	15.143	13.110	90.000	70.497	90.000	2453.342	2.0
4 P2_1, basis={(-1,1,0),(-1,-1,0),(0,0,2)}, origin=(-1/8,1/8,1/4)	28	543	4.768	534	15.132	15.143	21.413	90.000	89.993	90.000	4906.679	4.0
7 Pc, basis={(-1/2,1,-1/2),(1/2,0,-1/2),(-1/2,-1,-1/2)}, origin=(1/8,0,-1/8)	29	173	4.778	138	13.110	7.572	13.110	90.000	109.504	90.000	1226.670	1.0
1 P1, basis={(-1/2,1,-1/2),(-1/2,0,1/2),(1/2,1/2,0)}, origin=(0,0,0)	30	93	4.904	140	13.107	7.570	7.572	120.013	73.217	90.031	613.333	0.5

3.4.3.2 Visual Evidence

In order to support this model, there are two key facts that must be proven: firstly; that candidate #152 provides a good fit to all the structurally related features of the diffraction data and, secondly; that no candidate with fewer parameters can also do this.

Figure 3.7 addresses the first criterion, showing a fit to the diffraction data which is visually identical to that provided by the child subgroup (Figure 3.3a). In order to address the second criterion we start by identifying that candidate #170, with R_{wp} = 6.05 % is the highest ranking model with fewer parameters (66) than candidate #152. It has a $2a_\gamma \times \sqrt{2}a_\gamma \times a_\gamma/\sqrt{2}$ unit cell and orthorhombic space group $C222_1$. Figure 3.8 and Figure 3.9 show the fit to the diffraction data of candidate #152 and #170 respectively in the d = 1.25-1.50 Å region. We can see that there are several inadequacies in the fit obtained using candidate #170 compared to candidate #152 (it lacks Γ_4^- distortion modes which we will later see are important to providing a good fit to the data). If we also accept, without inspection, that no other candidate with fitness worse still than candidate #170 could provide an adequate fit to structural features of the diffraction data then the second criterion is met.

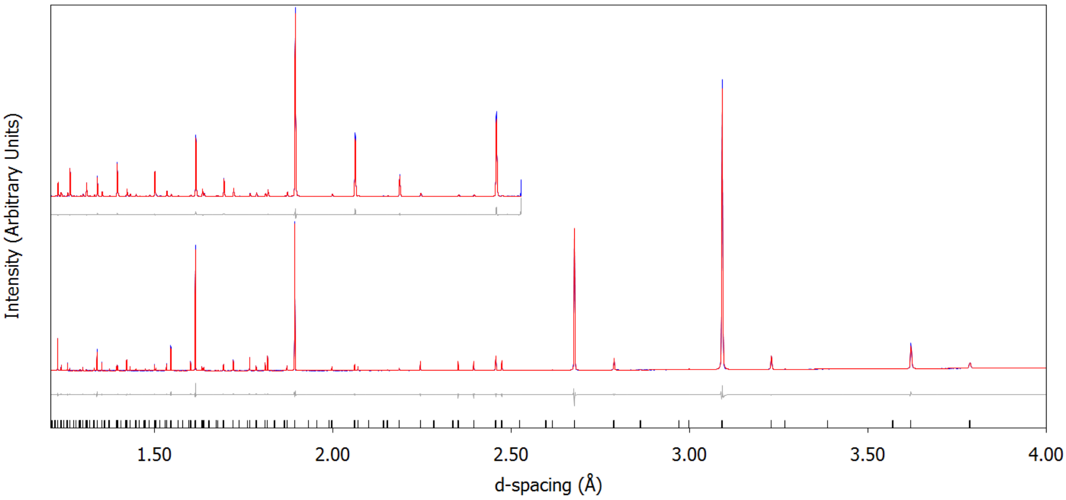

Figure 3.7: Combined fit to synchrotron X-ray (bottom) and HRPD neutron (top) powder diffraction data of β-$Bi_2Sn_2O_7$ after Rietveld refinement of candidate #152. Synchrotron X-ray / TOF neutron R_{wp} (R_{Bragg}) = 4.71 % (1.92 %) / 4.46 % (2.40 %).

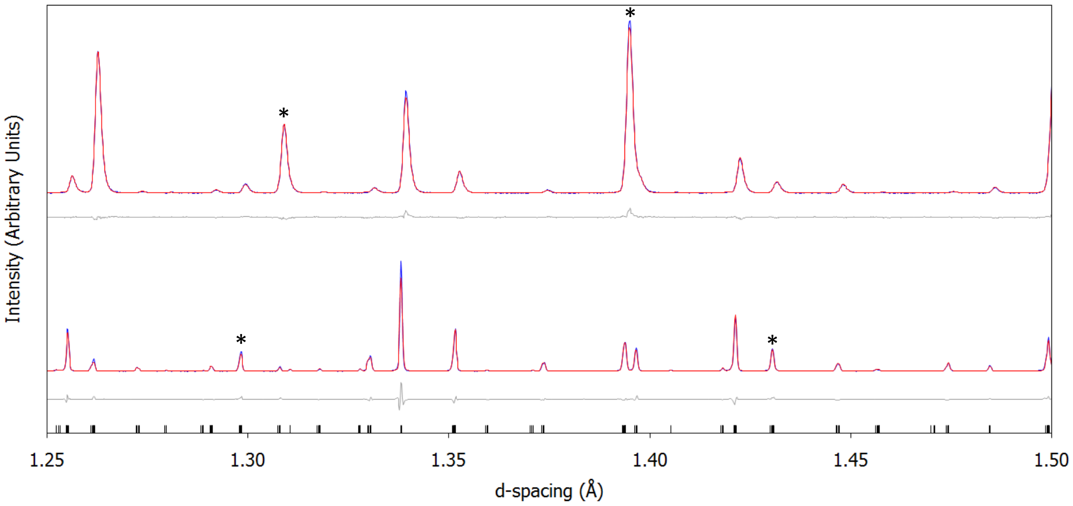

Figure 3.8: Combined fit to d = 1.25-1.5 Å region of synchrotron X-ray (bottom) and HRPD neutron (top) powder diffraction data of β-$Bi_2Sn_2O_7$ after Rietveld refinement of candidate #152. Synchrotron X-ray / TOF neutron R_{wp} (R_{Bragg}) = 4.71 % (1.92 %) / 4.46 % (2.40 %). Peaks that are well fit by candidate #152 but poorly by candidate #170 are marked with a *.

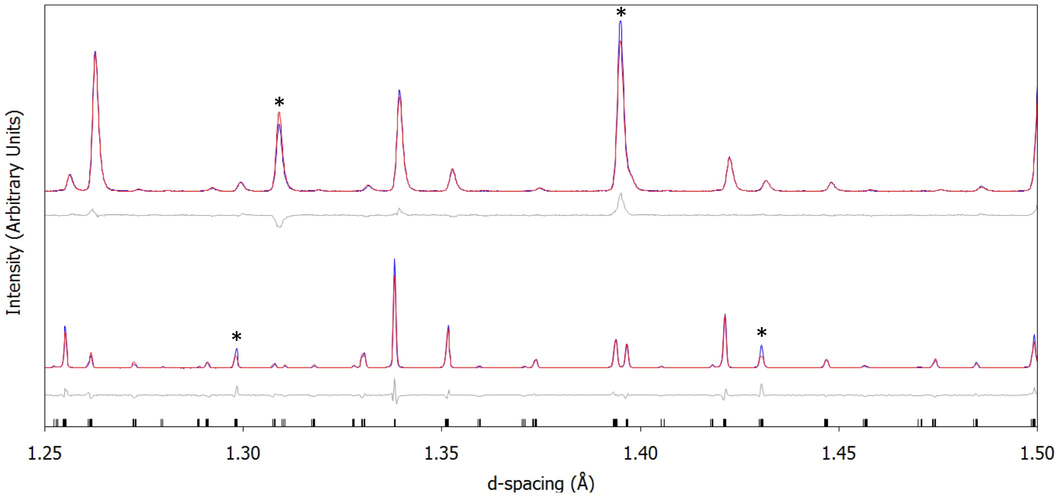

Figure 3.9: Combined fit to d = 1.25-1.5 Å region of synchrotron X-ray (bottom) and HRPD neutron (top) powder diffraction data of β-$Bi_2Sn_2O_7$ after Rietveld refinement of candidate #170. Synchrotron X-ray / TOF neutron R_{wp} (R_{Bragg}) = 6.10 % (3.20 %) / 5.99 % (3.24 %). Peaks that are well fit by candidate #152 but poorly by candidate #170 are marked with a *.

3.4.3.3 α-$Bi_2Sn_2O_7$

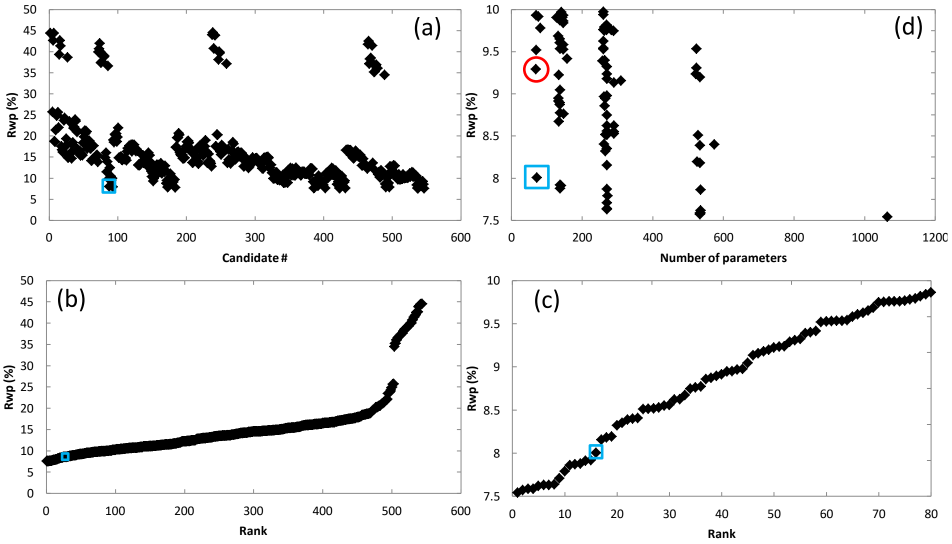

Figure 3.10: Combined R_{wp} obtained for each of 544 candidates after Rietveld refinement using synchrotron X-ray and HRPD neutron powder diffraction data of α- $Bi_2Sn_2O_7$. Individual panels show (a) R_{wp} as a function of tree candidate number (b) R_{wp} of all candidates in ranked order (c) R_{wp} of only best 80 candidates in ranked order and (d) R_{wp} of all candidates as a function of the number of structural parameters available. α-$Bi_2Sn_2O_7$ structural model chosen is shown in blue squares in all plots. Red circle shows β-$Bi_2Sn_2O_7$ model chosen (see Section 3.4.3.1).

Turning to α-$Bi_2Sn_2O_7$, we can see from Figure 3.10a that the candidates again divide into two categories; those with R_{wp} > 37 %, and those with R_{wp} < 25 %. The best solutions have R_{wp}< 8 %. Looking at the candidates in ranked order (Figure 3.10b), we can see that again candidates separate into several distinct R_{wp} plateaus the lowest two of which range from R_{wp} ~ 7.5-8.0 % and contain 16 candidates (Figure 3.10c). Small improvements in fit over this range result from additional Σ, Δ, X and W-point modes that are not required to fit structural features of the data. Figure 3.10d shows R_{wp} as a function of the number of structural parameters and reveals that of these 16 the one with the fewest parameters (72) has R_{wp} = 8.00 %. This is candidate #88 in our tree, which is ranked 16 with a $\sqrt{3/2}a_\gamma \times a_\gamma/\sqrt{2} \times \sqrt{3/2}a_\gamma$ unit cell and monoclinic space group Cc (see Table 3.3 for a list of basic structural parameters of the top 30 ranked models). All of the other 15 candidates on the lowest R_{wp} plateau are subgroups of #88; those with higher R_{wp} lack at least one key distortion. Again by this simple analysis we are able to obtain a new structural model for α-$Bi_2Sn_2O_7$ with significantly fewer structural parameters than previously thought.

Table 3.3 Structural parameters and combined X-ray / TOF neutron *R_{wp}* for the top 30 ranked candidates for α-$Bi_2Sn_2O_7$. The basis given in column 1 and V_{frac} in column 13 are relative to the parent.

Basis - origin	Rank	Candidate #	Rwp min/%	prms	a/Å	b/Å	c/Å	al/˚	be/˚	ga/˚	Volume/Å^3	V_{frac}
1 P1, basis={(0,0,2),(-1,-1,0),(1,-1,0)}, origin=(0,0,0)	1	547	7.541	1064	21.550	15.077	15.081	89.996	90.004	89.958	4900.037	4.0
7 Pc, basis={(0,0,2),(-1,-1,0),(1,-1,0)}, origin=(-3/8,-3/8,0)	2	538	7.571	534	21.550	15.081	15.077	90.000	90.040	90.000	4900.051	4.0
1 P1, basis={(0,0,-2),(-1,1,0),(1/2,1/2,0)}, origin=(0,0,0)	3	403	7.585	536	21.550	15.077	7.541	89.999	89.994	89.959	2450.015	2.0
7 Pc, basis={(-1,1,0),(-1,-1,0),(0,0,2)}, origin=(-3/8,-3/8,0)	4	537	7.585	534	15.077	15.081	21.550	90.000	89.959	90.000	4900.037	4.0
1 P1, basis={(-1/2,-1/2,-1),(-1,1,0),(1/2,1/2,-1)}, origin=(0,0,0)	5	432	7.618	536	13.084	15.163	13.077	89.659	70.801	90.353	2450.016	2.0
7 Pc, basis={(-1,1,0),(1/2,1/2,0),(0,0,-2)}, origin=(1/8,1/8,0)	6	386	7.630	270	15.077	7.541	21.550	90.000	90.041	90.000	2450.015	2.0
7 Pc, basis={(-1/2,-1/2,1),(-1,1,0),(-1,-1,0)}, origin=(0,0,0)	7	423	7.632	270	13.155	15.081	15.077	90.000	54.997	90.000	2450.031	2.0
7 Pc, basis={(-1/2,-1/2,-1),(-1,1,0),(1/2,1/2,-1)}, origin=(-1/8,1/8,0)	8	424	7.639	270	13.155	15.081	13.146	90.000	69.955	90.000	2450.015	2.0
7 Pc, basis={(0,0,-2),(-1/2,-1/2,0),(-1,1,0)}, origin=(-1/8,-1/8,0)	9	387	7.707	270	21.550	7.541	15.077	90.000	90.041	90.000	2450.021	2.0
1 P1, basis={(-1/2,-1,-1/2),(-1/2,1,-1/2),(1/2,0,-1/2)}, origin=(0,0,0)	10	184	7.789	272	13.085	13.077	7.581	90.340	90.358	109.201	1225.001	1.0
1 P1, basis={(-1,-1,0),(-1,1,0),(1,0,-1)}, origin=(0,0,0)	11	496	7.861	536	15.081	15.078	15.166	119.854	119.838	89.985	2450.003	2.0
9 Cc, basis={(1,-2,-1),(-1,0,-1),(1,0,-1)}, origin=(0,-1/4,-1/4)	12	491	7.871	270	26.309	15.082	15.076	90.000	54.997	90.000	4900.028	4.0
7 Pc, basis={(-1/2,1,-1/2),(1/2,0,-1/2),(-1/2,-1,-1/2)}, origin=(1/8,0,-1/8)	13	173	7.879	138	13.155	7.541	13.146	90.000	110.044	90.000	1225.003	1.0
1 P1, basis={(-1/2,1,-1/2),(-1/2,0,1/2),(1/2,1/2,0)}, origin=(0,0,0)	14	93	7.912	140	13.079	7.583	7.541	119.849	73.237	90.358	612.505	0.5
7 Pc, basis={(-1/2,1,-1/2),(1/2,0,-1/2),(-1,0,-1)}, origin=(0,0,0)	15	174	7.918	138	13.146	7.541	15.077	90.000	55.051	90.000	1225.007	1.0
9 Cc, basis={(-1/2,-1,-1/2),(-1/2,0,1/2),(-1/2,1,-1/2)}, origin=(-1/4,-1/4,0)	16	88	8.004	72	13.155	7.541	13.146	90.000	110.045	90.000	1225.008	1.0
7 Pc, basis={(1/2,1/2,0),(0,0,-2),(-3/2,1/2,0)}, origin=(0,0,0)	17	392	8.154	270	7.582	21.324	17.016	90.000	117.059	90.000	2450.004	2.0
4 P2_1, basis={(-1,1,0),(-1,-1,0),(0,0,2)}, origin=(-1/8,1/8,1/4)	18	543	8.181	534	15.080	15.078	21.550	90.000	89.961	90.000	4900.100	4.0
3 P2, basis={(-1,1,0),(-1,-1,0),(0,0,2)}, origin=(-1/8,1/8,1/4)	19	542	8.193	526	15.080	15.078	21.550	90.000	89.962	90.000	4900.053	4.0
5 C2, basis={(0,0,-2),(-1,-1,0),(-1,1,0)}, origin=(-1/2,-1/4,-3/4)	20	428	8.321	266	21.550	15.079	15.080	90.000	90.038	90.000	4900.034	4.0
4 P2_1, basis={(-1/2,-1/2,0),(-1,1,0),(0,0,-2)}, origin=(0,0,0)	21	400	8.351	270	7.540	15.078	21.550	90.000	89.962	90.000	2450.005	2.0
7 Pc, basis={(-1,1,0),(-1,-1,0),(-1,1,2)}, origin=(-3/8,-3/8,0)	22	539	8.387	534	15.077	15.081	26.309	90.000	54.997	90.000	4899.972	4.0
6 Pm, basis={(-1,1,0),(-1,-1,0),(0,0,2)}, origin=(-3/8,-3/8,0)	23	536	8.400	574	15.077	15.081	21.550	90.000	90.040	90.000	4899.965	4.0
3 P2, basis={(-1/2,-1/2,0),(-1,1,0),(0,0,-2)}, origin=(0,0,0)	24	399	8.405	262	7.540	15.078	21.550	90.000	89.962	90.000	2450.020	2.0
5 C2, basis={(-2,0,0),(0,-2,0),(0,0,2)}, origin=(-7/8,-7/8,1/8)	25	546	8.510	528	21.325	21.325	21.550	90.000	89.960	90.000	9800.027	8.0
7 Pc, basis={(-1,1,0),(0,0,-2),(-1/2,-1/2,0)}, origin=(0,0,0)	26	391	8.512	270	15.076	21.550	7.541	90.000	90.003	90.000	2450.017	2.0
5 C2, basis={(1,-2,-1),(-1,0,-1),(1,0,-1)}, origin=(1/4,-1/4,-1/2)	27	494	8.518	266	26.294	15.078	15.080	90.000	55.042	90.000	4900.028	4.0
8 Cm, basis={(0,0,-2),(-1,-1,0),(-1,1,0)}, origin=(-3/8,-3/8,-3/4)	28	420	8.528	290	21.550	15.081	15.077	90.000	90.040	90.000	4899.931	4.0
6 Pm, basis={(-1/2,-1/2,0),(-1,1,0),(0,0,-2)}, origin=(0,0,0)	29	389	8.549	290	7.539	15.081	21.550	90.000	89.960	90.000	2449.997	2.0
7 Pc, basis={(-1/2,-1/2,0),(-1,1,0),(0,0,-2)}, origin=(0,0,0)	30	390	8.558	270	7.539	15.081	21.550	90.000	90.039	90.000	2450.003	2.0

3.4.3.4 Visual Evidence

Based on the same criteria as used in section 3.4.3.2, we can show that our structural model has a combined fit to our data (Figure 3.11) visually as good as the child subgroup #547 (Figure 3.3b). The next best fit to the data using fewer parameters than candidate #88 is provided by candidate #152 (our β-$Bi_2Sn_2O_7$ structural model above, 69 parameters and R_{wp} = 9.29 %). Figure 3.12 and Figure 3.13 show the fit to the diffraction data of candidate #88 and #152 respectively in the *d* = 1.25-1.50 Å region. The fit with candidate #152 is clearly inferior (it lacks the correct specific Γ_4^- distortion modes). If we again assume that no candidate with an even worse R_{wp} than this can provide an adequate fit to our data then we have shown that candidate #88 represents the simplest possible structural model for α-$Bi_2Sn_2O_7$ that is consistent with its diffraction data.

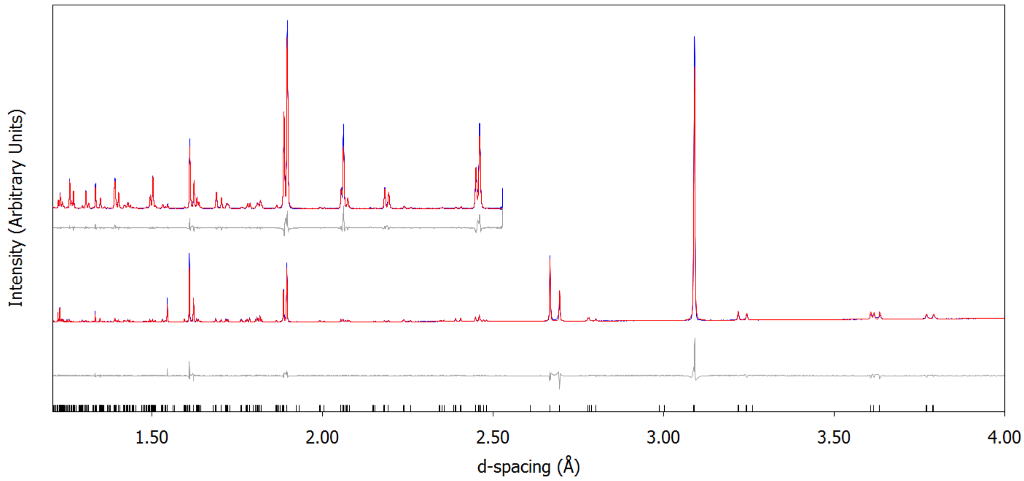

Figure 3.11: Combined fit to synchrotron X-ray (bottom) and HRPD neutron (top) powder diffraction data of α-$Bi_2Sn_2O_7$ after Rietveld refinement of candidate #88. Synchrotron X-ray / TOF neutron R_{wp} (R_{Bragg}) = 8.95 % (4.28 %) / 7.65 % (4.02 %).

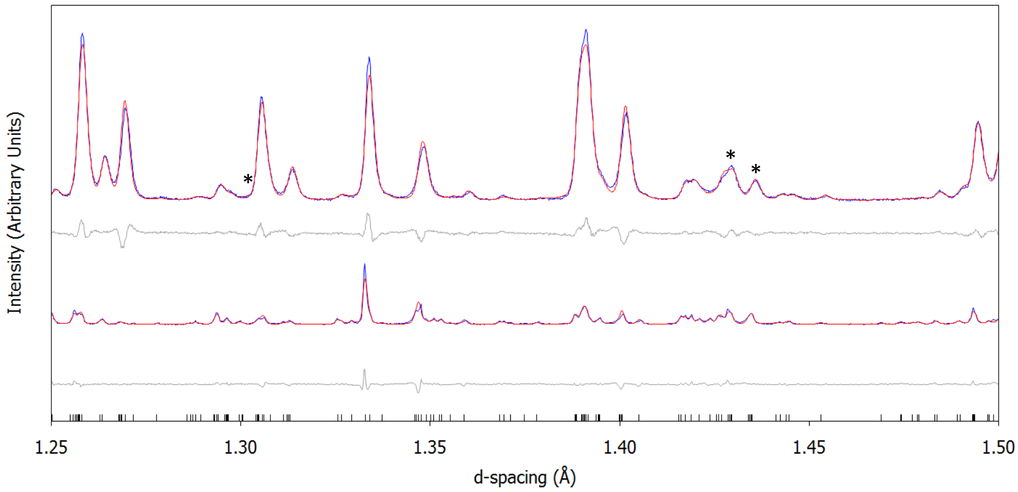

Figure 3.12: Combined fit to d = 1.25-1.5 Å region of synchrotron X-ray (bottom) and HRPD neutron (top) powder diffraction data of α-$Bi_2Sn_2O_7$ after Rietveld refinement of candidate #88. Synchrotron X-ray / TOF neutron R_{wp} (R_{Bragg}) = 8.95 % (4.28 %) / 7.65 % (4.02 %). Peaks that are fell fit by candidate #88 but poorly by candidate #152 are marked with a *.

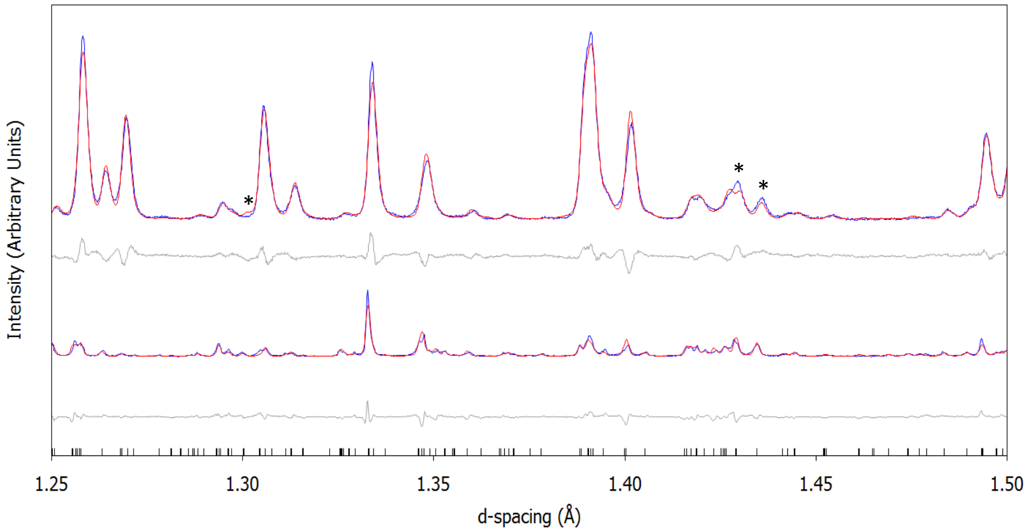

Figure 3.13: Combined fit to d = 1.25-1.5 Å region of synchrotron X-ray (bottom) and HRPD neutron (top) powder diffraction data of α-$Bi_2Sn_2O_7$ after Rietveld refinement of candidate #152. Synchrotron X-ray / TOF neutron R_{wp} (R_{Bragg}) = 10.44 % (5.38 %) / 8.85 % (5.21 %). Peaks that are fell fit by candidate #88 but poorly by candidate #152 are marked with a *.

3.4.3.5 Full Structural Refinements and Peakshape Effects

After identifying our α- and β-$Bi_2Sn_2O_7$ structural models from the exhaustive search we are then able to perform full Rietveld refinements using data over the full d-spacing range collected for synchrotron X-ray and TOF neutron, including the lower resolution 90˚ bank at HRPD. We also see that considerable peak broadening occurs between the β- and α-phases which arises due to strain broadening effects resulting from the significant cell metric change ($\Delta d/d \approx 1 \times 10^{-2}$). Furthermore peaks exhibit asymmetry with a slight hkl dependence. Therefore we introduce a Stephens-type[21] peakshape to our candidate #88 α-phase final Rietveld fit, reducing R_{wp} to 5.65 % (Figure 3.15). This is not required in our candidate #152 β-phase final Rietveld fit (Figure 3.14), with R_{wp} = 4.55 % over the full data ranges. A summary of the structural models including space group, atomic coordinates, unit cell parameters and isotropic temperature factors extracted from these fits together with fit quality indicators for each data set are given in Table 3.4.

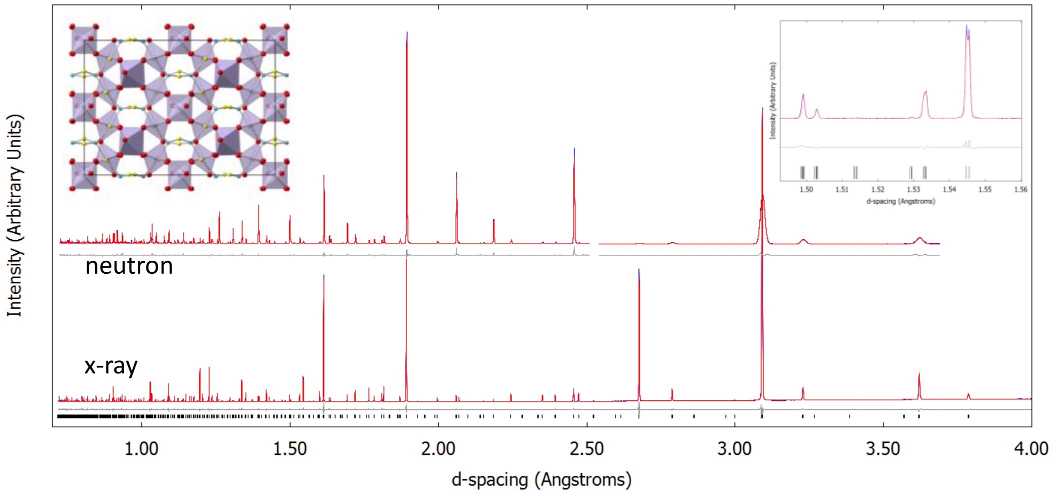

Figure 3.14: Final Rietveld fit to neutron (top) and X-ray (bottom) powder diffraction data of β-$Bi_2Sn_2O_7$. High d-spacing (d > 2.5Å) neutron data is from low resolution 90˚ bank. Upper right inset shows weak splitting at d ~ 1.545 Å that excludes a cubic structure. Upper left inset shows the structure viewed down [010] axis.

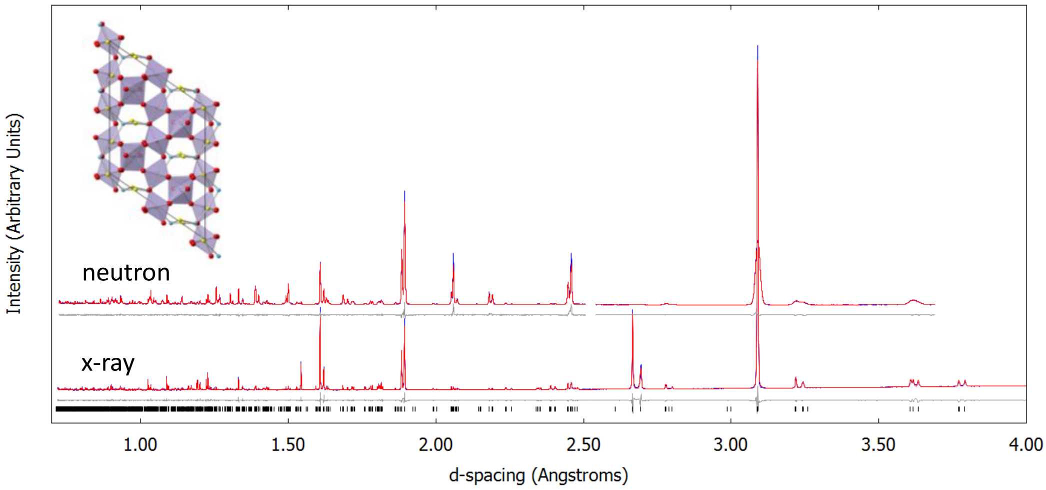

Figure 3.15: Final Rietveld fit to neutron (top) and X-ray (bottom) powder diffraction data of α-$Bi_2Sn_2O_7$ using a Stephens-type peakshape. High d-spacing (d > 2.5 Å) neutron data is from low resolution 90˚ bank. Inset shows structure viewed down [010] axis.

Table 3.4: Structural model parameters extracted from final Rietveld fits to (left) α-$Bi_2Sn_2O_7$ and (right) β-$Bi_2Sn_2O_7$ data. Individual fit quality indicators for each data set are summarised in lower section.

α-$Bi_2Sn_2O_7$, Space Group *Cc*					β-$Bi_2Sn_2O_7$, Space Group *Aba2*				
atom	**x**	**y**	**z**	***B*/Å^2**	**atom**	**x**	**y**	**z**	**B/Å^2**
Bi(1)	0.2369(2)	0.2673(3)	0.01442(17)	0.858(11)	Bi(1)	0.7097(2)	0.11466(9)	0.11170(13)	1.421(5)
Bi(2)	0.2743(2)	0.2245(3)	0.51155(17)	0.858(11)	Bi(2)	0.2894(2)	0.36431(9)	0.36150(13)	1.421(5)
Bi(3)	-0.0174(2)	-0.0446(3)	-0.02055(19)	0.858(11)	Bi(3)	0.0255(2)	0.23624(6)	0.00458(12)	1.421(5)
Bi(4)	0.0306(2)	0.0038(3)	0.75004(19)	0.858(11)	Bi(4)	0	0	0.23244(14)	1.421(5)
Sn(1)	0.7501(4)	0.2474(6)	0.7500(3)	0.485(10)	Bi(5)	0	0	0.76936(14)	1.421(5)
Sn(2)	0.7436(4)	0.2512(6)	0.2420(3)	0.485(10)	Sn(1)	0.7486(4)	0.37511(8)	0.12465(12)	0.602(5)
Sn(3)	0.4972(3)	0.0010(6)	0.7465(3)	0.485(10)	Sn(2)	0.2473(4)	0.62452(8)	0.37231(12)	0.602(5)
Sn(4)	0.4960(3)	0.0005(4)	0.4943(3)	0.485(10)	Sn(3)	0	0	-0.0003(2)	0.602(5)
O1(1)	0.6192(4)	0.2064(6)	0.7820(4)	0.738(9)	Sn(4)	0	0	0.4948(2)	0.602(5)
O1(2)	0.6158(4)	0.2065(6)	0.2751(4)	0.738(9)	Sn(5)	0.5021(3)	0.24797(12)	0.24736(15)	0.602(5)
O1(3)	0.1297(4)	0.3117(6)	0.0862(4)	0.738(9)	O1(1)	0.4473(9)	0.6872(3)	0.3492(4)	1.050(8)
O1(4)	0.1165(4)	0.2853(6)	0.5814(4)	0.738(9)	O1(2)	0.4537(9)	0.1888(3)	0.3564(4)	1.050(8)
O1(5)	0.8200(5)	-0.0005(6)	0.7907(4)	0.738(9)	O1(3)	-0.0488(9)	0.4350(3)	0.0967(4)	1.050(8)
O1(6)	0.4222(5)	-0.0126(6)	0.0849(4)	0.738(9)	O1(4)	-0.0536(9)	0.9394(3)	0.1065(4)	1.050(8)
O1(7)	0.8632(4)	0.3052(6)	0.9113(4)	0.738(9)	O1(5)	0.0635(9)	0.1918(3)	0.1471(4)	1.050(8)
O1(8)	0.8768(4)	0.2983(6)	0.4044(4)	0.738(9)	O1(6)	0.0400(9)	0.6828(3)	0.1520(4)	1.050(8)
O1(9)	0.3596(4)	0.1979(6)	0.1981(4)	0.738(9)	O1(7)	0.5406(9)	0.4352(3)	0.3998(4)	1.050(8)
O1(10)	0.3563(4)	0.1915(6)	0.6966(4)	0.738(9)	O1(8)	0.5552(9)	0.9410(3)	0.3983(4)	1.050(8)
O1(11)	0.1728(5)	0.0011(6)	0.2204(4)	0.738(9)	O1(9)	0.7208(7)	0.3412(2)	0.0008(4)	1.050(8)
O1(12)	0.5666(5)	-0.0221(6)	0.9057(4)	0.738(9)	O1(10)	0.2543(7)	0.5868(2)	0.2473(4)	1.050(8)
O2(1)	0.1443(6)	0.0057(6)	0.9446(4)	1.06(3)	O1(11)	0.7490(9)	0.0360(3)	0.0126(5)	1.050(8)
O2(2)	0.9004(6)	-0.0047(6)	0.0692(4)	1.06(3)	O1(12)	0.2541(8)	0.2866(3)	0.2608(5)	1.050(8)
					O2(1)	0.7482(14)	0.1902(3)	1	2.37(4)
					O2(2)	0.2472(11)	0.4394(3)	1	2.37(4)
a = 13.15493(6) Å, *b* = 7.54118(4) Å, *c* = 15.07672(7) Å, *β* = 125.0120(3)˚					*a* = 7.571833(8) Å, *b* = 21.41262(2) Å, *c* = 15.132459(14) Å				
Overall: R_{wp} = 5.6520 %, *Rp* = 3.8367 %, gof = 1.73					Overall: R_{wp} = 4.5524 %, *Rp* = 3.0530 %, gof = 1.76				
(XRPD = 5.9630 %, PND: bs / 90˚ = 5.5551 % / 2.1027 %)					(XRPD = 4.9334 %, PND: bs / 90˚ = 4.0717 % / 2.9444 %)				

We are also able to show that the peakshape effects observed in the α-phase could be equivalently accounted for using a series of structurally identical phases but varying the cell parameters and phase fractions using a 6 parameter function. This means that while 10 phases are included, only a small number of additional parameters are used to account for the peakshape effects and an even lower R_{wp} (4.9 %) is achieved. Figure 3.16 shows the fit to some of the most asymmetrically broadened peaks using the multi-phase model.

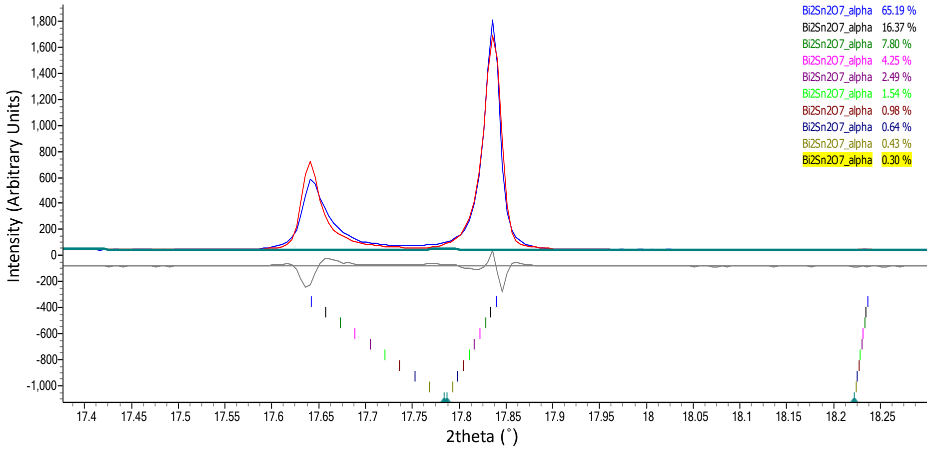

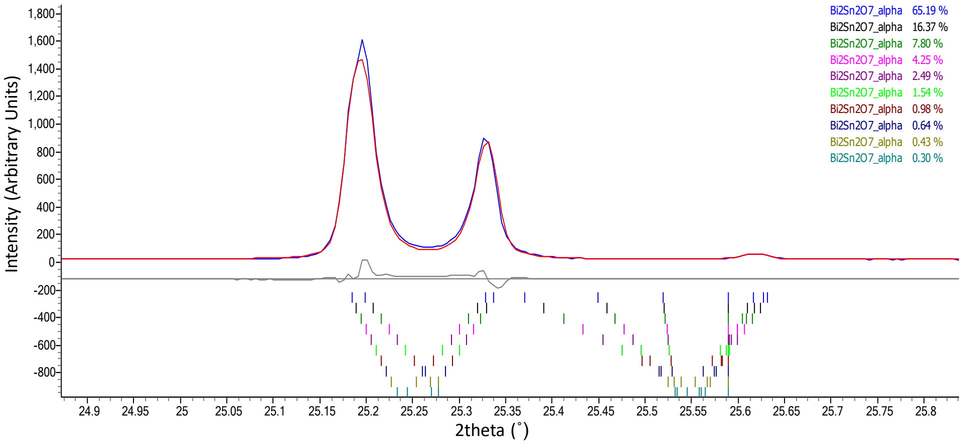

Figure 3.16: Rietveld fit to selected α-$Bi_2Sn_2O_7$ X-ray diffraction data ranges showing multi-phase model fit. Ten phases are generated with smoothly varying cell parameters and phase fractions, controlled by 6 additional parameters.

3.4.3.6 Repeatability

We are also able to show that we can repeat our exhaustive search three times and produce an equivalent result on each occasion. Figure 3.17 and Figure 3.18 show overlay plots of the fit achieved for each of the 544 candidates against β- and α-$Bi_2Sn_2O_7$ data respectively. This gives us confidence that our methodology correctly and exhaustively explores the parameter space.

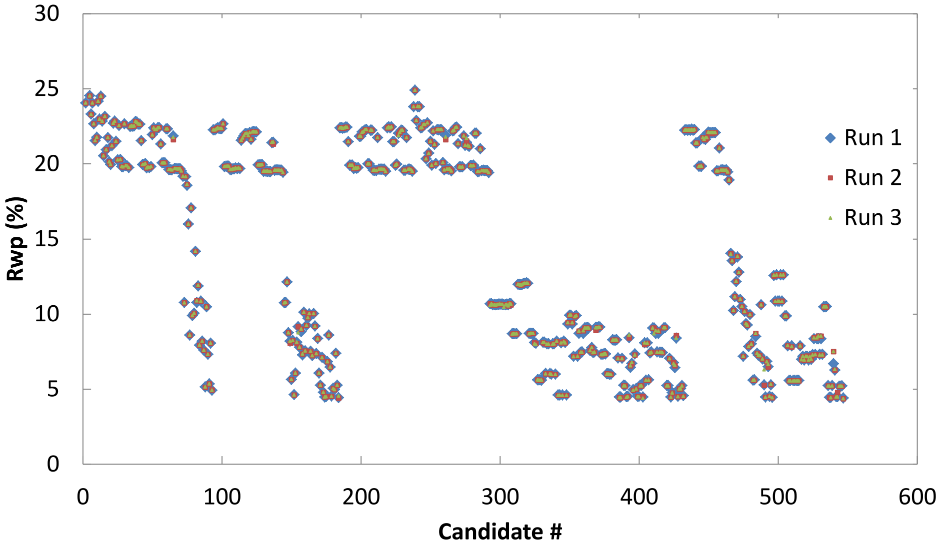

Figure 3.17: Overlay plot showing combined X-ray / TOF neutron R_{wp} found for each of the 544 candidates on three repeats of the exhaustive search process using β-$Bi_2Sn_2O_7$ diffraction data. An equivalent fit to the data is found in all three runs for all candidates.

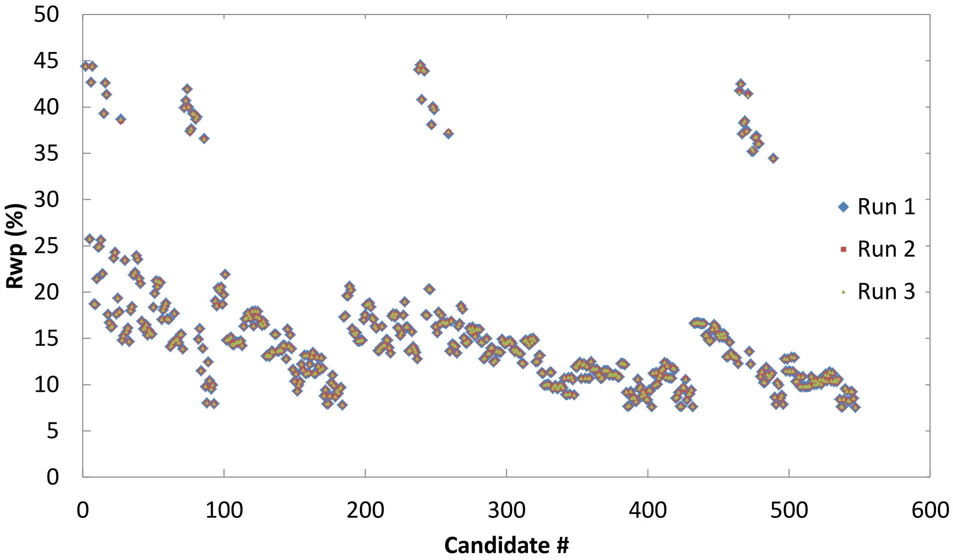

Figure 3.18: Overlay plot showing combined X-ray / TOF neutron R_{wp} found for each of the 544 candidates on three repeats of the exhaustive search process using α-$Bi_2Sn_2O_7$ diffraction data. An equivalent fit to the data is found in all three runs for all candidates.

3.4.4 Lattice Subgroup Search Results

Instead of the full exhaustive search discussed in section 3.4.3 we can also considerably simplify our search process by first searching only amongst the *P1* lattice subgroups of the γ-phase parent within our candidate tree. Once the correct lattice subgroup is identified for each phase we can then search amongst supergroups for the correct point symmetry. Figure 3.19 shows the 14 lattice subgroups within the tree and their relationship to each other.

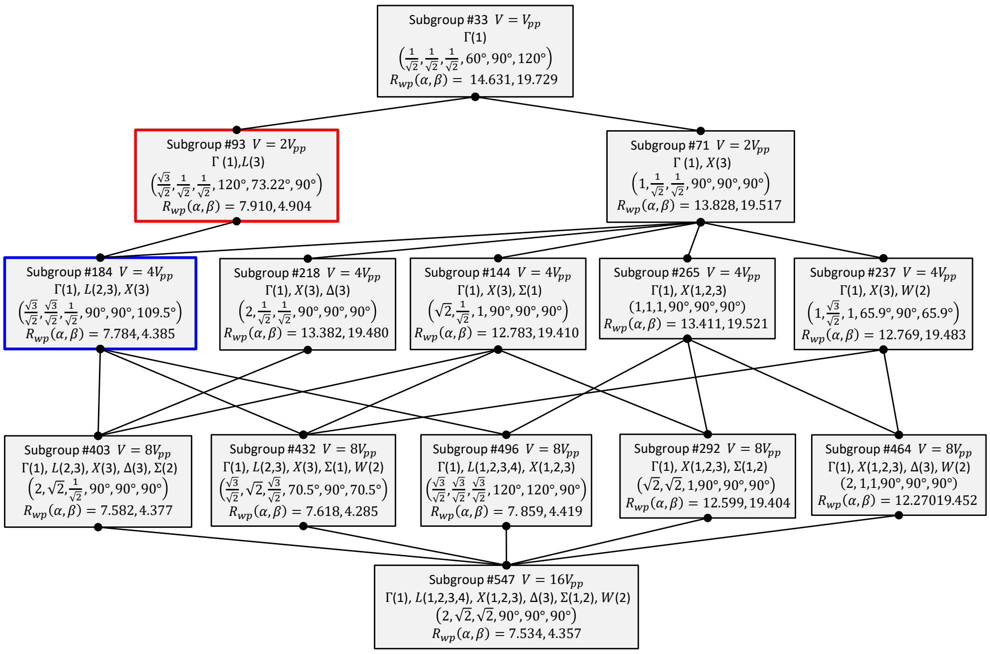

Figure 3.19: Lattice-sublattice relationships amongst the 14 lattice subgroups extracted from the tree of 547 candidate subgroups of the γ-phase parent. For each entry, the first line shows the candidate number and the cell volume (relative to that of the primitive parent cell, V_{pp} = 224 Å^3); the second line indicates the active k-vectors; the third line shows the unit cell parameters (a/a_γ, b/a_γ, c/a_γ, α, β, γ), with edge lengths presented relative to the cubic parent (a_γ = 10.72 Å) and angles in degrees. A given lattice is linked to each of its minimal superlattices and maximal sublattices with a solid black line. Active k-vectors are numbered corresponding to their positions in Table 3.5. For example, the set of active k-vectors of the lattice subgroup of candidate #184 includes the only arm of the star of Γ, the second and third of four arms of the star of L, and the third of three arms of the star of X. At a minimum, the set of active k-vectors of a given lattice must contain all of the active k-vectors of each of its maximal superlattices, though it will generally contain other k-vectors too. The lattice subgroups found for α- and β-$Bi_2Sn_2O_7$ are shown in red and blue boxes respectively.

We can identify the lattice subgroup for each phase by looking at the relationship between R_{wp} and the number of parameters in each of these lattice subgroups. Table 3.5 shows that, for β-$Bi_2Sn_2O_7$, a good fit to the data is found for lattice subgroups with candidate numbers #184, #403, #432, #496 and #547. Of these, #184 has by far the fewest parameters (candidates #403, #432 and #496 are maximal sublattices of #184 and candidate #547 is a maximal sublattice of those). For α-$Bi_2Sn_2O_7$, the lattice subgroups providing a good fit are those with candidate numbers #93, #184, #403, #432, #496 and #547. Again, given that candidate #93 has fewer parameters than the others and that the other lattice subgroups are sublattices of it, it is clear this is the correct lattice subgroup. It is already clear at this stage that α-$Bi_2Sn_2O_7$

cannot be a subgroup of β-$Bi_2Sn_2O_7$ as our α-$Bi_2Sn_2O_7$ lattice choice is a superlattice of our β-$Bi_2Sn_2O_7$ lattice choice. This arises because β-$Bi_2Sn_2O_7$ requires a very small X-point distortion in order to fit the peak splitting observed in our data that is not needed by α-$Bi_2Sn_2O_7$.

Table 3.5: Top: The 14 lattice subgroups and their fit to both β- and α-phase data. Candidate models are listed in the rank order of their combined X-ray / TOF neutron R_{wp} fit to β-data from the full 547 candidate tree. The active arms of the star of each k-vector are denoted numerically in reference to the possible arms. Bottom: For each type of reciprocal-space k-vector that contributes to the sublattices of one or more of the 547 intermediate candidates, we list the arms of the star of the k-vector. The active k-vectors of any candidate model must come from this list. Lattice subgroups above the red and blue lines have sufficient active k-points to fit the α- and β-phase data respectively.

Subgroup #	β Rank	β Rwp (%)	α Rank	α Rwp (%)	V_{frac}	# Prms	Γ	L	X	Δ	Σ	W	min superlattices	max sublattices
547	1	4.357	1	7.534	4.00	1056	1	1,2,3,4	1,2,3	3	1,2	2	292, 403, 432, 464, 496	none
403	2	4.377	4	7.582	2.00	528	1	2,3	3	3	2		184, 218, 144	547
184	3	4.385	10	7.784	1.00	264	1	2,3	3				93	403, 432, 496
496	6	4.419	11	7.859	2.00	528	1	1,2,3,4	1,2,3				184, 265	547
432	21	4.510	5	7.618	2.00	528	1	2,3	3		1	2	184, 144, 237	547
93	30	4.904	14	7.910	0.50	132	1	3					33	184
292	286	19.404	217	12.599	2.00	528	1		1,2,3		1,2		144, 265	547
144	287	19.410	225	12.758	1.00	264	1		3		1		71	403, 432, 292
464	288	19.452	207	12.270	2.00	528	1		1,2,3	3		2	237, 265	547
218	293	19.480	247	13.382	1.00	264	1		3	3			71	403
237	294	19.483	219	12.769	1.00	264	1		3			2	71	432, 464
265	302	19.521	249	13.411	1.00	264	1		1,2,3				71	292, 464, 496
71	301	19.517	273	13.828	0.50	132	1		3				33	144, 218, 237, 265
33	355	19.729	312	14.631	0.25	66	1						none	71, 93

k-point	1	2	3	4	5	6
Γ:	(0,0,0)					
L:	(1/2,1/2,1/2)	(-1/2,1/2,1/2)	(1/2,-1/2,1/2)	(1/2,1/2,-1/2)		
X:	(0,1,0)	(1,0,0)	(0,0,1)			
Δ:	(0,1/2,0)	(1/2,0,0)	(0,0,1/2)			
Σ:	(1/2,1/2,0)	(1/2,-1/2,0)	(1/2,0,1/2)	(1/2,0,-1/2)	(0,1/2,1/2)	(0,1/2,-1/2)
W:	(1/2,1,0)	(1,0,1/2)	(0,1/2,1)			

From this point we only need to search amongst a much smaller group of candidates to identify the point symmetry of each phase. For β-$Bi_2Sn_2O_7$ there are 40 candidates sharing a lattice with candidate #184 (candidates #145-184) while for α-$Bi_2Sn_2O_7$ there are 22 sharing a lattice with candidate #93 (candidates #72-93) and the fit provided by these candidates are shown in Figure 3.20 and Figure 3.21 respectively.

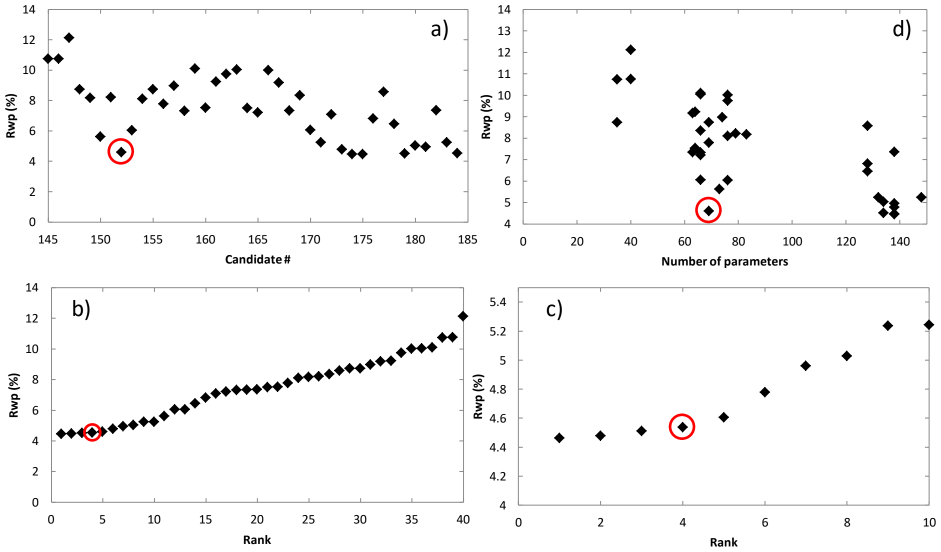

Figure 3.20: Combined R_{wp} obtained for candidates #145-184 after Rietveld refinement using synchrotron X-ray and HRPD neutron powder diffraction data of β- $Bi_2Sn_2O_7$. Individual panels show (a) R_{wp} as a function of tree candidate number (b) R_{wp} of all candidates in ranked order (c) R_{wp} of only best 10 candidates in ranked order and (d) R_{wp} of all candidates as a function of the number of structural parameters available to them. Red circle shows chosen candidate model.

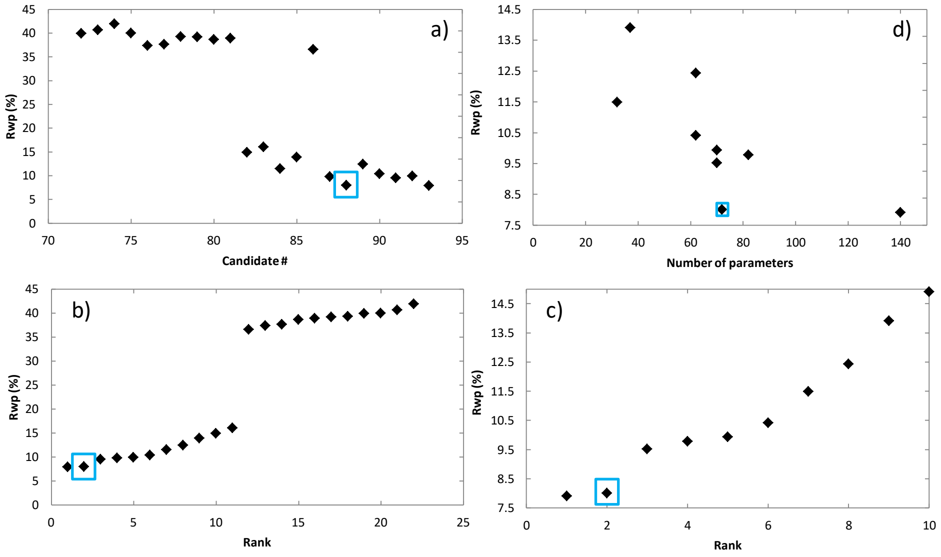

Figure 3.21: Combined R_{wp} obtained for candidates #72-93 after Rietveld refinement using synchrotron X-ray and HRPD neutron powder diffraction data of α- $Bi_2Sn_2O_7$. Individual panels show (a) R_{wp} as a function of tree candidate number (b) R_{wp} of all candidates in ranked order (c) R_{wp} of only best 10 candidates in ranked order and (d) R_{wp} of all candidates as a function of the number of structural parameters available to them. Blue square shows chosen candidate model.

As we were able to show earlier, it is again clear that candidates #152 and #88 are identifiable as the best choices for β- and α-$Bi_2Sn_2O_7$ respectively. For β- $Bi_2Sn_2O_7$, five candidates provide similar fits to the data but #152 has far fewer parameters than any other. For α-$Bi_2Sn_2O_7$, the situation is even simpler as only candidate #88 provides an equivalent fit to the lattice subgroup (candidate #93) and so is the obvious choice. By splitting the search to first identify the correct lattice subgroup of each phase before searching amongst supergroups sharing this lattice we can complete the search and identify the best candidate in ~ 148 hrs and ~ 145 hrs for β- and α-$Bi_2Sn_2O_7$ respectively.

3.5 Structural Discussion

In this section we discuss the structural implications of our new models for β- and α-$Bi_2Sn_2O_7$ and the relationship between the two structures.

3.5.1 Finding the Common Subgroup

The structural implications of our new models are best understood by looking at the large amplitude distortion modes that presumably drive the phase transitions. However, comparison of our α and β models is made more difficult by the fact they do not have a group-subgroup relationship. This is most obvious from the fact that our α-phase model does not provide a good fit to the β-phase data (i.e. there are some symmetry-breaking distortion modes that are active in the β-phase but not the α-phase). The implication of our new models is that the lattice distortion of β-$Bi_2Sn_2O_7$ is larger than that of α-$Bi_2Sn_2O_7$ but the point symmetry of α-$Bi_2Sn_2O_7$ is lower than that of β-$Bi_2Sn_2O_7$.

One way to overcome this difficulty is to find a model that is a subgroup of both β- and α-phases – a common subgroup. In this common subgroup setting we can obtain fits to β- and α-phase data using the same set of distortion modes which will allow us to compare the important distortions in each case. One obvious choice is to use the literature α_{old} model, which was derived partly on the assumption of a group-subgroup relationship with the β-phase, however there is a simpler choice. The highest common subgroup of both structures (i.e. the one with the fewest structural parameters) is candidate #174 in our candidate tree. It has space group Pc, a $\sqrt{3/2}a_\gamma \times a_\gamma/\sqrt{2} \times \sqrt{2}a_\gamma$, β = 54.74° supercell and 132 distortion modes, considerably fewer than the 528 of the α_{old} model. Candidate #174 is the highest common subgroup because it has the larger lattice of our β-phase model and the lower symmetry point group of our α-phase model. To obtain easily comparable models of β- and α-$Bi_2Sn_2O_7$ we simply have to map the lattice distortion of the α-model on to that of the β-model and lower the point symmetry of the β-model to that of the α-model. Step-by-step instructions of how to do this, including how to obtain the correct choice of domain, can be found in Appendix 11.

3.5.2 Distortion Mode Comparison

Despite being the highest common subgroup of our β- and α-$Bi_2Sn_2O_7$ models, candidate #174 still contains 10 X_4 distortion modes that are present in neither. We have therefore omitted these modes from the analysis below. Of the remaining 122 modes, Figure 3.22 shows that distortions are dominated by just a few large, primary Γ_5^- and L_2^+ modes that drive the phase transitions. There are also smaller, secondary Γ_4^- modes which are required for a good fit to the data. All of the modes with amplitude in excess of 0.3 Å belong to one of these three irreps while the vast majority of other mode amplitudes are very close to zero. Figure 3.23 highlights the amplitudes of these important modes for β- and α-$Bi_2Sn_2O_7$ in the common subgroup setting.

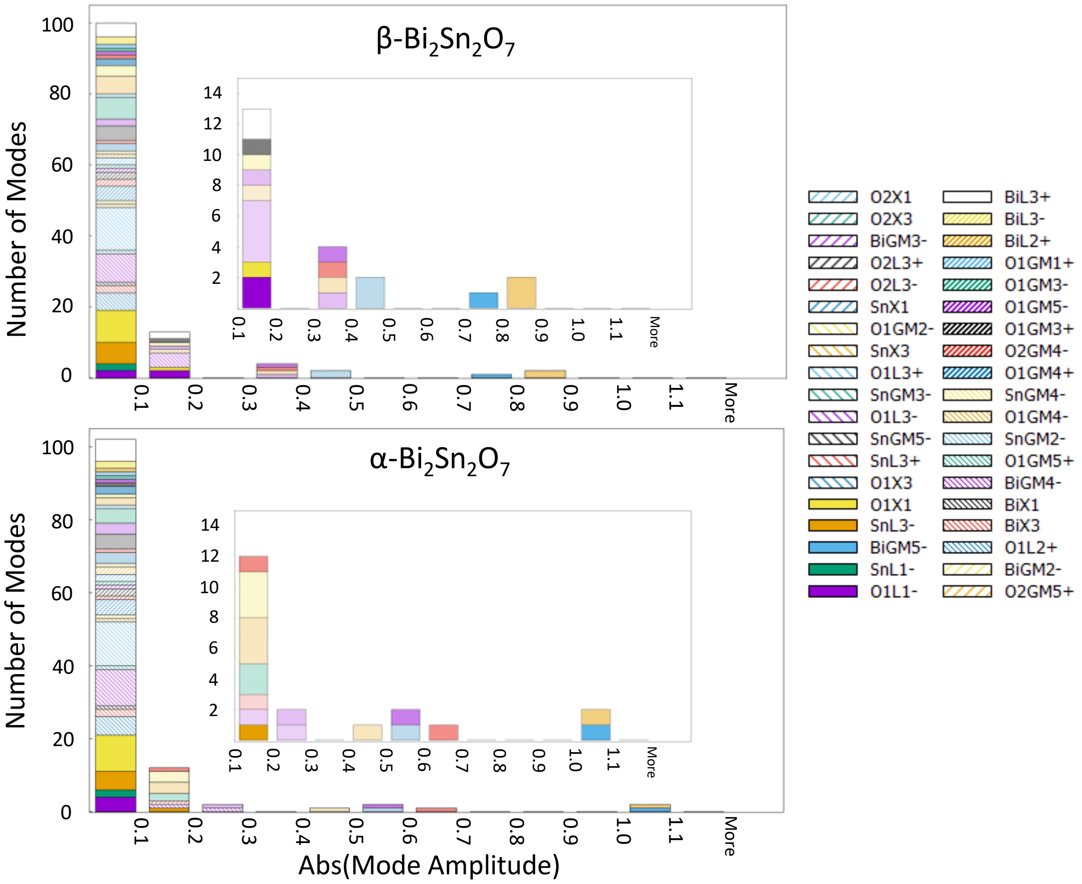

Figure 3.22: Absolute mode amplitudes in β- (top) and α- (bottom) $Bi_2Sn_2O_7$ when reduced to a common subgroup setting (*Pc*, #174). Modes are grouped into 0.1 Å bins and coloured and shaded by atom type and irrep. The small number of modes with amplitude > 0.3 Å drive the distortion. Insets show closer view of modes with amplitude > 0.1 Å.

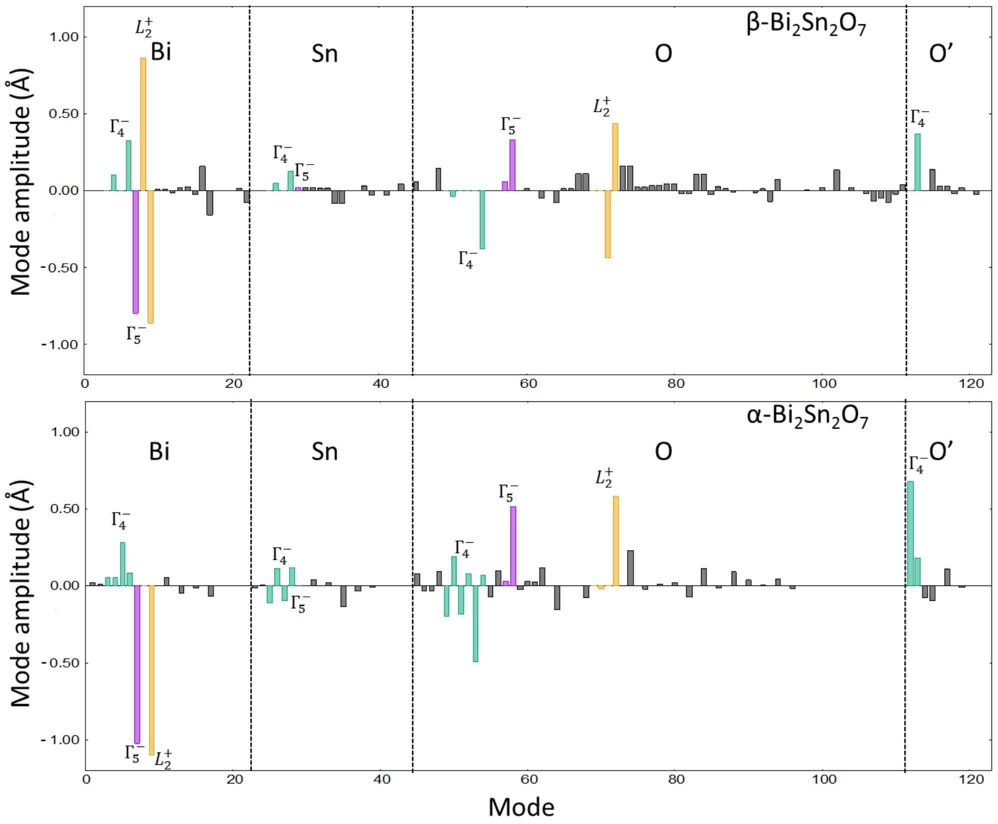

Figure 3.23: Mode amplitudes in β- (top) and α- (bottom) $Bi_2Sn_2O_7$ when reduced to a common subgroup setting (*Pc*, #174) with the appropriate domain and origin choice. Irreps not found in a structure are shown with zero amplitude. Irreps are plotted in order of parent atom type and colour coded by irrep (Γ_4^- - green, Γ_5^- - purple, $L_2{}^+$ - yellow, others grey). Absolute mode amplitude sums α- (β-): $\Sigma_{Bi} = 2.81$ Å $(3.46$ Å$)$, $\Sigma_{Sn} = 0.70$ Å $(0.56$ Å$)$, $\Sigma_{O1} = 3.87$ Å $(3.75$ Å$)$, $\Sigma_{O'} = 1.15$ Å $(0.63$ Å$)$.

The large Γ_5^- and L_2^+ Bi modes are associated with Bi_4O` tetrahedral rotations (with internal bond angles and distances almost unchanged from the undistorted parent). Figure 3.24 gives a visual comparison of the two structures as described below. The phase transition is driven by coupled rotations of undistorted tetrahedra similar to the situation in the β- to α-cristobalite phase transition ($Fd\bar{3}m$ to $P42_12$).

In both phases the specific OPD of the Γ_5^- contribution is $\Gamma_5^-(0,a,a)$ which rotates tetrahedra about an axis parallel to the <110> of the parent. This corresponds to a 6.0° rotation about the *a* axis in the case of β-$Bi_2Sn_2O_7$ and a 7.7° rotation about the *c* axis for α-$Bi_2Sn_2O_7$.

The effect of the L_2^+ modes, however, varies between the two structures. For α-$Bi_2Sn_2O_7$ the specific OPD is $L_2^+(0,a,0,0)$ which corresponds to an 8.2° rotation of Bi_3O`BiO`Bi_3

corner sharing tetrahedral units about the [111] axis of the parent. This specific O`-Bi-O` angle remains unchanged by the rotation but others that do not lie along the parent [111] axis are changed. In the case of β-$Bi_2Sn_2O_7$ the specific OPD is $\mathrm{L}_2^+(a,b,0{,}0)$ although the a and b branches are related by $a=-b$ in the true (candidate #152) setting and so the OPD may be best understood as $\mathrm{L}_2^+(a,-a,0{,}0)$. Note that the two active L_2^+ modes have equal amplitude but opposite sign for β-$Bi_2Sn_2O_7$ in Figure 3.23 to confirm this. The additional freedom of the β-phase corresponds to a rotation about the [1-11] axis of the parent. The combined effect for β-$Bi_2Sn_2O_7$ is one Bi_4O` unit rotates 10.7° and the other 7.5° about the c and a axes of the β-cell respectively. The effect of the additional rotational freedom in comparison to α-$Bi_2Sn_2O_7$ structure can be seen from the view down the 3-fold axis of the parent structure shown in the middle row of Figure 3.24.

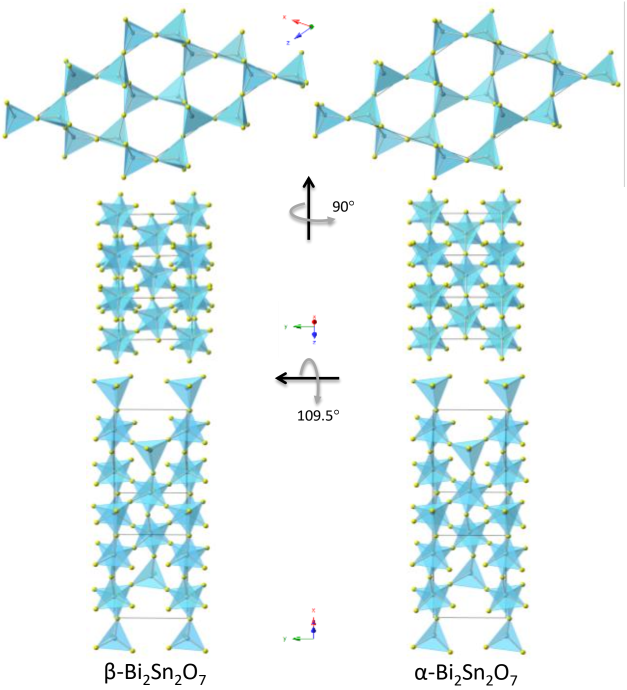

Figure 3.24: Views of Bi_2O` framework tetrahedral rotations dominated by Γ_5^- and L_2^+ modes in α- and β-$Bi_2Sn_2O_7$ shown in the common subgroup setting of candidate #174. Top view is down [0 1 0], middle view down [-2 0 1], lower view down [-2 0 3]; these correspond to [-1 0 1], [1 -1 1] and [111] of parent structure. Bi and O` atoms are shown in yellow and blue respectively. Animated views (see e-Appendix 11) and equivalent views of γ-$Bi_2Sn_2O_7$ (Appendix 12) are available.

The overall effect of these modes on Bi displacements is shown in Figure 3.25. For β-$Bi_2Sn_2O_7$, 4 of the 5 Bi atoms are displaced towards an edge of the O puckered hexagonal environment. Only Bi4 is left approximately in its parent position. For the 4 other Bi atoms we therefore see 2 short Bi-O distances (to O on the edge the Bi moves towards) with bond distances in the range 2.22-2.45Å and 4 long Bi-O distances in the range 2.47-3.19Å. For α-$Bi_2Sn_2O_7$, Bi atoms are displaced towards a vertex of the O hexagonal environment. This leads to 3 short Bi-O distances (to the O on the vertex the Bi moves towards and its neighbours) with bond distances in the range 2.10-2.45Å and 3 longer Bi-O distances in the range 2.85-3.17 Å. A table of bond distances and calculated bond valence sums (BVS) can be found in Table 3.6.

Table 3.6: Bond distances and BVS for Bi and Sn atoms in (top) β-$Bi_2Sn_2O_7$ and (bottom) α-$Bi_2Sn_2O_7$. Distances are listed shortest to longest for each of O and O`.

β-$Bi_2Sn_2O_7$									
atom	**O distances/Å**						**O' distances/Å**		**BVS**
Bi1	2.239(7)	2.275(7)	2.465(7)	2.850(7)	3.111(7)	3.192(7)	2.296(8)	2.452(8)	2.83
Bi2	2.272(7)	2.287(7)	2.502(7)	2.786(7)	3.133(7)	3.142(7)	2.305(8)	2.447(8)	2.74
Bi3	2.222(5)	2.375(7)	2.466(7)	2.868(7)	2.927(7)	3.221(7)	2.315(9)	2.328(10)	2.87
Bi4	2.342(7)	2.342(7)	2.639(5)	2.639(5)	2.904(7)	2.904(7)	2.317(8)	2.317(8)	2.77
Bi5	2.361(7)	2.361(7)	2.696(5)	2.696(5)	2.983(7)	2.983(7)	2.317(8)	2.317(8)	2.61
Sn1	2.021(7)	2.027(7)	2.033(7)	2.037(7)	2.044(7)	2.066(7)			4.19
Sn2	2.053(7)	2.058(7)	2.060(7)	2.067(7)	2.088(7)	2.095(7)			3.84
Sn3	2.030(7)	2.030(7)	2.060(6)	2.060(6)	2.112(7)	2.112(7)			3.89
Sn4	2.020(7)	2.020(7)	2.055(6)	2.055(6)	2.110(7)	2.110(7)			3.95
Sn5	2.033(7)	2.044(7)	2.057(7)	2.062(7)	2.109(7)	2.113(7)			3.86
α-$Bi_2Sn_2O_7$									
atom	**O distances/Å**						**O' distances/Å**		**BVS**
Bi1	2.241(5)	2.328(5)	2.453(5)	2.925(5)	3.000(5)	3.145(5)	2.239(5)	2.495(6)	2.82
Bi2	2.256(5)	2.357(5)	2.393(5)	2.853(5)	2.883(5)	3.170(5)	2.230(6)	2.514(6)	2.87
Bi3	2.252(5)	2.378(5)	2.408(5)	2.937(5)	3.025(5)	3.159(5)	2.184(6)	2.496(6)	2.87
Bi4	2.158(5)	2.384(5)	2.444(5)	2.952(5)	3.056(5)	3.162(5)	2.237(6)	2.410(6)	2.99
Sn1	2.018(6)	2.038(6)	2.042(6)	2.061(6)	2.076(6)	2.078(6)			4.04
Sn2	2.005(6)	2.022(6)	2.037(6)	2.044(6)	2.066(6)	2.068(6)			4.17
Sn3	2.027(6)	2.039(6)	2.068(6)	2.073(6)	2.113(6)	2.131(6)			3.81
Sn4	2.025(6)	2.046(6)	2.055(6)	2.063(6)	2.082(6)	2.117(6)			3.91

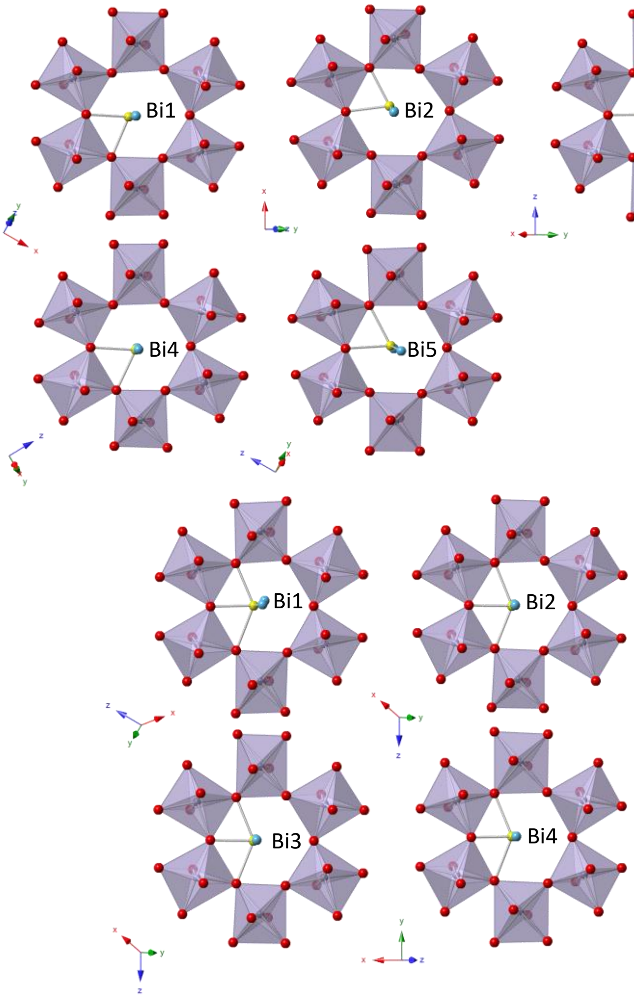

Figure 3.25: Bi coordination environments in β- (upper panel) and α- (lower panel) $Bi_2Sn_2O_7$. Bi and O` atoms are shown in yellow and blue respectively while Sn and O are in grey and red respectively.

3.6 Conclusion

Our exhaustive search method has been able to identify the first reliable structural model for β-$Bi_2Sn_2O_7$ as well as a new, considerably simpler, structural model for α-$Bi_2Sn_2O_7$.[1] In the case of β-$Bi_2Sn_2O_7$, the exhaustive search benefits from the use of new diffraction data (that shows previously unobserved peak splitting). By considering all possible symmetry losses (as far as a $\sqrt{2}a_\gamma \times \sqrt{2}a_\gamma \times 2a_\gamma$ child $P1$ subgroup) we could be certain to identify a reliable and simple structural model. Our ability to identify a new α-$Bi_2Sn_2O_7$ model arises from the removal of earlier assumptions about the β phase and the relationship between it and the α phase. The simpler structural model has an equivalent fit to diffraction data. However, as in Chapter 2, an important outcome of this work is not just the choice of structural model for each phase but the relationship between the symmetry of all candidate models in our tree and the fit to the data (i.e. Figure 3.6 and Figure 3.10). These figures represent a “structural map” from which decisions can be systematically made. We have not extensively explored quantitative ways to make such a choice such as Hamilton tests[22] or Bayesian statistics[23] but instead rely on inspection of the fits to diffraction data.

The exhaustive process also allows us to extract a reliable comparison between our β- and α-$Bi_2Sn_2O_7$ models. Having discovered there is no group-subgroup relationship between the two phases (by finding the X-point distortion active in the β-model but not in the α-model), we were able to identify the highest symmetry common subgroup of the two as candidate #174 in our tree. We were then able to show the key distortions affecting each phase and show that Bi moves primarily towards a vertex or edge of its hexagonal O environment in α- and β-$Bi_2Sn_2O_7$ respectively. The difference can also be observed in an additional rotation of Bi_4O` about the c axis present in β-$Bi_2Sn_2O_7$ but not α-$Bi_2Sn_2O_7$ due to $L_2^+(a,-a,0,0)$ and $L_2^+(0,a,0,0)$ OPDs respectively. The distortion mode approach allows the complex phase transition to be described in a very concise way.

Our structural models identified for α- and β-$Bi_2Sn_2O_7$ again show the value of our exhaustive structural search tool that has resolved a complex structural problem robustly and on a reasonable timescale.

3.7 References

(1) Lewis, J. W.; Payne, J. L.; Evans, I. R.; Stokes, H. T.; Campbell, B. J.; Evans, J. S. O. *Journal of the American Chemical Society* **2016**, *138*, 8031.

(2) Tian, Q.; Zhuang, J.; Wang, J.; Liu, P. *Applied Catalysis A: General* **2012**, *425*, 74.

(3) Coles, G. S. V.; Bond, S. E.; Williams, G. *Journal of Materials Chemistry* **1994**, *4*, 23.

(4) Devi, G. S.; Manorama, S. V.; Rao, V. J. *Journal of the Electrochemical Society* **1998**, *145*, 1039.

(5) Devi, G. S.; Manorama, S. V.; Rao, V. J. *Sensors and Actuators B: Chemical* **1999**, *56*, 98.

(6) Malinovskaya, T. D.; Aparnev, A. I.; Egorov, Y. P.; Yukhin, Y. M. *Russian Journal of Applied Chemistry* **2001**, *74*, 1864.

(7) Moens, L.; Ruiz, P.; Delmon, B.; Devillers, M. *Catalysis Letters* **1997**, *46*, 93.

(8) Moens, L.; Ruiz, P.; Delmon, B.; Devillers, M. *Applied Catalysis A: General* **1998**, *171*, 131.

(9) Moens, L.; Ruiz, P.; Delmon, B.; Devillers, M. *Applied Catalysis A: General* **1999**, *180*, 299.

(10) Mims, C. A.; Jacobson, A. J.; Hall, R. B.; Lewandowski, J. T. *Journal of Catalysis* **1995**, *153*, 197.

(11) Roth, R. S. *J. Res. Nat. Bur. Stand* **1956**, *56*, 17.

(12) Shannon, R. D.; Bierlein, J. D.; Gillson, J. L.; Jones, G. A.; Sleight, A. W. *Journal of Physics and Chemistry of Solids* **1980**, *41*, 117.

(13) Radosavljevic, I.; Evans, J. S. O.; Sleight, A. W. *Journal of Solid State Chemistry* **1998**, *136*, 63.

(14) Jones, R. H.; Knight, K. S. *Journal of the Chemical Society, Dalton Transactions* **1997**, 2551.

(15) Walsh, A.; Watson, G. W. *Chemistry of Materials* **2007**, *19*, 5158.

(16) Kennedy, B. J.; Ismunandar; Elcombe, M. In *Materials Science Forum*; Trans Tech Publ: 1998; Vol. 278, p 762.

(17) Evans, I. R.; Howard, J. A. K.; Evans, J. S. O. *Journal of Materials Chemistry* **2003**, *13*, 2098.

(18) Payne, J. L. Doctoral Thesis, Durham University, Durham, United Kingdom, 2010.

(19) Salamat, A.; Hector, A. L.; McMillan, P. F.; Ritter, C. *Inorganic Chemistry* **2011**, *50*, 11905.

(20) Campbell, B. J.; Stokes, H. T.; Tanner, D. E.; Hatch, D. M. *Journal of Applied Crystallography* **2006**, *39*, 607.

(21) Stephens, P. W. *Journal of Applied Crystallography* **1999**, *32*, 281.

(22) Hamilton, W. *Acta Crystallographica Section A: Crystal Physics, Diffraction, Theoretical and General Crystallography* **1969**, *25*, 194.

(23) Sivia, D.; David, W. *Acta Crystallographica Section A: Foundations of Crystallography* **1994**, *50*, 703.

Chapter 4 ZrP_2O_7: Structure Solution using Displacive and Rotational Distortion Modes

4.1 Introduction

This chapter introduces the use of combined displacive and rotational distortion modes to model the complex ZrP_2O_7 RT structure and develops search algorithms to identify the correct model from the available modes in a $P1$ child structure. As discussed below this example is considerably more challenging in its complexity. In addition to testing our structure solution methods, the main aim was to explore whether rotational distortion modes can further simplify structure solution and description. This second aim was partially successful.

As with other materials in the AM_2O_7 family, ZrP_2O_7 adopts a simple cubic structure at high temperature as first described by Peyronel and Levi[1]. This structure involves corner connected ZrO_6 octahedra and PO_4 tetrahedra which in turn also share a corner with a second PO_4 tetrahedron to create P_2O_7 units connected by a 180° P-O-P bond angle aligned along the 3-fold axis (Figure 4.1, space group $Pa\overline{3}$ and a_{parent} ~ 8.25 Å). These bridging O atoms are referred to as O2 atoms throughout this chapter while Zr-O-P oxygens are referred to as O1. Like other materials in the family, ZrP_2O_7 is of interest for very low positive thermal expansion (some members of the family exhibit negative thermal expansion)[2-5]. The unusual thermal expansion in these frameworks can be described as resulting from so called quasi rigid unit modes (qRUMs)[6]. A set of dimensionless Grüneisen[7,8] parameters ($\gamma = dlnv/dV$) can be calculated (either theoretically or from inelastic scattering) where the sign of the parameter indicates whether vibrational modes lead to positive or negative thermal expansion. Many negative parameters are associated with transverse vibrations of bridging oxygen atoms and involve relatively minor distortions of the constituent polyhedra.

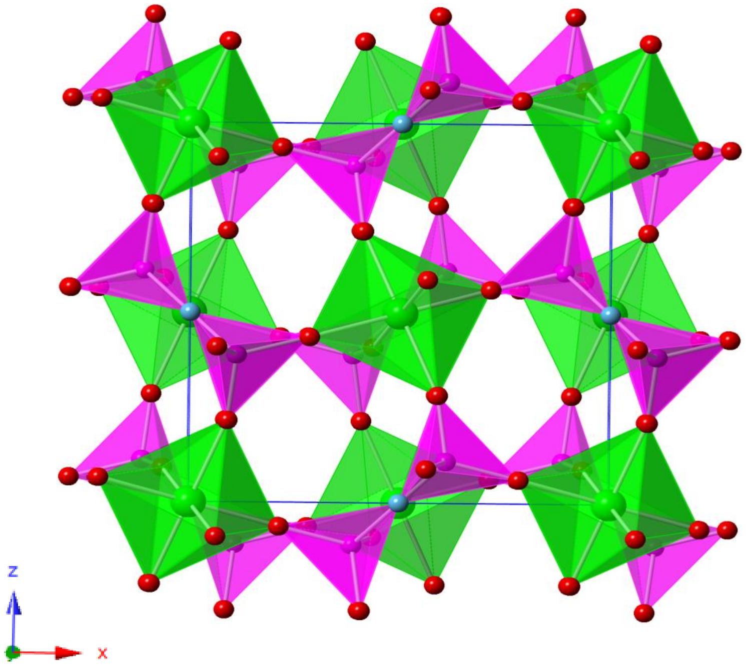

Figure 4.1: High temperature structure of ZrP_2O_7. ZrO_6 octahedra are in green, PO_4 tetrahedra are in pink. Individual atoms are: Zr – green, P – pink, O1 – red, O2 – blue.

On cooling there is a small 5-10˚C window around 290˚C in which an incommensurately modulated phase with a $3a_{parent}\times3a_{parent}\times3a_{parent}$ superstructure exists[9] before the material undergoes a phase transition to a complex RT phase with a $3a_{parent}\times3a_{parent}\times3a_{parent}$ superstructure, space group $Pbca$ and 136 atoms in the unit cell (Figure 4.2). The structure was initially thought[10] to remain cubic with space group $Pa\bar{3}$ but King et al.[11] observed more ^{31}P signals in 2D NMR than predicted by the proposed $Pa\bar{3}$ symmetry. They showed that the structure was instead consistent with $Pbca$ symmetry. In particular, NMR showed that 13 of the 14 $P_2O_7^{4-}$ units had inequivalent ^{31}P positions with only one $P_2O_7^{4-}$ unit having a single ^{31}P resonance. This uniquely defines $Pbca$ symmetry. The structure was later solved from synchrotron and neutron powder data and single crystal X-ray diffraction, confirming the $Pbca$ (a = 24.7390(2) Å, b = 24.71841(19) Å, c = 24.7431(2) Å) assignment with 27 unique P sites[12].

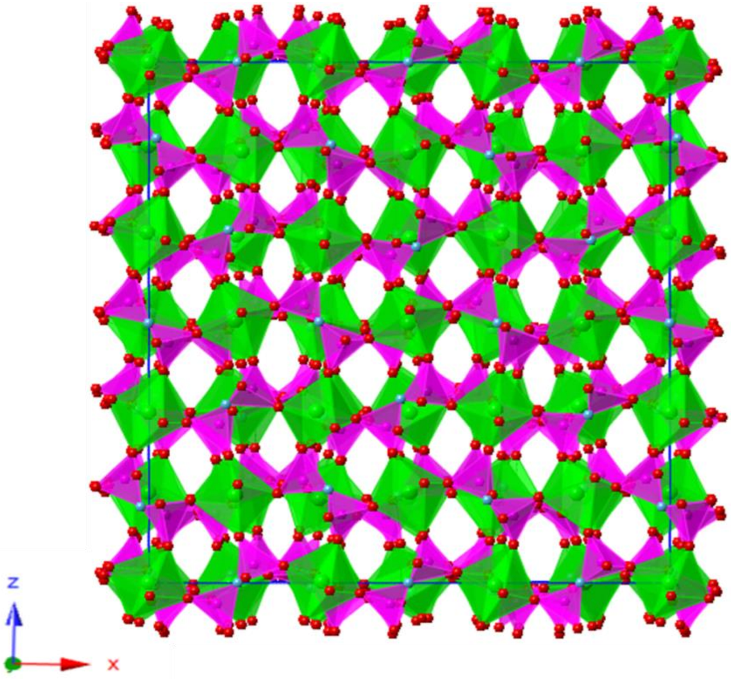

Figure 4.2: Room temperature *Pbca* superstructure of ZrP_2O_7. ZrO_6 octahedra are in green, PO_4 tetrahedra are in pink. Individual atoms are: Zr – green, P – pink, O1 – red, O2 – blue.

4.2 Sample Preparation and Data Collection

ZrP_2O_7 was synthesised by John Evans using $ZrOCl_2\cdot6.91H_2O$ and H_3PO_4 in a 2:1 molar ratio mixed intimately together in a Pt crucible. After drying at 350˚C, the sample was crushed, washed (distilled water) and separated using a centrifuge four times. The sample was then dried at 180˚C and heated to 850˚C (12 hours, 3˚C/minute) and reground. The sample was then heated again to 1000˚C (12 hours, 5˚C/minute) and pure ZrP_2O_7 verified by laboratory X-ray powder diffraction.

Synchrotron X-ray diffraction data at RT was collected on the X7A beamline at the National Synchrotron Light Source, Brookhaven National Laboratory, New York by Pat Woodward. Data was collected using a Ge(111) monochromator (λ = 0.8013 Å) in the range 2.00 - 67.06˚ 2θ in steps of 0.01˚.

TOF neutron powder diffraction data was collected on HRPD at ISIS by Evans. The sample was loaded into a 15 mm vanadium can and data collected on all data banks at RT. The backscattering bank data is discussed in this thesis (d ~ 0.70 – 2.36 Å).

4.3 Exhaustive Search with Displacive Modes

As a first step, we applied the exhaustive methods demonstrated in Chapter 2 to test their sensitivity for this more complex problem. A child model with space group *P1* with a $3a_{parent}\times3a_{parent}\times3a_{parent}$ supercell was used which makes no assumptions about the space group symmetry of the structure and only assumes that the supercell is sufficiently large to describe all observed peaks (as is well established for this family of materials). This model has the maximum possible 3 parameters for every atom in the supercell and gives the expected excellent fit to the diffraction data (Figure 4.3). A small peak due to V is excluded in the neutron fit.

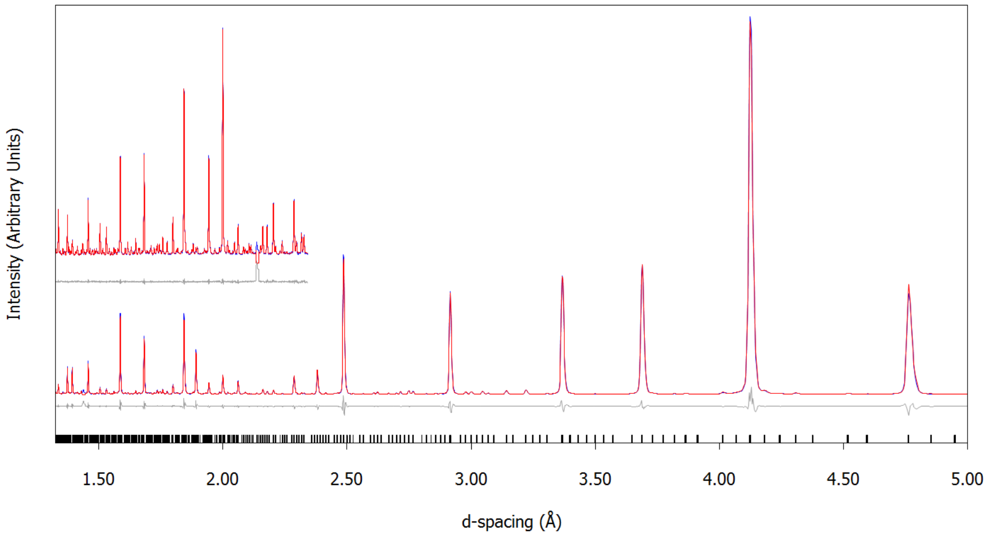

Figure 4.3: Fit to (top) HRPD TOF neutron and (bottom) synchrotron X-ray powder diffraction data of ZrP_2O_7 at RT using child *P1* model. X-ray R_{wp} (R_{Bragg}) = 8.74 % (2.35 %), TOF neutron R_{wp} (R_{Bragg}) = 2.18 % (1.00 %).

This refinement provides values for the non-structural parameters to use in the exhaustive search. The fit also confirms that the correct model lies somewhere between the child and parent models and so an exhaustive search is appropriate. The subgroup tree of candidate models between parent and child was obtained using ISODISTORT (see Appendix 13 for step-by-step instructions). The resulting tree contains 76 subgroups of which only one (#1, the parent) has no active distortion modes and so is not considered. A full list of the subgroup tree with all candidate model numbers can be found in e-Appendix 12.

As in the other exhaustive searches, it is effective to split the annealing process into two parts: the first of which focuses on obtaining the correct lattice distortion, and the second of which focuses on obtaining the correct distortion mode amplitudes. In the first step, a 1 % randomisation was used when annealing cell parameters (the child cell parameters above vary by no more than ~ 0.5 % from the undistorted $3a_{parent}$ model). In the second step, a 0.1 % cell randomisation was used in order to limit exploration of the search space to minor adjustments of near-optimal cell parameters alongside the simultaneously-annealed mode amplitudes. The search process otherwise follows the earlier protocol (see 2.5.2). The 112500 Rietveld iterations take ~ 53 hours on an ordinary desktop PC (3rd generation i5, 3.2 GHz) to complete.

4.3.1 Search Results

Figure 4.4 shows the best R_{wp} obtained for each candidate after the exhaustive search process. Figure 4.4a shows that candidates split roughly into two groups. Those with a poor fit (R_{wp} > 10 %) lack the necessary parameters of the important $\Lambda_2\Lambda_3$ distortion whereas those with R_{wp} < 10 % always contain it. Viewed in ranked order (Figure 4.4b), the models separate into plateaus. The lowest R_{wp} plateau contains 14 candidates as shown by Figure 4.4c. From Figure 4.4d, we can see that of those 14, candidate #67 (ranked 9 with R_{wp} = 4.11 %) has the fewest structural parameters (402). It has space group *Pbca* (*a* = 24.72604(11) Å, *b* = 24.7496(4) Å, *c* = 24.7494(4) Å) and matches the previously established model for RT ZrP_2O_7. Figure 4.5 shows the fit to the data provided by this model is comparable to that provided by the child (Figure 4.3). It is encouraging that this simple analysis of diffraction data alone (i.e. without NMR input) is sufficient to identify the correct symmetry.

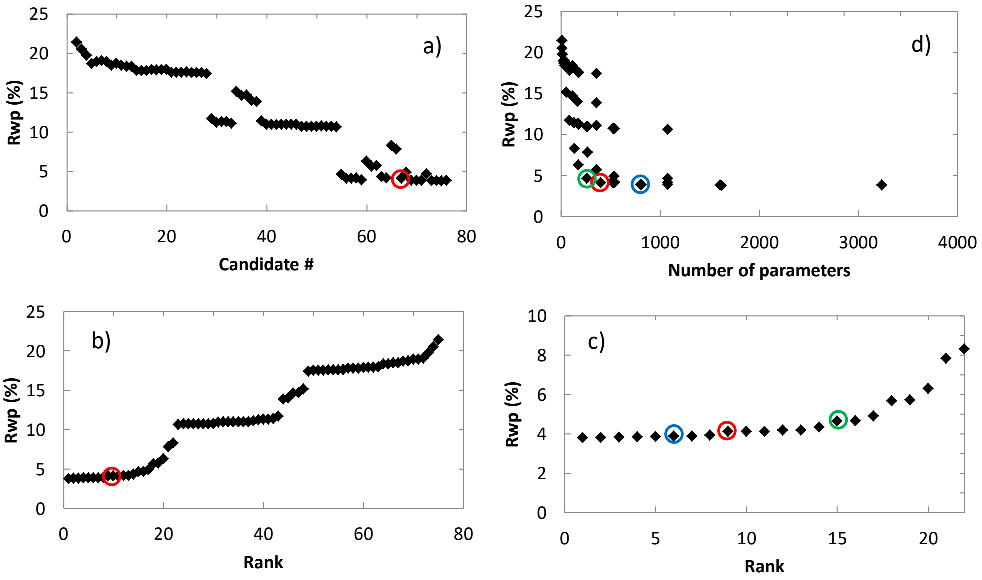

Figure 4.4: Combined X-ray / TOF neutron R_{wp} achieved by each candidate model in exhaustive subgroup search shown by: a) candidate number, b) ranked order, c) ranked order (best candidates) and d) number of parameters. The red circle indicates candidate

#67 – the correct *Pbca* model for RT ZrP_2O_7. The blue circle indicates the model with better R_{wp} than #67 with the fewest additional parameters (candidate #70). The green circle indicates the model with the best R_{wp} amongst those models with fewer parameters (candidate #55).

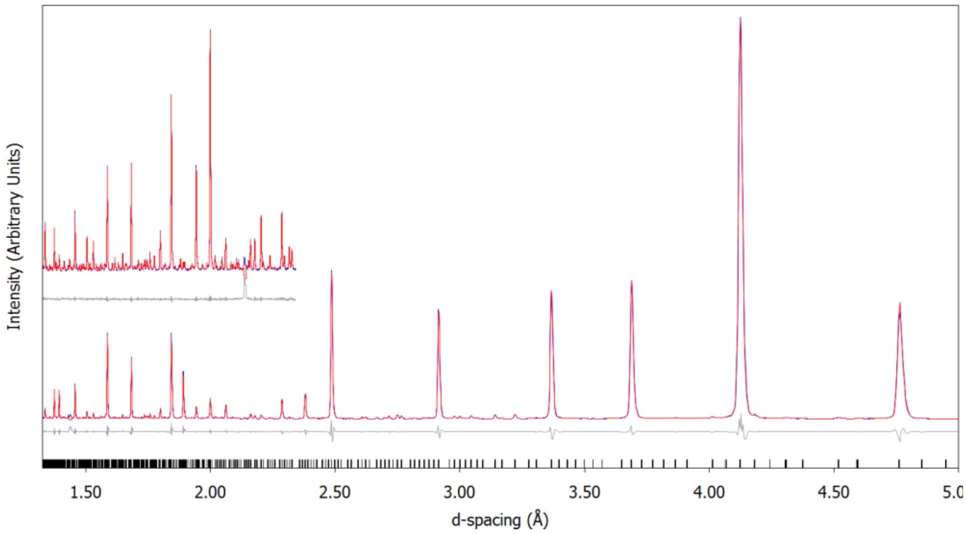

Figure 4.5: Fit to (top) HRPD TOF neutron and (bottom) synchrotron X-ray powder diffraction data of ZrP_2O_7 at RT using the candidate #67 *Pbca* model. X-ray R_{wp} (R_{Bragg}) = 9.09 % (2.23 %), TOF neutron R_{wp} (R_{Bragg}) = 2.42 % (1.32 %).

4.3.2 Visual Evidence

The main support we have for selecting this model is a visual inspection of the fit to the data provided by candidate #67 and competing models. The candidate with the next lowest number of parameters (804) in the lowest plateau grouping of 14 with a lower R_{wp} is candidate #70 (ranked 6th with R_{wp} = 3.88 %, $P2_1/c$, $3a_{parent}\times3a_{parent}\times3a_{parent}$). Figure 4.6 (and a detailed inspection of zoomed regions) shows the fit provided by this model is no better than that provided by candidate #67.

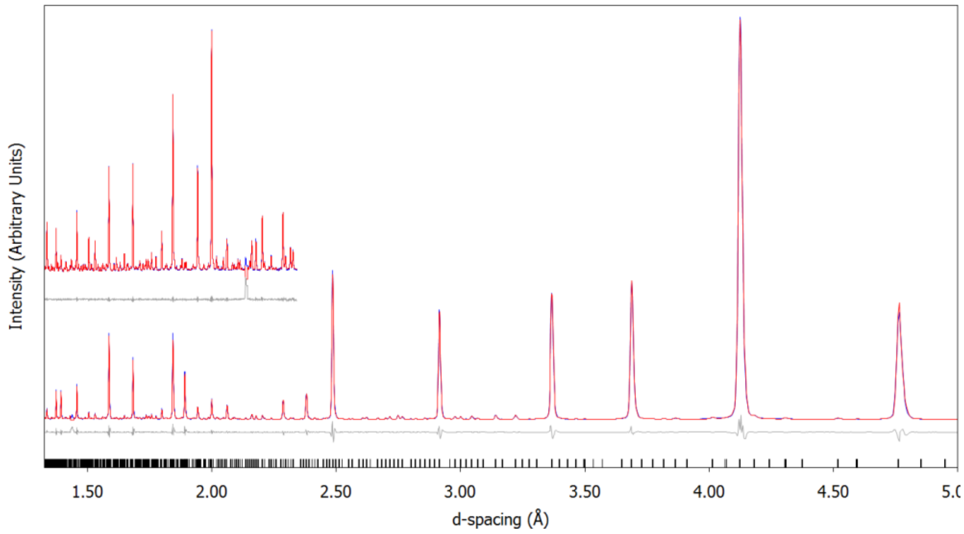

Figure 4.6: Fit to (top) HRPD TOF neutron and (bottom) synchrotron X-ray powder diffraction data of ZrP_2O_7 at RT using candidate #70 $P2_1/c$ model. X-ray R_{wp} (R_{Bragg}) = 8.70 % (2.00 %), TOF neutron R_{wp} (R_{Bragg}) = 2.19 % (1.05 %).

The highest ranked candidate outside the grouping of 14 with fewer parameters (264) than candidate #67 is candidate #55 (ranked 15 with R_{wp} = 4.66 %, $P2_1/c$, $\frac{3}{\sqrt{5}}a_{parent}\times 3a_{parent}\times \frac{3}{\sqrt{2}}a_{parent}$). Figure 4.7 shows the fit provided by this model, while Figure 4.8 shows close up views of parts of the TOF neutron fit where candidate #55 is clearly inferior to candidate #67. The TOF neutron data offers a better differentiation between the candidates because the distortion predominately involves movement of O atoms and O has a low scattering factor for X-rays.

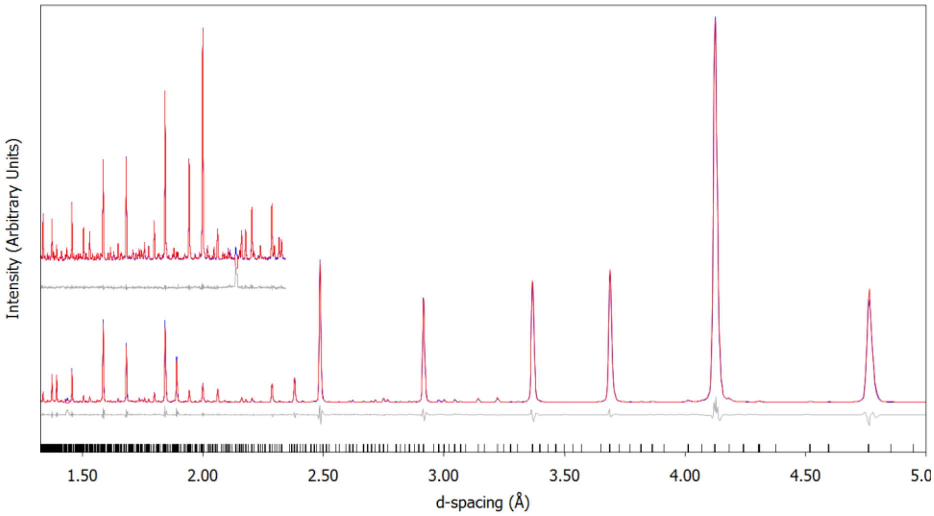

Figure 4.7: Fit to (top) HRPD TOF neutron and (bottom) synchrotron X-ray powder diffraction data of ZrP_2O_7 at RT using candidate #55 $P2_1/c$ model. X-ray R_{wp} (R_{Bragg}) = 9.77 % (2.62 %), TOF neutron R_{wp} (R_{Bragg}) = 3.04 % (1.70 %).

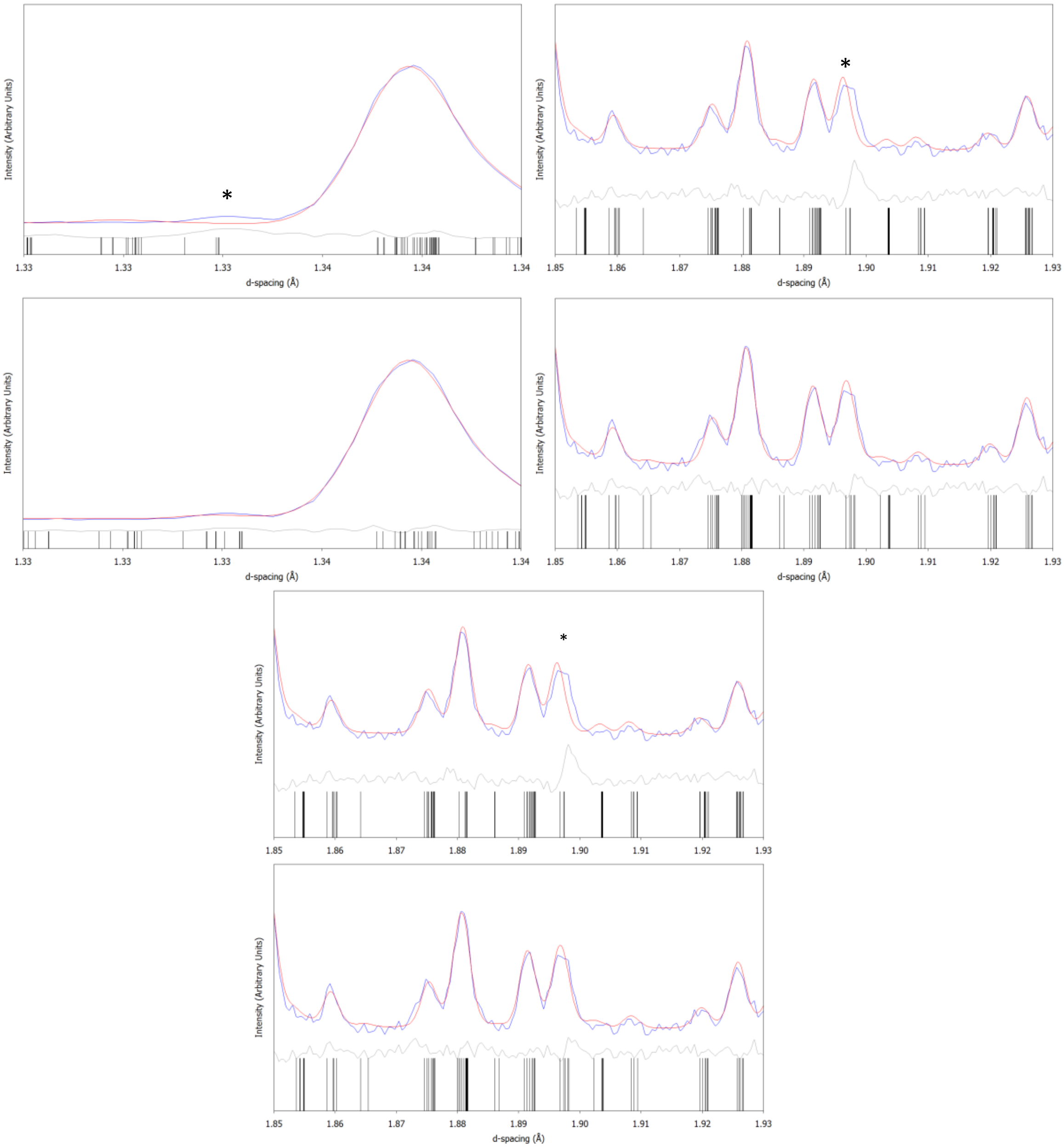

Figure 4.8: Selected close views of areas of the TOF neutron fit where candidate #55 (top of each pair) is significantly worse than candidate #67 (bottom of each pair). The * indicates a peak poorly modelled by candidate #55.

4.4 Repeatability

Our refinement protocol repeatedly obtains the same fit for all candidates over multiple runs. Figure 4.9 shows the R_{wp} obtained from three consecutive runs using our protocol.

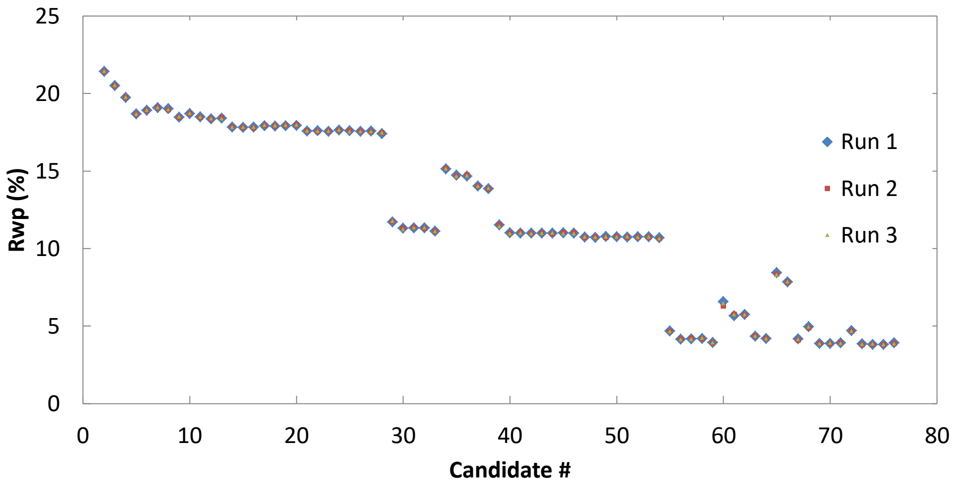

Figure 4.9: Combined R_{wp} found from fit to RT ZrP_2O_7 TOF neutron and synchrotron X-ray data. Repeat runs are shown as large blue diamonds underneath medium red squares underneath small green triangles. There is close agreement across all three runs for all 75 trialled candidates.

As further verification that our refinement protocol is effective we tested convergence in the most complicated (child) candidate. We converge to within 0.3 % R_{wp} of the minimum value seen in 29 of 39 cycles in the first step and to within 0.3 % R_{wp} of the minimum value seen in 22 of 24 cycles in the second step. It is likely that other candidates with fewer parameters will converge even more effectively if they do indeed have the requisite parameters.

4.5 Combining Displacive and Rotational Modes

Whilst the exhaustive approach is successful for ZrP_2O_7 a further simplification of the model would be useful both in itself and as a test case for other AM_2O_7 materials with even higher complexity. Since the phase transition can be described in terms of tilts of essentially rigid polyhedra, we have investigated whether the problem can be simplified through the use of rotational rigid bodies.

Rigid body symmetry modes were first used in the literature by Etter, Müller and Dinnebier[13] who used the term “constrainable atomic group” to differentiate their rotating groups from truly rigid bodies where no internal distortion of bond distances and angles can occur. Pure rotation of connected, truly rigid bodies is generally impossible as connecting atoms would be split between polyhedra (although in some circumstances this can be resolved with unit cell strain only). However, rather than following this approach, we apply rigid ZrO_6 octahedra and accept that some internal distortion of PO_4 polyhedra will be required as a result.

4.5.1 Rigid Body Set Up

In order to apply rotational modes to the model we must set up rigid polyhedra as described in Section 1.4.1. The ZrO_6 octahedra are anchored to a dummy position and rigid bodies are defined with rotational modes that cannot distort the internal bond distances and angles. In order to create the rigid bodies we chose to change the symmetry of the parent from the true $Pa\bar{3}$ structure to an artificial $Fm\bar{3}m$ aristotype structure by aligning all ZrO_6 octahedra such that Zr-O bonds point directly along the unit cell axes and placing the P at (¼, ¼, ¼) (details of these changes can be found in Table 4.1 and the artificial parent is shown in Figure 4.10).

Table 4.1: Comparison of artificial and real parent structures. Both have a_{parent} ~ 8.25 Å and a single symmetry unique atom of each type in the unit cell. P and O1 atoms in artificial parent lie on higher symmetry sites.

Atom	*Mult*	*Wyck*	$x\ (Pa\bar{3})$	$y\ (Pa\bar{3})$	$z\ (Pa\bar{3})$	$x\ (Fm\bar{3}m)$	$y\ (Fm\bar{3}m)$	$z\ (Fm\bar{3}m)$
Zr	4	a	0	0	0	0	0	0
P	8	c	0.61100	0.61100	0.61100	¼	¼	¼
O1	24	e	-0.08978	0.06339	-0.21571	¼	0	0
O2	4	b	½	½	½	½	½	½

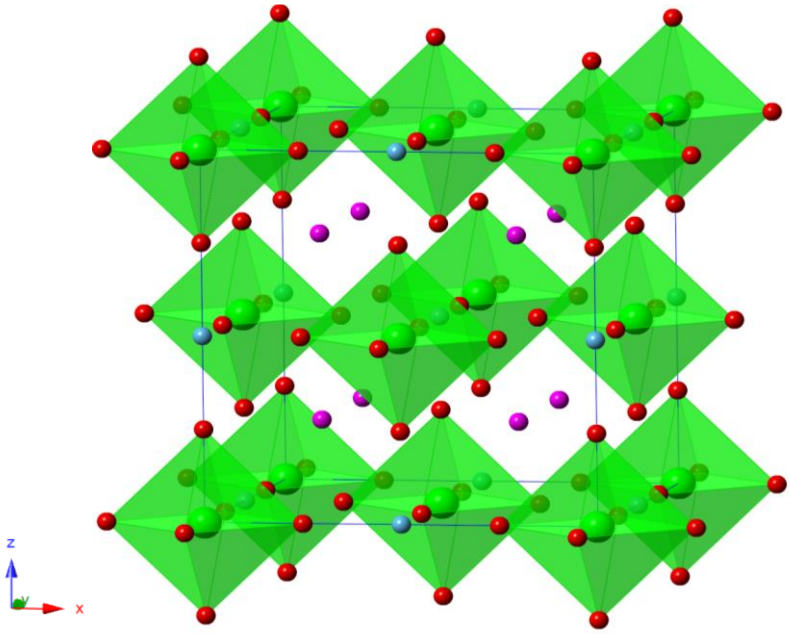

Figure 4.10: Artificial $Fm\bar{3}m$ parent structure created for generating rigid bodies and rotational distortion modes. Atoms are: Zr – green, P – pink, O1 – red, O2 – blue.

This is advantageous because the irreps of active distortions in the child structure are more distinguishable from the parent (i.e. are less likely to share an irrep with the parent). When considering distortions of the artificial high-symmetry parent, rotational irreps are highly distinguishable because a single irrep will initially move atoms exactly perpendicular to Zr-O bond vectors as they initially lie along a cell axis direction. Conversely, in the real parent structure (Figure 4.1), the octahedral tilt relative to the cell axes means that the initial movement of atoms in a pure rotation of polyhedra is described by a mixture of irrep contributions. At the time the process was undertaken, this was considered necessary in order to allow the ISOTILT routines that generate rigid bodies in ISODISTORT to work. However, development is ongoing and there is some discussion of new efforts to efficiently and robustly apply the necessary calculations to the real $Pa\bar{3}$ parent in order to build a simple model using quasi-cooperative rigid unit modes (quasi-CRUMs) in section 4.5.3.

Working with the artificial parent, a fixed set of baseline displacive distortion modes are applied to correct the model back to the true $Pa\bar{3}$ parent. These are obtained by decomposing the $Pa\bar{3}$ parent relative to the $Fm\bar{3}m$ parent following instructions in Appendix 14 which also gives the step-by-step process for obtaining corresponding $Pbca$ and $P1$ symmetry child structures.

Rotational distortion modes can then be incorporated into our model using ISODISTORT (following step-by-step instructions in Appendix 15) to output rigid bodies for each Zr pivot atom along with rotational modes allowed by the symmetry constraints of space group $Pbca$.

Once the rigid bodies are output by ISODISTORT the passenger atoms must then be determined. The undistorted structure has a $3a_{parent}$×$3a_{parent}$×$3a_{parent}$ $Pbca$ supercell. Each of the O1 atoms is attached to the correct “pivot” Zr atom automatically using scripts that read from a list of bond lengths and angles. Zr displacive modes are then redefined such that they act on the entire ZrO_6 rigid body, not only Zr atoms. All O1 displacive modes are removed from the search space except a single $\Gamma_1^+(a)$ mode – a “breathing mode” that allows all the ZrO_6 units to uniformly expand or contract. The result of this is to reduce the number of parameters of the correct $Pbca$ model from 402 for the fully displacive model discussed in Section 4.3 to a 202 parameter model here. This results from replacing 242 O1 displacive modes with just 42 rotational distortion modes of ZrO_6 (i.e. 3 rotations per rigid body). Figure 4.11 shows that the Rietveld fit achievable using this model is (reassuringly) very close to that achieved by the fully displacive model (Figure 4.5).

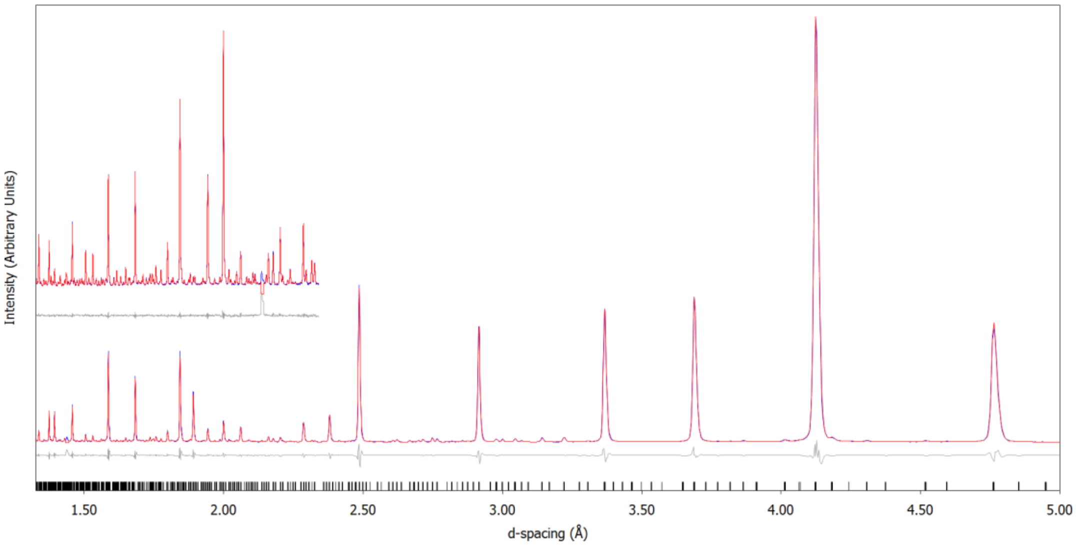

Figure 4.11: Fit to (top) HRPD TOF neutron and (bottom) synchrotron X-ray powder diffraction data of ZrP_2O_7 at RT using *Pbca* model but replacing 242 displacive distortion modes with 42 rotational distortion modes of ZrO_6 octahedra. X-ray R_{wp} (R_{Bragg}) = 9.27 % (2.04 %), TOF neutron R_{wp} (R_{Bragg}) = 2.56 % (1.52 %).

4.5.2 Search Algorithms

One unfortunate consequence of using an artificially high symmetry parent to simplify the rotational modes is a dramatic increase in the complexity of the subgroup tree between the parent and *P1* $3a_{parent}\times3a_{parent}\times3a_{parent}$ child. There are 1448 possible models in this tree compared to just 76 when using the real parent structure. This means an exhaustive subgroup search is not possible on a reasonable timescale using an ordinary desktop PC. There is also a considerable technical challenge in the assembly of rigid bodies and their passengers for 1448 different subgroups and the determination of each set of artificial to real parent mode baseline amplitudes.

An alternative approach is a simple inclusion type search (as discussed in Chapter 2) to see if it's possible to identify the key distortion modes needed and hence determine the correct space group symmetry. After applying the same set up tasks as discussed above to our *P1* child model there are 1621 distortion modes (1297 displacive and 324 rotational) available to this search compared to 3240 for a fully displacive model.

4.5.2.1 Only Penalties Refinement

Given the potential complexity of the search, an initial proof-of-concept test where models were refined against the distance between the atomic positions of the rotational mode model and the known correct positions was performed. This has the advantage of being significantly quicker than refinement against diffraction data and allows us to test the viability of our method in a reasonable time. The quantity minimised (penalty) in this simple refinement is the squared sum of the distance in Angstroms to the correct position as given by Equation 4.1, where for all atoms i in the unit cell: x_i, y_i and z_i are the rotation-mode derived fractional coordinates and x_i', x_i' and x_i' are the target fractional coordinates.

$$penalty = \sum_i \left(\left(\frac{x_i - x_i'}{a}\right)^2 + \left(\frac{y_i - y_i'}{b}\right)^2 + \left(\frac{z_i - z_i'}{c}\right)^2 \right)$$

Equation 4.1

While the results of this approach will not derive new structural information from diffraction data they will still be instructive. They should indicate how many of the 1621 possible modes are required to obtain an adequate model for RT ZrP_2O_7 and how separable the modes are in terms of the Cartesian description of the penalty function. If the important individual distortion modes move atoms directly towards their correct RT positions in xyz space, then this penalty will allow us to differentiate between "important" and "unimportant" modes. Conversely, if important individual distortion modes only move atoms directly towards ideal positions when part of a group of modes then this penalty won't be able to robustly identify important distortion modes. Figure 4.12 shows how the penalty changes on the introduction of each distortion mode identified by an inclusion search. This involves repeatedly trialling all available, inactive distortion modes individually and successively turning on the one with the largest R_{wp} improvement. The computational demands, even of this simple approach, are significant – it took 8 weeks to include the first 133 modes into the model (i.e. trialling 206815 potential models of increasing complexity) on a typical desktop computer (6th generation i7, 3.4 GHz).

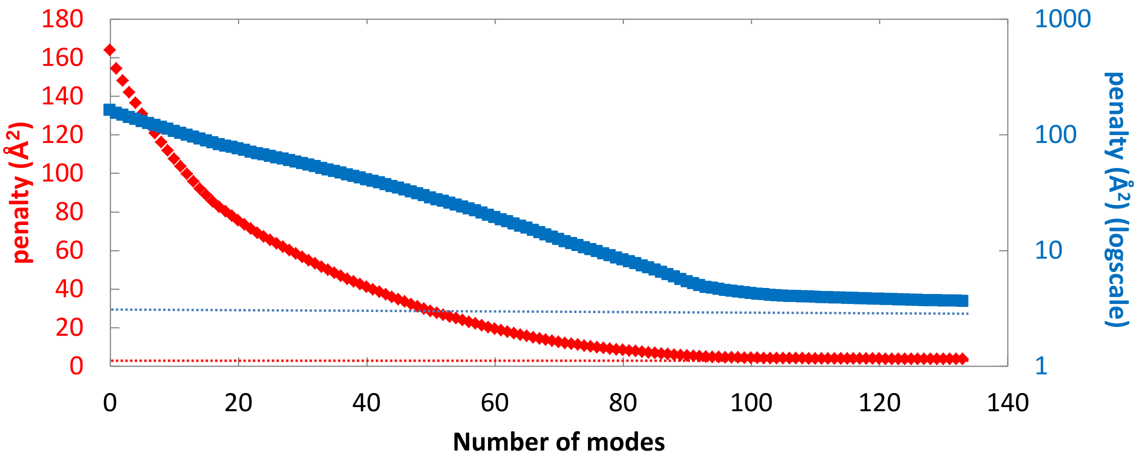

Figure 4.12: (Left, red): Penalty obtained by a simple inclusion search as distortion modes available in the *P1* child model are added. The penalty is plotted on a logarithmic scale (right, blue) to show that the improvement in distance from the ideal displacive model has plateaued after 93 modes have been added. Dashed lines show the *penalty* = 3.2 Å^2 minimum value when all 1621 modes are included.

The penalty initially reduces rapidly on including modes. This process continues smoothly with smaller decreases for each successive mode until 93 distortion modes are active at which point the penalty becomes essentially flat (*penalty* < 4.8 Å^2, meaning the 1080 atoms are on average ~ 0.06 Å from their correct positions); only very small improvements to the penalty are found even when many more modes being added. We therefore stopped the process after 133 modes had been included. The 93 mode point seems a reasonable point to declare that all significant modes necessary to describe RT ZrP_2O_7 have been activated. This is also the first point at which the structural model produced has space group *Pbca* identified by FINDSYM. At this point the required atomic position tolerance to identify *Pbca* is 0.1 Å (i.e. the furthest any atom is from a *Pbca* position is 0.1 Å). Given that we expect minor discrepancies in position to arise as a result of modelling polyhedra as completely rigid (as opposed to nearly rigid in an all-displacive mode model), this can be considered a good match to the correct structure. A one-off test using all 1621 available modes against the penalty function reveals a minimum value of *penalty* ~ 3.2 Å^2 – a small improvement for the addition of 1528 structural parameters. A table of all 1621 available distortion modes can be found in e-Appendix 13 which also gives the amplitude of those active in the 93 mode model.

Figure 4.13 shows the symmetry identified by FINDSYM using a 0.1 Å atomic position tolerance criteria for each model derived in the inclusion search. It is notable that a lower symmetry than *Pbca* is found for each model up until the 93 mode point. As activation of distortion modes usually removes, rather than creates, symmetry the expectation might have been that the symmetry would decrease gradually from the $Pa\bar{3}$ parent until $Pbca$ is obtained. The contrary outcome here reveals that we activate individual distortion modes that break $Pbca$ symmetry in the initial stages of the inclusion search. This can happen as space group $P1$ allows modes belonging to the same branch in $Pbca$ to activate independently and so, for example, a mode $(a,0)$ may be initially activated when $(a,\ a)$ is required. It is only when both modes (a,b) are activated (with approximately equal magnitude) that $Pbca$ symmetry returns. An alternative explanation is that modes completely disallowed by $Pbca$ symmetry are initially activated but that their amplitude falls to a value close to zero once other modes are identified.

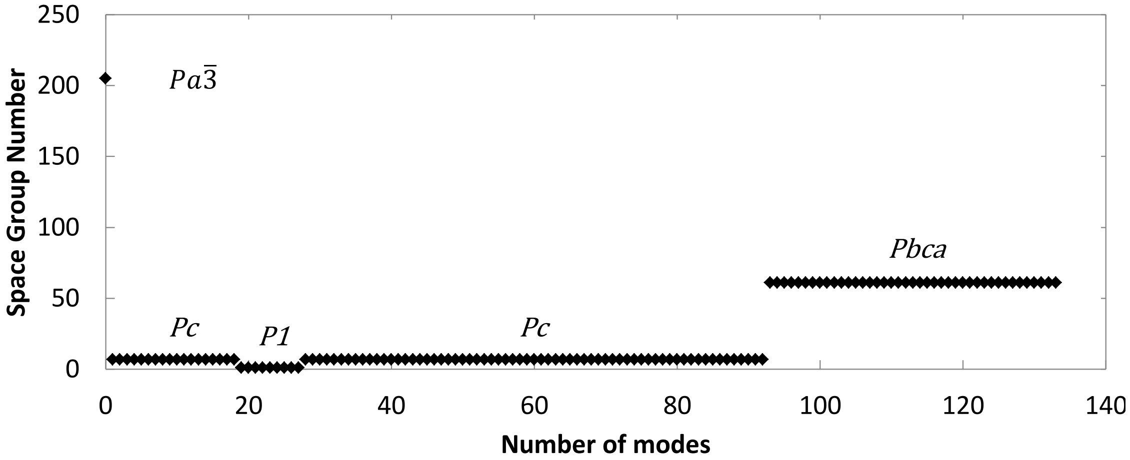

Figure 4.13: Space group symmetry identified by FINDSYM using a 0.1 Å atomic tolerance criteria for models identified by inclusion search. Lattice tolerance was 0.001 Å (sufficient to find a cubic unit cell with the fixed *P1* lattice parameters).

One (time consuming) option to test whether this is the case is to attempt an exclusion search, starting with the 93 mode model and removing modes that are no longer important to the fit once other important modes are present in the model. While this is an interesting avenue of future work, at this stage we simply note there are 8 modes (113, 115, 1186, 1188, 869, #871, 1489 and 1349) whose removal from the 93 mode model has a relatively minor effect on the *penalty* (it increases by < 0.3 Å^2). There are also several sets of modes whose amplitudes are clearly related in our 93-mode model. In each case they belong to the same OPD branch in the *Pbca* structure. Some examples are summarised by

Table 4.2. In such cases the individual effect of the modes to the penalty function may not be the same in the absence of paired modes and the individual modes may break $Pbca$ symmetry constraints.

Table 4.2: Examples of individually refined mode amplitudes that belong to the same OPD branch in the correct *Pbca* structure. Active modes of *P1* OPD are shown in bold.

Modes #	*Amplitudes in 93 mode model (Å)*	*P1 Irrep(OPD)*	*Pbca Irrep(OPD)*
869 and 871	-0.534 and 0.534	A1(a,b;c,d;e,f;g,h;i,j;k,l;m,n;o,p; **q**,r;**s**,t;u,v;w,x)	A1(0,0,0,0,0,0,0,0,0,0,0,0,a,0,-a,0,b,0,-b,0,c,0,-c,0)
870 and 872	-0.972 and 0.972	A1(a,b;c,d;e,f;g,h;i,j;k,l;m,n;o,p; q,**r**;s,**t**;u,v;w,x)	A1(0,0,0,0,0,0,0,0,0,0,0,0,a,0,-a,0,b,0,-b,0,c,0,-c,0)
1085 and 1087	0.864 and 0.864	SM2(**a**,b;**c**,d;e,f;g,h;i,j;k,l)	SM2(a,0,a,0,b,0,b,0,c,0,c,0)
1170 and 1172	-1.291 and 1.291	C1(a,b;c,d;e,f;g,h;i,j;k,l;m,n;o,p; **q**,r;**s**,t;u,v;w,x)	C1(a,0,a,0,-a,0,-a,0,b,0,-b,0,-b,0,b,0,c,0,-c,0,c,0,-c,0)
1174 and 1176	0.646 and -0.646	C1(a,b;c,d;e,f;g,h;i,j;k,l;m,n;o,p; q,r;s,t;**u**,v;**w**,x)	C1(a,0,a,0,-a,0,-a,0,b,0,-b,0,-b,0,b,0,c,0,-c,0,c,0,-c,0)
1186 and 1188	0.478 and -0.478	C1(a,b;c,d;e,f;g,h;**i**,j;**k**,l;m,n;o,p; q,r;s,t;u,v;w,x)	C1(a,0,a,0,-a,0,-a,0,b,0,-b,0,-b,0,b,0,c,0,-c,0,c,0,-c,0)
1190 and 1192	0.957 and -0.957	C1(a,b;c,d;e,f;g,h;i,j;k,l;**m**,n;**o**,p; q,r;s,t;u,v;w,x)	C1(a,0,a,0,-a,0,-a,0,b,0,-b,0,-b,0,b,0,c,0,-c,0,c,0,-c,0)

4.5.2.2 Using Diffraction Data

The results of this inclusion search show that our search method is viable even with the complex ZrP_2O_7 structure and large number of available distortion modes. However, performing an equivalent inclusion search using experimental X-ray and TOF neutron data will be even more time consuming. This is because the calculation and comparison of the powder diffraction patterns by TA is considerably more demanding than merely calculating the result of Equation 4.1. Therefore, we conclude that this type of search is currently not practicable with ordinary desktop computing resources. Given the TA Rietveld refinement software is a single node program it is not immediately possible to accelerate the process by outsourcing refinements to multi-node High Performance Computing (HPC). We do however note that the series of separate Rietveld refinements required in each cycle of an inclusion type search would be extremely well suited to this computational arrangement.

For reference, and as a starting point for future work, we note that at the time of writing we have been able to include 11 modes in an inclusion search using diffraction data over the course of 15 weeks (4th generation i5, 3.2 GHz). This 11 mode model has already broken sufficient symmetry to return space group *P1* at the 0.1 Å atomic position tolerance level in

FINDSYM. This suggests, similarly to the only penalties process above, that the pathway will involve the initial inclusion of mode amplitudes not permitted by *Pbca* symmetry.

We can, however, show how well the 93 mode-model identified using the penalty function fits the diffraction data (Figure 4.14). We know the model is close to that of the true *Pbca* structure at this point and there is a good fit to most diffraction features. Some features are not quite as well fit as they are by our full 202 or 402 parameter structural models (Figure 4.11) but this is not significantly improved by activating more modes in pursuit of a closer match to atomic positions.

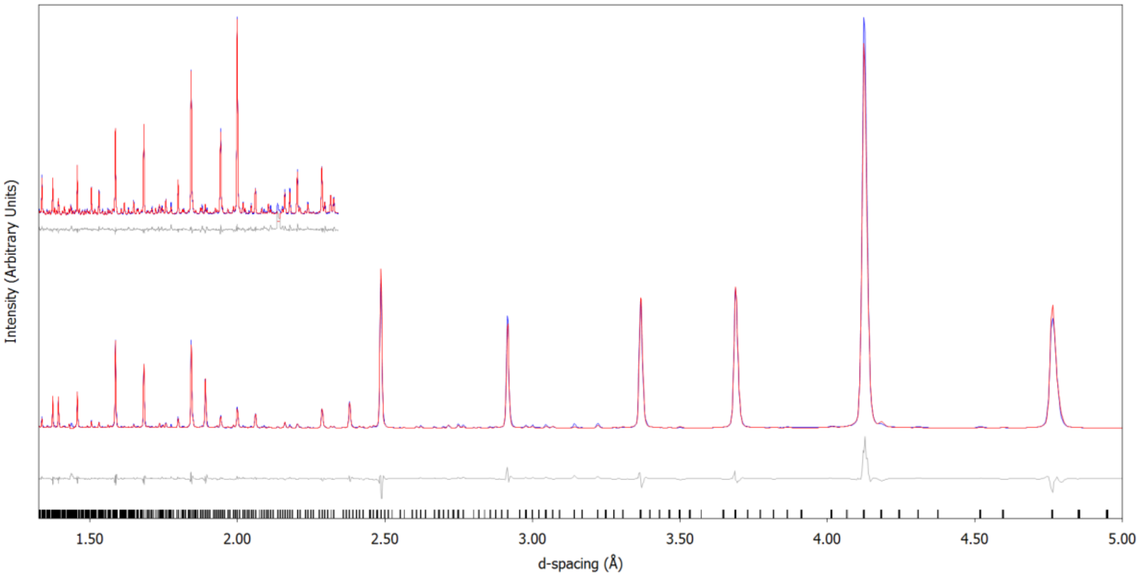

Figure 4.14: Fit to (top) HRPD TOF neutron and (bottom) synchrotron X-ray powder diffraction data of ZrP_2O_7 at RT using best 93 modes identified by inclusion search. X-ray R_{wp} (R_{Bragg}) = 14.38 % (5.50 %), TOF neutron R_{wp} (R_{Bragg}) = 5.44 % (4.20 %).

The fact the fit is inferior to the true *Pbca* model suggests that the 93 modes best suited to matching the atomic sites of the correct model is not quite the same set of modes best suited to achieving the optimum fit to the data. This is despite the fact that a model that precisely matches the atomic sites of the correct model will give an equivalent fit (when all other structural, experimental and instrumental parameters are the same as they are here). This occurs as the processes are performed in different minimisation spaces (Equation 4.1 and the fit to powder diffraction data respectively).

4.5.3 The Future: Identifying a quasi-CRUM Rigid Body Model using the $Pa\overline{3}$ Parent

We have also performed preliminary analysis of how the RT *Pbca* structure can be decomposed into rotations similar to cooperative rigid unit modes (CRUMs) of both ZrO_6

and PO_4 rigid bodies. Such modes would retain near-rigidity of polyhedra present in the $Pa\bar{3}$ real parent (i.e. they are quasi-CRUMs). New developments in ISOTILT have been initiated to identify such a quasi-CRUM description by searching for infinitesimal rotations that retain almost rigid polyhedra in ZrP_2O_7. The aim of this process is to identify a very simple model of the child structure consisting of only a few CRUMs and small displacive modes to describe internal distortions of polyhedra.

Due to current computational issues, no quasi-CRUM type model has yet been identified. Given the child structure consists of polyhedra with only very little internal distortion, we expect such a model should exist. The challenge of this example is that the connectivity prevents a search for a fully CRUM model while the freedom allowed by the inclusion of displacive modes to describe internal distortions of polyhedra obstructs the search for a simple model. Future work in search of this model could involve allowing a small degree of splitting of oxygen sites shared by octahedra and tetrahedra, then compensating for these using small internal distortions. This would achieve a low-parameter quasi-CRUM model. Unfortunately, time constraints and challenges in the construction of such a model prevent us from including this work in this thesis.

4.6 Conclusions

In this chapter we have shown that it is possible to apply the distortion mode basis to a large and complex system such as RT ZrP_2O_7. An exhaustive search process is possible for the full 76 subgroup candidate tree when using displacive modes with the $Pa\bar{3}$ parent structure, despite the large number of parameters involved in each candidate model (up to 3240 for the $3a_{parent}\times3a_{parent}\times3a_{parent}$ $P1$ child model). The process was able to identify the correct $3a_{parent}\times3a_{parent}\times3a_{parent}$ $Pbca$ model on a reasonable timescale on an ordinary desktop computer without relying on complementary information from NMR data.

By choosing to use an artificial parent with higher $Fm\bar{3}m$ symmetry and applying ZrO_6 rigid bodies and rotational modes in place of O1 displacive modes the model is simplified in terms of the number of refineable parameters needed for an almost-equivalent fit to powder diffraction data. The choice of the artificial parent for rotational mode work does however considerably increase the number of candidate models in the subgroup tree to our child structure. An exhaustive search is therefore challenging both technically and computationally. Preliminary work suggests a simple inclusion type algorithm followed by symmetry identification in FINDSYM may be an effective alternative in this case, even though it does not take the most direct route to the true symmetry. This approach allows a 93 mode description rather than using the 402 modes of the displacive model.

An ultimate goal in this system would be a CRUM-like model using far fewer parameters. New methodology for exploring rotations of rigid bodies has allowed us to start to explore this possibility, but we haven't yet identified a simple CRUM-like model. This may be a result of the connectivity of RT ZrP_2O_7 which does not allow CRUMs (only quasi CRUMs). Either this or another aspect of the complexity of ZrP_2O_7 is preventing the current algorithm from working.

4.7 References

(1) Levi, G. R.; Peyronel, G. *Zeitschrift für Kristallographie-Crystalline Materials* **1935**, *92*, 190.

(2) Korthuis, V.; Khosrovani, N.; Sleight, A. W.; Roberts, N.; Dupree, R.; Warren, W. W. J. *Chemistry of Materials* **1995**, *7*, 412.

(3) Evans, J. S. O. *Journal of the Chemical Society, Dalton Transactions* **1999**, 3317.

(4) Sleight, A. W. *Annual Review of Materials Science* **1998**, *28*, 29.

(5) Khosrovani, N.; Sleight, A. W.; Vogt, T. *Journal of Solid State Chemistry* **1997**, *132*, 355.

(6) Giddy, A. P.; Dove, M. T.; Pawley, G. S.; Heine, V. *Acta Crystallographica Section A: Foundations of Crystallography* **1993**, *49*, 697.

(7) Grüneisen, E. *Annalen der Physik* **1912**, *344*, 257.

(8) Barron, T. H. K. *Annals of Physics* **1957**, *1*, 77.

(9) Withers, R. L.; Tabira, Y.; Evans, J. S. O.; King, I. J.; Sleight, A. W. *Journal of Solid State Chemistry* **2001**, *157*, 186.

(10) Khosrovani, N.; Korthuis, V.; Sleight, A. W.; Vogt, T. *Inorganic Chemistry* **1996**, *35*, 485.

(11) King, I. J.; Fayon, F.; Massiot, D.; Harris, R. K.; Evans, J. S. O. *Chemical Communications* **2001**, 1766.

(12) Birkedal, H.; Krogh Andersen, A. M.; Arakcheeva, A.; Chapuis, G.; Norby, P.; Pattison, P. *Inorganic Chemistry* **2006**, *45*, 4346.

(13) Etter, M.; Müller, M.; Dinnebier, R. E. *Zeitschrift für Anorganische und Allgemeine Chemie* **2014**, *640*, 3079.

Chapter 5 Stacking Faults and Magnetic Ordering in 3D Oxychalcogenides

5.1 Introduction

This chapter describes new methods we have developed to investigate important structural features of layered oxychalcogenide materials. In particular we describe a new method for modelling stacking faults that are common in these and many other systems; and how our search method of earlier chapters can be extended and applied to determine new magnetic structures.

Oxychalcogenides are a family of mixed anion materials containing an oxide anion as well as another anion from group 16 of the periodic table. A number of materials in the family are of particular interest for superconductivity[1-4] as well as magnetic, electronic and optical properties[5-10]. In this chapter we focus on quaternary oxychalcogenides of general formula $LnO_2M_xSe_2$ where Ln = La^{3+} or Ce^{3+} or a mixture of both and M = Cu^+, Mn^{2+}, Fe^{2+}, Zn^{2+} or a mixture of two of these four. The differing ionic radii and chemical preferences of the oxide and selenide anions mean that they adopt layered structures where each anion bonds preferentially with one of the two different metal sites. The oxide ions bond with more ionic character and favour the small, "hard" ions of the Ln site and the selenium bonds to the M site to complete the coordination sphere.

The 2D structure found in these materials consists of separate layers of $[M_xSe_2]^{2-}$ (where x = 2 for a M^{1+} or x = 1 for a M^{2+} cation) and $[Ln_2O_2]^{2+}$ units. The $[MSe_2]^{2-}$ layers contain half occupied MSe_4 tetrahedral sites leading to tetrahedra connected either by corners, edges or a mixture of the two. In $[M_2Se_2]^{2-}$ layers all sites are fully occupied. $[Ln_2O_2]^{2+}$ layers consist of more rigid A_4O edge sharing tetrahedra. This is a useful description because composition-dependent structural variation within the layers is typically limited to the $[M_xSe_2]^{2-}$ layers. Ainsworth et al.[11] developed a naming system for the 2D ordering in the selenide layers where a material is referred to on the basis of the ratio of corner (C) sharing to edge (E) sharing units found within the layer. For example a material containing three corner-sharing tetrahedra to one edge-sharing is referred to as 3C-1E. We persist with that naming methodology here. The pattern of corner and edge sharing within $[M_xSe_2]^{2-}$ layers for each material investigated in this chapter is shown in Figure 5.1.

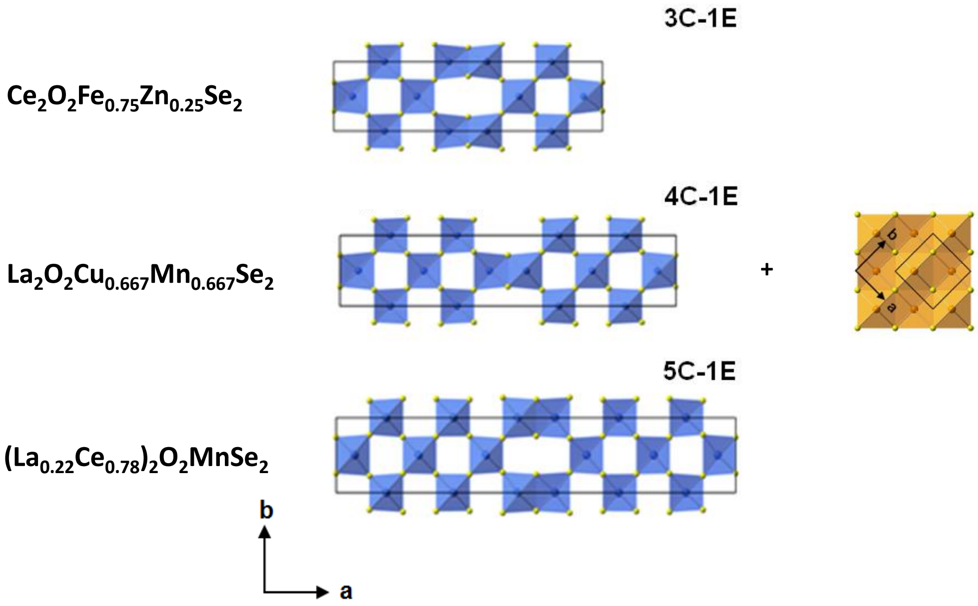

Figure 5.1: Intra-layer structures of materials investigated in this chapter. Atom colours: blue - *M* = Fe^{2+}, Zn^{2+}, Cu^{+} or Mn^{2+}, yellow – Se. Reproduced in part from Ainsworth et al.[11]

For all materials discussed in this chapter these individual layers are stacked in an alternating sequence of $[M_xSe_2]^{2-}$ and $[Ln_2O_2]^{2+}$ (Figure 5.2). The $Ce_2O_2Fe_{0.75}Zn_{0.25}Se_2$ RT structure has Fe^{2+} and Zn^{2+} disordered within each layer and the material does not appear to separate into distinct $[FeSe_2]^{2-}$ and $[ZnSe_2]^{2-}$ layers. $La_2O_2Cu_{0.667}Mn_{0.667}Se_2$ and $La_2O_2Cu_{0.667}Cd_{0.667}Se_2$ have a more complex sequence than this. They exhibit additional ordering of $[Cu_2Se_2]^{2-}$ and $[MSe_2]^{2-}$ layers along the *c* axis which is discussed in detail in section 5.5.

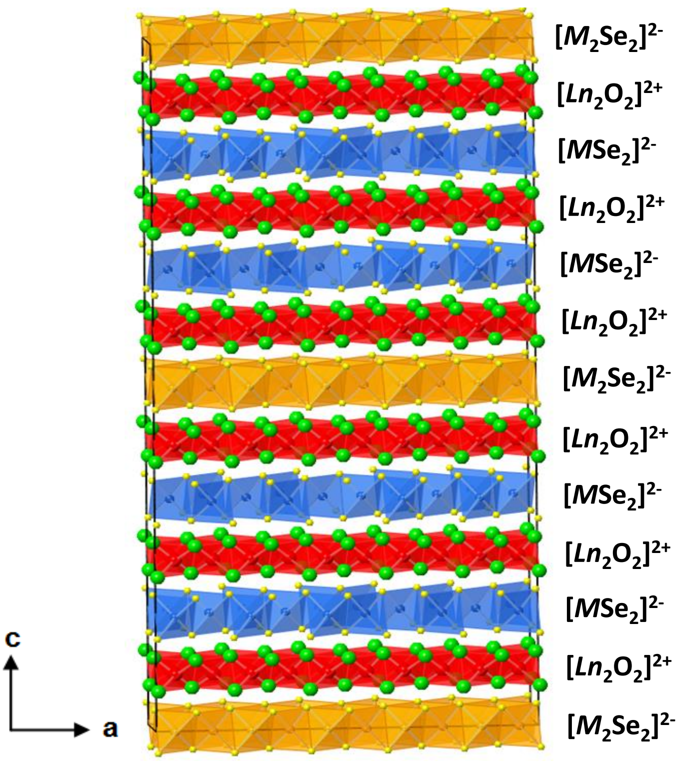

Figure 5.2: Side view of the layered structure of $AO_2M_xSe_2$ type oxychalcogenides investigated in this chapter. Variation in colour of $[M_xSe_2]^{2-}$ layers indicates ordering of separate $[M_2Se_2]^{2-}$ and $[MSe_2]^{2-}$ layers. Atom colours: green – $Ln = La^{3+}$ or Ce^{3+}, red – O, yellow – Se, blue - $M = Fe^{2+}$, Zn^{2+} or Mn^{2+}, orange – $M = Cu^+$. Adapted from Ainsworth[12].

5.2 Stacking Faults

Real layered materials do not always adopt fully regular ordering over long range. One type of deviation from the regular pattern is caused by stacking faults. If the energetic penalty for the material to adopt a faulted arrangement is small then stacking faults may be sufficiently numerous to have a noticeable effect on powder diffraction data. For this reason, an accurate structural model of these materials must include stacking faults. The earliest attempt to construct these models is with DiffaX[13], which allows the simulation of diffraction patterns using stacking fault probabilities on the basis of a theoretical infinitely large crystal. It is not, however, able to perform fitting to observed diffraction data. DiffaX+[14] does allow least squares fitting of simulated patterns as does FAULTS[15], both by modification of the original DiffaX algorithm. To date there is no rapid, fully functional approach to allow Rietveld refinement of stacking faulted materials.

A challenge in constructing such an approach is that a finite sized model of irregular faults cannot be created with regular sized unit cells and a supercell must be used to allow a reasonable approximate model to be constructed. One method to construct a faulted model is by placing layers successively in the stacking direction (*c* throughout this chapter). As each layer is placed there is an associated probability of a stacking fault occurring in the model. This process continues until a supercell is constructed that is believed to be a reasonable approximation of the real structure. The larger the supercell (the more layers that are added), the more accurately the model can approximate a real crystal. However, the larger the supercell constructed the greater the computational workload in calculation of a diffraction pattern due to the need for summation of a larger number of *hkl* reflections. Figure 5.3 shows a representation of how faults can be approximated using a supercell.

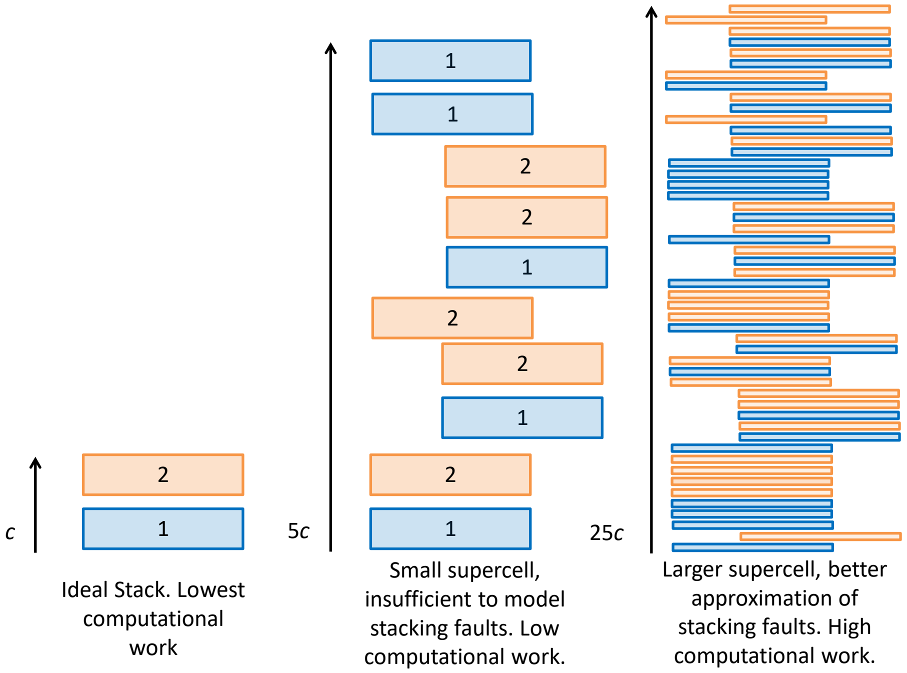

Ideal Stack. Lowest computational work

Small supercell, insufficient to model stacking faults. Low computational work.

Larger supercell, better approximation of stacking faults. High computational work.

Figure 5.3: Example of faults in a simple 2 layer system. Two types of fault are shown: the first involves a change in the repeating order of layers, and the second involves the stack also being offset perpendicular to the stacking direction.

There have also been attempts allow Rietveld-like refinements of large faulted structures by Ufer et al.[16-18] using BGMN software[19] and by Wang et al.[20] using TA software[21]. The modelling is limited only to stacking faults resulting in intensity changes to 00*l* reflections and *hk*0 reflections separately (Ufer) or is severely limited in the size of supercells that may be modelled (Wang). More recently, at a similar time to the work presented in this chapter, Bette et al.[22] modelled stacking faults for a 36 layer system in TA software (just a 12 fold cell size increase on the regular unfaulted 3 layer model). They were able to perform Rietveld refinements and a grid search of possible fault frequencies but refinements took 2-7 days per point and were limited in terms of the fault probabilities they could assess.

5.3 A New Approach to Stacking Faults

Previous attempts to provide Rietveld refineable stacking fault models have been limited by the large increase in complexity of the calculation of the diffraction pattern for the large supercells required for a good approximation of stacking faults. We introduce new methods that allow a dramatic increase in the size of models to which Rietveld refinement can be applied describe how these have been integrated into the TA software. This section outlines the methodology improvements that have been made and uses $La_2O_2Cu_{0.667}Cd_{0.667}Se_2$ as an example material. Methodology improvements in the Rietveld refinement of faulted stacks were made over the course of two collaborations and my contributions to each is highlighted.

5.3.1 New Rietveld Refinement Methodology

The first refinement methodology improvements are published in Ainsworth, Lewis, Wang, Coelho, Johnston, Brand and Evans ("*3D Transition Metal Ordering and Rietveld Stacking Fault Quantification in the New Oxychalcogenides* $La_2O_2Cu_{2-4x}Cd_{2x}Se_2$")[11]. My role in this work concerned the construction of stacks using python scripting and integration of them into TA software rather than the Rietveld calculation speed improvements below.

The work was enabled by four major changes to Rietveld calculations: Firstly, a significant computational saving can be made by recognising that the number of unique fractional atomic coordinates in the non-stacking directions (x and y) of a supercell is usually small. Therefore the summation of atomic contributions to calculate the structure factor can be performed over a small group of unique x and y coordinates. This achieves a significant saving as long as layers are stacked with a small number of xy offsets. Where there are a large number of different xy positions, the savings cannot be made.

Secondly, due to the enormous unit cell, individual *hkl* reflections may be spaced more closely in 2θ than observed data points. In this case the intensity from the set of reflections spanning two neighbouring data points can be assigned to the two reflections at the ends of the set (i.e. at the positions of the two data points) with no loss in accuracy. This process reduces the number of *hkl* reflections to be summed in the calculation of the diffraction pattern, saving computational work.

Thirdly, by refining the internal geometry of each layer based on its type rather than allowing variation of atomic positions in each individual layer, the number of independent parameters refined can be considerably reduced. This means the calculation of the derivatives of coordinates in the stacking direction can be done in a similar timescale to a subcell even with a large number of layers.

Finally, the use of a so-called “peaks-buffer” allows efficient computational handling of *hkl*-dependent quantities needed for calculations such as peak shapes in TA. This allows efficient Rietveld calculations even for large numbers of *hkl* reflections.

5.3.2 $La_2O_2Cu_{0.667}Cd_{0.667}Se_2$ Example

The ideal unfaulted structure of $La_2O_2Cu_{0.667}Cd_{0.667}Se_2$ is shown in Figure 5.4. It involves $[CdSe_2]^{2-}$ and $[Cu_2Se_2]^{2-}$ layers separated by $[La_2O_2]^{2+}$ layers. The ideal ordering pattern can be described as Cu|Cd|$\underline{\mathrm{Cd}}$|Cu|$\underline{\mathrm{Cd}}$|Cd where Cu and Cd refer to $[Cu_2Se_2]^{2-}$ and $[CdSe_2]^{2-}$ layers respectively while | indicates the $[La_2O_2]^{2+}$ layer separating them. The underlining indicates an (±*a*/2, ±*b*/2, 0) offset of the layer from non-underlined layers in the stack. The structure of $[CdSe_2]^{2-}$ layers in the *ab* plane has a 1C-0E ordering (i.e. fully corner-sharing tetrahedra).

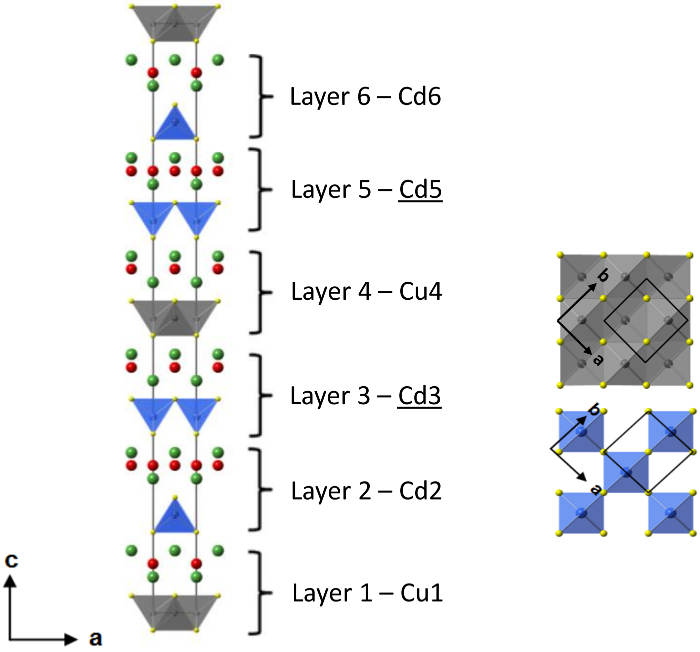

Figure 5.4: Structure of $La_2O_2Cu_{0.666}Cd_{0.666}Se_2$ if an ideal stack is followed. Refer to Table 5.1 for how the order of layers is changed by “a” and “b” faults. Atom colours: blue – Cd, yellow – Se, grey – Cu, green – La, red – O Reproduced from Ainsworth et al.[11]

This ideal structure provides a good fit to most observed reflections in the observed powder diffraction data however some reflections are poorly fit (Figure 5.5). This is because the crystallites contain stacking faults. Two types are considered: an “a” type fault; where a layer is repeated such that the local stack is Cu|Cu|Cd|$\underline{\mathrm{Cd}}$ (an extra Cu layer) or Cu|Cd|$\underline{\mathrm{Cd}}$|Cd (an extra Cd layer), and a “b” type fault; where the *ab* plane Cd layer offset either side of a

Cu layer is not retained such that the local stack is, for example, Cu|Cd|$\underline{\mathrm{Cd}}$|Cu|Cd|$\underline{\mathrm{Cd}}$. The variables *pa* and *pb* refer to the probability of “a” and “b” type faults occurring respectively. Table 5.1 gives the probabilities of each possible layer transition as the stack is progressively constructed.

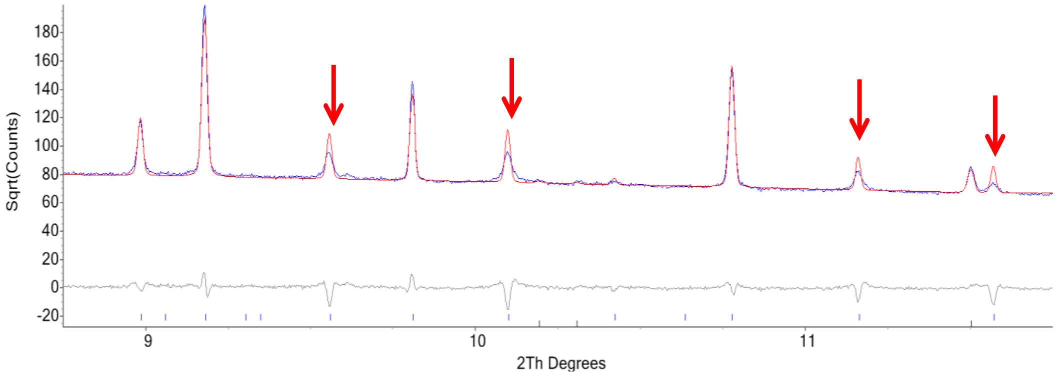

Figure 5.5: Rietveld refinement showing fit to key peaks in synchrotron powder diffraction. View shows fit without stacking faults (ideal stack) and arrows indicating small intensity discrepancies of some calculated reflections. Reproduced from Ainsworth et al.[11]

Table 5.1: Probability of transitioning from current layer to all possible other layers in $La_2O_2Cu_{0.667}Cd_{0.667}Se_2$ stacking model.

TO → FROM ↓	1 – Cu	2 – Cd	3 – $\underline{\mathrm{Cd}}$	4 – Cu	5 – $\underline{\mathrm{Cd}}$	6 – Cd
1 – Cu	0	1-*pa*-*pb*	0	*pa*	*pb*	0
2 – Cd	0	0	1-*pa*	0	*pa*	0
3 – $\underline{\mathrm{Cd}}$	0	0	0	1-*pa*	0	*pa*
4 – Cu	*pa*	*pb*	0	0	1-*pa*-*pb*	0
5 – $\underline{\mathrm{Cd}}$	0	*pa*	0	0	0	1-*pa*
6 – Cd	1-*pa*	0	*pa*	0	0	0

We note that of the 6 layers defined in Table 5.1, there are only 3 unique layers (Cu, Cd and $\underline{\mathrm{Cd}}$). The choice to define 6 layers is simply for convenience and clarity so that the ideal stacking order can follow the pattern 1|2|3|4|5|6|1|2|3…etc. Using pseudo-random numbers and the probability rules in Table 5.1 a python-scripted algorithm was written to construct a proposed stack for each of a list of trial values of *pa* and *pb* as outlined in Figure 5.6. The algorithm protects the inherent composition of the model by ensuring *pa* faults involving extra $[Cu_2Se_2]^{2-}$ layers are matched by *pa* faults involving extra $[CdSe_2]^{2-}$ layers. As *c* direction ordering is restricted to $[M_xSe_2]^{2-}$ layers it is simple to construct the stack by having a separating $[La_2O_2]^{2+}$ layer automatically placed whenever a selenide layer is chosen.

Therefore each of the 6 numbered, pre-defined layers also contains the sites of an adjacent $[La_2O_2]^{2+}$ layer so that the $[M_xSe_2]^{2-}$-$[La_2O_2]^{2+}$ alternating stack is constructed correctly.

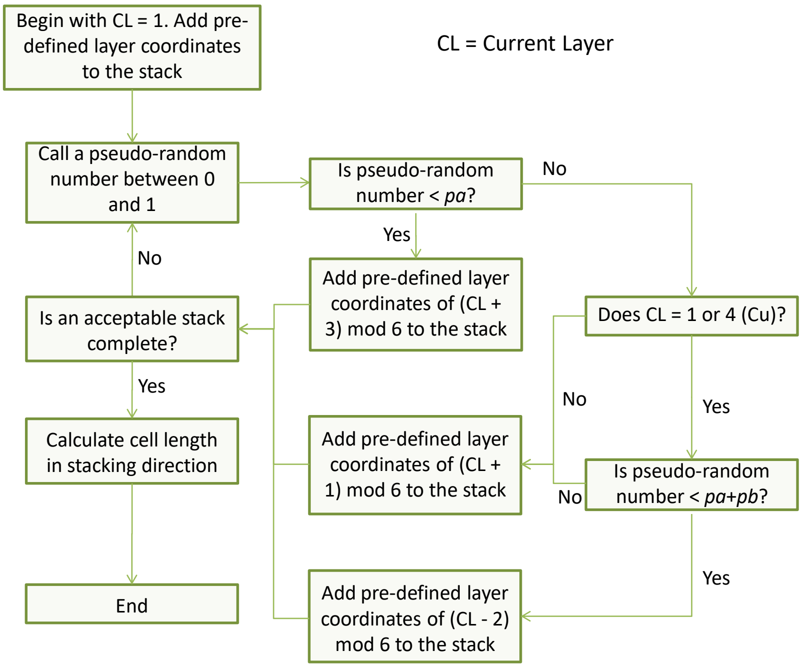

Figure 5.6: Iterative process for stacking layers from given probabilities in the $La_2O_2Cu_{0.667}Cd_{0.667}Se_2$ material

A stack of 960 layers (N_v = 960, ~ 7000 atoms in the unit cell) was constructed in this fashion and refined in TA for each point on a grid of *pa* and *pb* values. The process is repeated 100 times. The surface of minimum R_{wp} and points representing each stack trialled at each grid point is shown in Figure 5.7. The spread of R_{wp} found at each grid point reflects the variations in both the actual number of faults in each stack and their relative positions. As a benchmark, the grid search shown in Figure 5.7 took ~ 15 hours to complete on an ordinary desktop computer (6th generation i7, 3.4 GHz). Analysis of the R_{wp} surfaces produced show that the best fit to experimental data is found when 1.6 % “a” type stacking faults are included in the model. No evidence of “b” type stacking faults is found. The inclusion of 1.6 % “a” type stacking faults is sufficient to allow a good fit be obtained for peaks that are overcalculated using an ideal stack (Figure 5.8). It also successfully models the *hkl* dependence of peak widths of reflections due to TM ordering. This method was successfully applied to 8 different materials in the $La_2O_2Cu_{2-4x}Cd_{2x}Se_2$ family and the probability of “a” and “b” type faults was found to vary systematically with *x*. Five of the materials trialled were found to have “a” or “b” type faults. All of those found to have “b” type faults lie in the

Cu rich region ($x < 0.25$) with seemingly random offsetting ($pb = 0.5$) reached for $x = 0.2$. The probability of “a” type faults seems to be highest for those materials furthest in composition from the unfaulted $x = 0.25$ sample apart from the $x = 0$ and $x = 0.5$ end members containing only $[Cu_2Se_2]^{2-}$ or $[CdSe_2]^{2-}$ layers respectively to which “a” type faults clearly cannot apply. For additional information, refer to the paper “3D Transition Metal Ordering and Rietveld Stacking Fault Quantification in the New Oxychalcogenides $La_2O_2Cu_{2-4x}Cd_{2x}Se_2$” attached at the end of this thesis .

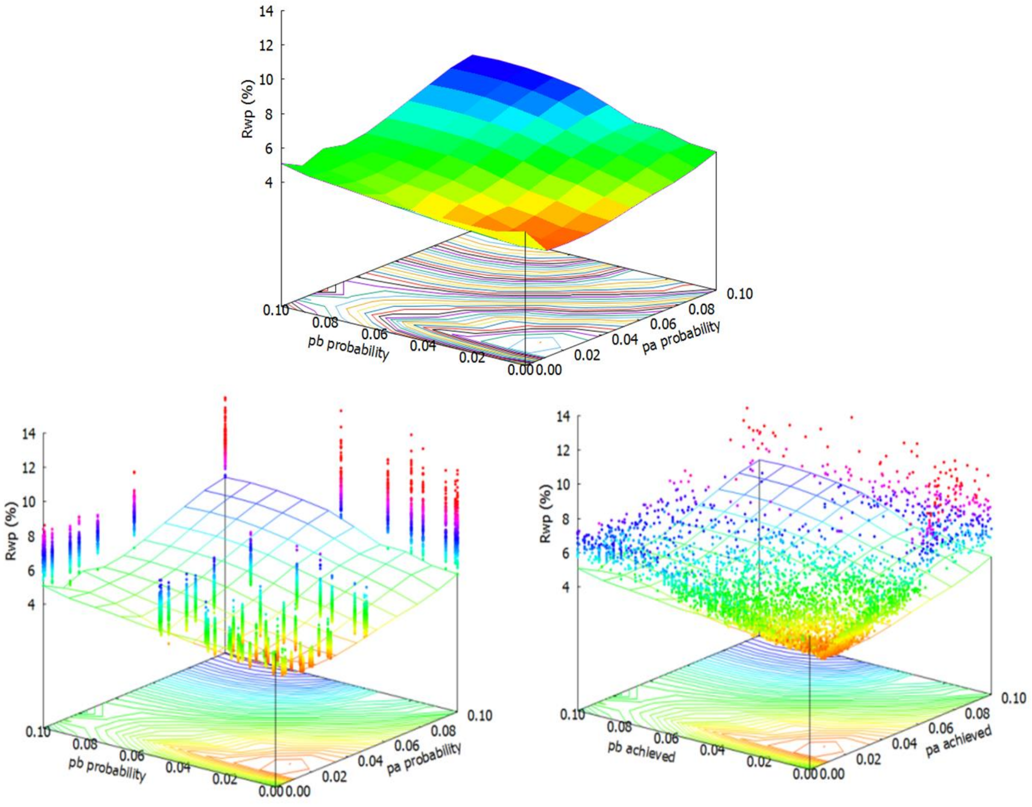

Figure 5.7: R_{wp} surface plot for pa and pb type faults in $La_2O_2Cu_{0.667}Cd_{0.667}Se_2$. Top: R_{wp} plotted is the minimum of 100 stacks with 960 layers each. Bottom Left: R_{wp} of each individual stack plotted with the minimum surface as a guide. Bottom Right: R_{wp} of each individual stack but plotted as a function of the actual number of each type of fault in the stack created with the minimum surface as a guide. Reproduced from Coelho et al.[23]

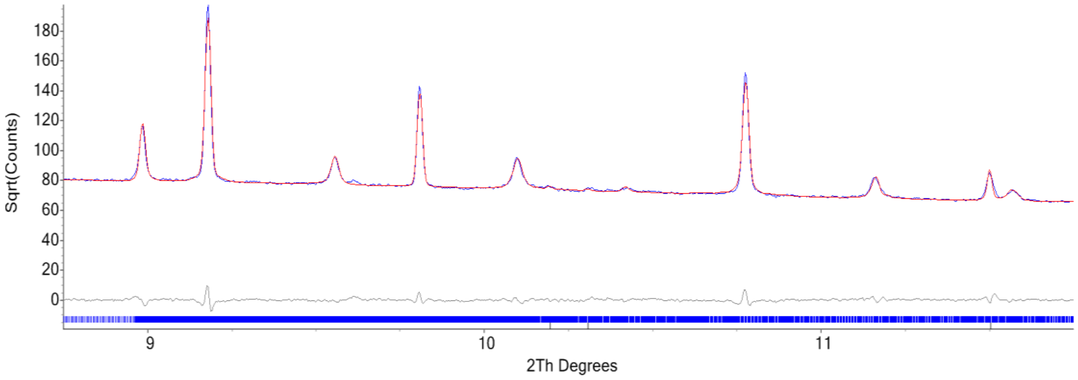

Figure 5.8: Rietveld refinement showing fit to key peaks in synchrotron powder diffraction. View shows fit with 1.6 % *pa* stacking faults (0 % *pb* faults). Reproduced from Ainsworth et al.[11]

5.3.3 Further Methodology Developments

A second, later set of methodology improvements were developed and published in Coelho, Lewis and Evans ("*Averaging the intensity of many-layered structures for accurate stacking-fault analysis using Rietveld refinement*")[23]. My role in this work concerned the development and testing of direct stack generation in TA and the integration of external minimisation algorithms rather than Rietveld calculation speed improvements.

While a single stacked structure gives a reasonable approximation of the collection of crystallites in a powder diffraction experiment, a real sample contains crystallites that will not have an identical distribution or frequency of stacking faults. For this reason it can be helpful to model multiple structures (N_{str}) where each structure is a separate stack generated using the methodology outlined in Figure 5.6. In contrast to the earlier work, all stacks are averaged into a single calculated diffraction pattern and a single Rietveld refinement carried out in TA software. Ordinarily this would require a huge increase in computational work, however, further improvements to the software heavily mitigate this.

Firstly, stacks produced on the basis of a given set of stacking fault probabilities with the same number of layers, are likely to have a similar *c* axis. It is therefore possible to calculate an average intensity for a large number of stacks by calculating only the structure factor for any given *hkl* peak in each stack and convoluting the peak shapes to synthesise the final y_{calc} powder pattern only once. This does require the assumption of an average *c* lattice parameter, and in reality it may vary slightly between stacks due to different *c*-offsets between layers included in the stack. This approach means the time penalty for including N_{str} stacks is much less than N_{str} fold (which would be the penalty if separate diffraction patterns were first calculated and then averaged). In practice we find only a ~ 10 % time penalty for 100 stacks compared to a single stack in simple test examples.

Secondly, a broadening function can be convoluted that spreads out the attributed intensity over the range spanning two *hkl* reflections. This "smooths-out" ripples in intensity calculated for reflections, particularly when N_v is small (i.e. a small *c*-axis) and reflections are well spaced. This permits a reasonable model of the observed data to obtained with lower computational work (lower N_v).

Improvements have also been made to the generation of stacked structures. Stacks are generated directly in TA software using a new algorithm. This is considerably faster and more convenient than the earlier external python scripts. Stacks can also be generated so that the number of faults in a given stack precisely matches the expectation of the probabilities provided by the user. For example, if the probability of an "a" type stacking fault is pa = 0.1 then stacks can be generated that have precisely 10 % "a" type stacking faults rather than a Gaussian distribution of faults centred on 10 % as in the python routine. Figure 5.9 compares the processes at each stage of development.

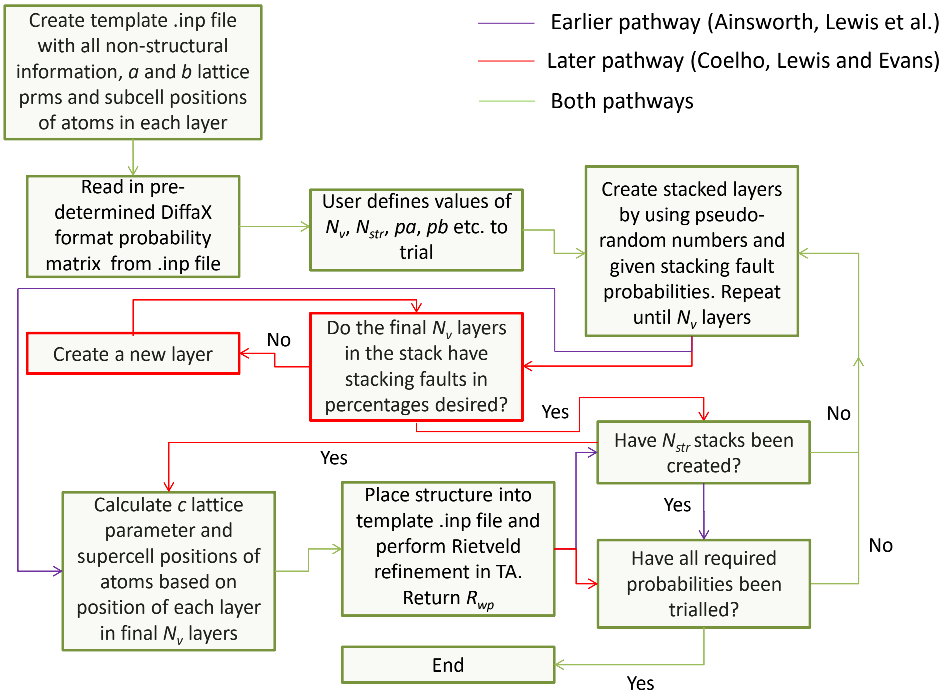

Figure 5.9: Python process for creating and evaluating faulted stacks. Earlier pathway used in Ainsworth, Lewis et al[11] creates individual stacks and performs individual Rietveld refinements. Later pathway used in Coelho, Lewis and Evans[23] performs single Rietveld refinement based on averaged structure of all stacks.

The speed increases mean we have also been able to directly integrate other minimisation algorithms to search for optimal fault probabilities. One successful method was a simple downhill greedy algorithm, which involves starting at a random position in the *pa*/*pb* search space and then incrementally changing parameters and accepting the change if and only if the change results in a reduction in the fitness (measured by R_{wp} here). In our example implementation on the $La_2O_2Cu_{0.667}Cd_{0.667}Se_2$ material discussed above we allow for changes in only one of *pa* or *pb* (selected randomly) in any given step and operate only within the $0 < pa/pb < 0.1$ search space. The degree of change in either *pa* or *pb* in each step decreases linearly from 0.01 to 0 over 100 steps until the algorithm terminates (this is analogous to reducing the simulated temperature in a Monte Carlo approach). Figure 5.10 shows that this simple greedy downhill algorithm could quickly identify the correct *pa* and *pb* type stacking fault probabilities for the $La_2O_2Cu_{0.667}Cd_{0.667}Se_2$ material from any starting point in just a few minutes. More detailed discussion of computational time savings arising from this work and the application to other examples can be found in the paper "Averaging the intensity of many-layered structures for accurate stacking-fault analysis using Rietveld refinement" attached at the end of the thesis.

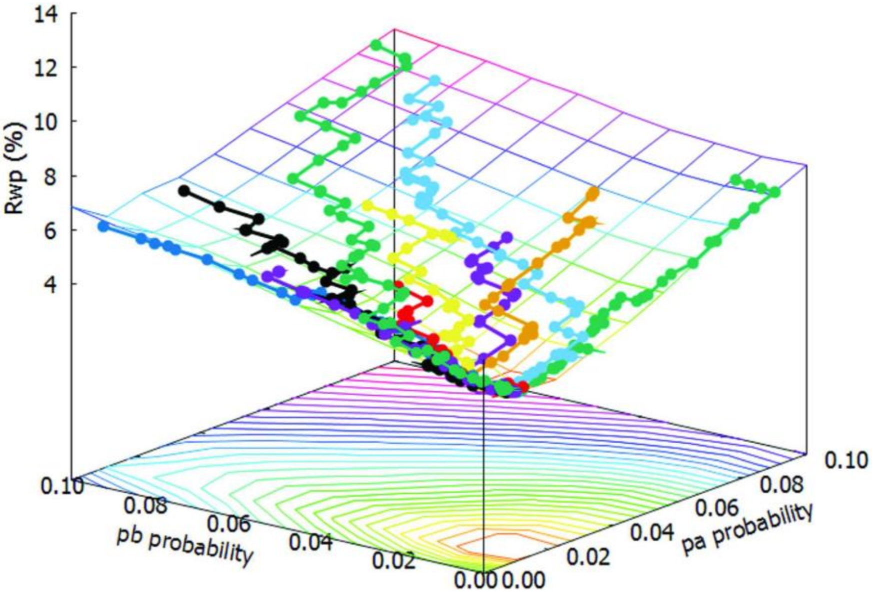

Figure 5.10: Minimisation pathways for *pa* and *pb* using a simple greedy downhill algorithm from 10 random starting points in the range $0 < pa < 0.1$, $0 < pb < 0.1$. The models lie on the same surface as Figure 5.7. Reproduced from Coelho, Lewis and Evans[23].

As an example of the scale of speed improvement offered by the updated methodology, a repeat of the earlier grid search on $La_2O_2Cu_{0.667}Cd_{0.667}Se_2$ using N_v = 960 and N_{str} = 100 (~ 700,000 atoms) was carried out. This is directly comparable to the 100 repeats of N_v = 960 shown in Figure 5.7 and takes just 160 s (compared to 15 hrs) and produces essentially the same minimum R_{wp} surface.

5.4 Sample Preparation and Data Collection

$La_2O_2Cu_{0.667}Mn_{0.667}Se_2$ was synthesised by Chris Ainsworth using stoichiometric quantities of La_2O_3, Cu, Mn and Se. The reagents were intimately ground, sealed in a silica ampoule and heated in a furnace for 12 hours at 1100˚C. A 110 % molar amount of aluminium oxygen getter was used to control oxygen composition. The sample was later reground and heated for a further 12 hours at 1100˚C. Synchrotron X-ray data was collected on the powder diffraction beamline at the Australian Synchrotron in a 0.5 mm capillary using a wavelength of 0.6355792(5) Å and a Mythen microstrip detector over a 2θ range of 2-81˚. The experiment was repeated with a 0.5˚ offset to cover detector gaps and then the data was combined into a single data set.

5.5 Stacking Faults in $La_2O_2Cu_{0.667}Mn_{0.667}Se_2$

In this section we will show how we used this stacking fault methodology to try and model faults in a much more complex new oxychalcogenide material, $La_2O_2Cu_{0.667}Mn_{0.667}Se_2$. This presents a new challenge for the methodology as the complexity of each layer (70 atoms per Mn layer and 80 atoms per Cu layer, both including an adjacent $[La_2O_2]^{2+}$ layer) far exceeds that of the $La_2O_2Cu_{0.667}Cd_{0.667}Se_2$ material (7 atoms per Cd layer and 8 atoms per Cu layer, both including an adjacent $[La_2O_2]^{2+}$ layer, see Figure 5.1). This is because the in-plane structure of $La_2O_2Cu_{0.667}Cd_{0.667}Se_2$ is a simple full corner sharing (1C-0E) while $La_2O_2Cu_{0.667}Mn_{0.667}Se_2$ has 4C-1E units. The structure along the stacking direction follows the sequence $\mathrm{Mn|\underline{Mn}|Cu|\underline{Mn}|Mn|Cu}$ where Mn refers to $[MnSe_2]^{2-}$ layers and Cu to $[Cu_2Se_2]^{2-}$ layers. The underlining indicates an (±*a*/2, ±*b*/2, 0) offset relative to the non-underlined layers. The structure is shown in Figure 5.11.

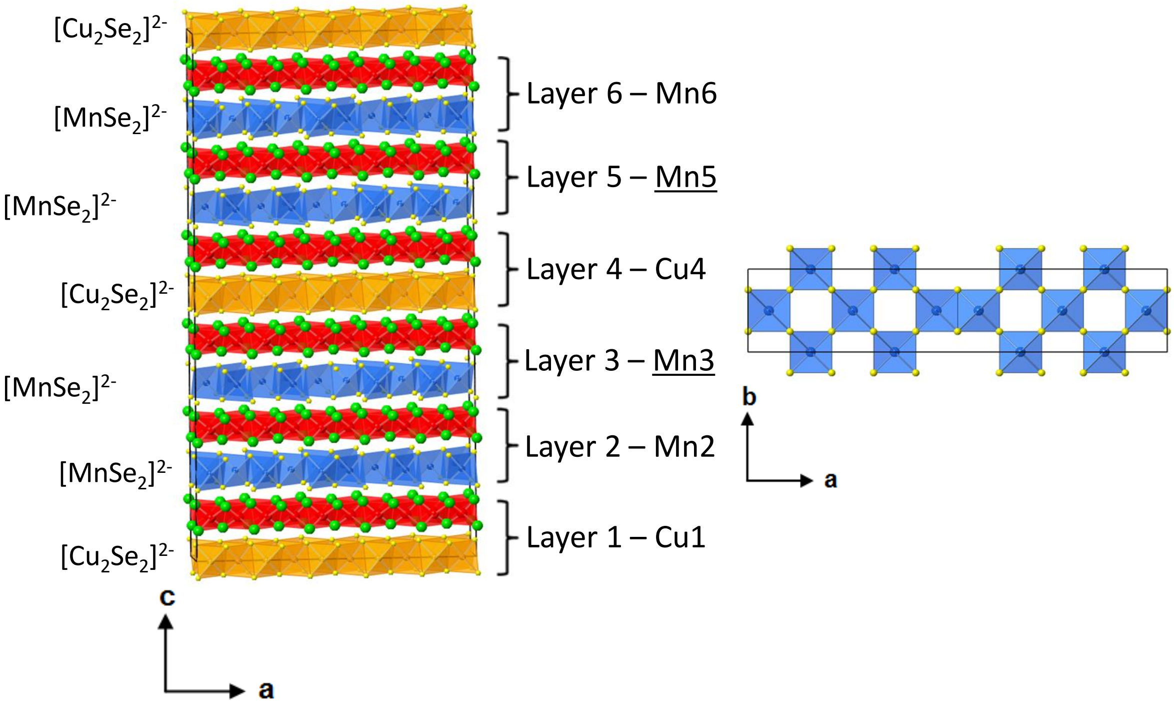

Figure 5.11: Left: Ideal stacking sequence for $La_2O_2Cu_{0.667}Mn_{0.667}Se_2$. Right: 4C-1E structure within $[MnSe_2]^{2-}$ layers. Atom colours: blue – Mn, yellow – Se, orange – Cu, green – La, red – O. Refer to Table 5.2 for how stacking faults change ideal stacking sequence. Reproduced from Ainsworth[12].

A model that accounts for most peaks in the $La_2O_2Cu_{0.667}Mn_{0.667}Se_2$ synchrotron data had already been identified by Chris Ainsworth prior to this work (see Figure 5.12). However some weak 00*l* reflections are calculated where no intensity is observed in the powder diffraction pattern when using the ideal stacking sequence.

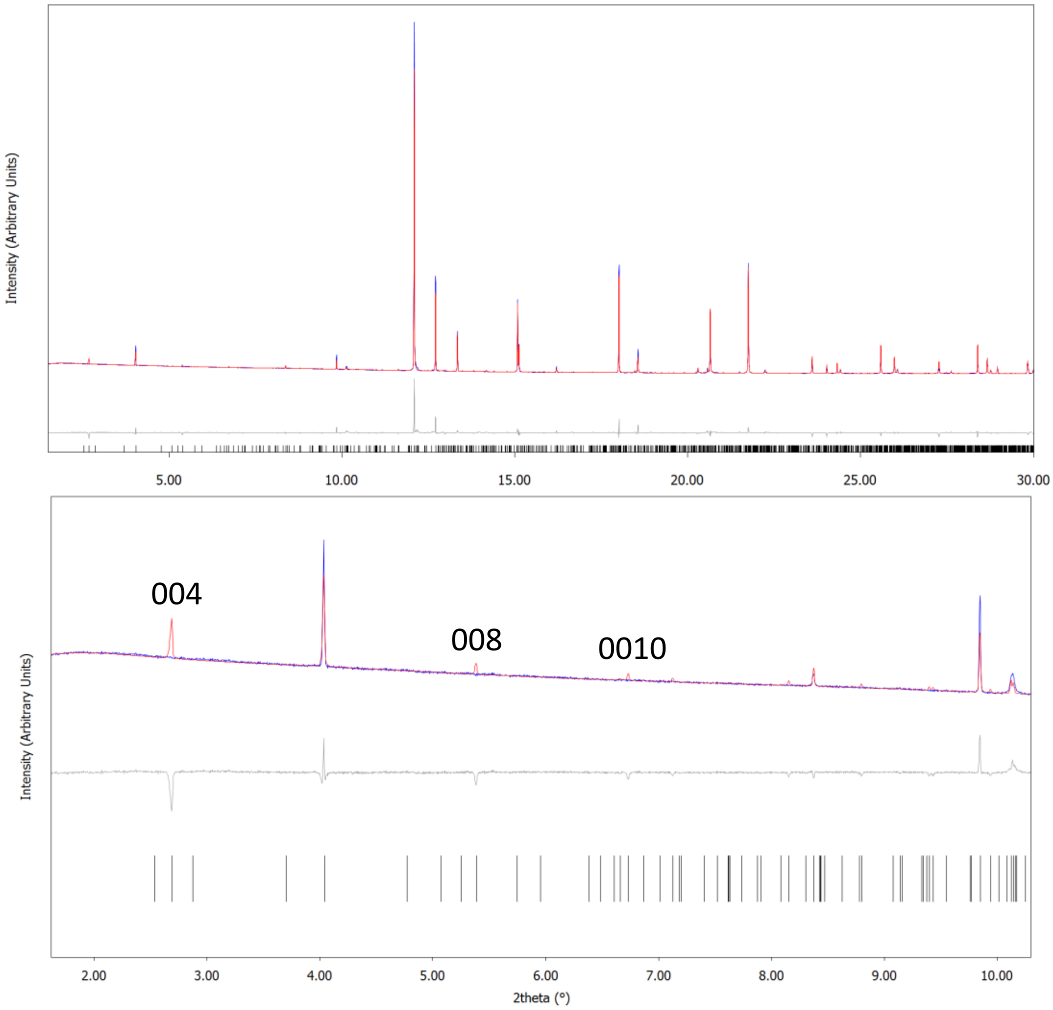

Figure 5.12: Fit to RT $La_2O_2Cu_{0.667}Mn_{0.667}Se_2$ synchrotron X-ray data using ideal 6 layer subcell structure (space group *Ibam*, *a* = 5.74117(5) Å, *b* = 28.6971(2) Å, *c* = 54.0916(3) Å). R_{wp} = 7.42 %, R_{Bragg} = 8.44 %.

One possibility is that these peaks are not observed due to stacking faults and so our stacking fault methodology was tested. As the over-calculated peaks are 00*l* reflections that are completely unobserved, the type of fault involved appears to be the “a” type fault discussed in 5.3.3. Any “b” type faults would not affect 00*l* intensities as they describe only the relative offset of layers in the non-stacking plane.

In addition to overcalculated intensities of 00*l* reflections there are additional small calculated peaks (see Figure 5.13, showing the fit using the subcell model on a logarithmic scale) for which no intensity is observed. There is also significant undercalculated intensity for some subcell peaks as a result of the attempt to minimise the total difference between observed and calculated patterns.

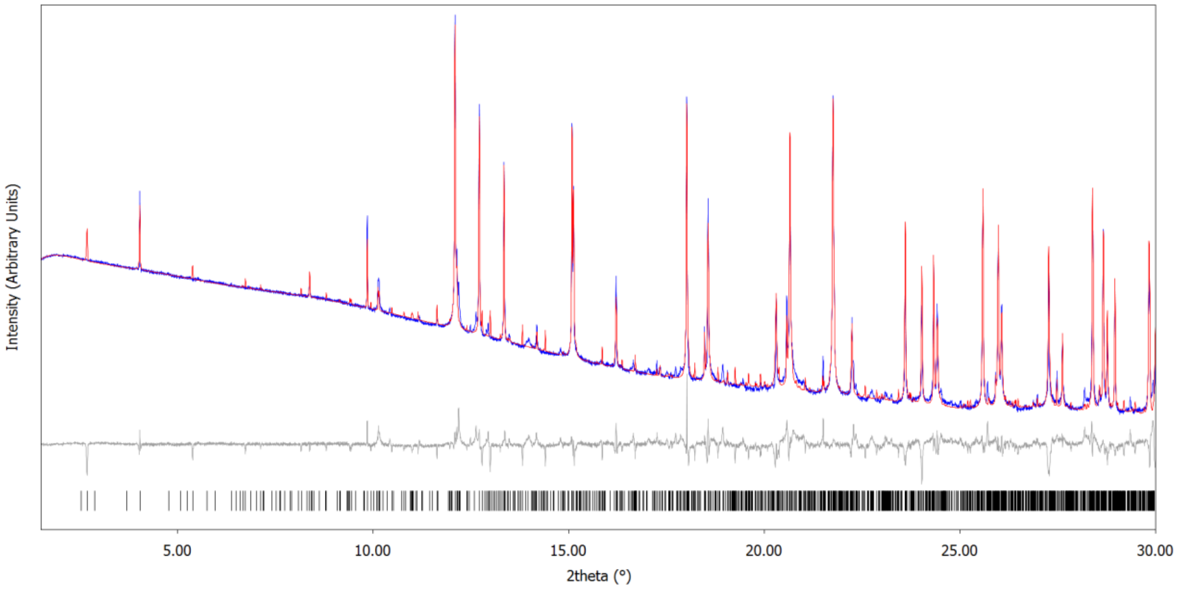

Figure 5.13: Fit to RT $La_2O_2Cu_{0.667}Mn_{0.667}Se_2$ synchrotron X-ray data using ideal 6 layer subcell structure on a logarithmic scale emphasising small intensity peaks that are poorly fit by the existing model.

In this example only "a" type faults which, as previously discussed, result in a local excess of either $[Cu_2Se_2]^{2-}$ or $[MnSe_2]^{2-}$ layers are considered as there is no diffraction evidence to suggest a significant effect of "b" type (stack offset in the *ab* plane) faults on the observed data. Therefore the layer transition probabilities are as given in Table 5.2.

Table 5.2: Probability of transitioning from current layer to all possible other layers in $La_2O_2Cu_{0.667}Cd_{0.667}Se_2$ stacking model.

TO → FROM ↓	**1 – Cu**	**2 – Mn**	**3 – Mn**	**4 – Cu**	**5 – Mn**	**6 – Mn**
1 – Cu	0	1-*pa*	0	*pa*	0	0
2 – Mn	0	0	1-*pa*	0	*pa*	0
3 – Mn	0	0	0	1-*pa*	0	*pa*
4 – Cu	*pa*	0	0	0	1-*pa*	0
5 – Mn	0	*pa*	0	0	0	1-*pa*
6 – Mn	1-*pa*	0	*pa*	0	0	0

Figure 5.14 shows the result of Rietveld refinement of models containing different *pa* fault frequencies. As a result of the complexity of each layer, a stacked model generated by averaging 100 stacks each with 300 layers (N_{str} = 100, N_v = 300, ~ 2,200,000 atoms) lies close to the limit of memory (16 GB) of an ordinary desktop PC in addition to being processor-intensive during refinement. A single Rietveld convergence cycle at each of the 23 trial *pa* values in Figure 5.14 takes ~ 3 hrs.

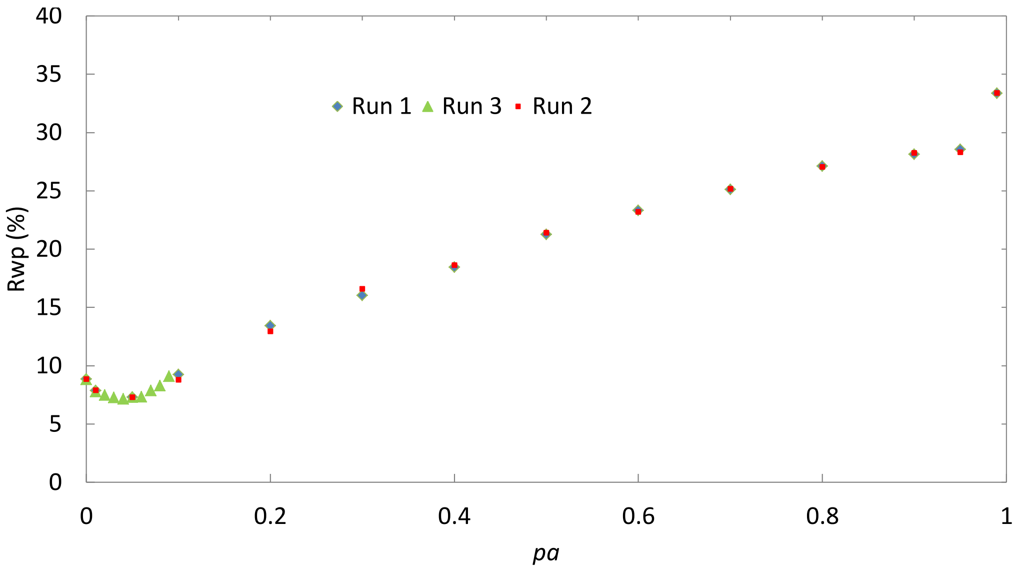

Figure 5.14: R_{wp} obtained from fit to RT $La_2O_2Cu_{0.667}Mn_{0.667}Se_2$ synchrotron X-ray data achieved using N_v = 300 and N_{str} = 100 with varying *pa* type stacking fault probabilities. There is agreement between two repeat runs.

Both runs 1 and 2 agree on how the R_{wp} varies with increasing *pa*. In addition, a third run showing how "a" faults affect the fit in the important $0 < pa < 0.1$ region is shown. Initially R_{wp} decreases on the addition of stacking faults up to $pa = 0.04$ (4 % faults, $R_{wp} = 7.16$ %). The fit then deteriorates as a larger number of *pa* type faults are included, particularly at very high values of *pa* where stacks consist of large separated domains of Cu and Mn layers with few Cu|Mn neighbours. Due to the different layer thicknesses of Cu and Mn layers this leads to an incorrect prediction of the position of peaks in the pattern, with different regions within the stack being significantly larger (excess Cu layers) or smaller (excess Mn layers) in the stacking direction. The routine starts to become unstable very close to $pa = 1$ as stacks consist almost entirely of repeats of the same layer and it becomes difficult to protect the stoichiometry of the stack.

Figure 5.15 shows the fit provided by each model with $0 \leq pa \leq 0.1$. The over-calculation of 00*l* reflections is significantly reduced with 4 % faults (the maximum calculated intensity of the subcell 004 reflection relative to the background is 20 % of that calculated by the unfaulted model). By $pa = 0.1$ (10 % faults, $R_{wp} = 8.80$ %) nearly all intensity from over-calculated 00*l* peaks has been removed (4 % of maximum intensity for the subcell 004 reflection remains, which is comparable to the experimental noise). However this model offers a worse fit overall because the calculated intensity of other reflections begin to deviate more from the observed intensity as 6 layer units within the stack become irregularly sized.

Increasing N_v and N_{str} may help to average out these effects but they are computationally inaccessible on an ordinary desktop PC.

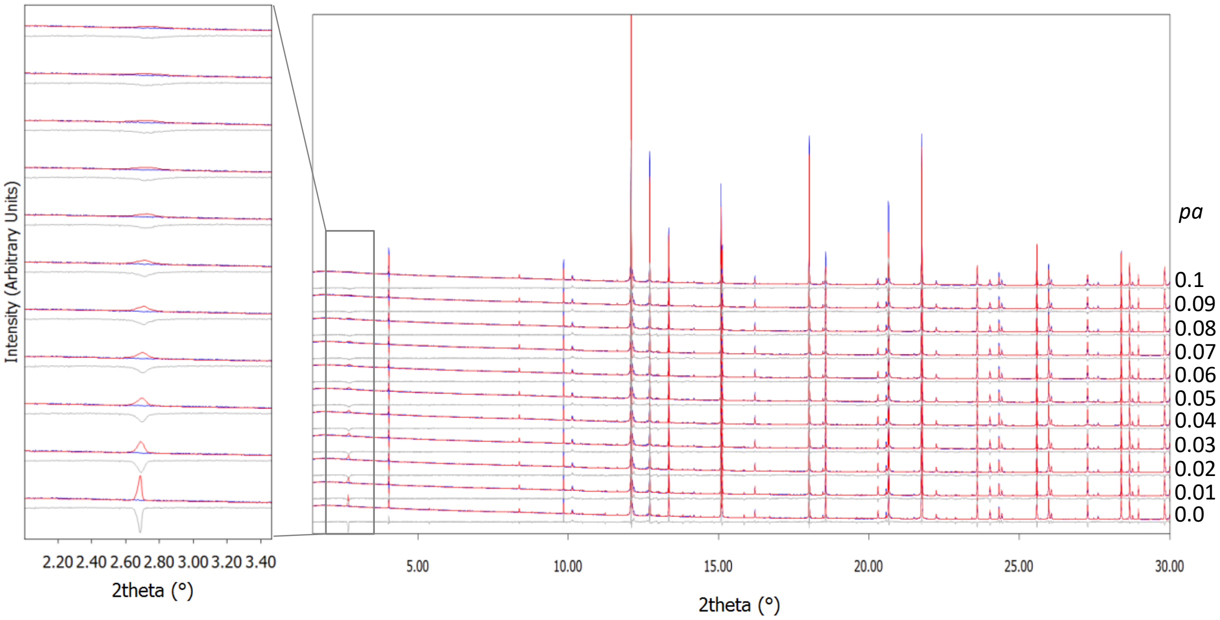

Figure 5.15: Fit to RT $La_2O_2Cu_{0.667}Mn_{0.667}Se_2$ synchrotron X-ray data achieved using N_v = 300 and N_{str} = 100 with varying *pa* type stacking fault probabilities. Right panel shows full 2θ range while left panel focuses on 004 reflection of the 6 layer subcell at ~ 2.7° 2θ.

Using a very broad peaks buffer, which significantly reduces computational time by collating similar peak shape calculations together, and restricting the model to N_v = 120, N_{str} = 100, a Stephens[24] peakshape can be incorporated into the 4 % and 10 % fault models to attempt to describe *hkl* dependent strain broadening in the subcell. This also requires multiple Rietveld cycles in order to have the best chance of finding the global minimum for these parameters. Each Rietveld iteration takes, on average, ~ 7.5 minutes and refinements below are based on ~ 9 hour refinements of each model allowing 10 Rietveld refinement cycles. It is not possible to be sure that the 7 additional parameters have found their global minimum value. Figure 5.16 and Figure 5.17 show the fit obtained for the 4 % and 10 % fault models including a Stephens type peakshape. The logarithmic scale allows a comparison of the overcalculated 00*l* intensities relative to the other anomalies in the fit.

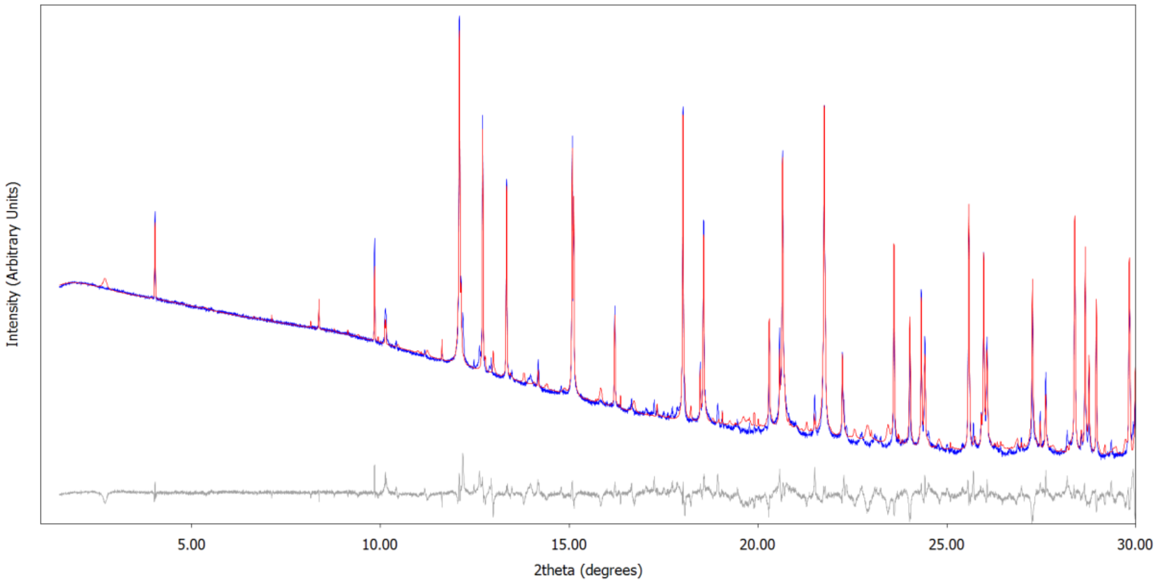

Figure 5.16: Fit to RT La$_2$O$_2$Cu$_{0.667}$Mn$_{0.667}$Se$_2$ synchrotron X-ray data achieved using N_v = 300 and N_{str} = 100 with 4 % *pa* type stacking faults. R_{wp} = 6.99 %

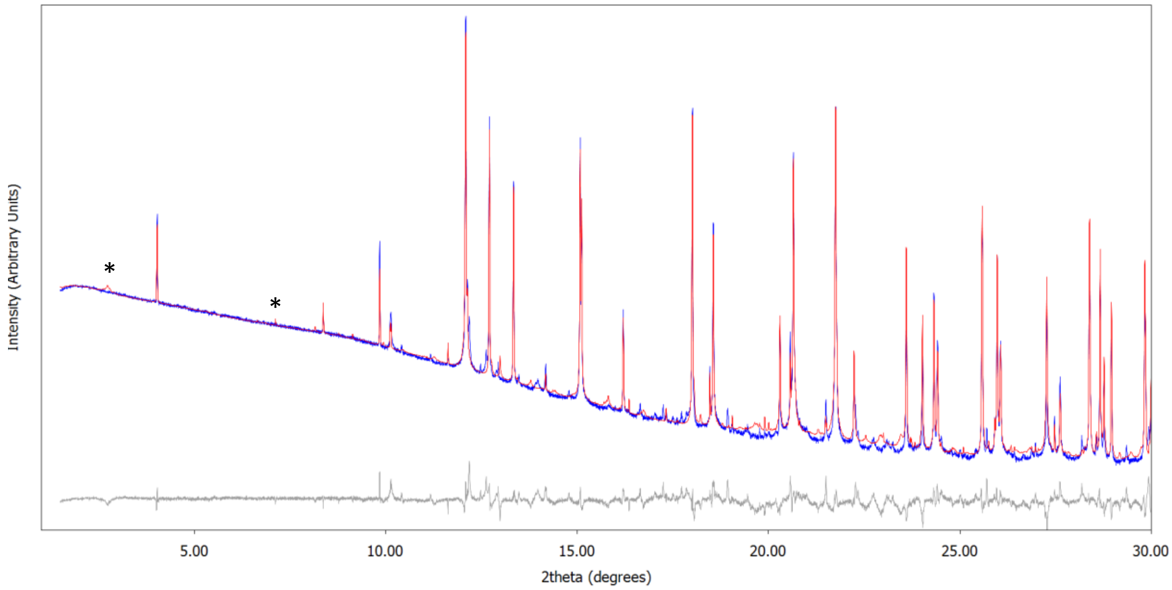

Figure 5.17: Fit to RT La$_2$O$_2$Cu$_{0.667}$Mn$_{0.667}$Se$_2$ synchrotron X-ray data achieved using N_v = 300 and N_{str} = 100 with 10 % *pa* type stacking faults. R_{wp} = 6.82 %

The fact that 10 % *pa* stacking faults offers a slightly better fit in R_{wp} terms than 4 % faults when a Stephens type peakshape is included may suggest that the true level of stacking faults is closer to 10 %. It is difficult however to make precise conclusions due to the computational limitations and the uncertainty of optimal convergence when the calculated intensity of 00*l* reflections is reduced to a level similar to that of other discrepancies in the final model. Even at 10 % *pa* stacking faults the above Stephens fit still has visible intensity calculated for 004 and 008 reflections (marked by a star) where none is observed. It appears that it is not possible to further reduce the intensity of these reflections with a larger number of stacking faults without reducing the quality of the fit to other poorly modelled reflections such that the addition of faults makes the overall fit worse in R_{wp} terms.

It is therefore only possible to conclude that stacking faults are likely to be present in RT $La_2O_2Cu_{0.667}Mn_{0.667}Se_2$ and that they may be modelled using our stacking fault methodology despite the structural complexity. Further work is required to present a definitive structure description of this material.

5.6 Low Temperature Magnetic Ordering in Oxychalcogenides

Magnetic materials are of interest for a range of applications. This section discusses oxychalcogenides that show magnetic ordering as they contain one or more sites with at least one unpaired electron. This section discusses two materials, $(Ce_{0.78}La_{0.22})_2O_2MnSe_2$ and $Ce_2O_2Fe_{0.75}Zn_{0.25}Se_2$ in which Mn^{2+} ($3d^5$) and Fe^{2+} ($3d^6$) (both high spin) order magnetically at low temperature. The *Ln* site Ce^{3+} ($4f^15d^1$) may also order although the magnetic moments arising from the $4f^1$ of Ce^{3+} is expected to be lower than that from the transition metals.

When materials order magnetically the magnetic distortion is typically described by a single irrep. This is because second-order magnetic phase transitions on cooling typically energetically favour distortions that can be described with related vectors for any k-point and so the symmetry of the low temperature structure can usually be described without the need to superpose irreps. The use of the distortion mode basis, generating magnetic distortion modes in ISODISTORT[25], opens up the possibility of using search algorithms to identify the irrep that is responsible for the magnetic distortions in these materials in a similar fashion to the work with displacive and rotational distortion modes. As the complex superposition of irreps often needed to describe displacive or rotational distortions is not likely, a simplification of our earlier search methodology that treats irreps rather than individual modes as the “on/off” attributes of each model was developed. This is described further in 5.8.1.

We first show how these methods can be applied to derive the previously known low temperature magnetic structure of $(Ce_{0.78}La_{0.22})_2O_2MnSe_2$ and then how the low temperature magnetic ordering of $Ce_2O_2Fe_{0.75}Zn_{0.25}Se_2$ can be determined for the first time using a GA or inclusion type search.

5.7 Experimental

$(Ce_{0.78}La_{0.22})_2O_2MnSe_2$ was synthesised by Dr Chun-Hai Wang using stoichiometric quantities of La_2O_3, CeO_2, Mn and Se. The materials were sealed in a silica tube with a 105 % molar amount Ti oxygen getter to control the oxygen composition. The tube was then evacuated to $<10^{-2}$ mbar and heated to 600˚C for 24 hrs followed by 1000˚C for 48 hrs. The samples were reground before again heating to 1000˚C for 48 hrs. TOF neutron powder diffraction data was collected on GEM at the ISIS spallation source. The sample was loaded into an 8 mm vanadium can and neutron scattering data was collected over d ~ 0.18-36 Å across all 6 detector banks at RT for 2 hrs and 30 K for 3.5 hrs.

$Ce_2O_2Fe_{0.75}Zn_{0.25}Se_2$ was synthesised by Chris Ainsworth using stoichiometric quantities of CeO_2, Fe, Zn and Se. The materials were intimately ground and heated in a furnace for 12 hours at 1100˚C. A 110 % molar amount aluminium oxygen getter was used to control oxygen composition. The sample was later reground and heated for a further 12 hours at 1100˚C. TOF neutron powder diffraction data was collected on GEM. The sample was loaded into a 6 mm vanadium can and neutron scattering data was collected on all detectors covering over d ~ 0.18-36 Å at RT for 2 hrs, 10 K for 2.5 hrs and for 5 mins in ~ 10 K steps between 10 K and 255 K.

5.8 Magnetic Ordering in $(Ce_{0.78}La_{0.22})_2O_2MnSe_2$: A Test Case

The low temperature magnetic structure of $(Ce_{0.78}La_{0.22})_2O_2MnSe_2$ was previously determined[10] in magnetic space group (Shubnikov group) 62.455 (P_cnma) with Mn^{2+} spins arranged antiferromagnetically within each layer with moments of equal magnitude (4.12(1) μ_B) pointing along the stacking direction (unusually the a direction in this Shubnikov setting). Mn^{2+} positions in successive layers (v1 and v2 in Figure 5.17b) are offset from each other along the stacking direction. Ce^{3+} moments are also all equal (0.85(1) μ_B) and are aligned in the plane of the layers. Those lying close to an edge sharing $MnSe_4$ are aligned directly along the a axis while those close to a corner sharing $MnSe_4$ are aligned at 45˚ to it and are oppositely aligned to neighbouring 45˚ Ce^{3+} moments. Figure 5.18 shows the magnetic structure viewed from the side of the layers and looking directly down the stacking axis.

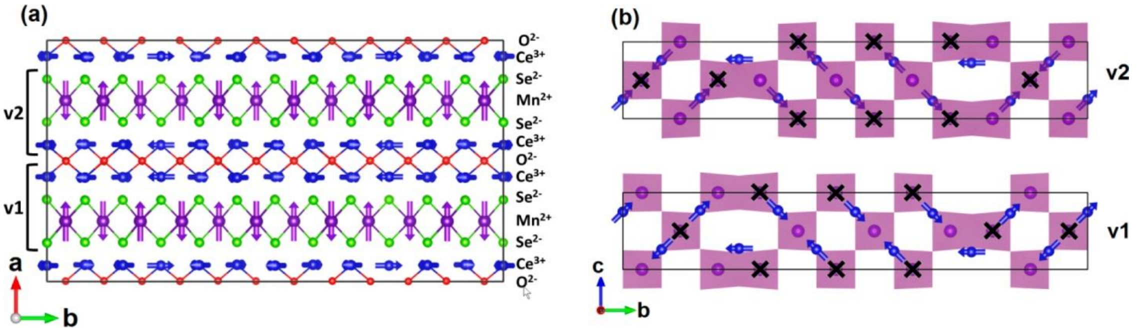

Figure 5.18: Magnetic structure of $(Ce_{0.78}La_{0.22})_2O_2MnSe_2$ viewed a) perpendicular to the layers showing Mn^{2+} moments (purple) aligned antiferromagnetically and b) in the plane of the layers showing Ce^{3+} moments (blue) with Mn^{2+} moments out of the plane (circles) or into the plane (crosses). Reproduced from Wang et al[10].

The distortion is driven by a mY_2^- irrep that allows up to 15 magnetic distortion modes (9 Ce^{3+}, 6 Mn^{2+}) but, due to the equal magnetic moments and their parallel alignment, just two independent amplitudes are needed (1 Ce^{3+}, 1 Mn^{2+}). The following section explains how we can reproduce this result using the GA and inclusion search methods that were introduced in Chapter 2.

As all the magnetic peaks observed in the low temperature model can be modelled using the RT nuclear unit cell, there is no need to consider a larger unit cell. However, a formulaic approach (required as a first step for both GA and inclusion searches discussed below) to magnetic structure solution dictates that, if this was unknown, the correct cell should be established. A *P1* Pawley fit, which models only the unit cell and not a structure by automatically matching the intensity of peaks to the data, would be carried out. This establishes that a good fit to the low temperature data is possible using the proposed cell as long as the structure is of sufficiently low symmetry. In the present example, by reducing the symmetry of the nuclear-only RT *Cmca* structure to magnetic space group 1.1 (*P1*), no assumptions are made about the magnetic symmetry ahead of either a GA or inclusion type search. It is therefore likely the magnetic peaks can be modelled by a structure that lies within the search space of all models with symmetry between the *Cmca* parent (the RT structure) and *P1* child. Appendix 16 provides a step-by-step guide on how to obtain this model in ISODISTORT. The resulting child structure has 216 magnetic modes amongst which there are 16 unique irreps available (see e-Appendix 14 for a full list).

5.8.1 GA Approach

The first magnetic structure search approach discussed here is a GA. In this case instead of each of the 216 available magnetic modes being a changeable attribute of each candidate model in the GA, the irreps are the attributes. This means that all magnetic distortion modes belonging to an irrep will either be “on” or all will be “off”, using the fact that magnetic distortions can typically be modelled by a single irrep. This means that the GA contains just 16 independent bits each related to one of the 16 available irreps in the child model. This leads to a significant reduction in the number of possible models within the search space from 2^{216} to just 2^{16}. Our GA infrastructure is capable of activating this operation mode by a simple True/False switch in the control file. Furthermore, the concept of block crossover is no longer relevant as the exchange of groups of attributes (i.e. irrep blocks in the Chapter 2 implementation) between two mating individual models will be handled by the bit crossover process (as irreps are the individual attributes in this implementation). The GA otherwise operates as described in Chapter 2. As was the case there, the number of iterations per evaluation used a criterion based on the number of active distortion modes, not irreps. We consistently find this is sufficient for repeated convergence to what appears to be the global minimum when the number of active modes is low.

To perform the magnetic structure determination we chose to use bank 3 GEM data between 3.9-17 ms (1.38-6.04 Å), which contains 5 clearly identifiable magnetic Bragg peaks not modelled by the RT structure (Figure 5.19). Bank 3 represents a good compromise between covering a sufficient *d*-spacing range to incorporate observed magnetic peaks in the LT data and high resolution.

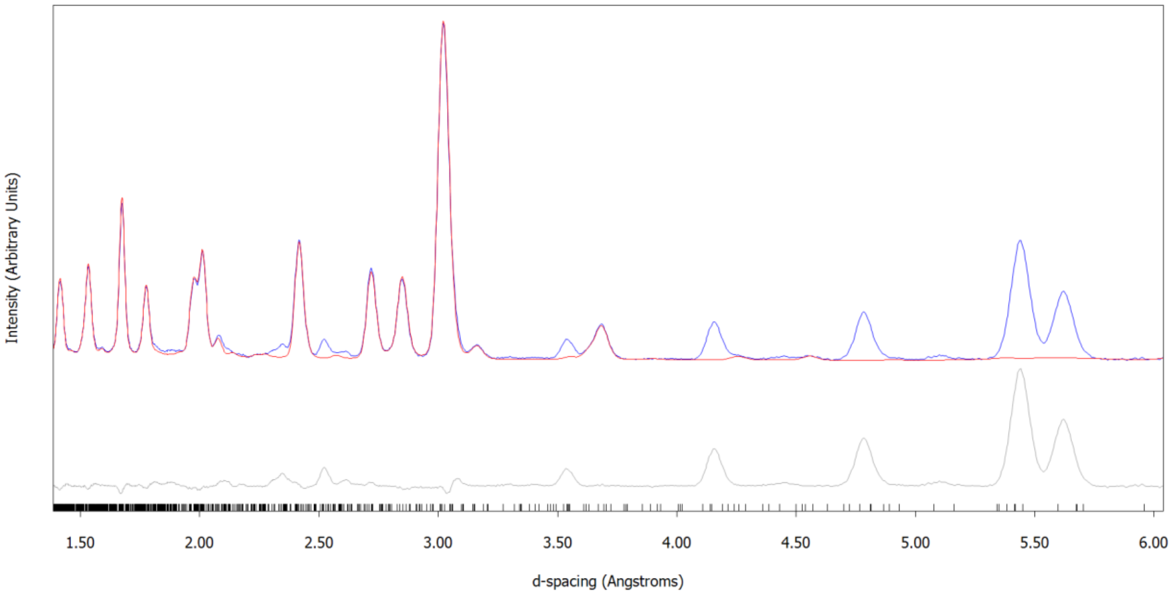

Figure 5.19: Fit to $(Ce_{0.78}La_{0.22})_2O_2MnSe_2$ bank 3 GEM data at 30 K using RT *Cmca* model. The most notable peaks resulting from magnetic ordering are at d ~ 5.6 Å, 5.5 Å, 4.8 Å, 4.2 Å and 3.5 Å. R_{wp} = 15.18 %, R_{Bragg} = 1.57 %.

The first check must be that the child model has the required parameters available to it to fit the data implying that a model with the correct magnetic symmetry should lie within the search space. Figure 5.20 shows this is the case for the magnetic space group 1.1 child model. Non-distortion mode parameters can be extracted from this fit and retained throughout the refinement of all possible models considered in the search in order to save computational work.

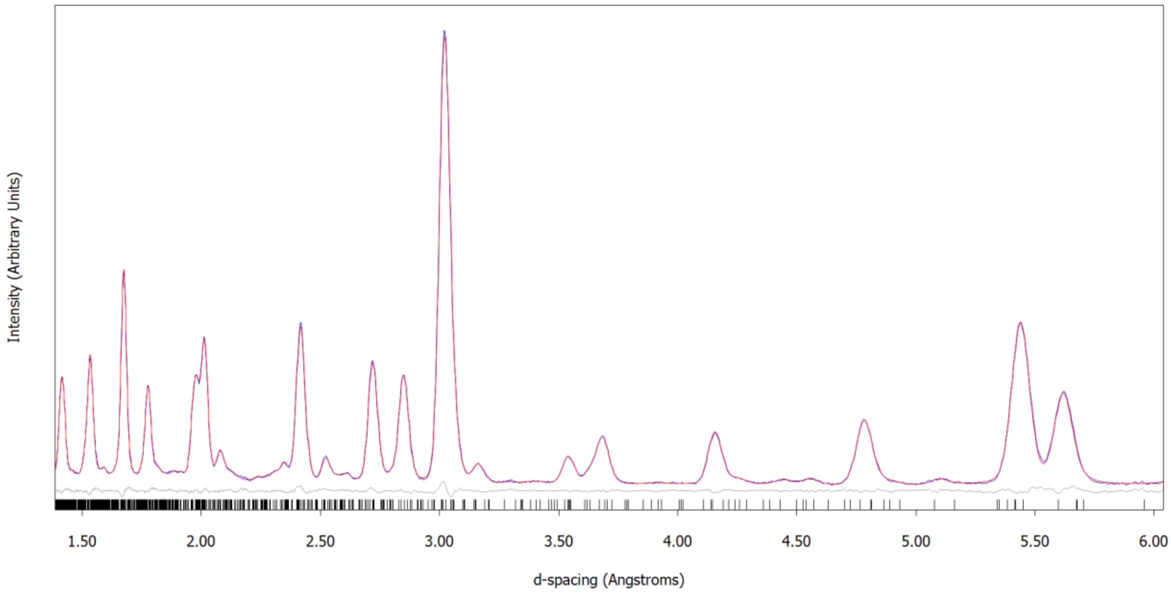

Figure 5.20: Fit to $(Ce_{0.78}La_{0.22})_2O_2MnSe_2$ bank 3 GEM data at 30 K in magnetic space group 1.1. *a* = 5.675(4) Å, *b* = 18.155(4) Å, *c* = 34.07(2) Å, *α*, *β*, *γ* = 90˚. R_{wp} = 1.46 %, R_{Bragg} = 0.45 %

As before, it is helpful to normalise the R_{wp} term of the fitness function against the best fit obtainable. The fitness function is still as given by Equation 2.1 with the variation that *n* now refers to the number of active irreps and *p* refers to the penalty per irrep (rather than per mode). R_{wp}(min) = 1.6 % is used on the basis of reasonable preliminary *P1* child model. A range of *p* values were trialled and Figure 5.21 shows the irreps activated in the model chosen by the GA.

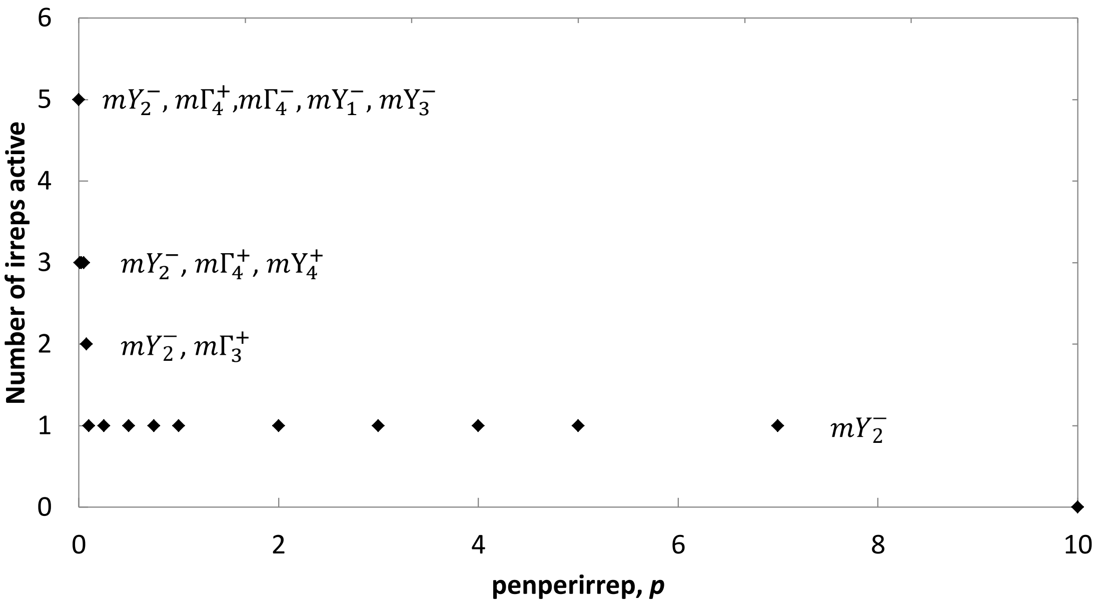

Figure 5.21: Number of irreps identified as active by GA with varying *p*.

Initially when p is set very high (≥10) no irreps give a sufficient improvement in the fit to the data to overcome the penalty. Once p is reduced to 7 the mY_2^- irrep becomes active and it is not until p is much smaller (≤0.075) that additional irreps become active. While the particular range of p for which a single irrep is the best model is dependent on the choice of R_{wp}(min), the fact the range is broad is excellent initial evidence that the distortion is driven by just this one irrep. Reductions in R_{wp} resulting from irreps after the first are small (see Table 5.3) and as such p dominates the changes to the fitness in the $n \geq 2$ region. The process may not (and does not need to) reliably identify the correct irreps for $n \geq 2$. In the $n = 1$ region the best model is found 100 times out of 100 using our 10 minute termination criteria.

Table 5.3: R_{wp} achieved by best 0, 1, 2, 3 and 5 irrep models identified by the GA.

Number of Irreps	Active Irreps in best model	R_{wp} (%)
0	None	15.18
1	mY_2^-	1.70
2	$mY_1^+, m\Gamma_3^+$	1.57
3	$mY_2^-, m\Gamma_4^+, mY_4^+$	1.47
5	$mY_2^-, m\Gamma_4^+, m\Gamma_4^-, mY_1^-, mY_3^-$	1.45

We did not invest significant time in optimising GA parameters for this approach. For comparative purposes (all times are for 6th generation i7, 3.4 GHz), the best irrep was identified most quickly when $p = 2$ (in ~ 34 s on average) while the record across all runs was ~ 5 s. The time taken to complete each repeat of the full sweep of p values shown in Figure 5.21, including the (overkill) 10 minute wait period after identifying the best model, was ~ 4 hrs.

Figure 5.22 shows that the fit provided by mY_2^- modes alone is as good as that provided by all available irreps (Figure 5.20) and is significantly better than the fit provided by no magnetic distortions (Figure 5.19).

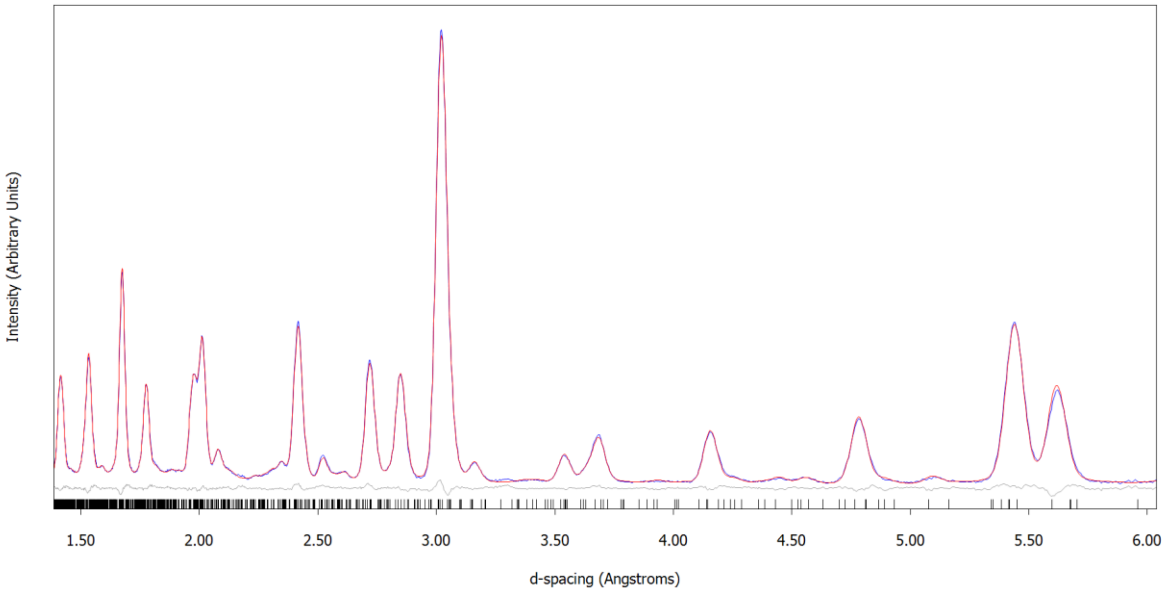

Figure 5.22: Fit to $(Ce_{0.78}La_{0.22})_2O_2MnSe_2$ bank 3 GEM data at 30 K using magnetic space group 1.1 model with only mY_2^- modes active. R_{wp} = 1.70 %, R_{Bragg} = 0.78 %.

Once the mY_2^- irrep has been identified as driving the phase transition the true magnetic space group can be directly determined to be 62.455. This can be done be loading the resulting structure into the FINDSYM tool and using the default magnetic moment tolerance of 0.001 μ_B. Alternatively the magnetic space group can be determined by directly superposing the mY_2^- onto the parent structure using ISODISTORT and following the instructions in Appendix 17.

On inspection of the distortion mode amplitudes it is clear that many have the same or related amplitudes and, as we knew from the model of Wang et al., only 2 DOF are in fact required. However, the purpose of this type of search is to identify the correct magnetic space group symmetry of the material and not to reveal how the available DOF in that symmetry are used. A complete tutorial with step-by-step instructions for setting up, running and analysing this GA is available in Appendix 18.

5.8.2 Simple Inclusion Approach

As there are just 16 irreps available it is also relatively simple to try each irrep available to the P1 child model in turn. If the best irrep is selected and all remaining irreps are trialled in conjunction with it, then this is equivalent to the first two rounds of an inclusion search as explained in Chapter 2. Figure 5.23 shows the results of this approach.

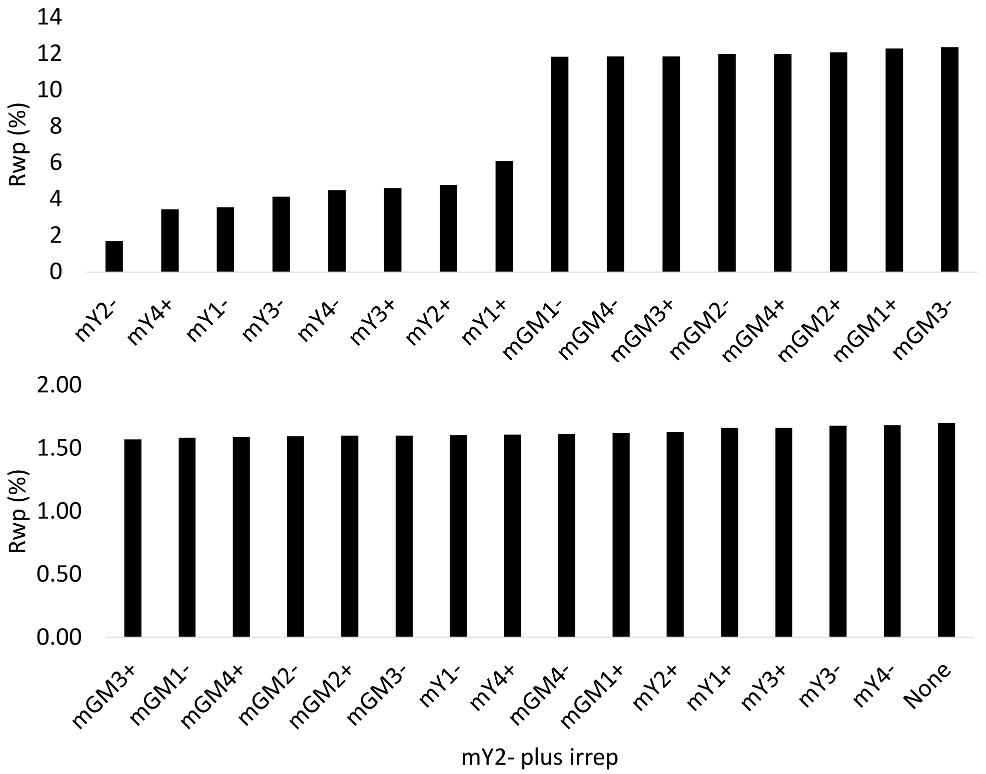

Figure 5.23: Top: R_{wp} achieved by each of 16 available irreps individually fitting LT $(Ce_{0.78}La_{0.22})_2O_2MnSe_2$ bank 3 GEM data at 30 K. Bottom: R_{wp} achieved when a second irrep is used in addition to mY_2^-. "None" indicates the R_{wp} of the mY_2^- alone.

We again conclude that mY_2^- alone is the best possible model. It provides the best fit to the diffraction peaks not modelled by the RT structure and any additional irreps provide only a negligible improvement in the fit. As the improvement has already become negligible at this point there is no need for any further inclusions. From this point the correct symmetry has been identified (as discussed above) and the only remaining task is to identify the two DOF required from the 15 available magnetic modes. This two-step process takes ~ 20 mins to the point of realising that the mY_2^- irrep alone is the best model.

5.9 Magnetic Ordering in $Ce_2O_2Fe_{0.75}Zn_{0.25}Se_2$

Similar approaches to those discussed above have been applied to the previously unsolved magnetic structure of $Ce_2O_2Fe_{0.75}Zn_{0.25}Se_2$. Previous work by Chris Ainsworth[12] has identified the RT structure to be *Bmab* (*a* = 22.74948(10) Å, *b* = 5.69246(3) Å, *c* = 17.63155(6) Å). However, there are several additional peaks in the low temperature data that are not accounted for by this model. Figure 5.24 shows the bank 3 data (2-18 ms, 0.71-6.40 Å) which provides a good compromise between resolution and including key magnetic peaks.

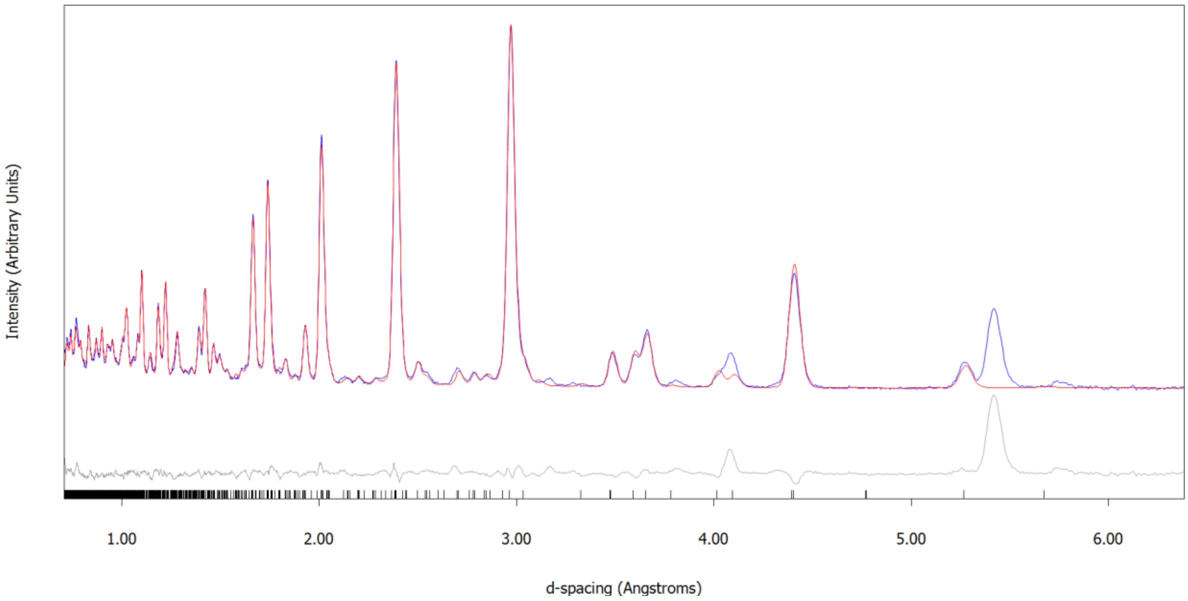

Figure 5.24: Fit to $Ce_2O_2Fe_{0.75}Zn_{0.25}Se_2$ bank 3 GEM data at 10 K using RT model. Peaks arising from magnetic ordering are not fit by this model. R_{wp} = 7.39 %, R_{Bragg} = 2.04 %.

A *P1* Pawley fit using the nuclear unit cell will fit all the additional magnetic peaks (Figure 5.25) and so there is no need for an increase in the size of the unit cell to account for magnetic ordering. The symmetry can be reduced to magnetic space group 1.1 (*P1*) following the earlier methodology (Appendix 16). There are 144 available magnetic distortion modes belonging to 16 unique irreps (see e-Appendix 15 for a full list). The child model clearly has sufficient parameters available to fit the LT diffraction data (Figure 5.26), suggesting that the true magnetic structure is within the search space and giving R_{wp}(min) ~ 3 % for our GA search. This fit also provides values for structural (excluding the magnetic distortion modes) and non-structural parameters allowing us to avoid refining these parameters during the search processes.

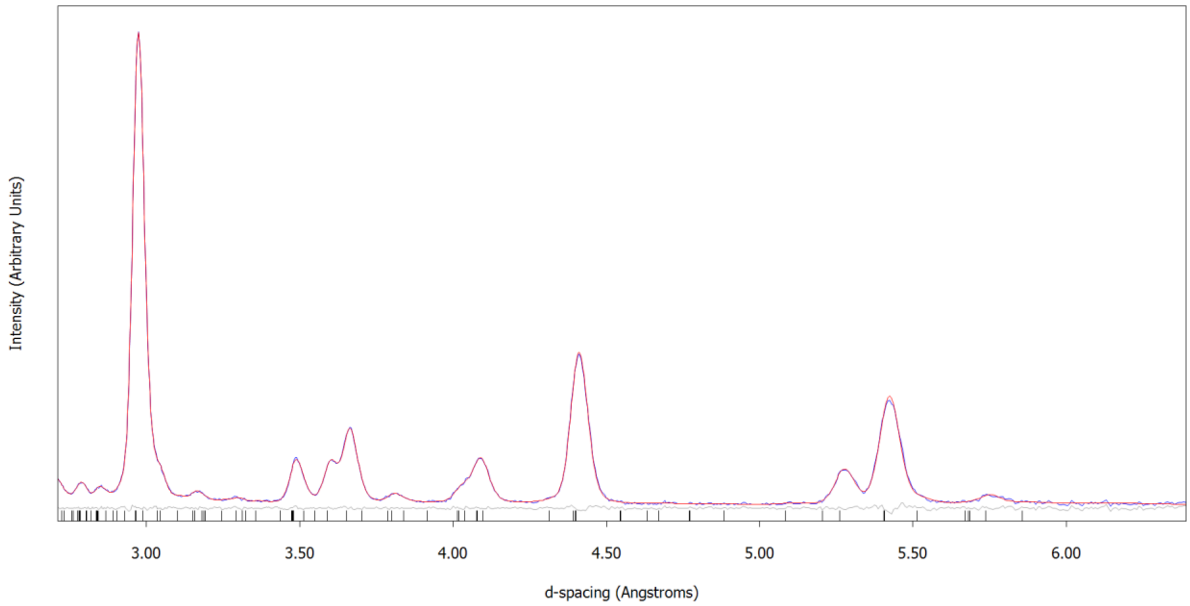

Figure 5.25: Pawley fit $Ce_2O_2Fe_{0.75}Zn_{0.25}Se_2$ bank 3 GEM data at 10 K using RT nuclear unit cell in space group *P1*. The cell is able to model the LT magnetic peaks correctly.

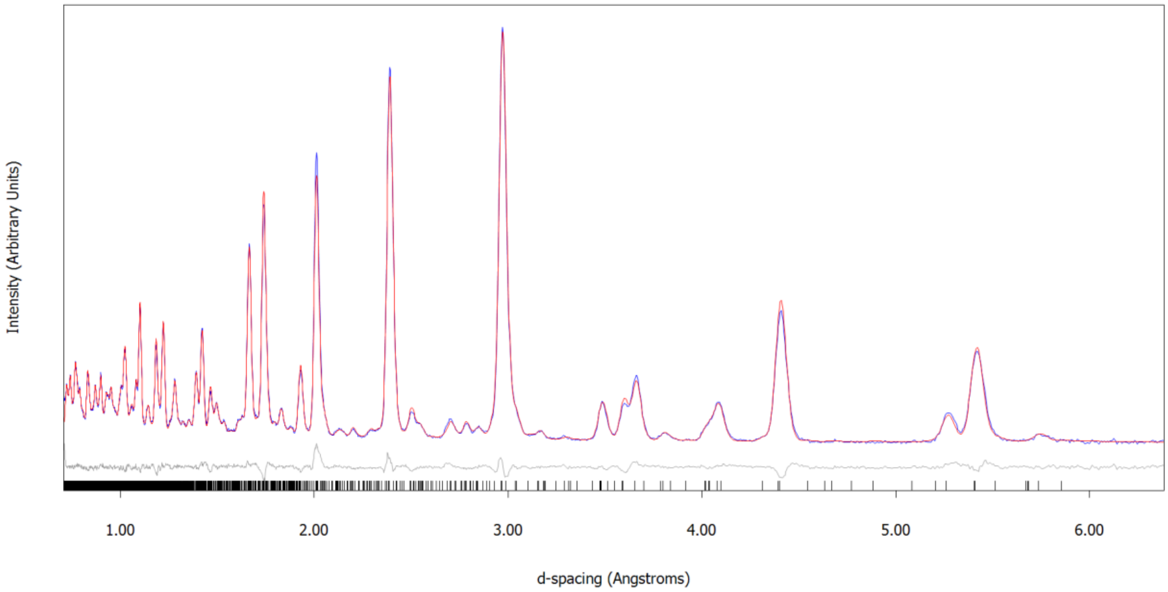

Figure 5.26: Fit to $Ce_2O_2Fe_{0.75}Zn_{0.25}Se_2$ bank 3 GEM data at 10 K using all available magnetic distortion modes in magnetic space group 1.1. *a* = 17.5689(14) Å, *b* = 5.6839(14) Å, c = 22.721(5) Å, α, β, γ = 90˚, R_{wp} = 3.14 %, R_{Bragg} = 1.87 %. The fit which contains all parameters used is given in e-Appendix 16.

5.9.1 GA Approach

A sweep through values of *p* shows the relative importance of different irreps in fitting the data. The irreps active as *p* varies are shown by Figure 5.27. As in the $(Ce_{0.78}La_{0.22})_2O_2MnSe_2$ case, multiple runs repeatedly found the same low fitness minimum.

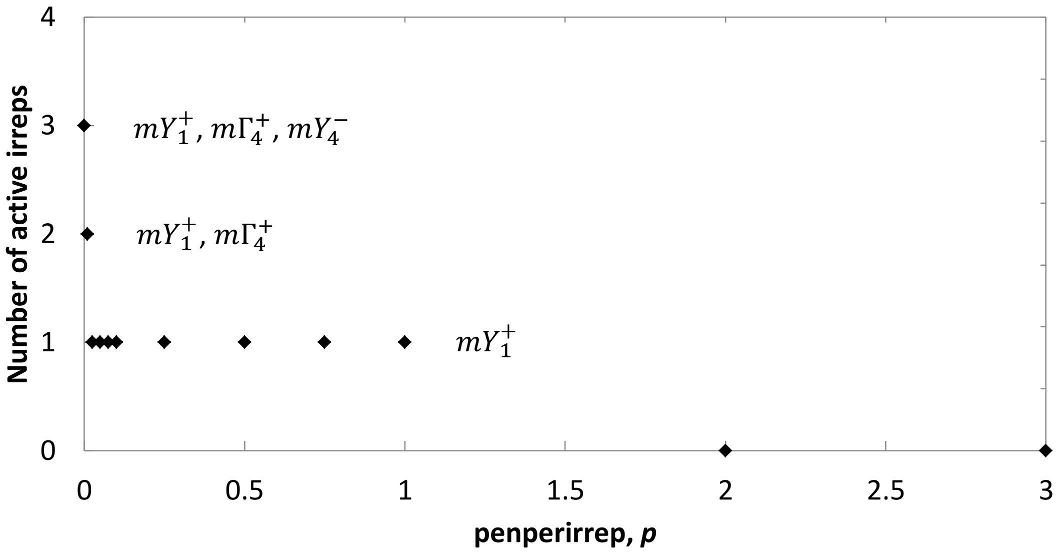

Figure 5.27: Optimal number of irreps active for varying values of *p*. Note that the optimal number does not increase past 3 because no improvement at all (to 2 decimal places) in the fit to the data can be found when further irreps are added.

No modes provide a sufficient improvement in the fit to the data to be turned on until $p \leq 1$ at which point a single mY_1^+ irrep is activated. It is not until the penalty is very small ($p \leq 0.01$) that additional irreps are included. The broad region where a single irrep is activated suggests that the distortion is likely to be driven by a single mY_1^+ irrep. In this region, the single irrep mY_1^+ model was identified 80 times out of 80 which gives us confidence in this model. The addition of extra modes beyond the first has a negligible impact on R_{wp} (Table 5.4).

Table 5.4: R_{wp} achieved by best 0, 1, 2 and 3 irrep models identified by the GA.

Number of Irreps	Active Irreps in best model	R_{wp} (%)
0	None	8.19
1	mY_1^+	3.21
2	$mY_1^+, m\Gamma_4^+$	3.15
3	$mY_1^+, m\Gamma_4^+, mY_4^-$	3.14

The GA identified the best $n = 1$ model (mY_1^+) most quickly when $p = 0.25$. It was identified on average in ~ 62 s and the record over all runs was ~ 13 s. Each repeat of the full sweep of p values shown in Figure 5.27, including the 10 minute wait time after the best model is identified, takes ~ 3 hrs.

The fit provided by using the single mY_1^+ irrep fully accounts for the magnetic peaks in the data (Figure 5.28) and the fit is essentially as good as provided by all available irreps (Figure 5.26). It is therefore clearly superior to the zero irrep fit (Figure 5.24). Running this structure through FINDSYM with magnetic moment tolerance of 0.001 μ_B shows the true magnetic space group is 53.335 (P_cmna) where just 7 magnetic distortion modes are available (5 Ce^{3+} and 2 Fe^{2+}). The same conclusion can be reached by directly superposing the mY_1^+ irrep onto the parent in ISODISTORT by again following the instructions in Appendix 17.

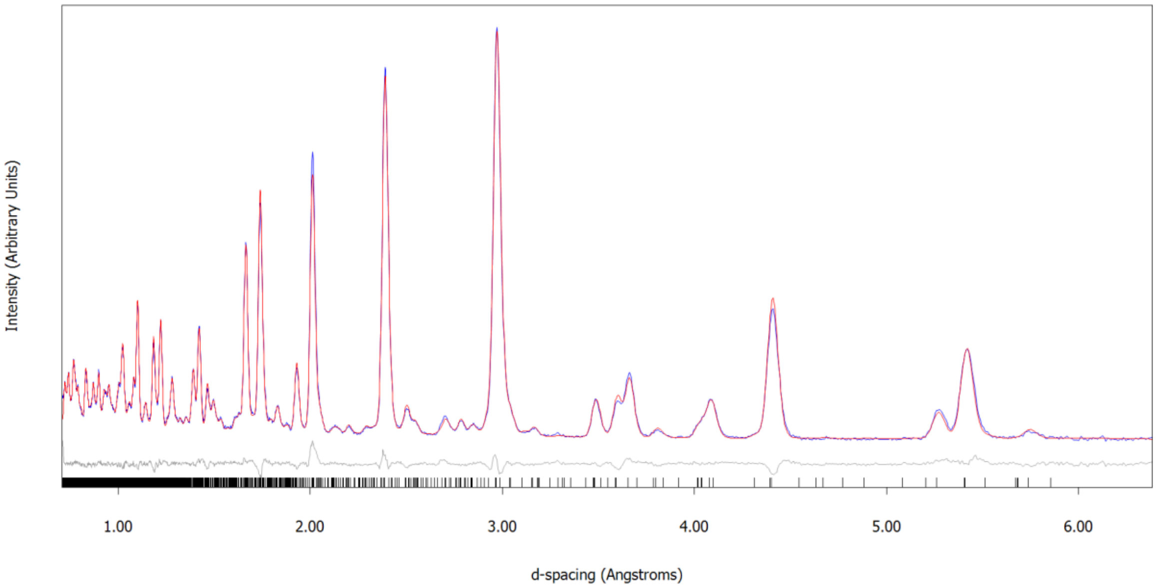

Figure 5.28: Fit to $Ce_2O_2Fe_{0.75}Zn_{0.25}Se_2$ bank 3 GEM data at 10 K using mY_1^+ magnetic distortion modes in magnetic space group 1.1. R_{wp} = 3.21 %, R_{Bragg} = 2.03 %.

5.9.2 Simple Inclusion Approach

A similar conclusion can also be reached by simply trying all 16 available irreps in the $P1$ child model, selecting the best and then trying to add additional irreps in a simple inclusion type search. Figure 5.29 shows the improvement in fit from the first irrep (for which mY_1^+ is the best choice) is very significant but the improvement becomes negligible when any other irrep is added to the model. Both bank 2 and bank 3 data are used for this search. This confirms space group 53.335 and the overall two-step process takes ~ 45 mins to the point of realising that the mY_1^+ irrep alone is the best model.

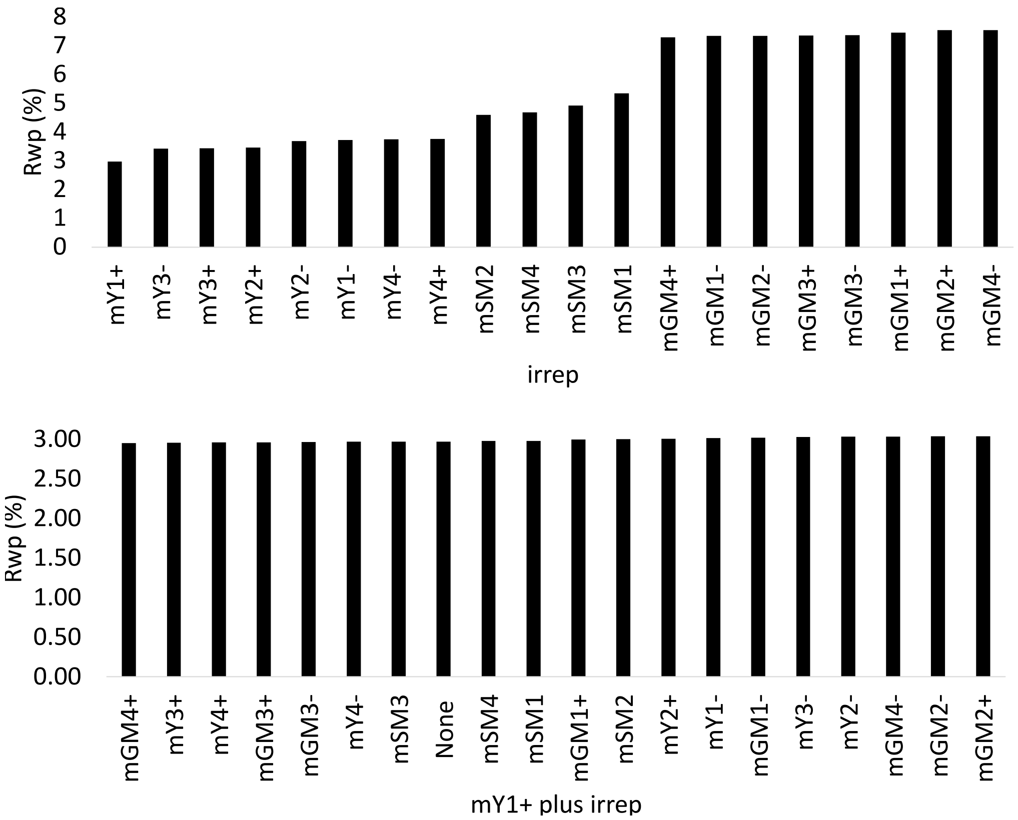

Figure 5.29: Top: Combined R_{wp} achieved by each of 16 available irreps individually fitting LT $Ce_2O_2Fe_{0.75}Zn_{0.25}Se_2$ bank 2 + 3 GEM data at 10 K. Bottom: R_{wp} achieved when a second irrep is used in addition to mY_1^+. "None" refers to the mY_1^+ only model.

5.9.3 Magnetic Structure of $Ce_2O_2Fe_{0.75}Zn_{0.25}Se_2$

Inspection of the magnetic distortion modes and further refinement of the structure (using all 6 detector banks) reveals that the two available Fe^{2+} modes have equal magnitude but opposite sign and that the quality of fit is unaffected by using a single parameter. The Fe^{2+} moments point along the a axis with Fe^{2+} ordering antiferromagnetically across corner sharing (C) tetrahedra and ferromagnetically across edge sharing (E) tetrahedra. All Fe^{2+} moments have the same magnitude (3.55(2) μ_B). Figure 5.30 shows the Fe^{2+} magnetic moments visually.

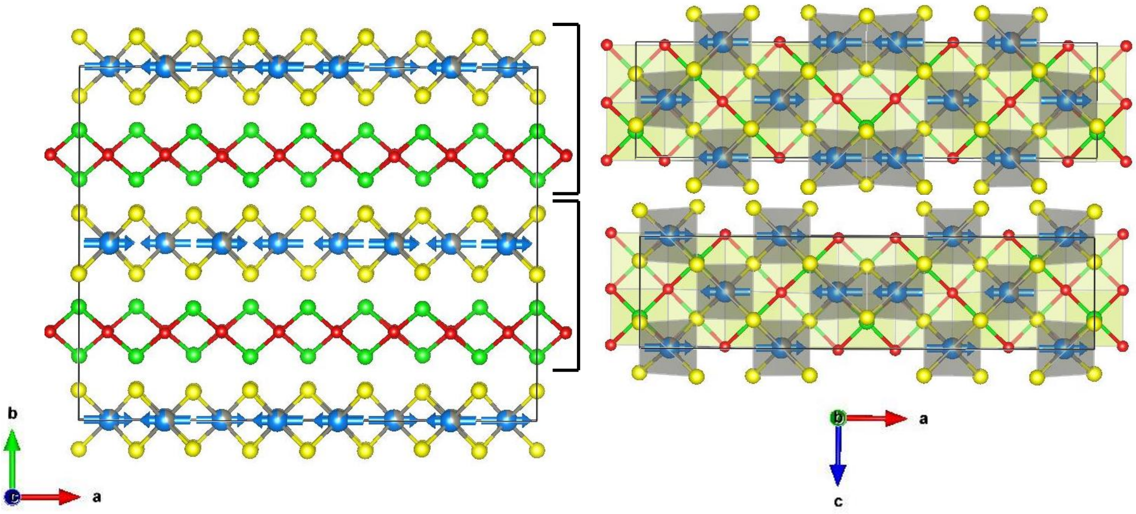

Figure 5.30: Magnetic moments of Fe^{2+} in magnetic space group 53.335 model. Ce^{3+} moments are excluded. Left view shows moments in each $[FeSe_2]^{2-}$ layer. Right view shows moments in individual layers down *b* axis. Atom colours are: Ce green, Fe blue (with Zn occupancy of these sites indicated by the size of grey segment), O red, Se yellow.

In order to compare our structure to the Goodenough-Kanamori[26,27] rules, we consider the coupling of Fe^{2+} 3d orbitals via bridging anion p orbitals may occur via two potential pathways. The first, between corner-sharing $FeSe_4$ tetrahedra, predominately involves Fe^{2+} 3d orbital overlap with orthogonal p orbitals of a single bridging Se atom with a bridging angle of ~ 105˚ (when adjacent to an edge sharing tetrahedra) or ~ 110˚ (between corner sharing tetrahedra). The second pathway, between edge-sharing $FeSe_4$ tetrahedra, predominately involves Fe^{2+} 3d orbital overlap with orthogonal p orbitals of two bridging Se atoms with a bridging angle of ~ 75˚. The angles involved in both pathways is shown for a single $[FeSe_2]^{2-}$ layer in Figure 5.31.

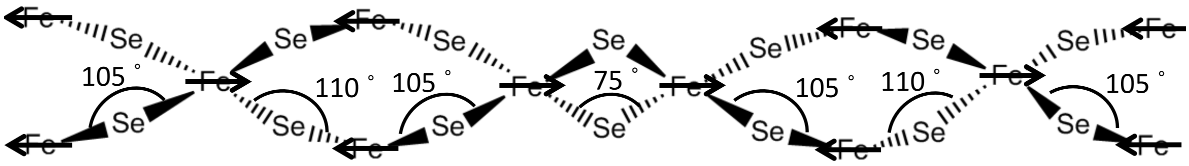

Figure 5.31: Bond angles for Fe^{2+} coupling pathways in a single $[FeSe_2]^{2-}$ layer (as shown in bottom right of Figure 5.30.

In the case of 90˚ bridging angles, there can be no exchange interaction between Fe^{2+} d-orbitals and the exchange interaction is instead with separate orthogonal bridging p-orbitals. The lowest energy arrangement is for the electrons in the orthogonal p-orbitals to have the same spin (triplet state). Given both d-orbitals can exchange with these p-orbitals the most favourable arrangement is for them to both have opposite spin to the p-orbital electrons (so they are ferromagnetically aligned) in order to avoid breaking the Pauli exclusion principle on exchange. However, an antiferromagnetic alignment could be allowed by adopting the higher energy singlet state between orthogonal p-orbital electrons so the effect weakly favours a ferromagnetic alignment of Fe^{2+}.

The Goodenough rules suggest that as the bridging angle varies from 90˚ one increasingly expects to observe antiferromagnetic alignment. This is because coupling is increasingly possible between Fe^{2+} d-orbitals as they increasingly overlap the same bridging p-orbital. This leads to a strong competing antiferromagnetic effect as any exchange between ferromagnetically aligned Fe^{2+} d electrons must break the Pauli exclusion principle. This effect seems to control the ordering in the corner-sharing case where antiferromagnetic alignment is observed but not in the edge-sharing case even though the deviation of the bond angle from 90˚ is similar. However, the observed ferromagnetic alignment of Fe^{2+} moments across edge sharing tetrahedra has been observed previously in $Ce_2O_2FeSe_2$[28]. In that work exchange interactions were probed using neutron diffraction, inelastic neutron scattering and DFT calculations. Both experiment and calculations concluded that ferromagnetic coupling of $FeSe_{4/2}$ edge-sharing chains is most favourable. Our structure is therefore consistent with the literature, giving further support for our Fe^{2+} ordering pattern.

The fit to the experimental data provided using Fe^{2+} magnetic distortion modes alone is good (Figure 5.32) but close inspection shows that a couple of reflections are overcalculated (d ~ 5.7 Å and 8.2 Å). A free refinement of Ce^{3+} moments provides a good fit to all the data (Figure 5.33) but each Ce^{3+} adopts a different moment and all point in unrelated directions. Furthermore, there seems to be more than one possible arrangement that will provide a good fit with no clear visual evidence from the fits to determine between them. Our attempts to constrain the model to find a chemically simple and intuitive ordering pattern were unsuccessful. This may be because the constraints of space group 53.335 simultaneously forbid some Ce^{3+} from having a moment with a component not pointing in the stacking direction and others from having a component pointing in the stacking direction. Removing the constraints of space group 53.335 and performing the refinement in space group *1.1* did not yield a more intuitive ordering pattern. One possible explanation is the very small influence of Ce^{3+} moments on the powder diffraction data has caused us to choose symmetry higher than that actually adopted by Ce^{3+} moments. Alternatively the anomalies in the Fe^{2+}-

only fit could arise from Zn^{2+} occupancy clustering effects or other structural phenomena not included in our model.

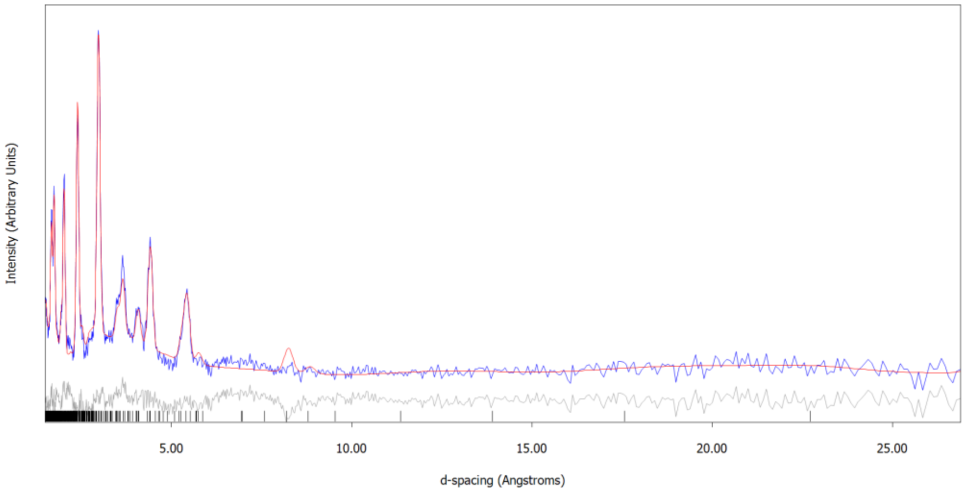

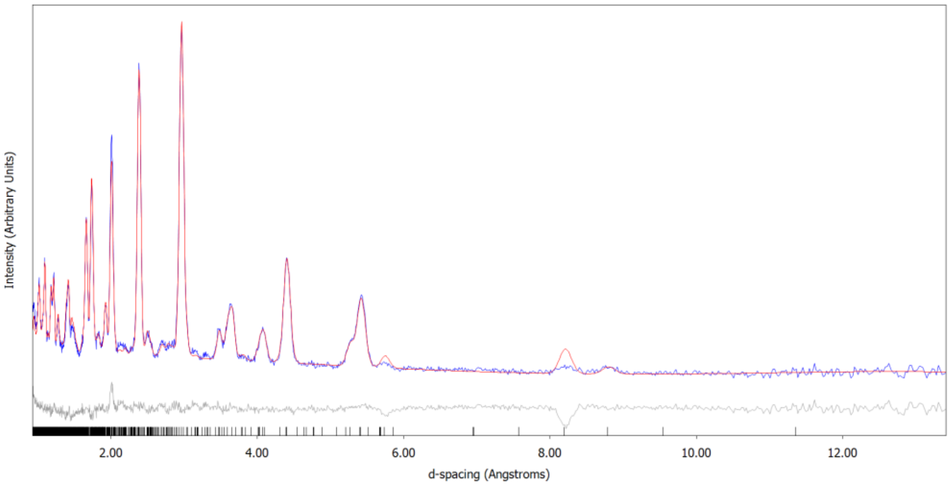

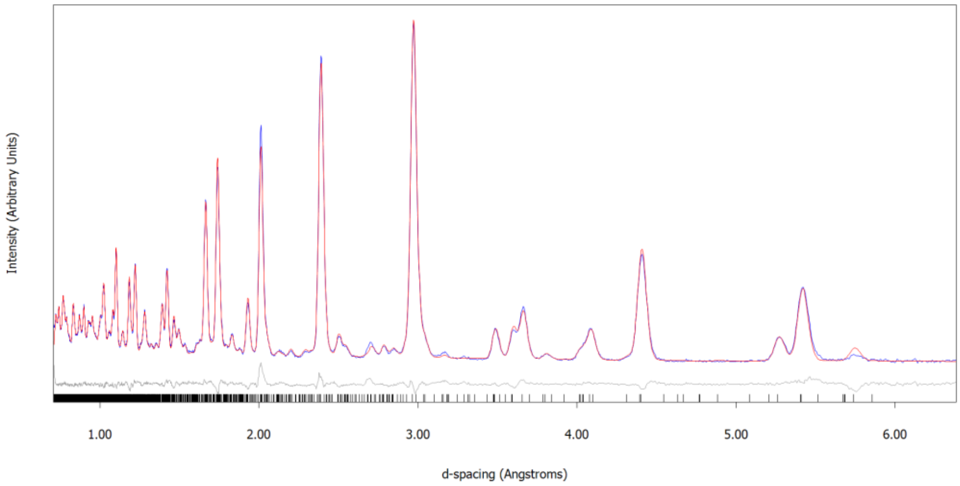

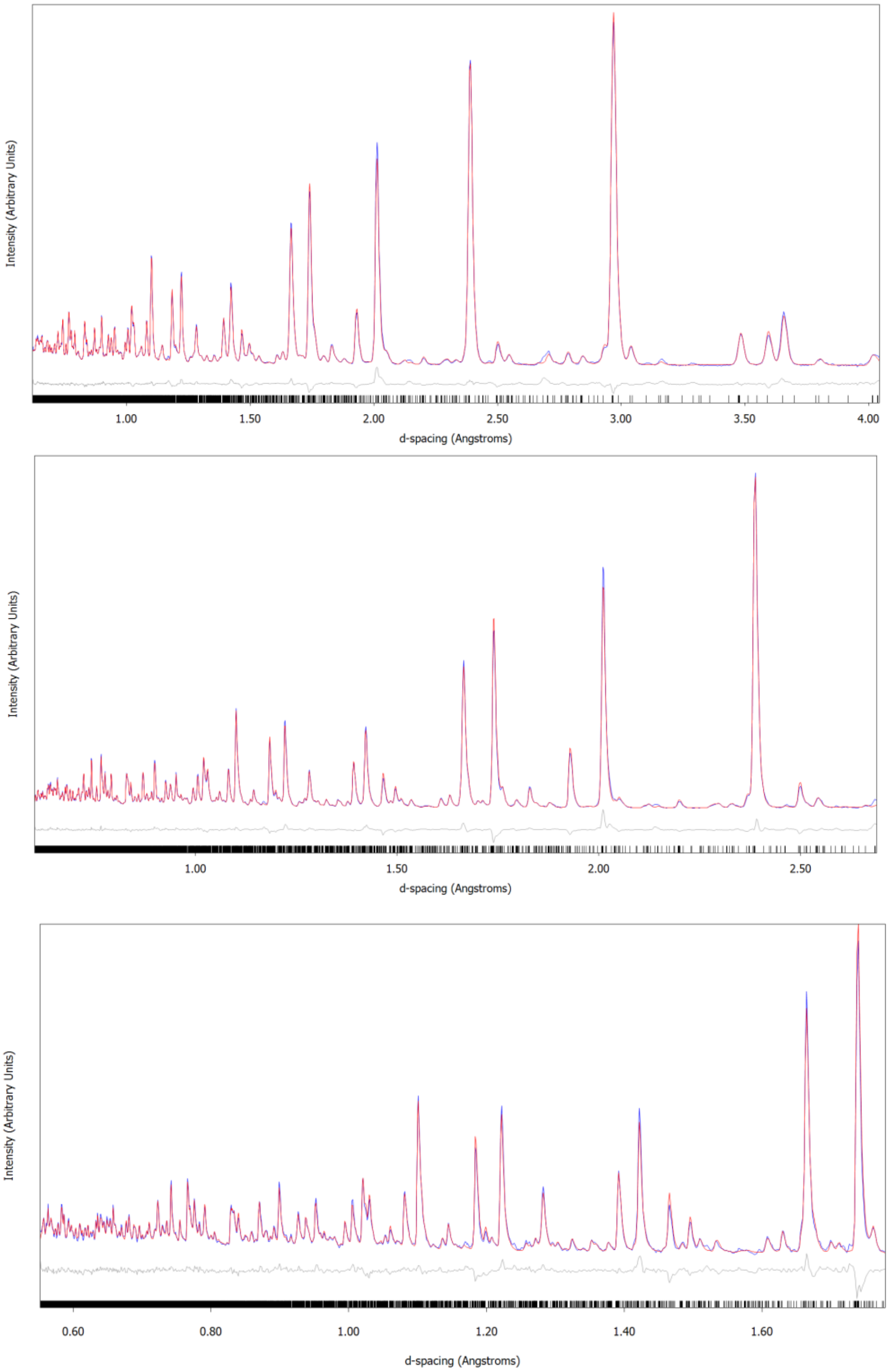

Figure 5.32: Fit to $Ce_2O_2Fe_{0.75}Zn_{0.25}Se_2$ GEM data at 10 K using mY_1^+ magnetic distortion modes in magnetic space group 53.335. Data shown (from top to bottom): Bank 1, Bank 2, Bank 3, Bank 4, Bank 5, Bank 6. Only the 2 available Fe^{2+} modes are used with a single DOF. The peaks at *d* ~ 5.7 Å and 8.2 Å cannot be correctly fit by Fe^{2+} modes alone. R_{wp} (combined overall / bank 1 / bank 2 / bank 3 / bank 4 / bank 5 / bank 6) = 4.15 % / 3.21 % / 3.70 % / 3.41 % / 4.29 % / 4.50 % / 4.37 %, R_{Bragg} (bank 1 / bank 2 / bank 3 / bank 4 / bank 5 / bank 6) = 1.95 % / 2.05 % / 2.08 % / 2.82 % / 3.52 % / 3.61 %.

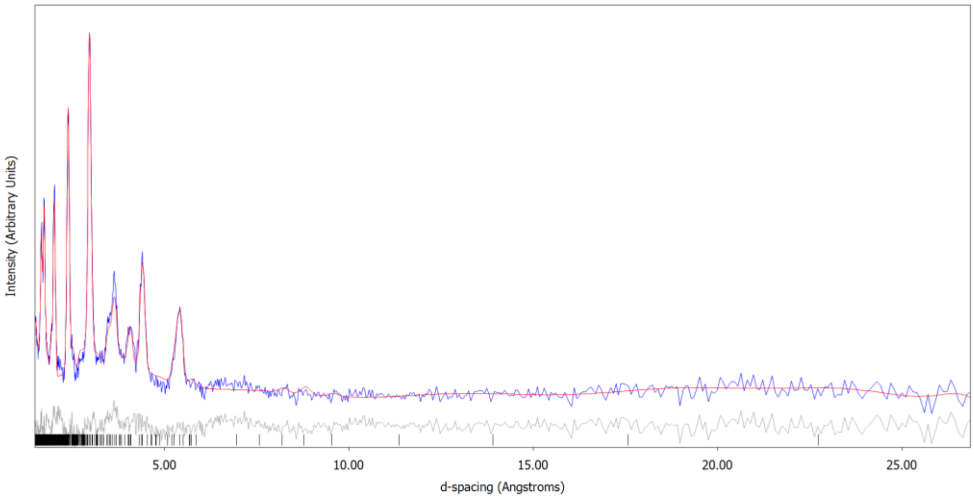
Intensity (Arbitrary Units)
5.00
10.00
15.00
20.00
25.00
d-spacing (Angstroms)

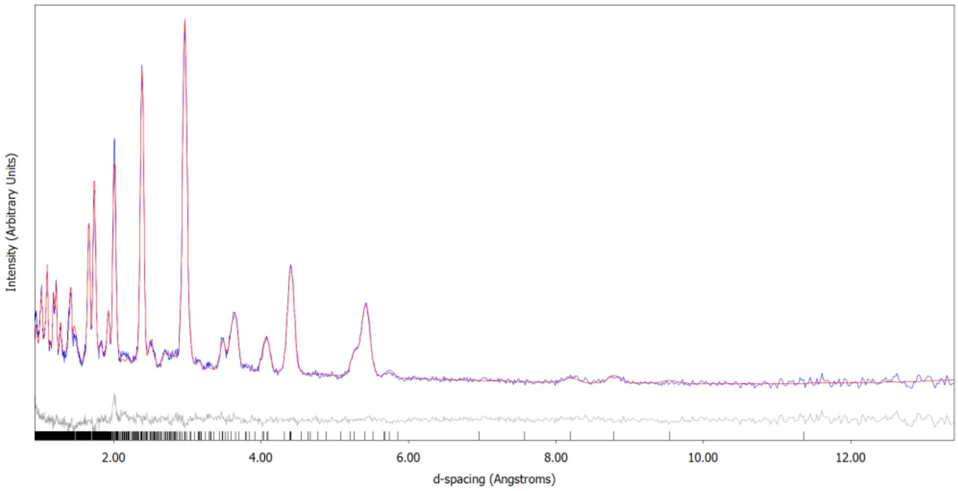
Intensity (Arbitrary Units)
2.00
4.00
6.00
8.00
10.00
12.00
d-spacing (Angstroms)

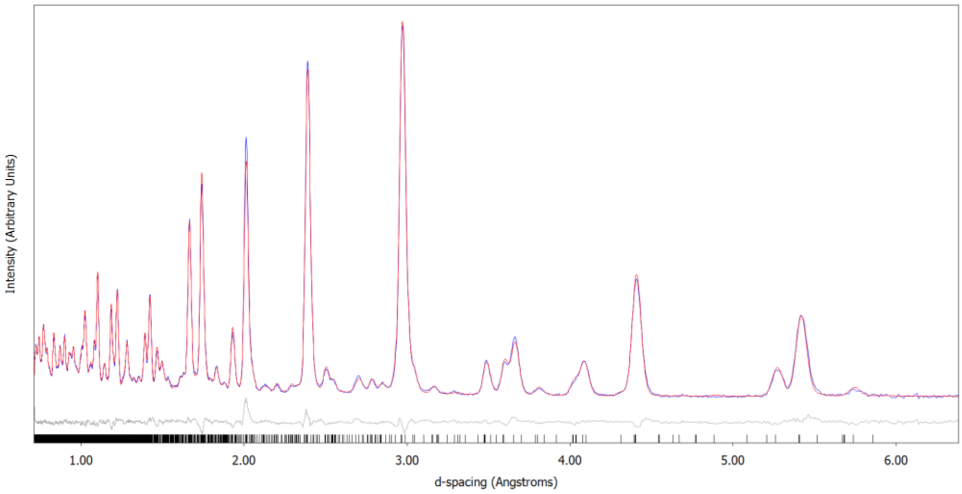
Intensity (Arbitrary Units)
1.00
2.00
3.00
4.00
5.00
6.00
d-spacing (Angstroms)

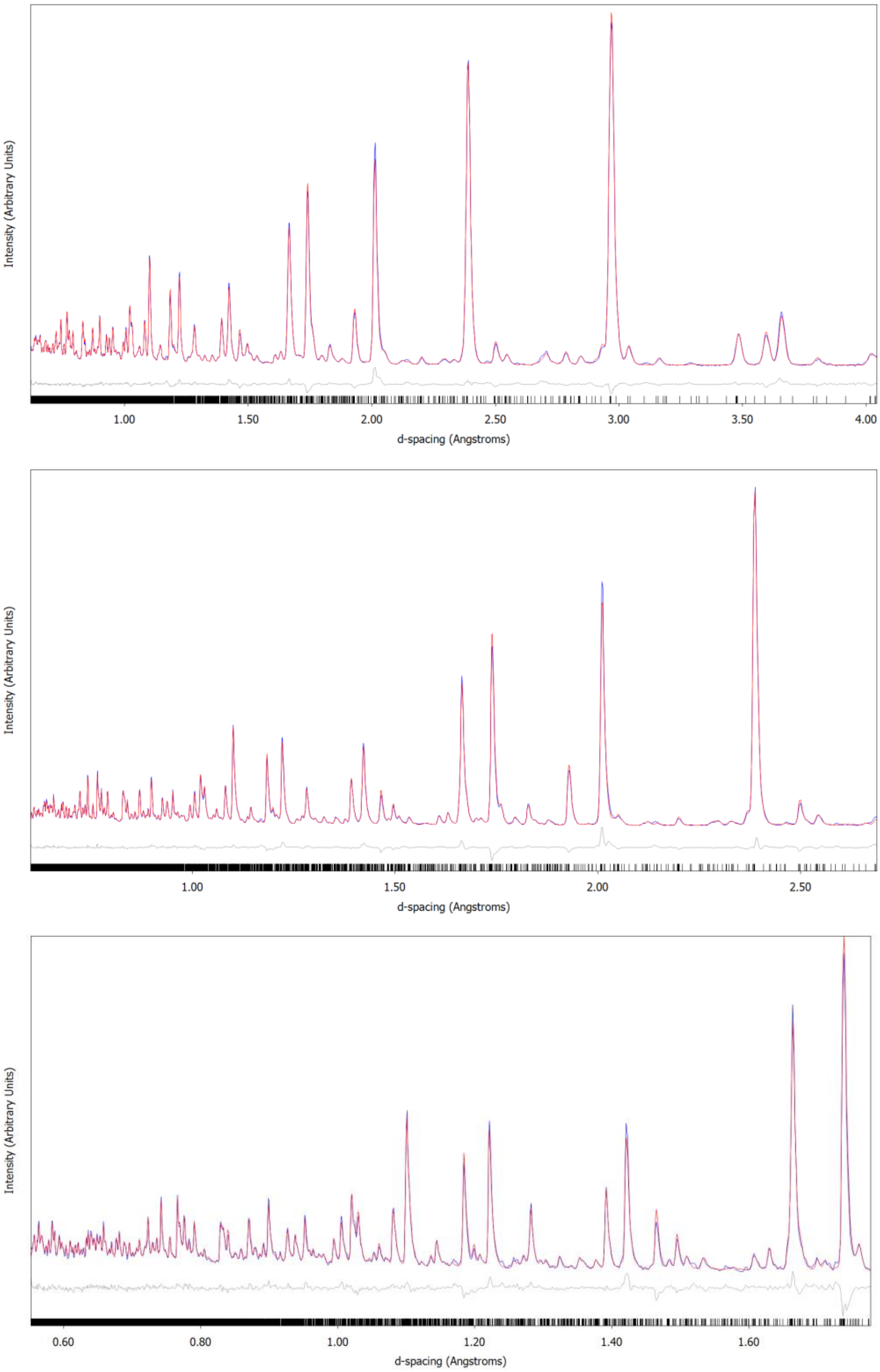

Figure 5.33: Fit to $Ce_2O_2Fe_{0.75}Zn_{0.25}Se_2$ GEM data at 10 K using mY_1^+ magnetic distortion modes in magnetic space group 53.335. Data shown (from top to bottom): Bank 1, Bank 2, Bank 3, Bank 4, Bank 5, Bank 6. 5 free Ce^{3+} modes are used in addition to the 2 available Fe^{2+} modes used with a single DOF. R_{wp} (combined overall / bank 1 / bank 2 / bank 3 / bank 4 / bank 5 / bank 6) = 3.96 % / 2.99 % / 3.13 % / 3.19 % / 4.03 % / 4.45 % / 4.37 %, R_{Bragg} (bank 1 / bank 2 / bank 3 / bank 4 / bank 5 / bank 6) = 1.73 % / 1.63 % / 1.92% / 2.80 % / 3.51 % / 3.63 %.

5.9.4 $Ce_2O_2Fe_{0.75}Zn_{0.25}FeSe_2$ Magnetic Moment with Temperature

It is also possible to see how magnetic scattering develops with temperature to try to understand the Ce^{3+} ordering. Figure 5.34 shows variable temperature data as a 3D plot. A refinement of the magnetic modes of our LT model (magnetic space group 53.335) against powder diffraction data from GEM data banks 2-6 at each temperature was carried out. Magnetic mode penalties are used to ensure that non-zero magnetic moments are only obtained if required by the data. The magnetisation at each temperature is shown in Figure 5.35. A critical model ($\mu = \mu_0(1 - T/T_c)^{\beta}$) suggests that Fe^{2+} magnetic ordering begins to emerge below T_c ~ 105 K and the moment increases to μ_0 ~ 3.7 μ_B as the temperature approaches 0 K with a critical exponent, β ~ 0.3. There is weak evidence to suggest that small Ce^{3+} moments emerge below ~ 65˚C and increase to ~ 0.8 μ_B at 10 K. There is, however, significant uncertainty in the Ce^{3+} moment. It seems likely that if Ce^{3+} moments do order at these temperatures then, as observed by Wang et al. in the $(Ce_{0.78}La_{0.22})_2O_2MnSe_2$ system, the Ce^{3+} moments are induced by the larger Fe^{2+} moments. Regardless of whether there is sufficient evidence from short variable temperature data sets to conclude on the onset of Ce^{3+} ordering, Ce^{3+} moments are required to fully fit our long scans at LT.

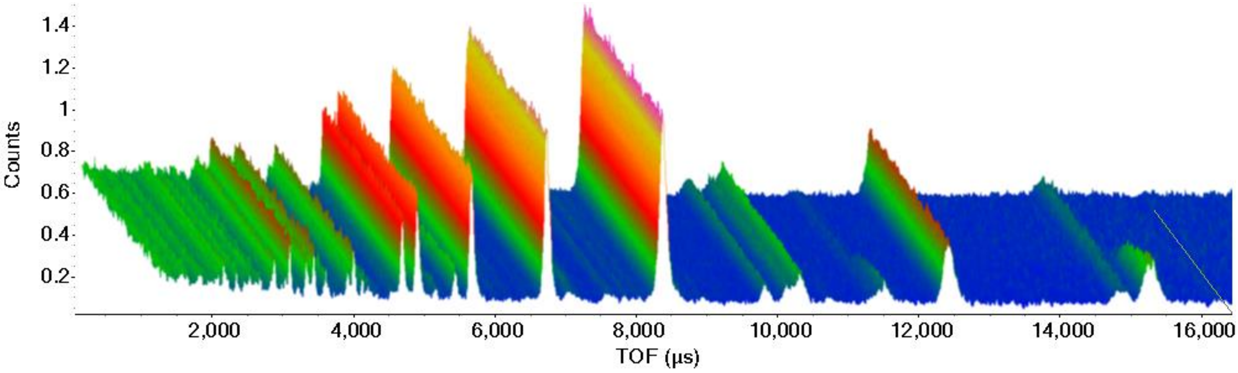

Figure 5.34: Variable temperature data from bank 3 of GEM. Highest temperature (255 K) dataset is at the back and the lowest temperature (10 K) dataset is at the front. The most notable magnetic peaks appear at ~ 15.4 ms and ~ 11.4 ms with significant intensity from T < ~ 100 K.

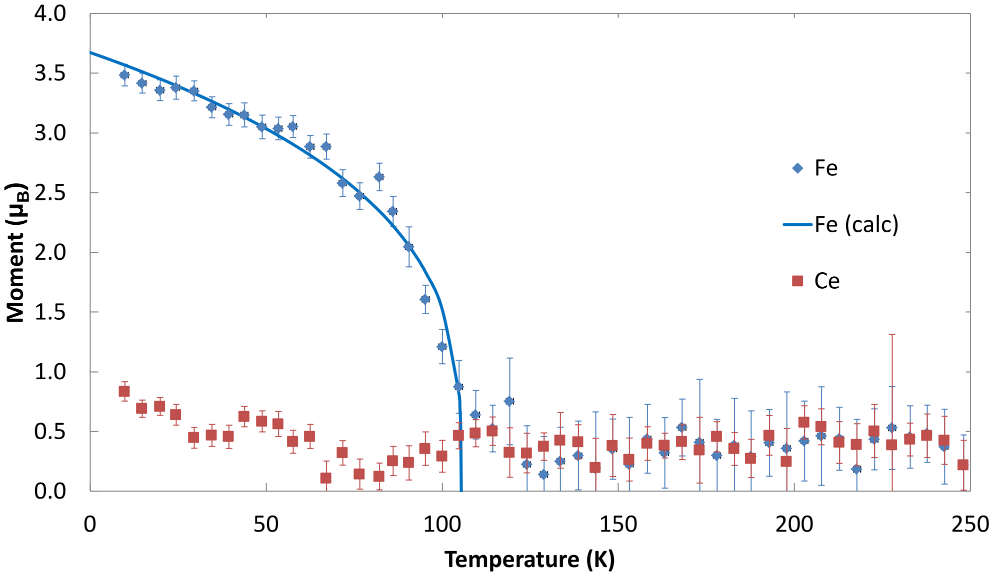

Figure 5.35: Moment of Fe^{2+} and Ce^{3+} from Rietveld refinement of magnetic space group 53.335 model against GEM bank 2-5 variable temperature data between 10 K and 255 K. The calculated moment shown uses a critical model using all data points for which $T < T_c$. The fit is extrapolated to the y-intercept to obtain μ_0 and to the x-intercept to show T_c.

5.10 Conclusions

We have described a new stacking fault methodology, developed and used in collaboration with others, to publish a new stacking fault description for a series of layered oxychalcogenides. The new techniques for Rietveld refinement of large stacked structures extended allowed ~ 1000 stacked layers (~ 7,500 atoms for the $La_2O_2Cu_{0.667}Cd_{0.667}Se_2$ material) to be modelled and refined. Further developments, later published in collaboration, allowed unprecedented complexity in a Rietveld refinement by using models with ~ 100,000 layers (~ 750,000 atoms) and incorporating 100 individual stacks into a single refinement. We have used these techniques to model stacking faults in $La_2O_2Cu_{0.667}Mn_{0.667}Se_2$ for the first time. Despite the additional complexity of each layer, we were able to find “a” type stacking faults of ~ 4 - 10 % from averaging over 100 stacks each with 300 layers (30,000 layers with ~ 2,200,000 atoms). The model lies on the limit of what is achievable on an ordinary desktop PC for extremely complex stacked structures even with powerful new innovations in Rietveld refinement.

We have shown how we can solve magnetic structures using distortion modes and a GA type search using irreps rather than individual distortion modes as the variable attributes. We also used simple inclusion type searches relying on the magnetic distortions typically being driven by a single irrep. We verified the magnetic structure of an existing oxychalcogenide model as a test, and then applied the same techniques to find magnetic ordering in a new oxychalcogenide. Magnetic ordering in $Ce_2O_2Fe_{0.75}Zn_{0.25}Se_2$ appears to onset at ~ 120 K with Fe moments ferromagnetically aligned across edge sharing tetrahedra but antiferromagnetically aligned across corner sharing tetrahedra with a magnetic moment of 3.55(2) μ_B which is consistent with the existing literature. We have created tutorials explaining this methodology online (see Appendix 18) as a tool available for future structure solution work.

5.11 References

(1) Li, L.; Parker, D.; Babkevich, P.; Yang, L.; Ronnow, H.; Sefat, A. *Physical Review B* **2015**, *91*, 104511.

(2) Mizuguchi, Y.; Fujihisa, H.; Gotoh, Y.; Suzuki, K.; Usui, H.; Kuroki, K.; Demura, S.; Takano, Y.; Izawa, H.; Miura, O. *Physical Review B* **2012**, *86*, 220510.

(3) Yazici, D.; Huang, K.; White, B.; Chang, A.; Friedman, A.; Maple, M. *Philosophical Magazine* **2013**, *93*, 673.

(4) Zhai, H.-F.; Zhang, P.; Wu, S.-Q.; He, C.-Y.; Tang, Z.-T.; Jiang, H.; Sun, Y.-L.; Bao, J.-K.; Nowik, I.; Felner, I. *Journal of the American Chemical Society* **2014**, *136*, 15386.

(5) Ishikawa, K.; Kinoshita, S.; Suzuki, Y.; Matsuura, S.; Nakanishi, T.; Aizawa, M.; Suzuki, Y. *Journal of The Electrochemical Society* **1991**, *138*, 1166.

(6) Ueda, K.; Takafuji, K.; Hosono, H. *Journal of Solid State Chemistry* **2003**, *170*, 182.

(7) Ueda, K.; Hiramatsu, H.; Hirano, M.; Kamiya, T.; Hosono, H. *Thin Solid Films* **2006**, *496*, 8.

(8) Ueda, K.; Inoue, S.; Hosono, H.; Sarukura, N.; Hirano, M. *Applied Physics Letters* **2001**, *78*, 2333.

(9) Pitcher, M. J.; Smura, C. F.; Clarke, S. J. *Inorganic Chemistry* **2009**, *48*, 9054.

(10) Wang, C.-H.; Ainsworth, C. M.; Gui, D.-Y.; McCabe, E. E.; Tucker, M. G.; Evans, I. R.; Evans, J. S. O. *Chemistry of Materials* **2015**, *27*, 3121.

(11) Ainsworth, C. M.; Lewis, J. W.; Wang, C.-H.; Coelho, A. A.; Johnston, H. E.; Brand, H. E. A.; Evans, J. S. O. *Chemistry of Materials* **2016**, *28*, 3184.

(12) Ainsworth, C. M. *Synthesis, Structure and Properties of Metal Oxychalcogenides* **2016**, *PhD Thesis*.

(13) Treacy, M.; Newsam, J.; Deem, M. In *Proceedings of the Royal Society of London A: Mathematical, Physical and Engineering Sciences*; The Royal Society: 1991; Vol. 433, p 499.

(14) Leoni, M.; Gualtieri, A. F.; Roveri, N. *Journal of Applied Crystallography* **2004**, *37*, 166.

(15) Casas-Cabanas, M.; Rodríguez-Carvajal, J.; Canales-Vázquez, J.; Laligant, Y.; Lacorre, P.; Palacín, M. *Journal of Power Sources* **2007**, *174*, 414.

(16) Ufer, K.; Roth, G.; Kleeberg, R.; Stanjek, H.; Dohrmann, R.; Bergmann, J. *Zeitschrift für Kristallographie-Crystalline Materials* **2004**, *219*, 519.

(17) Ufer, K.; Kleeberg, R.; Bergmann, J.; Dohrmann, R. *Clays and Clay Minerals* **2012**, *60*, 535.

(18) Ufer, K.; Kleeberg, R.; Bergmann, J.; Dohrmann, R. *Clays and Clay Minerals* **2012**, *60*, 507.

(19) Bergmann, J.; Friedel, P.; Kleeberg, R. *CPD Newsletter* **1998**, *20*.

(20) Wang, X.; Li, J.; Hart, R. D.; Van Riessen, A.; McDonald, R. *Journal of Applied Crystallography* **2011**, *44*, 902.
(21) Coelho, A. A. *Bruker AXS, Karlsruhe, Germany* **2007**.
(22) Bette, S.; Dinnebier, R. E.; Freyer, D. *Journal of Applied Crystallography* **2015**, *48*, 1706.
(23) Coelho, A. A.; Evans, J. S. O.; Lewis, J. W. *Journal of Applied Crystallography* **2016**, *49*, 1740.
(24) Stephens, P. W. *Journal of Applied Crystallography* **1999**, *32*, 281.
(25) Stokes, H. T.; Hatch, D. M.; Campbell, B. J. *URL http://www.iso.byu.edu* **2007**.
(26) Goodenough, J. B. *Physical Review* **1955**, *100*, 564.
(27) Kanamori, J. *Journal of Physics and Chemistry of Solids* **1959**, *10*, 87.
(28) McCabe, E. E.; Stock, C.; Bettis Jr, J. L.; Whangbo, M.-H.; Evans, J. S. O. *Physical Review B* **2014**, *90*, 235115.

Chapter 6 Summary

The work in this thesis develops and uses new methods for structural characterisation work. In this short chapter we briefly summarise the work carried out in constructing and developing these methods.

Using WO_3 as a test bed, exhaustive searches, Genetic Algorithms (GAs) and inclusion/exclusion type searches were developed. All of these fundamentally rely on the distortion mode basis to allow symmetry to be broken or not broken by a simple “on/off” parameter. All of these processes were able to quickly and reliably solve the relatively simple WO_3 structures tested. This was achieved through constant development, updating of the protocols and improvement of the functionality to efficiently integrate the algorithms with Rietveld refinements in TA and improve exploration of possible structures.

The exhaustive method was used to find new structures for α- and β-$Bi_2Sn_2O_7$ including the first reliable structure for β-$Bi_2Sn_2O_7$. These searches required a large number of complex structures to be trialled; however the searches were completed on a reasonable timescale using an ordinary desktop PC. The search can be simplified by considering only lattice subgroups while still not making any additional prior assumptions. This approach allowed us to identify the simplest (highest symmetry) possible models that can account for the α- (Cc, a = 13.15493(6) Å, b = 7.54118(4) Å, c = 15.07672(7) Å, β = 125.0120(3)°) and β-$Bi_2Sn_2O_7$ ($Aba2$, a = 7.571833(8) Å, b = 21.41262(2) Å, c = 15.132459(7) Å) diffraction data. Analysis of the distortion modes responsible using the highest common subgroup revealed that both are driven by large Γ_5^- and L_2^+ modes. The key difference is the α-phase $L_2^+(0,a,0,0)$ distortion leads to Bi being displaced towards a corner of the surrounding hexagonal O environment while the β-phase $L_2^+(a,-a,0,0)$ distortion displaces it towards an edge.

Exhaustive searches have also been applied to the complex structure of RT ZrP_2O_7. The search was fast and effective when considering only displacive distortions of the $Pa\bar{3}$ parent and identified the correct $Pbca$ structure of ZrP_2O_7. In order to determine whether rotational distortions of rigid bodies could further simplify structure solution, a new artificial $Fm\bar{3}m$ parent was created. The greatly increased number of candidate structures in the subgroup tree and the technical challenge of creating the rigid bodies for all candidates ruled out an exhaustive search. Using this parent, the structure could be modelled with considerably fewer structural parameters when rigid body rotations were incorporated. It has not yet been possible to directly search for the important modes of this parameterisation using any of our search techniques. However, an inclusion search based on attempting the match atomic positions of the known structure produced a reasonable structural model with just 93 parameters. New developments in rotational distortion analysis (ISOTILT) may allow rapid identification of even simpler models using rigid body quasi CRUM rotations while working with the $Pa\bar{3}$ parent. This would allow our search algorithms to be applied to these models, testing them against powder diffraction data in a reasonable timescale.

GAs and simple inclusion searches were also applied to the low temperature magnetic structures of two oxychalcogenide materials. The $(Ce_{0.78}La_{0.22})_2O_2MnSe_2$ example was used to prove the techniques could be applied to magnetic structures. An adaptation of the GA routine to consider irreps rather than individual modes as the attributes considerably simplified the search process. The novel low temperature magnetic structure of $Ce_2O_2Fe_{0.75}Zn_{0.25}Se_2$ was then investigated, concluding that the distortion is driven by mY_1^+ distortion modes with no distortion of the RT cell leading to magnetic space group 53.335. Fe^{2+} moments were found to be antiferromagnetically aligned across corner-sharing tetrahedra, although ferromagnetically aligned across edge-sharing tetrahedra with a moment of 3.55(2) μ_B. The result was consistent with the literature although we were not able to determine the Ce^{3+} moment ordering with certainty.

Finally, stacking faults in layered materials were investigated using new routines and improvements to Rietveld refinement. This allows unprecedented complexity in faulted models. $La_2O_2Cu_{0.667}Cd_{0.667}Se_2$ was used as an example system to demonstrate the new capabilities, before investigating "a" type stacking faults in $La_2O_2Cu_{0.667}Mn_{0.667}Se_2$, which is more complex due to the 4C-1E structure within the $[MnSe_2]^{2-}$ layers. Stacking faults between 4 and 10 % increasingly reduced the over-calculated intensity of $00l$ reflections in the unfaulted structure although some other non-systematic problems with the fit have not been resolved. This faulted structure tests the limits of what is computationally possible even with the significant improvements in Rietveld methodology.

Overall this work has produced a range of useful new methodologies which may be further exploited in the future. The overarching aim of these methodologies has been to provide a robust and efficient approach to structure determination and this has been demonstrated with new and existing examples in this work. Several of the examples have been published[1-3] or are in preparation. We have also developed our methods into on-line tutorials which are available at https://community.dur.ac.uk/john.evans/topas_workshop/topas_user_menu.htm (see tutorial numbers 39, 40, 42 and 43) and include python scripts in order to make our methods available to others.

6.1 References

(1) Lewis, J. W.; Payne, J. L.; Evans, I. R.; Stokes, H. T.; Campbell, B. J.; Evans, J. S. O. *Journal of the American Chemical Society* **2016**, *138*, 8031.
(2) Ainsworth, C. M.; Lewis, J. W.; Wang, C.-H.; Coelho, A. A.; Johnston, H. E.; Brand, H. E. A.; Evans, J. S. O. *Chemistry of Materials* **2016**, *28*, 3184.
(3) Coelho, A. A.; Evans, J. S. O.; Lewis, J. W. *Journal of Applied Crystallography* **2016**, *49*, 1740.

Appendixes

1. ISODISTORT Process for WO_3 Pm-3m to 2x2x2 P1 Subgroup Tree

i) Go to http://stokes.byu.edu/iso/isodistort.php

ii) Next to "Import parent structure from a CIF structure file", browse to the wo3_pm3m_parent.cif on your computer and click "OK".

iii) Under "Space Group Preferences", check the monoclinic cell choice 2 box and click "Change"

iv) Under Method 3, select space group symmetry "1 P1 C1-1", enter the basis {(2,0,0),(0,2,0),(0,0,2)} row by row, and click "OK".

v) Choose the only option: "1 P1, basis={(0,0,2),(0,2,0),(-2,0,0)}, origin=(0,0,0), s=8, i=384" and click "OK".

vi) To obtain the subgroup tree, scroll to the bottom of the page and check the "Generate TOPAS.STR output for subgroup tree" box. Then return to the top of the page, check the "Subgroup tree" radio button, and click "OK".

vii) After a couple of minutes you should find that 1427 subgroups have been generated. Note that subgroups 1 (the parent), 2-4, 7, 217-219, 221, 223 and 225 do not have any active distortions. Click "Download zip file" at the bottom of the page to download 1416 topas.str structure files of the remaining subgroups plus the parent. Extract them to your tutorial directory.

2. ISODISTORT Process for WO_3 Pm-3m to √2x√2x2 P4 Subgroup Tree

i) Go to http://stokes.byu.edu/iso/isodistort.php

ii) Next to "Import parent structure from a CIF structure file", browse to the wo3_pm3m_parent.cif on your computer and click "OK".

i) Under Method 3, select space group symmetry "75 P4 C4-1", enter the basis {(1,1,0),(-1,1,0),(0,0,2)} row by row, and click "OK".

ii) Choose the first of two options: "75 P4, basis={(-1,1,0),(-1,-1,0),(0,0,2)}, origin=(0,0,0), s=4, i=48" and click "OK".

iii) To obtain the subgroup tree, scroll to the bottom of the page and check the "Generate TOPAS.STR output for subgroup tree" box. Then return to the top of the page, check the "Subgroup tree" radio button, and click "OK".

iv) After a few seconds you should find that 72 subgroups have been generated. Note that subgroups 1 (the parent), 2 and 31 do not have any active distortions.

Click "Download zip file" at the bottom of the page to download 69 topas.str structure files of the remaining subgroups plus the parent.

3. Plots of fitness evolution for all repeats of probindmut/probindcx experiments

i) probindmut = 0.2, probindcx = 0.8

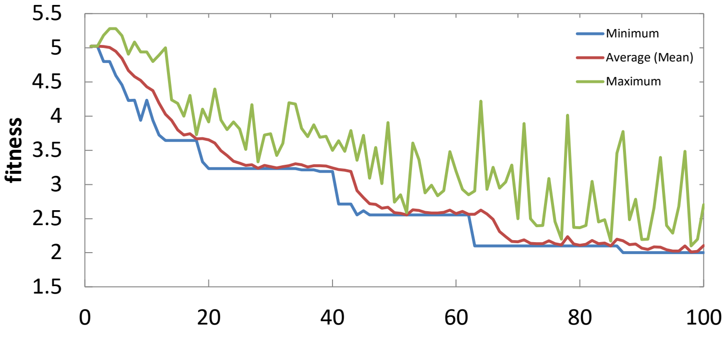

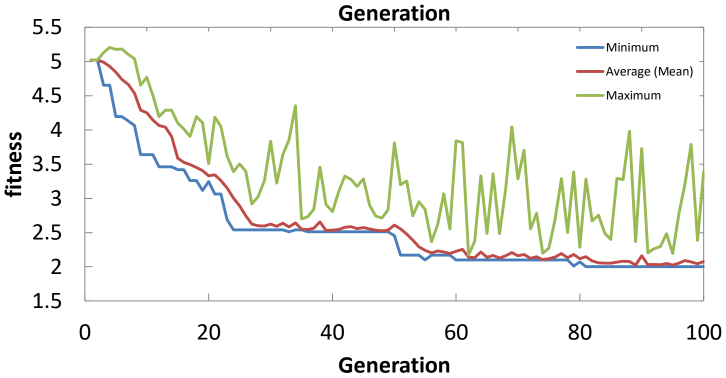

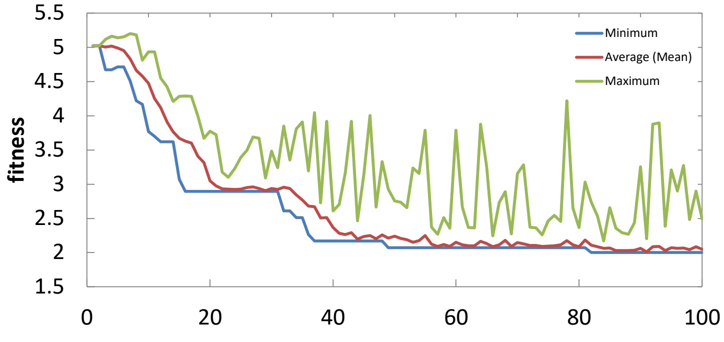
fitness
Generation
5.5
5
4.5
4
3.5
3
2.5
2
1.5
0
20
40
60
80
100
Minimum
Average (Mean)
Maximum

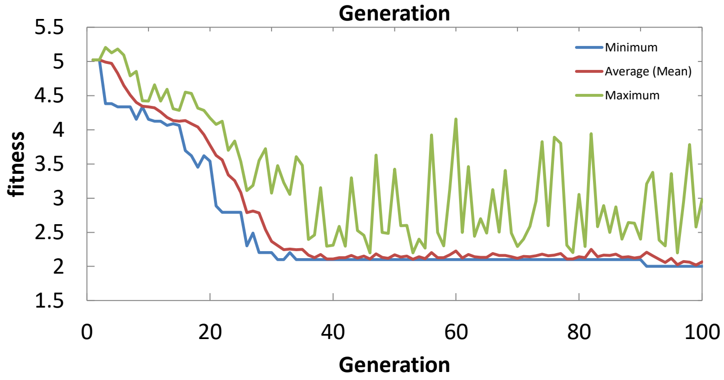
fitness
Generation
5.5
5
4.5
4
3.5
3
2.5
2
1.5
0
20
40
60
80
100
Minimum
Average (Mean)
Maximum

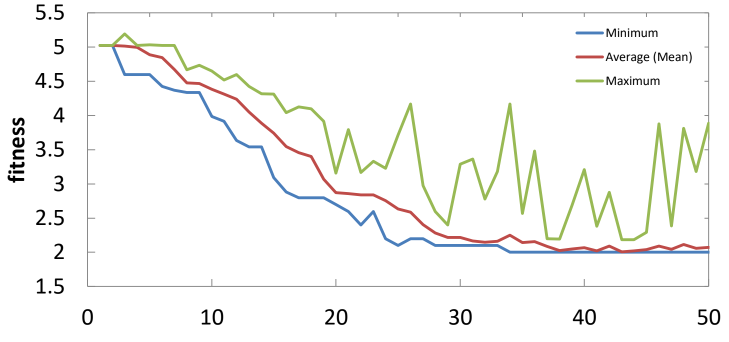
fitness
Generation
5.5
5
4.5
4
3.5
3
2.5
2
1.5
0
10
20
30
40
50
Minimum
Average (Mean)
Maximum

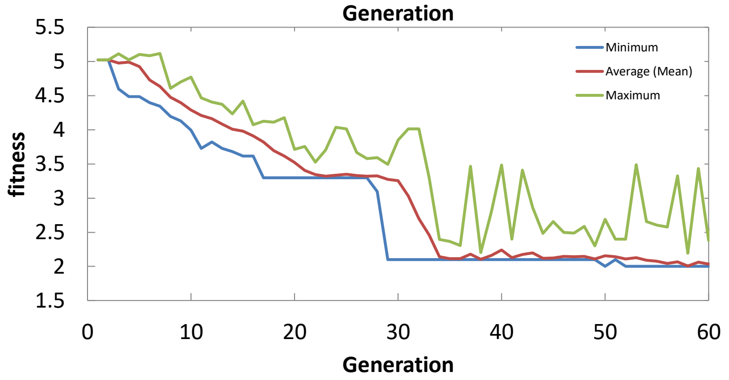
fitness
Generation
5.5
5
4.5
4
3.5
3
2.5
2
1.5
0
10
20
30
40
50
60
Minimum
Average (Mean)
Maximum

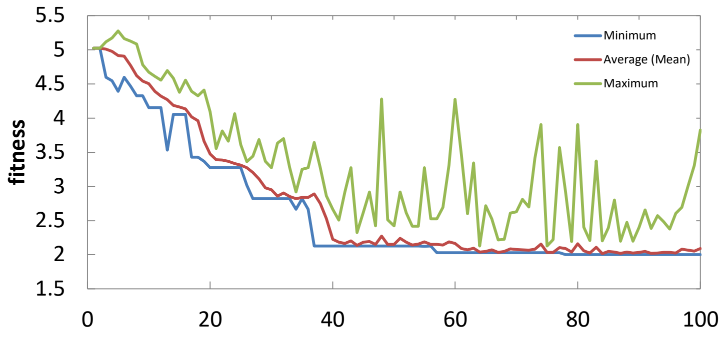
5.5
5
4.5
4
3.5
3
2.5
2
1.5
fitness
0
20
40
60
80
100
Generation
Minimum
Average (Mean)
Maximum

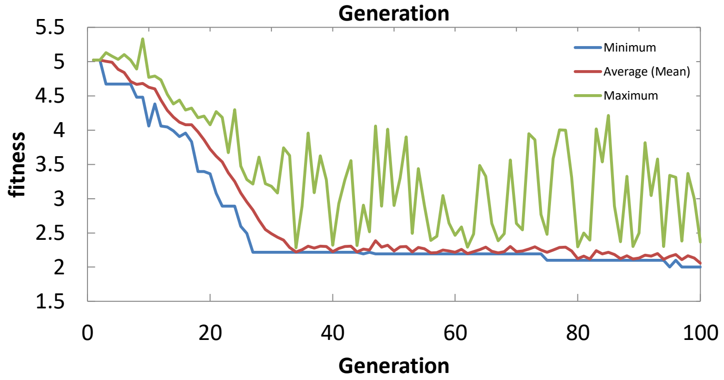
5.5
5
4.5
4
3.5
3
2.5
2
1.5
fitness
0
20
40
60
80
100
Generation
Minimum
Average (Mean)
Maximum

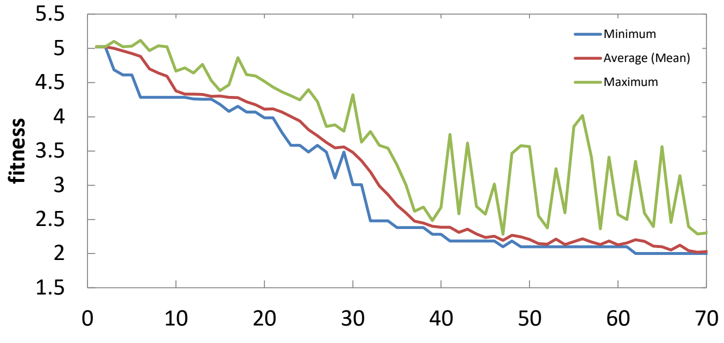
5.5
5
4.5
4
3.5
3
2.5
2
1.5
fitness
0
10
20
30
40
50
60
70
Generation
Minimum
Average (Mean)
Maximum

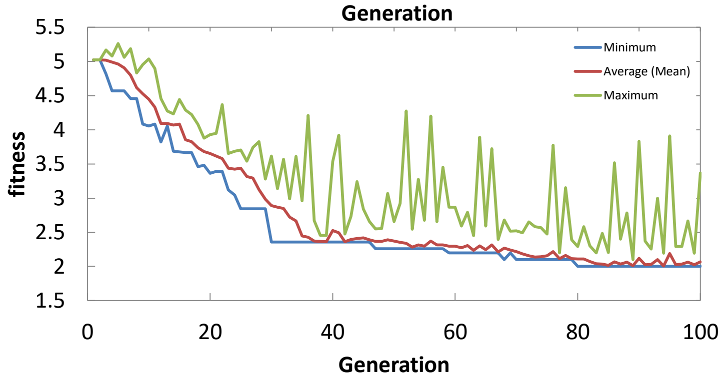
5.5
5
4.5
4
3.5
3
2.5
2
1.5
fitness
0
20
40
60
80
100
Generation
Minimum
Average (Mean)
Maximum

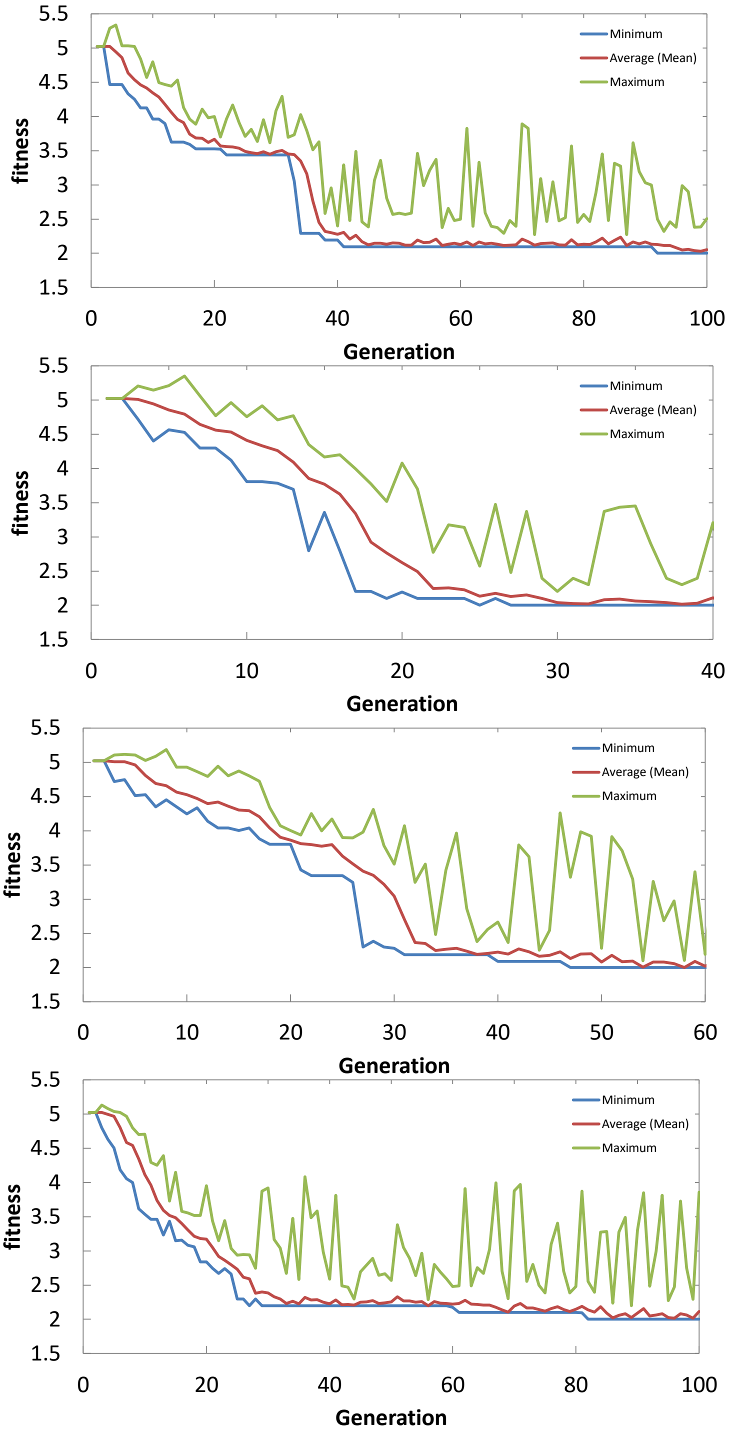

Figure S 1: GA pathways for repeat runs with probindmut = 0.2, probindcx = 0.8

ii) probindmut = 0.75, probindcx = 0.25

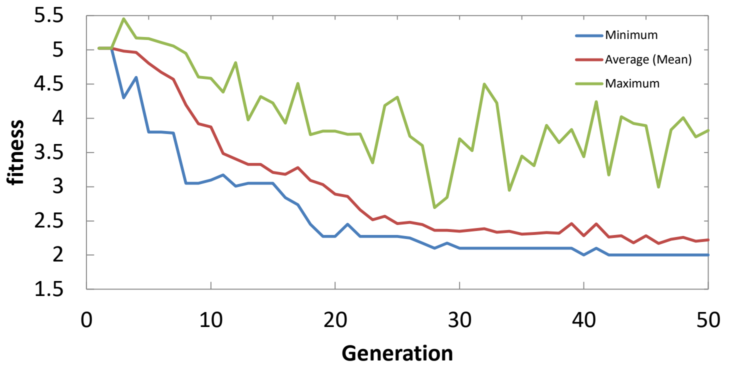
fitness
5.5
5
4.5
4
3.5
3
2.5
2
1.5
0
10
20
30
40
50
Generation
Minimum
Average (Mean)
Maximum

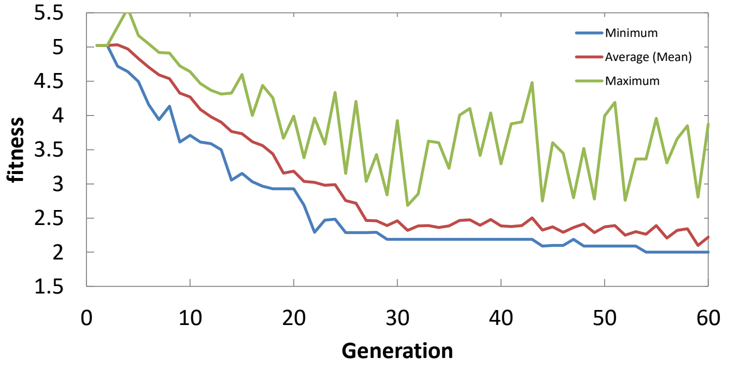
fitness
5.5
5
4.5
4
3.5
3
2.5
2
1.5
0
10
20
30
40
50
60
Generation
Minimum
Average (Mean)
Maximum

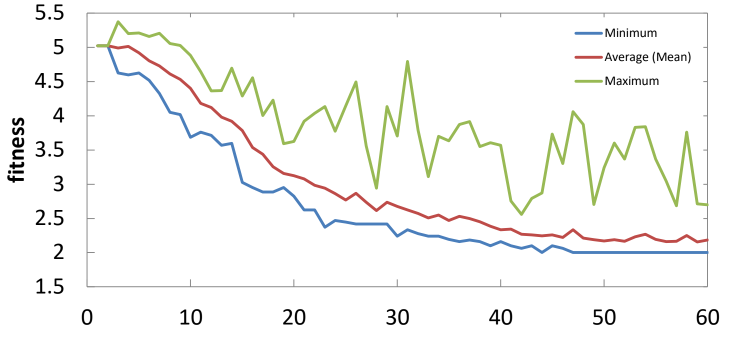
fitness
5.5
5
4.5
4
3.5
3
2.5
2
1.5
0
10
20
30
40
50
60
Generation
Minimum
Average (Mean)
Maximum

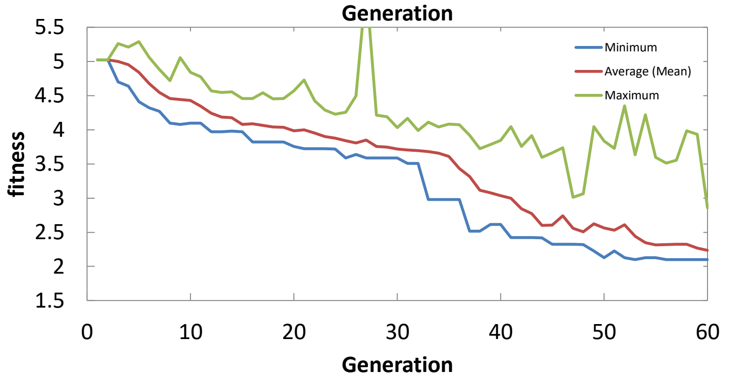
fitness
5.5
5
4.5
4
3.5
3
2.5
2
1.5
0
10
20
30
40
50
60
Generation
Minimum
Average (Mean)
Maximum

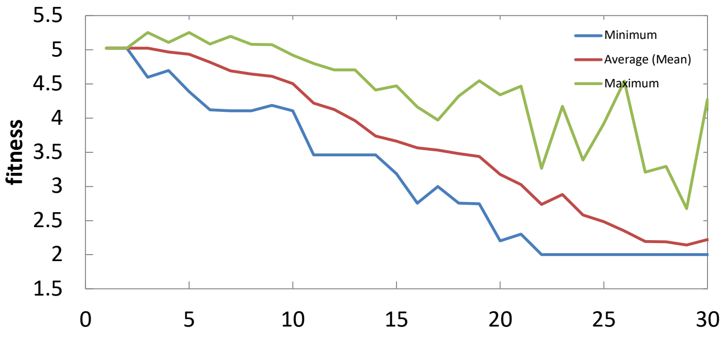
fitness
5.5
5
4.5
4
3.5
3
2.5
2
1.5
0
5
10
15
20
25
30
Generation
Minimum
Average (Mean)
Maximum

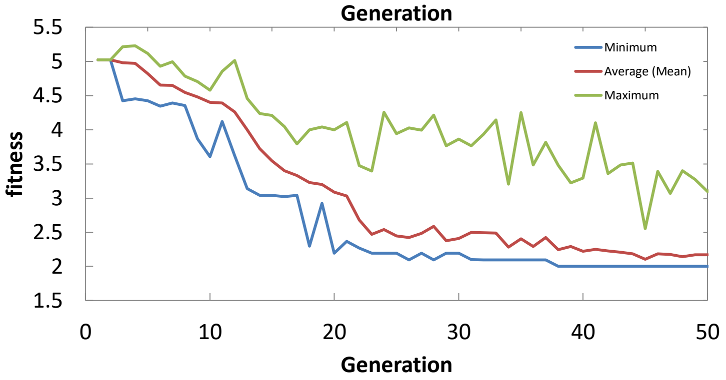
fitness
5.5
5
4.5
4
3.5
3
2.5
2
1.5
0
10
20
30
40
50
Generation
Minimum
Average (Mean)
Maximum

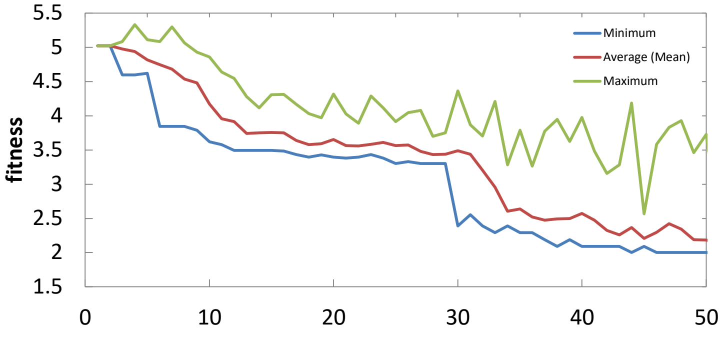
fitness
5.5
5
4.5
4
3.5
3
2.5
2
1.5
0
10
20
30
40
50
Generation
Minimum
Average (Mean)
Maximum

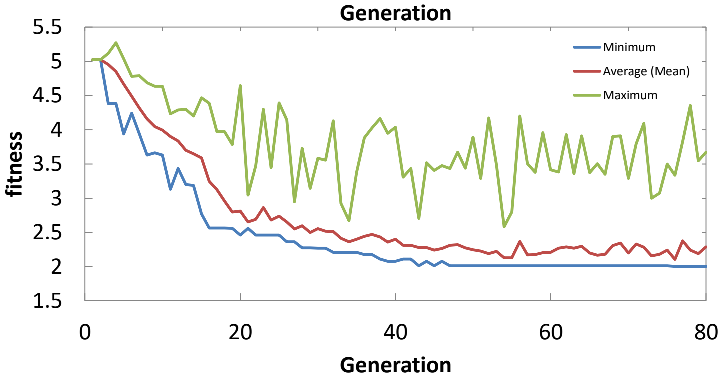
fitness
5.5
5
4.5
4
3.5
3
2.5
2
1.5
0
20
40
60
80
Generation
Minimum
Average (Mean)
Maximum

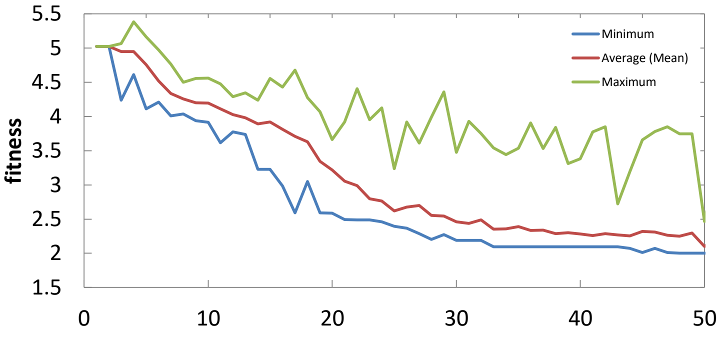
fitness
5.5
5
4.5
4
3.5
3
2.5
2
1.5
0
10
20
30
40
50
Generation
Minimum
Average (Mean)
Maximum

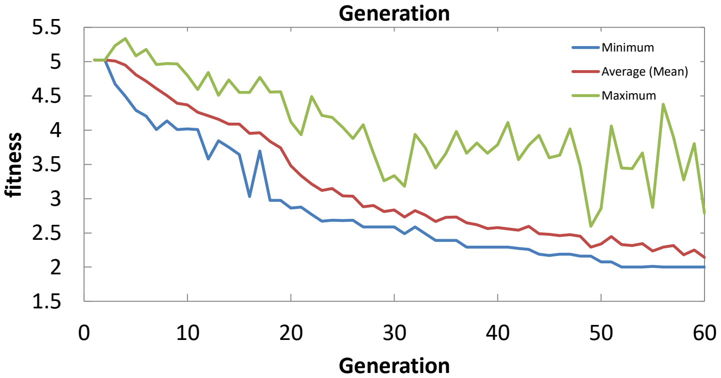
fitness
5.5
5
4.5
4
3.5
3
2.5
2
1.5
0
10
20
30
40
50
60
Generation
Minimum
Average (Mean)
Maximum

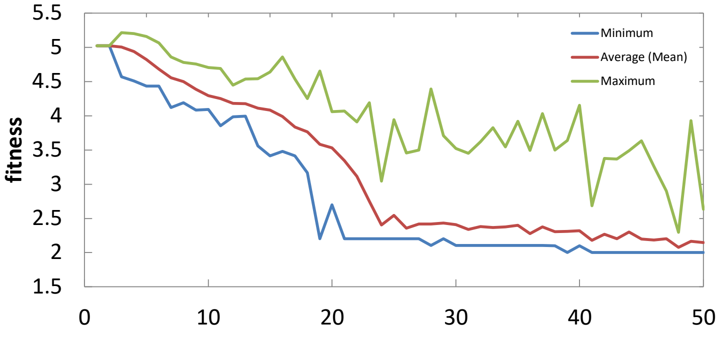
fitness
5.5
5
4.5
4
3.5
3
2.5
2
1.5
0
10
20
30
40
50
Generation
Minimum
Average (Mean)
Maximum

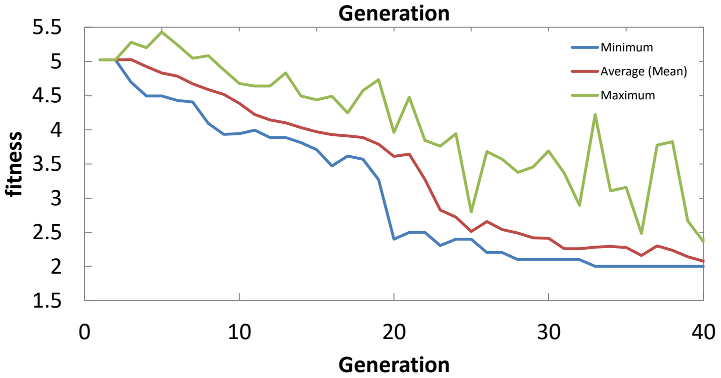
fitness
5.5
5
4.5
4
3.5
3
2.5
2
1.5
0
10
20
30
40
Generation
Minimum
Average (Mean)
Maximum

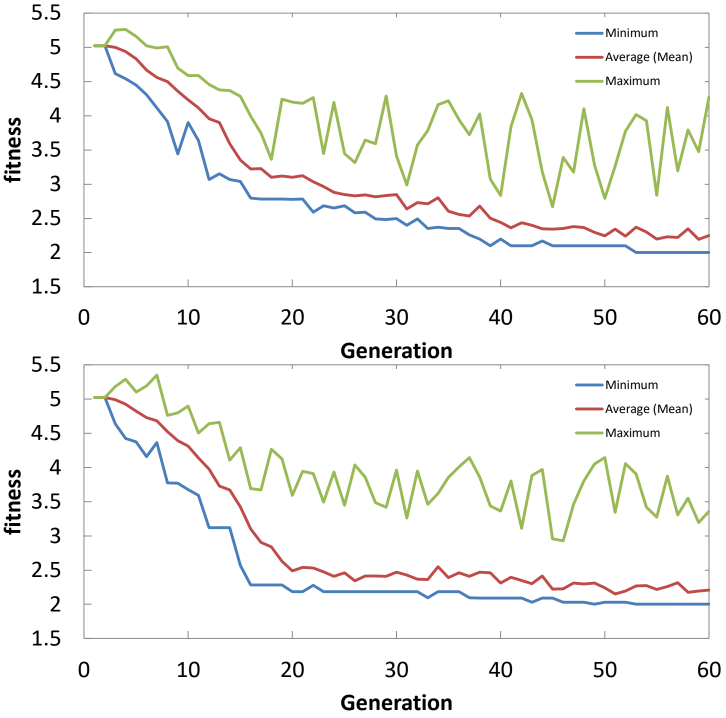

Figure S 2: GA pathways for repeat runs with probindmut = 0.75, probindcx = 0.25

4. Exhaustive Search Tutorial

We have created a tutorial that gives step-by-step instructions on implementing on the exhaustive search approach for the simple HT WO_3 example. The tutorial is available at http://community.dur.ac.uk/john.evans/topas_workshop/tutorial_exhaustive_symmetry.htm

5. Genetic Algorithm Tutorial

A detailed GA tutorial which runs through how to use the GA script based on the RT WO_3 example is available online at http://community.dur.ac.uk/john.evans/topas_workshop/tutorial_GA_wo3.htm

6. Distortion Modes available to WO_3 P1 child subgroup

Table S 1: Distortion modes available to WO_3 *P1* child model and their amplitudes.

Mode Number	Atom Type	Irrep(OPD)	Degeneracy Label	Amplitude/Å
1	W	GM4-(a,b,c)	T1u(a)	-.39(3)
2	W	GM4-(a,b,c)	T1u(b)	.02(7)
3	W	GM4-(a,b,c)	T1u(c)	-.24(4)
4	W	R4-(a,b,c)	T1u(a)	.08(3)

5	W	R4-(a,b,c)	T1u(b)	.04(4)
6	W	R4-(a,b,c)	T1u(c)	.06(4)
7	W	X3-(a,b,c)	T1u(a)	.03(5)
8	W	X3-(a,b,c)	T1u(b)	-.08(2)
9	W	X3-(a,b,c)	T1u(c)	.00(5)
10	W	X5-(a,b,c,d,e,f)	T1u(a)	-.02(5)
11	W	X5-(a,b,c,d,e,f)	T1u(b)	-.01(6)
12	W	X5-(a,b,c,d,e,f)	T1u(c)	-.65(1)
13	W	X5-(a,b,c,d,e,f)	T1u(d)	-.14(2)
14	W	X5-(a,b,c,d,e,f)	T1u(e)	.06(3)
15	W	X5-(a,b,c,d,e,f)	T1u(f)	.03(3)
16	W	M3-(a,b,c)	T1u(a)	.70(1)
17	W	M3-(a,b,c)	T1u(b)	-.02(7)
18	W	M3-(a,b,c)	T1u(c)	-.01(2)
19	W	M5-(a,b,c,d,e,f)	T1u(a)	.01(1)
20	W	M5-(a,b,c,d,e,f)	T1u(b)	-.04(4)
21	W	M5-(a,b,c,d,e,f)	T1u(c)	-.03(3)
22	W	M5-(a,b,c,d,e,f)	T1u(d)	-.04(2)
23	W	M5-(a,b,c,d,e,f)	T1u(e)	-.04(5)
24	W	M5-(a,b,c,d,e,f)	T1u(f)	.05(2)
25	O	GM4-(a,b,c)	A2u(a)	.00(2)
26	O	GM4-(a,b,c)	A2u(b)	-.03(4)
27	O	GM4-(a,b,c)	A2u(c)	.00(3)
28	O	GM4-(a,b,c)	Eu(a)	-.09(4)
29	O	GM4-(a,b,c)	Eu(b)	.00(4)
30	O	GM4-(a,b,c)	Eu(c)	.03(3)
31	O	GM5-(a,b,c)	Eu(a)	.01(3)
32	O	GM5-(a,b,c)	Eu(b)	.08(4)
33	O	GM5-(a,b,c)	Eu(c)	.17(4)
34	O	R1+(a)	A2u(a)	.05(7)
35	O	R3+(a,b)	A2u(a)	.01(6)
36	O	R3+(a,b)	A2u(b)	.09(8)
37	O	R4+(a,b,c)	Eu(a)	1.06(1)

38	O	R4+(a,b,c)	Eu(b)	-.78(1)
39	O	R4+(a,b,c)	Eu(c)	.09(5)
40	O	R5+(a,b,c)	Eu(a)	-.03(1)
41	O	R5+(a,b,c)	Eu(b)	.00(1)
42	O	R5+(a,b,c)	Eu(c)	.08(6)
43	O	X1+(a,b,c)	A2u(a)	.01(9)
44	O	X1+(a,b,c)	A2u(b)	.05(4)
45	O	X1+(a,b,c)	A2u(c)	.00(5)
46	O	X5+(a,b,c,d,e,f)	Eu(a)	-.06(1)
47	O	X5+(a,b,c,d,e,f)	Eu(b)	-.16(1)
48	O	X5+(a,b,c,d,e,f)	Eu(c)	.02(5)
49	O	X5+(a,b,c,d,e,f)	Eu(d)	.02(6)
50	O	X5+(a,b,c,d,e,f)	Eu(e)	.01(5)
51	O	X5+(a,b,c,d,e,f)	Eu(f)	.17(4)
52	O	X3-(a,b,c)	Eu(a)	.03(5)
53	O	X3-(a,b,c)	Eu(b)	-.15(4)
54	O	X3-(a,b,c)	Eu(c)	-.04(5)
55	O	X4-(a,b,c)	Eu(a)	.04(6)
56	O	X4-(a,b,c)	Eu(b)	.07(4)
57	O	X4-(a,b,c)	Eu(c)	.07(4)
58	O	X5-(a,b,c,d,e,f)	A2u(a)	.13(4)
59	O	X5-(a,b,c,d,e,f)	A2u(b)	.00(7)
60	O	X5-(a,b,c,d,e,f)	A2u(c)	-.21(1)
61	O	X5-(a,b,c,d,e,f)	A2u(d)	.08(4)
62	O	X5-(a,b,c,d,e,f)	A2u(e)	.02(4)
63	O	X5-(a,b,c,d,e,f)	A2u(f)	.02(3)
64	O	X5-(a,b,c,d,e,f)	Eu(a)	.07(5)
65	O	X5-(a,b,c,d,e,f)	Eu(b)	.01(6)
66	O	X5-(a,b,c,d,e,f)	Eu(c)	.30(2)
67	O	X5-(a,b,c,d,e,f)	Eu(d)	.10(4)
68	O	X5-(a,b,c,d,e,f)	Eu(e)	-.18(3)
69	O	X5-(a,b,c,d,e,f)	Eu(f)	.02(3)
70	O	M1+(a,b,c)	A2u(a)	.04(5)

71	O	M1+(a,b,c)	A2u(b)	.00(1)
72	O	M1+(a,b,c)	A2u(c)	-.02(5)
73	O	M2+(a,b,c)	A2u(a)	.06(5)
74	O	M2+(a,b,c)	A2u(b)	.01(1)
75	O	M2+(a,b,c)	A2u(c)	.03(5)
76	O	M3+(a,b,c)	Eu(a)	-.01(6)
77	O	M3+(a,b,c)	Eu(b)	-.98(1)
78	O	M3+(a,b,c)	Eu(c)	.13(5)
79	O	M4+(a,b,c)	Eu(a)	-.03(4)
80	O	M4+(a,b,c)	Eu(b)	.02(1)
81	O	M4+(a,b,c)	Eu(c)	-.07(5)
82	O	M5+(a,b,c,d,e,f)	Eu(a)	.01(5)
83	O	M5+(a,b,c,d,e,f)	Eu(b)	.09(4)
84	O	M5+(a,b,c,d,e,f)	Eu(c)	.01(8)
85	O	M5+(a,b,c,d,e,f)	Eu(d)	.06(6)
86	O	M5+(a,b,c,d,e,f)	Eu(e)	-.02(5)
87	O	M5+(a,b,c,d,e,f)	Eu(f)	-.12(4)
88	O	M3-(a,b,c)	A2u(a)	.11(1)
89	O	M3-(a,b,c)	A2u(b)	.0(1)
90	O	M3-(a,b,c)	A2u(c)	.04(3)
91	O	M5-(a,b,c,d,e,f)	Eu(a)	-.03(2)
92	O	M5-(a,b,c,d,e,f)	Eu(b)	-.07(5)
93	O	M5-(a,b,c,d,e,f)	Eu(c)	-.23(3)
94	O	M5-(a,b,c,d,e,f)	Eu(d)	.01(4)
95	O	M5-(a,b,c,d,e,f)	Eu(e)	-.02(6)
96	O	M5-(a,b,c,d,e,f)	Eu(f)	-.02(1)

7. Traditional Coordinates available to WO_3 P1 child subgroup

Table S 2: Traditional coordinates in WO_3 *P1* child model and there perturbation from $Pm\bar{3}m$ parent sites

Coordinate Number	Atom	Cartesian Axis	Distance from Parent Position/Å
1	W1_1	x	-.03(4)

2	W1_1	y	-.40(4)
3	W1_1	z	-.16(3)
4	W1_2	x	-.01(3)
5	W1_2	y	-.51(4)
6	W1_2	z	.36(3)
7	W1_3	x	.01(3)
8	W1_3	y	.00(4)
9	W1_3	z	.52(3)
10	W1_4	x	.04(3)
11	W1_4	y	-.05(4)
12	W1_4	z	-.03(3)
13	W2_1	x	-.08(4)
14	W2_1	y	-.49(5)
15	W2_1	z	-.12(4)
16	W2_2	x	-.02(3)
17	W2_2	y	-.49(5)
18	W2_2	z	.41(3)
19	W2_3	x	.01(4)
20	W2_3	y	-.03(5)
21	W2_3	z	.39(3)
22	W2_4	x	.04(3)
23	W2_4	y	.00(4)
24	W2_4	z	-.01(3)
25	O1_1	x	-.07(4)
26	O1_1	y	.00(5)
27	O1_1	z	-.17(4)
28	O1_2	x	-.08(4)
29	O1_2	y	-.08(5)
30	O1_2	z	.38(4)
31	O1_3	x	-.11(5)
32	O1_3	y	-.50(4)
33	O1_3	z	.43(4)
34	O1_4	x	-.20(3)

35	O1_4	y	-.56(4)
36	O1_4	z	-.02(3)
37	O2_1	x	-.13(4)
38	O2_1	y	-.60(4)
39	O2_1	z	-.23(4)
40	O2_2	x	-.18(4)
41	O2_2	y	-.53(4)
42	O2_2	z	.28(5)
43	O2_3	x	-.14(4)
44	O2_3	y	-.02(5)
45	O2_3	z	.30(4)
46	O2_4	x	-.10(4)
47	O2_4	y	-.05(6)
48	O2_4	z	-.21(3)
49	O3_1	x	.20(3)
50	O3_1	y	-.29(6)
51	O3_1	z	.42(3)
52	O3_2	x	-.33(3)
53	O3_2	y	-.29(7)
54	O3_2	z	-.11(4)
55	O3_3	x	-.31(3)
56	O3_3	y	-.15(6)
57	O3_3	z	-.04(4)
58	O3_4	x	.14(3)
59	O3_4	y	-.17(6)
60	O3_4	z	.46(3)
61	O4_1	x	-.53(2)
62	O4_1	y	-.35(4)
63	O4_1	z	-.19(3)
64	O4_2	x	.14(3)
65	O4_2	y	-.31(6)
66	O4_2	z	.14(4)
67	O4_3	x	.25(3)

68	O4_3	y	-.18(5)
69	O4_3	z	.16(4)
70	O4_4	x	-.20(3)
71	O4_4	y	-.17(5)
72	O4_4	z	-.09(3)
73	O5_1	x	.15(5)
74	O5_1	y	-.08(5)
75	O5_1	z	.12(4)
76	O5_2	x	-.45(4)
77	O5_2	y	-.03(5)
78	O5_2	z	.09(4)
79	O5_3	x	-.35(4)
80	O5_3	y	-.25(5)
81	O5_3	z	.18(4)
82	O5_4	x	.03(4)
83	O5_4	y	-.24(5)
84	O5_4	z	.00(3)
85	O6_1	x	.15(4)
86	O6_1	y	-.61(5)
87	O6_1	z	.13(4)
88	O6_2	x	-.41(4)
89	O6_2	y	-.52(4)
90	O6_2	z	.14(4)
91	O6_3	x	-.21(4)
92	O6_3	y	.03(5)
93	O6_3	z	.00(3)
94	O6_4	x	.09(4)
95	O6_4	y	.01(5)
96	O6_4	z	.14(5)

8. ISODISTORT Process for $Bi_2Sn_2O_7$ $Fd\bar{3}m$ to √2x√2x2 P1 Subgroup Tree

i) Go to http://stokes.byu.edu/iso/isodistort.php

ii) Under "Import parent structure from a CIF structure file", browse to the gamma_parent.cif on your computer and click "OK".

iii) Under Method 3, select space group symmetry "1 P1 C1-1", enter the basis {(0,0,2),(-1,-1,0),(1,-1,0)} row by row, and click "OK".

iv) Choose the only option: "1 P1, basis={(1,-1,0),(-1,-1,0),(0,0,-2)}, origin=(0,0,0), s=16, i=768" and click "OK".

v) To obtain the subgroup tree, scroll to the bottom of the page and check the "Generate TOPAS.STR output for subgroup tree" box. Then return to the top of the page, check the "Subgroup tree" radio button, and click "OK".

9. Benchmarking Computer/TA Setups

Here we benchmark the speed of each setup using the time taken to perform a standardised 5000 iterations of Rietveld refinement of 547th subgroup in the $Bi_2Sn_2O_7$ tree (1064 parameters) fitting to both X-ray and TOF neutron powder diffraction data from command line with no graphical output.

Table S 3: Speed of computational set-ups against a benchmarking test

Setup	Details	Time Taken (s)
JSOE03-2014, TA v5	Dual Core 3rd generation i5 processor (3.2 GHz)	92.32
JSOE02-2016, TA v6	Quad Core 6th generation i7 processor (3.4 GHz)	37.86

10. Comparison of Fit without Distortion Modes in Lattice Refinement Step

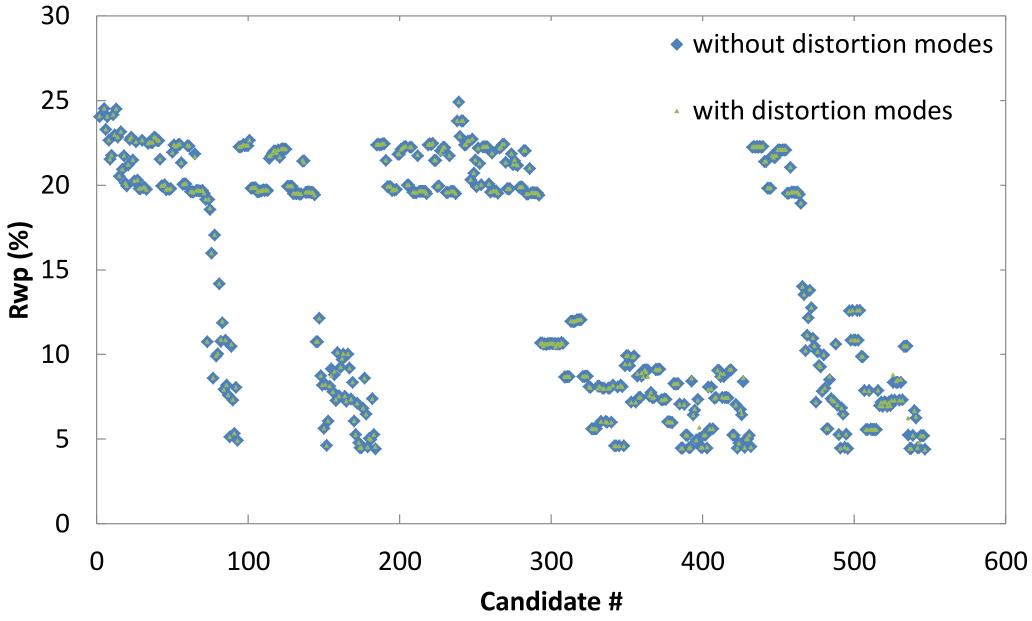

Figure S 3: Overlay plot showing combined X-ray / TOF neutron R_{wp} found for each of the 544 candidate subgroups for the exhaustive search process against β-$Bi_2Sn_2O_7$ diffraction data when distortion modes are and are not included in the lattice refinement step. An equivalent fit is found in both cases.

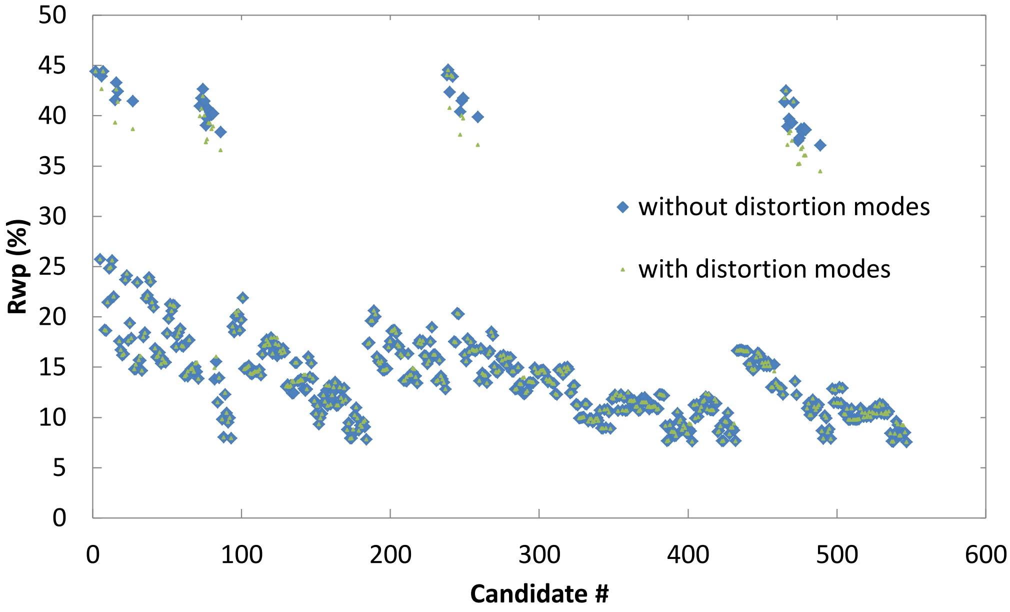

Figure S 4: Overlay plot showing combined X-ray / TOF neutron R_{wp} found for each of the 544 candidate subgroups for the exhaustive search process against α-$Bi_2Sn_2O_7$ diffraction data when distortion modes are and are not included in the lattice refinement step. An equivalent fit is found for all significant candidates. A slightly improved fit is obtained for some poor candidates when distortion modes are included.

11. Obtaining the Highest Common Subgroup Setting of β- and α-$Bi_2Sn_2O_7$

The following notes describe how to obtain equivalent and easily comparable mode-amplitude descriptions of the α and β structures in their highest common subgroup, which is candidate #174.

When artificially lowering the symmetry of both structures to the highest-common subgroup, it is important to choose matching distortion domains for them. The #174 subgroup has $12\times4\times2 = 96$ distinct distortion domains: 12 external orientations of the supercell basis, 4 origin shifts, and 2 internal orientations of the point group within the supercell. To see a complete list, decompose the #174 candidate relative to the γ-parent in ISODISTORT and view the "Domains" output.

i) Start by creating a candidate #174 .cif file. This can be done by outputting the .cif from a standard .inp format file created using the candidate #174 .str file. Set all displacive modes to zero amplitude so that this is just the γ-parent structure in the artificially-low symmetry of candidate subgroup #174.

ii) Load the β structure into ISODISTORT as the parent. Then use Method 4 to decompose #174 relative to the β parent using basis = [(0,1/2,1/2),(-1,0,0),(0,0,1)] and a fixed origin of (1/4,-1/8,-1/8) so that origin_z doesn't slide. The resulting unit cell should be *a* = 13.11003 Å, *b* = 7.57183 Å, *c* = 15.13246 Å, *α* = *β* = *γ* = 90°. Manually zero all of the mode amplitudes on the distortion page so that the parent β-structure is retained, and save as beta_st174_unshifted.cif. We now have recast the β-structure in the lower-symmetry of candidate-#174.

iii) Repeat the previous step for the α structure with the following modification: use basis = {(1,0,1),(0,1,0),(0,0,1)} and a fixed origin at (0,0,0) so that origin_x and origin_z don't slide, and name the output file alpha_st174_unshifted.cif. The resulting unit cell should be *a* = 13.14432 Å, *b* = 7.54118 Å, *c* = 15.07672 Å, *α* = 90°, *β* = 55.05408°, *γ* = 90°. We now have recast the α-structure in the lower-symmetry candidate-#174 setting with a lattice basis and origin to match those of the β structure.

iv) In ISODISTORT load the γ-phase structure as the parent and use Method 4 to decompose beta_st174_unshifted.cif with basis = {(1,1/2,1/2),(0,1/2,-1/2),(0,1,1)}. Use the "View Distortion" output to visualise the results with "axes on", and see that shifting the origin of beta_st174_unshifted by (0,0,+¼) in the coordinate system of #174 will overlay the β and γ origins. To implement the origin shift, load beta_st174_unshifted.cif into ISOCIF and use “Change Lattice and Origin” to slide the origin by (0,0,+¼), saving the result as beta_st174.cif. Do the same for alpha_st174_unshifted.cif and save the result as alpha_st174.cif. Because we have now overlayed the α and β origins with the γ origin, the ferroelectric GM4- mode amplitudes will not need to take on large values to compensate for an origin difference.

v) Candidate #174 (space group Pc) lacks a point symmetry (two-fold rotation) present in the point group of its monoclinic lattice; this missing operator toggles the α or β models between two distinct internal-orientations within the same unit cell. In order to make our comparison of the α or β-structures most effective, we want the features common to both structures to be in the same internal orientation. We already have one orientation for β; to generate the other, load beta_st174 into ISOCIF, apply the missing two-fold rotation about the monoclinic *b* axis [{-1,0,0},{0,1,0},{0,0,-1}], and save the result as beta_st174_domain17.cif. This internal orientation of β proves to best match to our α-structure file.

vi) In ISODISTORT load the γ-structure as the parent, use Method 4 to decompose alpha_st174.cif relative to γ, and save the result as alpha_st174-gamma.str using the “TOPAS.STR” output option. Then repeat for beta_st174_domain17.cif and save the result as beta_st174_domain17-gamma.str. We can now perform a detailed comparison of the mode-amplitudes in these two .str files in an ascii text editor.

vii) To readily visualize the differences between the α and β structures, use Method 4 in ISODISTORT to decompose beta_st174_domain17.cif relative to alpha_st174.cif with a unit basis and fixed origin at (0,0,0). Then use the interactive “View distortion” option to animate the linear evolution from one to the other.

viii) To isolate the key differences between α and β, which primarily affect the O`Bi$_{4/2}$ network, decompose the beta_st174_domain17.cif and alpha_st174.cif structures relative to γ parent in separate browser windows. Use the grey irrep-master sliders at the bottom of the interactive slider panel to turn off all but the L2+ and GM5+ distortions, and individually explore the effects of the L2+ and GM5+ contributions to either structure (using the appropriate irrep-master sliders).

12. Expanded View of β-, α- and γ-$Bi_2Sn_2O_7$ Distorted Structures

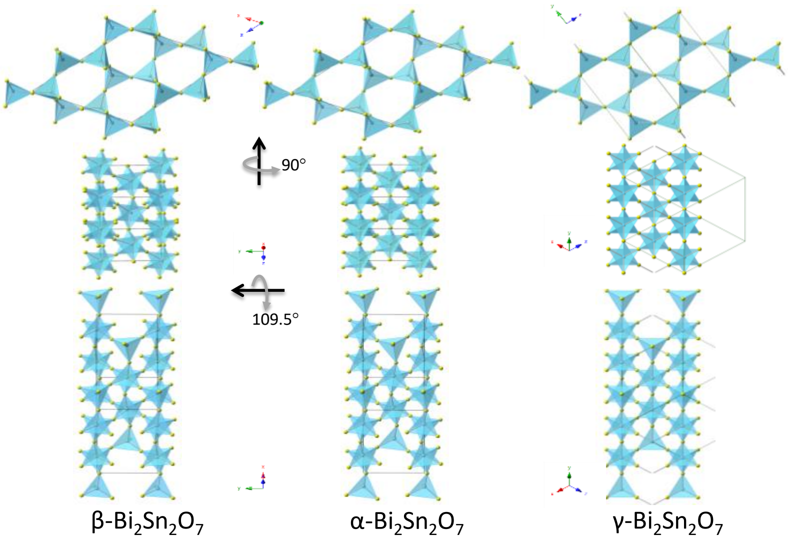

β-$Bi_2Sn_2O_7$ α-$Bi_2Sn_2O_7$ γ-$Bi_2Sn_2O_7$

Figure S 5: Views of Bi_2O\` framework tetrahedral rotations dominated by Γ_5^- and L_2^+ modes in α- and β-$Bi_2Sn_2O_7$ shown in the common subgroup setting of candidate #174. Top view is down [0 1 0], middle view down [-2 0 1], lower view down [-2 0 3]; these correspond to [-1 0 1], [1 -1 1] and [111] of parent structure. Bi and O\` atoms are shown in yellow and blue respectively. The undistorted γ-$Bi_2Sn_2O_7$ is also shown for comparison.

13. ISODISTORT Process for ZrP_2O_7 $Pa\overline{3}$ to P1 Subgroup Tree

i) Go to http://stokes.byu.edu/iso/isodistort.php

ii) Load Pa-3_real_parent.cif into ISODISTORT and click "OK"

iii) Under "Types of distortion to be considered" uncheck strain modes and click "Change"

iv) Under Method 3 enter space group *P1* and basis = {(3,0,0),(0,3,0),(0,0,3)} and click "OK"

v) On the distorted structure page select "1 P1, basis={(0,0,3),(0,3,0),(-3,0,0)}, origin=(0,0,0), s=27, i=648" and click "OK"

vi) To obtain the subgroup tree, scroll to the bottom of the page and check the "Generate TOPAS.STR output for subgroup tree" box. Then return to the top of the page, check the "Subgroup tree" radio button, and click "OK".

14. Methodology for Decomposition of Artificial $Fm\overline{3}m$ Parent to Real $Pa\overline{3}$ Parent

To decompose $Fm\overline{3}m$ parent relative to $Pa\overline{3}$ parent:

i) Go to http://stokes.byu.edu/iso/isodistort.php

ii) Load aristo_Zr225.cif into ISODISTORT and click "OK"

iii) Under “Types of distortion to be considered” uncheck strain modes and click “Change”

iv) Under Method 4 load Pa-3_real_parent.cif and click “OK”

v) On the distorted structure page select “{(1,0,0),(0,1,0),(0,0,1)}” from the dropdown list and click “OK”

vi) On the distortion page check the CIF file radio button and click “OK”. Rename this resulting CIF aristo_Zr225-pa-3_real_parent.cif

To obtain *Pbca* child structure:

vii) Go back to http://stokes.byu.edu/iso/isodistort.php

viii) Load aristo_Zr225-pa-3_real_parent.cif into ISODISTORT and click “OK”

ix) Under “Types of distortion to be considered” uncheck strain modes and click “Change”

x) Under method 3 enter space group *Pbca* and basis = {(3,0,0),(0,3,0),(0,0,3)} and click “OK”

xi) On the distorted structure page select “61 Pbca, basis={(3,0,0),(0,3,0),(0,0,3)}, origin=(0,0,0), s=27, i=81”

xii) On the distortion page check the CIF file radio button and click “OK”. Name it aristo_Zr225-pa-3_real_parent-Pbca_3x3x3.cif

xiii) Go to http://stokes.byu.edu/iso/isodistort.php

xiv) Load aristo_Zr225.cif into ISODISTORT and click “OK”

xv) Under “Types of distortion to be considered” uncheck strain modes and click “Change”

xvi) Under Method 4 load aristo_Zr225-pa-3_real_parent-Pbca_3x3x3.cif and click “OK” (you may need to check the site labels match)

xvii) On the distorted structure page select basis={(3,0,0),(0,3,0),(0,0,3)} from the dropdown list and click “OK”

xviii) On the distortion page check the topas.str radio button and click “OK” to obtain child structure with artificial to real parent modes.

To obtain *P1* child structure:

xix) Go to http://stokes.byu.edu/iso/isocif.php

xx) Load aristo_Zr225-pa-3_real_parent-Pbca_3x3x3.cif into ISOCIF and click “OK”

xxi) Click the “Reduce Symmetry to P1” button”

xxii) Click “Save CIF file” at the bottom of the page and name it aristo_Zr225-pa-3_real_parent-P1_3x3x3.cif

xxiii) Repeat steps 13-18 using aristo_Zr225-pa-3_real_parent-P1_3x3x3.cif in step 16 and selecting basis={(0,0,3),(0,3,0),(-3,0,0)} in step 17.

15. ISODISTORT Process for ZrP_2O_7 $Fm\overline{3}m$ to *P1* Subgroup Tree

1. Go to http://stokes.byu.edu/iso/isodistort.php
2. Load aristo_Zr225.cif into ISODISTORT and click “OK”
3. Under “Types of distortion to be considered” uncheck strain modes and click “Change”
4. Under Method 3 enter space group *P1* and basis = {(3,0,0),(0,3,0),(0,0,3)} and click “OK”
5. On the distorted structure page select “1 P1, basis={(0,0,3),(0,3,0),(-3,0,0)}, origin=(0,0,0), s=108, i=5184” and click “OK”
6. To obtain the subgroup tree, scroll to the bottom of the page and check the “Generate TOPAS.STR output for subgroup tree” box. Then return to the top of the page, check the “Subgroup tree” radio button, and click “OK”.

16. Reduce RT $(Ce_{0.78}La_{0.22})_2O_2MnSe_2$ / $Ce_2O_2Fe_{0.75}Zn_{0.25}Se_2$ to Shubnikov Group 1.1 in ISODISTORT

1. Go to http://stokes.byu.edu/iso/isodistort.php
2. Click browse, load find_mag_cmca_01.cif / Ce2O2Fe0_75Zn0_25Se2_CIF.cif and click “OK”
3. Under “Types of distortions to be considered” uncheck strain modes and check Ce and Mn / Fe magnetic modes and then click “Change”. As the distortion from RT to LT structure is entirely magnetic, you may uncheck all the displacive distortions but the magnetic GA tutorial explains how you can decide whether to include the displacive modes in the GA if you retain them.
4. On the distorted structure page select the option “1.1 P1, basis={(0,0,1),(0,1,0),(-1,0,0)}, origin=(0,0,0), s=2, i=32” and click “OK”
5. On the distortion page check the “TOPAS.STR” button and and click “OK”

17. Determine Magnetic Space Group by Superposing Irrep in ISODISTORT for $(Ce_{0.78}La_{0.22})_2O_2MnSe_2$ / $Ce_2O_2Fe_{0.75}Zn_{0.25}Se_2$

1. Load find_mag_cmca_01.cif / Ce2O2Fe0_75Zn0_25Se2_CIF.cif into ISODISTORT and click “OK”

2. Under “Types of distortions to be considered” uncheck all types except for magnetic Ce and Mn / Fe modes
3. Under Method 2 choose the Y point from the drop down list and click “OK”
4. On the distorted structure page select mY2- / mY1+ from the drop down list and click “OK”
5. On the order parameter direction page select “P1 (a) 62.455 P_Cnma, basis={(0,1,0),(1,0,0),(0,0,-1)}, origin=(1/4,1/4,0), s=2, i=2, k-active= (1,0,0)” / “P1 (a) 53.335 P_Cmna, basis={(1,0,0),(0,0,1),(0,-1,0)}, origin=(0,0,0), s=2, i=2, k-active= (1,0,0)” and click “OK”
6. On the distortion page check the “TOPAS.STR” radio button and click “OK” to obtain a structure file

18. Magnetic GA Tutorial

A full tutorial for using a GA to search magnetic space group symmetry using $(Ce_{0.78}La_{0.22})_2O_2MnSe_2$ as an example is available at https://community.dur.ac.uk/john.evans/topas_workshop/tutorial_GA_magnetic.htm

Guide to e-Appendixes

A DVD is attached to this thesis containing the following:

1. *P1* child RT and *P4* child HT WO_3 fits with fixed non-structural parameters extracted

The baseline .inp file for RT / HT WO_3 searches is in: e-appendix\1\RT_WO3_child_fit.inp/ HT_WO3_child_fit.inp.

2. Exhaustive Search Script

This is an exhaustive search python script with line by line comments showing subgroups structural information is added to start files, refined in TA and outputs collected in iterative fashion. It can be found in: e-appendix\2\All_in_one_Exhaustive_Searcher_4.py.

3. Subgroups in the WO_3 RT Tree

A table listing all candidates in the RT WO_3 exhaustive search tree can be found in e-appendix\3\WO3 RT Subgroups.docx.

4. Subgroups in the WO_3 HT Tree

A table listing all candidates in the HT WO_3 exhaustive search tree can be found in e-appendix\4\WO3 HT Subgroups.docx.

5. Convergence Cycles in the WO_3 RT Search

A table of statistics from each convergence cycle in the RT WO_3 search can be found in e-appendix\5\WO3 RT Convergences.docx.

6. Convergence Cycles in the WO_3 HT Search

A table of statistics from each convergence cycle in the HT WO_3 search can be found in e-appendix\6\WO3 HT Convergences.docx.

7. *P1* Child Fits to β- and α-$Bi_2Sn_2O_7$

The baseline .inp file for the fit of the *P1* $Bi_2Sn_2O_7$ child to both β- and α- data can be found in e-appendix\7\beta\topas0547_best.inp and e-appendix\7\alpha\topas0547_best.inp respectively.

8. Subgroups in the $Bi_2Sn_2O_7$ tree

A table listing all candidates in the $Bi_2Sn_2O_7$ exhaustive search tree can be found in e-appendix\8\Bi2Sn2O7 Subgroups.docx.

9. Convergence Cycles in the β-$Bi_2Sn_2O_7$ Search

A table of statistics from each convergence cycle in the β-$Bi_2Sn_2O_7$ search can be found in e-appendix\9\beta Bi2Sn2O7 Convergencess.docx.

10. Convergence Cycles in the α-$Bi_2Sn_2O_7$ Search

A table of statistics from each convergence cycle in the α-$Bi_2Sn_2O_7$ search can be found in e-appendix\10\alpha Bi2Sn2O7 Convergencess.docx.

11. Distorted β- and α-$Bi_2Sn_2O_7$ Structure Files for ISODISTORT Visualisation

A series of distortion files can be found in e-appendix\11 including:

i) alpha_st174-gamma_distortion.txt (the alpha structure in common subgroup setting).

ii) beta_st174_domain17-gamma_distortion.txt (the beta structure in common subgroup setting).

iii) bi2o_gamma_alpha_st174_bi4o_distortion.txt (equivalent alpha structure focussing on Bi_2O` framework).

iv) bi2o_gamma_beta_st174_domain17_bi4o_distortion equivalent beta structure focussing on Bi_2O` framework).

12. Subgroups in ZrP_2O_7 $Pa\bar{3}$ to *P1* Subgroup Tree

A table listing all candidates in the ZrP_2O_7 $Pa\bar{3}$ to $P1$ exhaustive search tree can be found in e-appendix\12\ZrP2O7 Subgroups.docx.

13. All Distortion Modes Available to ZrP_2O_7 *P1* Child

A table listing all distortion modes available to ZrP_2O_7 in the rotational mode decomposition and their amplitude in our 93 mode model can be found in e-appendix\13\ZrP2O7 Distortion Modes.docx.

14. All Distortion Modes Available to $(Ce_{0.78}La_{0.22})_2O_2MnSe_2$ Magnetic Space Group 1.1 Child

A table listing all distortion modes available to $(Ce_{0.78}La_{0.22})_2O_2MnSe_2$ in the magnetic mode decomposition and their amplitude in the magnetic space group 62.455 model can be found in e-appendix\15\Ce0_78La0_22OMn0_5Se Distortion Modes.docx.

15. All Distortion Modes Available to $Ce_2O_2Fe_{0.75}Zn_{0.25}Se_2$ Magnetic Space Group 1.1 Child

A table listing all distortion modes available to $Ce_2O_2Fe_{0.75}Zn_{0.25}Se_2$ in the magnetic mode decomposition and their amplitude in the magnetic space group 53.335 model can be found in e-appendix\15\Ce2O2Fe0_75Zn0_25Se2 Distortion Modes.docx.

16. Magnetic Space Group 1.1 $Ce_2O_2Fe_{0.75}Zn_{0.25}Se_2$ model

The baseline .inp file for the fit of the magnetic space group 1.1 $Ce_2O_2Fe_{0.75}Zn_{0.25}Se_2$ child model can be found in e-appendix\14\Ce2O2Fe0_75Zn0_25Se2_CIF-magSG_1pt1_all_modes.inp.

CHEMISTRY OF MATERIALS
Article
pubs.acs.org/cm

3D Transition Metal Ordering and Rietveld Stacking Fault Quantification in the New Oxychalcogenides $La_2O_2Cu_{2-4x}Cd_{2x}Se_2$

Chris M. Ainsworth,[†] James W. Lewis,[†] Chun-Hai Wang,[†,‡] Alan A. Coelho,[§] Hannah E. Johnston,[†,⊥] Helen E. A. Brand,[∥] and John S. O. Evans*,[†,#]

[†]Department of Chemistry, University Science Site, Durham University, South Road, Durham DH1 3LE, United Kingdom
[§]72 Cedar Street, Wynnum, 4178 Brisbane, Australia
[∥]Australian Synchrotron, 800 Blackburn Road, Clayton, Victoria 3168, Australia
[#]ANSTO (Australian Nuclear Science and Technology Organisation), New Illawarra Road, Rutherford Avenue, Lucas Heights, New South Wales 2234, Australia

Ⓢ *Supporting Information*

ABSTRACT: A number of LnOCuCh (Ln = La–Nd, Bi; Ch = S, Se, Te) compounds have been reported in the literature built from alternating layers of fluorite-like $[Ln_2O_2]^{2+}$ sheets and antifluorite-like $[M_2Se_2]^{2-}$ sheets, where M is in the +1 oxidation state leading to full occupancy of available $MSe_{4/2}$ tetrahedral sites. There is also a family of related $LnOM_{0.5}Se$ (Ln = La & Ce, M = Fe, Zn, Mn & Cd) compounds built from alternating layers of $[Ln_2O_2]^{2+}$ sheets and $[MSe_2]^{2-}$ sheets, where M is in the +2 oxidation state with half occupancy of available tetrahedral sites and complex ordering schemes in two dimensions. This paper reports a new family of compounds containing both +1 and +2 metal ions in the $La_2O_2Cu_{2-4x}Cd_{2x}Se_2$ family. We show how Cu^{1+} and Cd^{2+} ions segregate into distinct fully occupied and half occupied checker-board-like layers respectively, leading to complex long-range superstructures in the third (stacking) dimension. To understand the structure and microstructure of these new materials we have developed and implemented a new methodology for studying low and high probability stacking faults using a Rietveld-compatible supercell approach capable of analyzing systems with thousands of layers. We believe this method will be widely applicable.

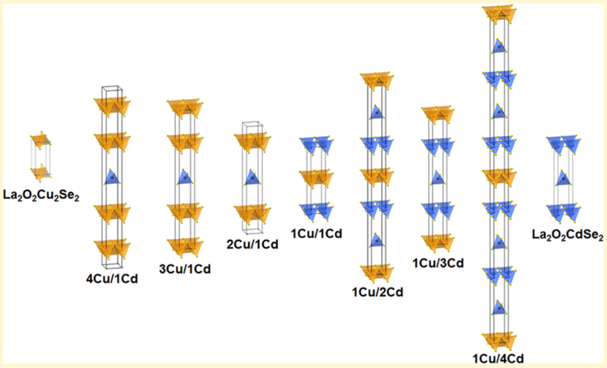

■ INTRODUCTION

Mixed-anion materials display a wealth of fascinating exploitable properties based on their superconductivity, thermoelectric behavior, optical properties, intercalation and ion-exchange chemistry, magnetism, and others.[1−14] These properties are, of course, intimately related to their 3D structure and influenced by the specific architectures enforced or enabled by the simultaneous bonding requirements of different cation/anion combinations. We have previously described how combining rigid-geometry oxide building blocks with more flexible or adaptive chalcogenide layers can lead to infinitely adaptive structures with remarkable structural complexity (though governed by simple rules) in two dimensions.[14,15] Here we show that this complexity can be extended to three dimensions in a new family of mixed-metal oxychalcogenides. We unravel their crystal chemistry from powder diffraction studies, despite stacking faults leading to nonroutine peak shapes. We show how it is possible to reproduce these complex experimental observations in a quantitative Rietveld approach using a simple two-parameter description across the entire structural series.

The compounds we report are structurally related to LnOCuCh (Ln = La–Nd, Bi; Ch = S, Se, Te) materials[16,17] (though we use a doubled $La_2O_2Cu_2Ch_2$ formula for convenience in most of the paper). These adopt the tetragonal ZrCuSiAs structure, space group *P*4/*nmm* (Figure 1, left). The structure is built up from alternating layers of fluorite-like $[Ln_2O_2]^{2+}$ sheets and antifluorite-like $[Cu_2Ch_2]^{2-}$ sheets. The oxidation state of Cu within these structures is +1, with full occupancy of available tetrahedral sites. These materials are of particular interest for their unusual optical/electronic properties combining high transparency and high electronic conductivity. For example, the La compounds are wide band gap systems (3.1/2.8 eV for S/Se) with p-type conductivity up to 910 S cm^{-1}. The high conductivity arises from either Cu vacancies or Sr doping generating holes at the largely Cu 3d/Se 4p derived valence band maximum.[16−20] Strong blue to UV emission is also observed and a room temperature blue emitting diode has

Received: March 4, 2016
Revised: March 31, 2016
Published: April 4, 2016

DOI: 10.1021/acs.chemmater.6b00924
Chem. Mater. 2016, 28, 3184−3195

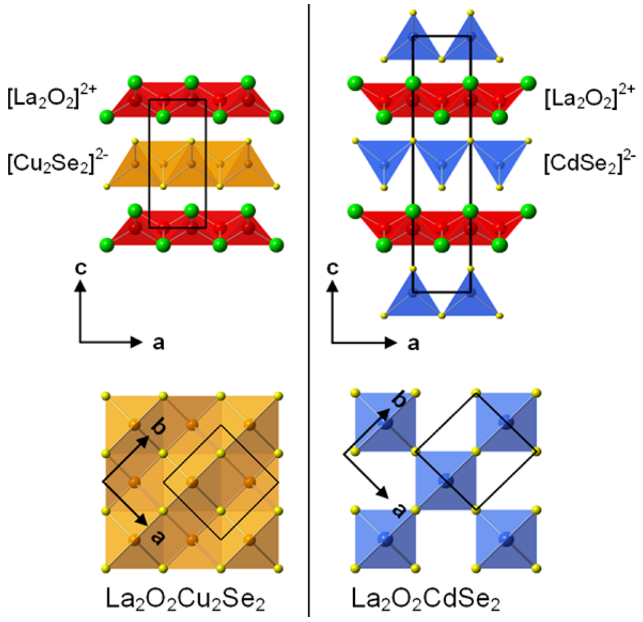

Figure 1. ZrCuSiAs-derived structures reported for (left) $La_2O_2Cu_2Se_2$, *P*4/*nmm* symmetry, (right) $La_2O_2CdSe_2$, *P*4$_2$/*nmc* symmetry. Top figures show the fluorite-like sheets of edge-sharing Ln_4O tetrahedra (red) and antifluorite-like sheets of MSe_4 tetrahedra (orange/blue). Bottom figures are the view down [001], showing the arrangement of MSe_4 tetrahedra. La^{3+} cations are shown in green, O^{2-} anions in red, Cu^{1+} cations in orange, Cd^{2+} cations in blue, and Se^{2-} anions in yellow.

been demonstrated.[21] Recently the low thermal conductivity and relatively high electrical conductivity of BiOCuSe ($\sigma \approx 10$ S cm^{-1}, $\kappa = 1.0$ W m^{-1} K^{-1}) have created significant interest in thermoelectric applications and $zT\left(=\frac{\alpha^2\sigma}{\kappa}\right)T$ values up to 1.4 have been reported.[5−7] Perhaps the most famous compounds with this structure type are derived from LaOFeAs, and[16−20]superconduct at temperatures up to 55 K.[1,2]

We and others have recently reported the structures of a range of related compounds containing 2+ metals, where charge balance leads to half the available metal sites in the tetrahedral layers being occupied and composition $Ln_2O_2MSe_2$.[13−15,22−27] In the case of M = Cd this leads to the simple checkerboard (or Z_4^-) ordering pattern of Figure 1 in which tetrahedra are exclusively corner-shared.[23] In other systems (M = Fe, Mn, Zn, Cd and combinations thereof), the high rigidity of the $[Ln_2O_2]^{2+}$ layer can be used to tune the M^{2+} architecture from exclusively corner-sharing (e.g., La/Cd) to exclusively edge-sharing (e.g., Ce/Fe). Between these extremes, we can generate compounds with different corner- to edge-sharing (C:E) integral ratios such as 5:1 (e.g., (Ce,La)/Mn), 4:1 (e.g., Ce/Zn), 3:1 (e.g., La/Zn) as well as incommensurate intermediate structures.[14,15] As such, we can prepare an infinitely adaptive series with large and complex superstructures in the *ab* plane.

In this work, we report the synthesis and characterization of the first M^{1+}/M^{2+} systems, the $LaOCu_{1-2x}Cd_xSe$ or $La_2O_2Cu_{2-4x}Cd_{2x}Se_2$ family. We again find a remarkable degree of long-range cation ordering, this time along the *c*-axis of the structures and show that we can access each of the new structure types shown schematically in Figure 2 for $x = 0$ (all Cu) to $x = 0.5$ (all Cd). As might be anticipated for layered materials with long-range periodicities, a variety of low-level stacking faults are suggested by the widths and asymmetry of weak superstructure peaks in the powder pattern that evidence this ordering. To derive full information on both the structure and microstructure of these materials has required development

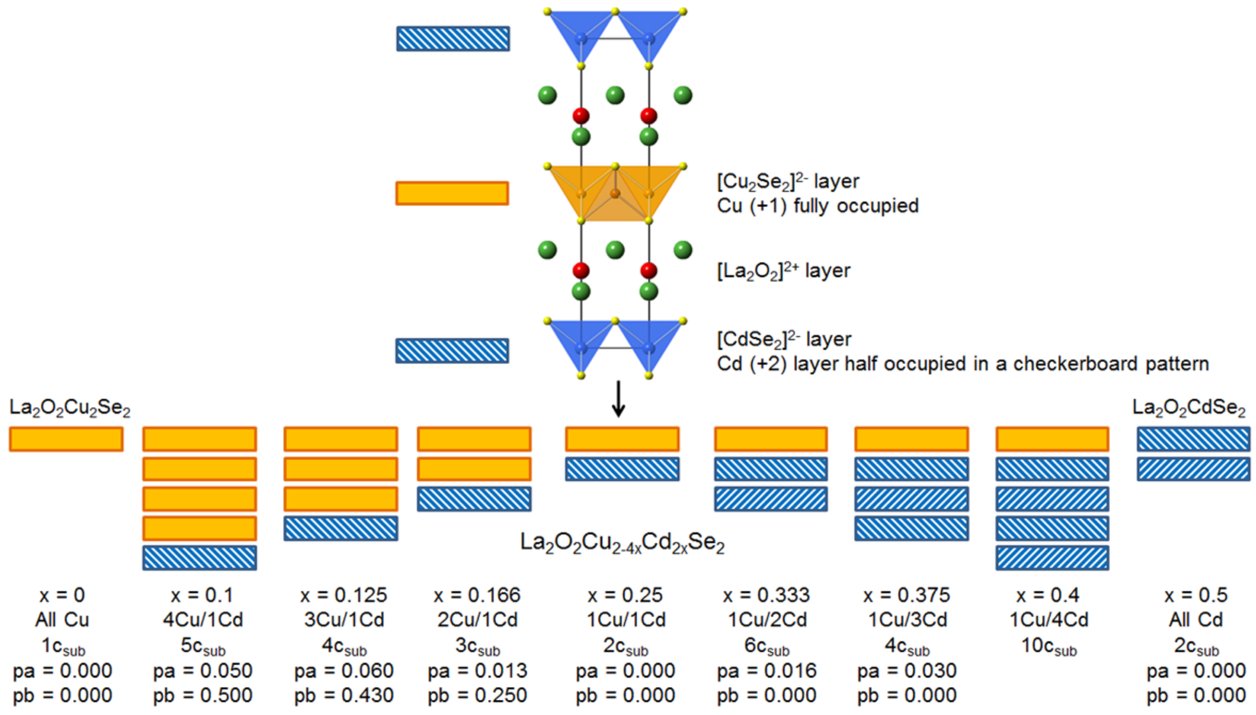

Figure 2. Schematic showing the unique crystallographic layers in samples prepared in the $La_2O_2Cu_{2-4x}Cd_{2x}Se_2$ solid solution. The *c* axis length relative to a $Ln_2O_2Cu_2Ch_2$ subcell model is shown along with the fraction of *pa* and *pb*-type faults present (discussed later in the text). Direction of blue hatching reflects different positions in the *ab* plane of Cd-centered tetrahedra.

DOI: 10.1021/acs.chemmater.6b00924
Chem. Mater. 2016, 28, 3184−3195

of a DIFFaX-like[28] approach to the treatment of stacking faults in a Rietveld refinement. We demonstrate for the first time that this approach is both possible and highly effective with models containing thousands of stacked layers and show how it leads to a simple description of the diffraction patterns of all the materials using two faulting probabilities.

Structure faults of this type are extremely common in a range of different materials and can have significant impact on their properties and function.[29] Examples include a wide range of battery materials,[30−36] zeolites,[37−44] metals,[45,46] clays,[47,48] diamond,[49,50] ice,[50,51] nitrides,[52−54] carbides,[55−57] catalysts,[58] layered hydroxides, and other intercalation/ion-exchange hosts.[59−62] The Rietveld method we describe will be applicable to all these systems and will allow detailed and precise information to be obtained on the structure of individual phases and quantification of phase mixtures and their evolution in operando.

EXPERIMENTAL SECTION

Fifteen samples in the $La_2O_2Cu_{2-4x}Cd_{2x}Se_2$ solid solution were prepared as polycrystalline powders. All samples were prepared according to the equation below, using the following reagents: La_2O_3 (99.99%, Sigma-Aldrich, heated to 1000 °C before use), Cu (99.9%, Alfa Aesar), Cd (99.5%, Alfa Aesar), Se (99.999%, Alfa Aesar), Al (99.5%, Alfa Aesar).

$$La_2O_3 + (2-4x)Cu + 2xCd + 2Se + \frac{2}{3}Al \rightarrow La_2O_2Cu_{(2-4x)}Cd_{2x}Se_2 + \frac{1}{3}Al_2O_3$$

Reagents were intimately ground and placed in an alumina crucible. Al powder (10% molar excess) was placed in a second alumina crucible to act as an oxygen getter, forming Al_2O_3 during the reaction. These two crucibles were placed in an evacuated ($<1 \times 10^{-3}$ atm) silica tube and slowly heated to a final dwell temperature of 1100 °C for 12 h, before cooling to room temperature.

For Rietveld analysis, X-ray data were collected on the powder diffraction beamline at the Australian synchrotron. Samples were loaded in a 0.3 mm capillary, and data collected using the Mythen microstrip detector from 1−81° 2θ with a wavelength of 0.6354462(7) Å. To cover the gaps between detector modules, 2 data sets were collected with the detector set 0.5° apart and then merged to a single data set using in-house data processing software, PDViPeR. Standard Rietveld refinements were performed using the Academic version of the TOPAS software.[63−65]

Stacking faults leading to broadening and asymmetry of peaks in the powder diffraction patterns were investigated using a DIFFaX-like Rietveld approach in TOPAS. Details of the method are included in the Results and Discussion section. In brief, the crystal structure is described in terms of layers containing fixed blocks of atoms. These are stacked on top of each other in a supercell of the basic 9 Å cell of $La_2O_2Cu_2Se_2$ using the format defined in the Topas manual.[64] This description allows significant simplification of structure factor calculations. The vectors describing possible transitions between layers and the probability rules for different layer-to-layer transitions are included in the TOPAS input file using a format similar to that of the DIFFaX software package. An external Python routine reads this information and produces a series of input files for Rietveld refinement in which stacking probabilities are systematically varied. The Python script submits each stack to TOPAS for Rietveld refinement and analyses and tabulates fault distributions and the model's fit to the diffraction data. A large number of different layer types can be stacked with up to six independent layer-to-layer probabilities *pn* which are expressed symbolically using the format *pa*, *pb*, 1−*pa*, 1−*pa*−*pb*, etc., such that the sum of probabilities from any layer is 1.0. This gives sufficient flexibility to define a variety of different faults and memory effects. Recent speed enhancements made in TOPAS v6 mean that we could explore large supercells with low probability faults. We discuss investigations on supercells with up to 5000 layers, *c*-axis dimensions up to 35 000 Å and up to 28 000 atoms in the primitive unit cell. Note that despite the large number of atoms in a supercell description, the linking of coordinates between different layers means that complex structural descriptions are possible with a small (e.g., just one or two stacking fault probabilities) number of additional parameters.

RESULTS AND DISCUSSION

Stacking Fault Methodology. The powder diffraction data of several of the new compounds described below showed significant *hkl*-dependence to peak widths and/or marked Warren-like[66] peak shapes, which are suggestive of stacking faults.[67] Such faults are commonly found in layered materials, and although there have been various analytical and computational approaches to quantify them, readily accessible Rietveld-like approaches are limited. One implementation is the DIFFaX + suite of Leoni et al., which places the Treacy, Newsam and Deem DIFFaX algorithm in a least-squares framework to allow refinement of stacking fault probabilities, though the approach is computationally demanding.[68] A second is the FAULTS approach of Casas-Cabanas et al.[69] To fully characterize our materials we have therefore developed and applied a DIFFaX-like[28] methodology for Rietveld refinement in the TOPAS suite which offers significant speed and flexibility advantages over previous approaches. It allows analysis of stacking faults alongside all the other features of TOPAS (multiphase, multidata set, user-defined fitting functions and convolutions, parametric refinements, symmetry mode refinements, magnetism, etc.). Our method builds on the supercell approach described by Ufer and co-workers[47,48,70] which has been applied in a Rietveld-like context for systems with a limited number of layers by Wang and Bette.[71,72] In this method the structure is described in terms of a stack of individual layers in a supercell defined along the *c*-axis of the basic crystallographic cell. Individual layers in this supercell may differ in terms of chemical composition, internal structure or overall position in *x*, *y* or *z* relative to a reference layer. For a perfect or unfaulted stacking sequence the calculated pattern from the supercell will be identical to a conventional crystallographic subcell description (as all supercell reflections will have zero intensity). As faults are introduced into the stack, the superposition of multiple closely spaced supercell reflections will sum to produce the complex peak shapes observed experimentally. By embedding this in a Rietveld package such as TOPAS, one can obtain simultaneous information about structure and microstructure of new materials. In our implementation the probabilities *pn* of layer-to-layer transitions are defined using a probability matrix of the format defined in the DIFFaX software package of Treacy et al.[28] A python routine reads this matrix and produces an input file suitable for Rietveld refinement in TOPAS. For structures containing layers of different chemical composition, the user can control the overall composition.

One of the major issues with this approach has been the size of the supercell that can be used. There are many potential advantages of using a large supercell: low probability stacking faults can be identified, the closely spaced *hkl* reflections better approximate the continuous diffuse scatter expected in reciprocal space, and an individual supercell description is likely to be a good statistical approximation of the ensemble of different crystallites contributing to the powder pattern. There are, however, significant computational bottlenecks associated with calculating the powder pattern from a large supercell, in particular the large number of reflections that must be summed to produce the calculated pattern, y_{calc}. In previous work, this has required handling *00l* and *hk0* reflections separately for turbostratic systems,[47,48] or the use of relatively small supercells to approximate materials.[71,72] In this work, we have introduced new approximations to the Rietveld method which circumvent this problem. The most significant of these impacts the peaks buffer. TOPAS uses a peaks buffer for computational efficiency when calculating peak shapes over a defined narrow 2θ range. Peak shapes only need to be calculated for reflections at the start and end of a 2θ range; these end peaks are then interpolated or stretched to realize intervening peaks, leading to significant speed gains. Peaks invariably comprise the convolution of instrument and sample aberrations with the emission profile to form the final peak shape. The number of peaks stored in the peaks buffer (or the number of 2θ ranges needed to fit the whole pattern) is determined by looking at allowed changes in these aberrations as a function of 2θ. When changes exceed predefined limits a new 2θ range is created. These predefined aberration limits can be modified but in practice this is rarely done because of the complexity of the procedure. In cases where aberrations are *hkl*-dependent, anisotropic peak broadening for example, TOPAS traditionally eliminates the peaks buffer and instead a new peak is calculated for each reflection regardless of any similarities in peak shapes. This process works well in typical Rietveld refinements where a few hundred to maybe a few thousand reflections are present.

In the present work, supercells can result in hundreds of thousands to even millions of *hkl* reflections each potentially having a unique peak shape due to a *hkl*-dependent aberration. To speed up the process TOPAS now allows tolerances to be defined at the parameter level with subsequent peak groupings handled automatically. Parameters can, for example, correspond to peak positions, peak widths, or even the magnitude of any *hkl*-dependent function. Multiple criteria can be used where peak groups can be further subdivided. The net result is that a whole pattern can be described using hundreds rather than hundreds of thousands of peaks.

An additional speedup in calculation comes at the stage where the reduced number of peaks is summed onto the diffraction pattern. For a sequence of closely spaced *hkl* reflections belonging to a particular group the peak intensities are apportioned to a pair of *hkl* reflections at the start and end of the sequence. The final result is the ability to synthesize diffraction patterns in a fraction of the time with little or no loss in precision, allowing Rietveld refinement with very little impact on the fit quality or the derived parameters. Of equal importance is the reduction in computer memory usage realized through the reduction in the size of the peaks buffer; Rietveld refinement without such a reduction in memory would not otherwise be possible.

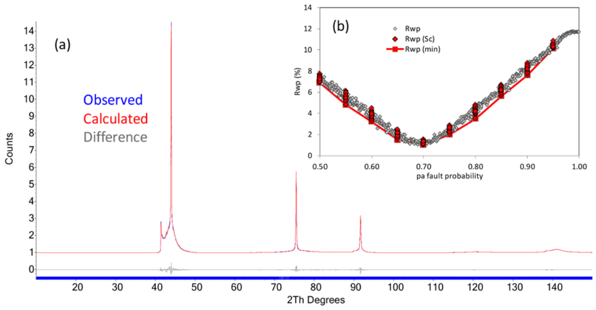

Figure 3. (a) Stacking mode Rietveld fit to a DIFFaX-simulated powder pattern of faulted cubic/hexagonal diamond. 5000 layers with a fault probability of 0.7 give excellent agreement to the simulated data. The blue "bar" at the bottom of the figure represents tick markers for each of the 236884 *hkl* reflections predicted over this 2θ range. (b) Dependence of R_{wp} on *pa*. Gray open points are a series of stacks with different *pa*; closed red points are a series of 100 repeat stacks at discrete *pa* values.

As an illustration of this approach we used the test input file dia.dat distributed with the DIFFaX suite to calculate the expected powder pattern for a sample of stacking-faulted diamond containing intergrowths of the cubic diamond and hexagonall lonsdaelite forms with a 0.7 probability (*pa*) of ideal c−c and h−h stacking and a 0.3 probability (1−*pa*) of h−c or c−h faults. This example is discussed in the literature and produces the complex peak shapes shown in Figure 3.[28] These simulated data were then fitted using our Rietveld approach with a supercell containing 5000 carbon layers and unit-cell parameters $a = 2.518$, $b = 2.518$, $c = 10292$ Å, giving a total of 236884 predicted *hkl* reflections from 10 to 150° 2θ. As described in the DIFFaX manual, this cell is a superstructure of the hexagonal setting of the diamond cell, with a 5000 × 2.05859 Å supercell along the *c*-axis (parallel to [111] of the cubic cell). Using the peaks buffer approach the pattern could be well-approximated using just 285 *hkl* reflections with no change in R_{wp}. Figure 3a shows the Rietveld fit for this model using just 7 refined parameters (1 scale, 2 isotropic peak shape parameters, 4 background terms) for a faulting probability of *pa* = 0.7. An excellent agreement is observed between the simulated data and the Rietveld fit, and the complex peak shapes are extremely well reproduced.

Figure 3b shows the Rietveld agreement factor R_{wp} as the stacking fault probability *pa* is systematically varied from 0.5 to 1.0. A clear minimum in R_{wp} is found at *pa* = 0.7 showing that the fault probability can be well quantified for this system. To produce this figure two methods were used. In a first run 500 models were tested as *pa* was changed in steps of 0.01. In a second run, 50 repeat stacks were analyzed at *pa* values from 0.50 to 0.95 in 0.05 steps. The vertical scatter in R_{wp} above the minimum therefore gives an indication of how different stacks produced using the same stacking probability influence R_{wp}. The scatter in R_{wp} (standard deviation 0.1 close to the *pa* minimum) shows that a 5000 layer stack gives a good statistical model for the infinite stack simulated by DIFFaX. These calculations can be performed rapidly on a modest PC. On an i7 3.4 GHz single core desktop computer each Rietveld cycle took <0.35 s with a peak memory use of 110 Mb such that the 1000 repeat refinements of Figure 3b took around 3 h. Without the peak buffer improvements, 2.9 Gb of memory is needed even for this simple system and cycles are 10 times slower.

Using fewer layers in the Rietveld model gives an increase in the R_{wp} spread, but the minimum remains reasonably defined even with only 100 layers. The increased spread of R_{wp} arises due to the different superstructure peak intensities from different specific layer sequences in the stacks. When investigating low probability faults in small stacks it is important to fit multiple stacks generated with a given set of transition probabilities to the diffration data. The best fit to the data is typically achieved by averaging the calculated patterns of multiple models to better represent the ensemble of crystallites in a sample.[67] This approach was applied to the different $La_2O_2Cu_{2-4x}Cd_{2x}Se_2$ phases prepared in this work.

New $La_2O_2Cu_{2-4x}Cd_{2x}Se_2$ Materials. Samples across the $La_2O_2Cu_{2-4x}Cd_{2x}Se_2$ solid solution were synthesized over 12 h at 1100 °C with an aluminum oxygen getter to control oxygen composition. $La_2O_2Cu_2Se_2$ and $La_2O_2CdSe_2$ were colored khaki and sienna, respectively, whereas all other samples were yellow-ochre. These colors are shown visually in the Table S1.

Powder X-ray diffraction data showed that in all cases, layered ZrCuSiAs-related phases had formed with a unit cell $a = b \approx 4$ Å, $c \approx 9$ Å (the subcell), explaining the main peaks present. Weak additional reflections were observed at low angles for all samples (with the exception of $Ln_2O_2Cu_2Ch_2$, where full occupancy of the Cu site gives no supercell reflections), which could not be attributed to known impurity phases. It is shown below that these arise from transition metal ordering. The layered phases account for >98.5% weight percentage in all the new compounds prepared, with a minor La_2O_2Se impurity. Table S2 gives the weight percentages of the phases formed for all samples.

Unit cell volumes (Figure 4) showed a smooth variation across the series suggesting a smooth change in structure with composition. The a cell parameter remains relatively unchanged across the series (see Figure S1), whereas the c-axis expands rapidly. As in related materials, this shows the high rigidity of Ln_2O_2 layers relative to M_nSe_2 layers. The compositions we discuss in detail below contained a single layered phase (the red points of Figure 4). For some other compositions we see evidence of phase segregation. For example at a nominal $x = 0.45$ we see three similar layered phases with cell volumes corresponding to $x = 0.4$, $x = 0.46$, and $x = 0.5$ in a ∼ 5:14:1 ratio as indicated by the three vertical gray points for this nominal composition. This implies an inherent stability of the ordered structures shown in Figure 2 and discussed below.

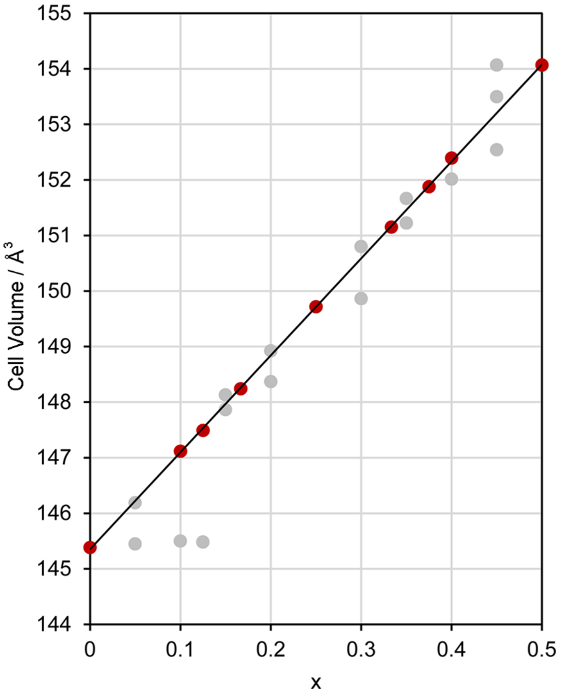

Figure 4. Variation in cell volume of phases formed across the $La_2O_2Cu_{2-4x}Cd_{2x}Se_2$ solid solution. Red and gray circles are explained in the text.

$x = 0$ (all Cu) and $x = 1$ (all Cd). $La_2O_2Cu_2Ch_2$ and $La_2O_2CdSe_2$ end members were synthesized and diffraction data were fully consistent with the structures previously reported in the literature and shown in Figure 1. PXRD data are included in Figure 12. Minor (2%) impurities are present in the Cd end member under these synthetic conditions. Fully pure samples can be made at 950 K.[23] For this work, we deliberately chose a single set of synthesis conditions for all compositions.

$x = 0.25$ $La_2O_2CuCd_{0.5}Se_2$ (1Cu/1Cd layer). Synchrotron data of the $x = 0.25$ composition showed that a layered ZrCuSiAs-related phase had formed with a unit cell $a = b = 4.07$ Å, $c = 9.05$ Å (the subcell), explaining the main peaks present. Figure 5a shows a $La_2O_2Cu_2Se_2$ model, $P4/nmm$ (red) refined against the experimental data (blue). Weak additional reflections are clearly observed. Figure 5b shows a refined $La_2O_2CdSe_2$ model, space group $P4_2/nmc$, which fits some but not all of the supercell reflections.

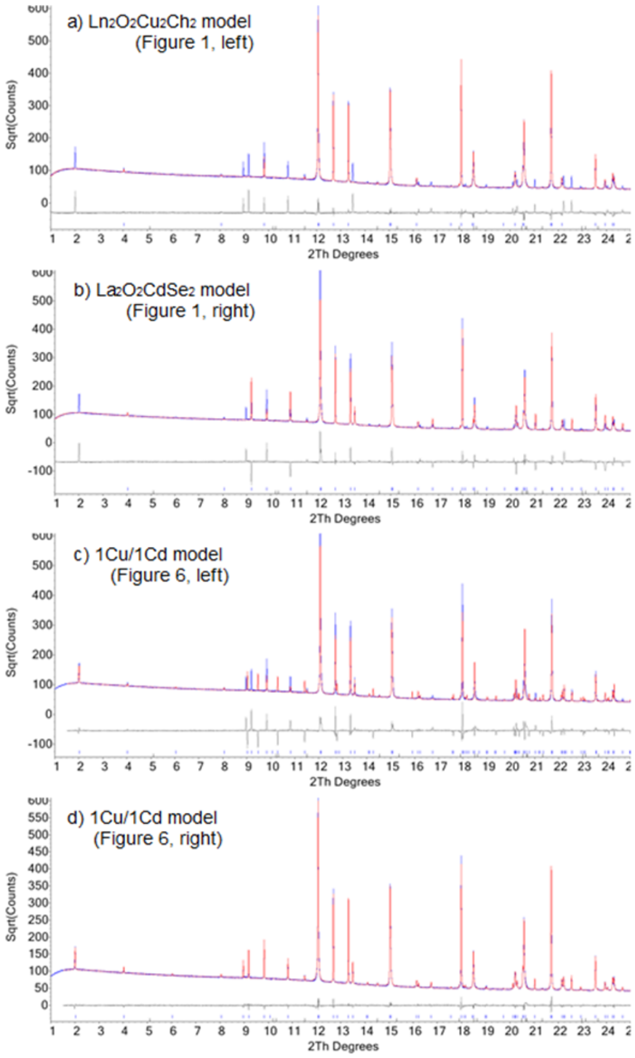

Figure 5. Rietveld refinement profiles of synchrotron powder diffraction data for $La_2O_2CuCd_{0.5}Se_2$ using the structural models discussed in the text. The correct model is that given in Figure 6, right. A $\sqrt{I}$ y-scale is used to emphasize the weaker supercell reflections.

The ionic radii of Cu^{1+} and Cd^{2+} ions differ considerably; Shannon's tables give values of 0.6 and 0.78 Å for Cu^{1+} and

DOI: 10.1021/acs.chemmater.6b00924
Chem. Mater. 2016, 28, 3184−3195

Cd^{2+}, respectively.[73] Models were therefore investigated which have Cu and Cd in distinct layers. If this occurs, a sample with composition $La_2O_2CuCd_{0.5}Se_2$ would need to have a 1:1 ratio of Cu^{1+} layers (fully occupied) to Cd^{2+} layers (half occupied). Perhaps the most likely structural model of this sort would have alternating Cu and Cd layers, with the Cd occupying alternate checkerboard sites either side of a given Cu layer. This model is shown in Figure 6 (left), and would have space group $P4_2/nmc$. Figure 5c shows this model refined against the experimental data, but it is clearly incorrect.

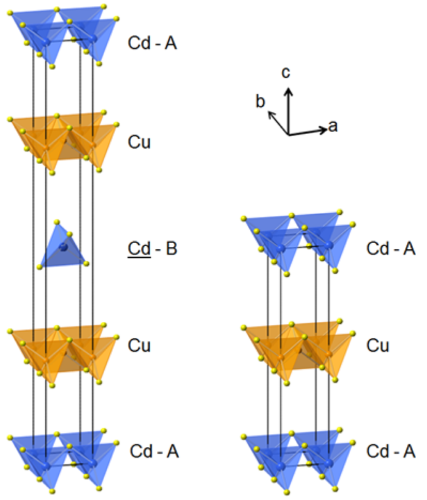

Figure 6. Two possible structural models for $La_2O_2CuCd_{0.5}Se_2$ with alternating layers of Cu and Cd. The model with Cd occupying equivalent sites either side of a Cu layer (right) is the correct model. Cu^{1+} cations are shown in orange, Cd^{2+} cations in blue and Se^{2-} anions in yellow. $[La_2O_2]^{2+}$ layers are omitted for clarity.

A second possible model would also have alternating Cu and Cd layers, but with the Cd occupying the same sites either side of a given Cu layer, shown in Figure 6 (right), space group $P\bar{4}m2$. Figure 5d shows this model refined against the experimental data. It provides an excellent fit. Full crystallograhic details of the final model (and other refinements in the paper) are included as Table S3.

Cd-Rich Samples: x = 0.333, 0.375, 0.4, 0.45 (1Cu/2Cd, 1Cu/3Cd, 1Cu/4Cd, 1Cu/9Cd). Compounds expected to contain more Cd than Cu layers were investigated for x = 0.333, 0.375, 0.4, and 0.45. In all cases the formation of $La_2O_2Cu_2Se_2$-derived phases was clear from powder diffraction data. For x = 0.333 a model was constructed with a 1:2 ratio of Cu:Cd layers, with Cd occupying equivalent sites either side of a given Cu layer as suggested by the x = 0.25 structure, and opposite sites when in adjacent layers as found in $La_2O_2CdSe_2$ (Figure 7a) This leads to space group $P4_2/nmc$.

On initial inspection, the refined model seems to provide a satisfactory fit to experimental data (Figure 8a), with R_{wp} = 5.92%. However, upon closer inspection, several of the weak supercell peaks show minor discrepancies in both peak intensity and widths (Figure 8b, peaks marked with arrows). Note that Figure 8 is drawn with a $\sqrt{I}$ scale such that these reflections are ~0.25% of the strongest subcell reflections.

Analysis of individual reflections showed a clear broadening of all hkl reflections where $l \neq 3n$. Therefore, an additional parameter was introduced to model antiphase domain walls perpendicular to c*, using the approach employed in the refinements of MgB_2H_8,[74] but with an $l = 3n$ condition. This leads to an improved fit of supercell reflections (Figure 8c), R_{wp} = 5.01%, and refined fault domain size value of ~380 Å, suggesting the presence of a fault every ~7 unit cells (42 layers).

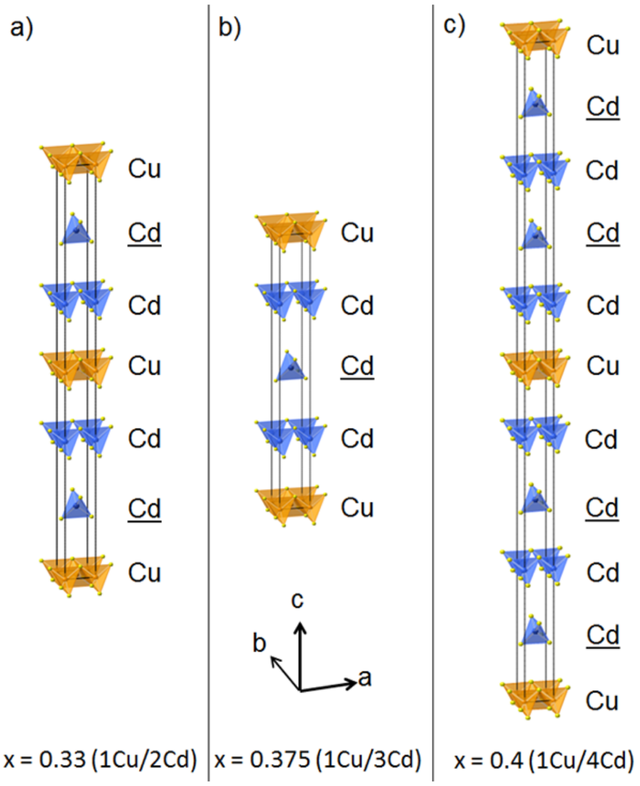

Figure 7. Structural models for (a) $La_2O_2Cu_{0.66}Cd_{0.66}Se_2$ (1Cu/2Cd), (b) $La_2O_2Cu_{0.50}Cd_{0.75}Se_2$ (1Cu/3Cd) and (c) $La_2O_2Cu_{0.40}Cd_{0.80}Se_2$ (1Cu/4Cd), space groups $P4_2/nmc$, $P\bar{4}m2$, and $P4_2/nmc$ respectively. Cu^{1+} cations are shown in orange, Cd^{2+} cations in blue, and Se^{2-} anions in yellow. $[La_2O_2]^{2+}$ layers are omitted for clarity.

Because the other members of the $La_2O_2Cu_{2-4x}Cd_{2x}Se_2$ series show more complex broadenings of the supercell reflections, we have applied our DIFFaX-Rietveld approach to these data. The alternating $[La_2O_2]^{2+}$ and either $[CdSe_2]^{2-}$ or $[Cu_2Se_2]^{2-}$ 2D units in these structures mean that we can easily describe the structure in terms of $[LaOLaSe(Cu_2/Cd)Se]$ layers stacked along c and that two types of stacking fault are likely for x = 0.33 (Figure 9). First one could break the (Cu|Cd|Cd) repeat by introducing an additional layer of either metal to form (Cu|Cu|Cd|Cd) or (Cu|Cd|Cd|Cd) local faults. We call this a *pa*-type fault throughout the paper. These correspond to a local intergrowth of x = 0.25 and x = 0.375 phases, and chemical composition requirements mean that their number must be balanced. The cell volume plot of Figure 4 and single-phase nature of this sample provide strong evidence that the composition is that expected.

A second possibility is a fault of the type shown in Figure 6, left, where neighboring Cd atoms layers are offset by ± (a/2, b/2) in the ab plane across a Cu layer. We call this a *pb*-type fault. The structure of faulted x = 0.33 $La_2O_2Cu_{0.66}Cd_{0.66}Se_2$ can then be described by stacking 6 layers labeled Cd1, Cd2, Cu3, Cd4, Cd5, Cu6 as shown in Figure 9, with transition probabilities from layer to layer as defined in the accompanying probability matrix. In this description an underlined Cd atomic layer is offset by (a/2, b/2). The ideal structure is generated by

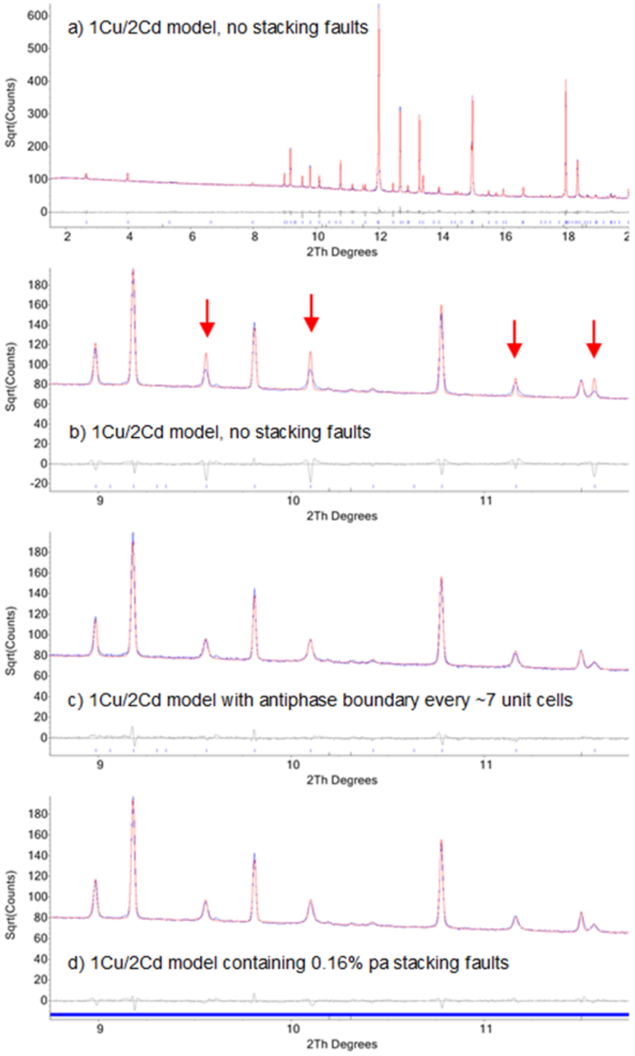

Figure 8. Rietveld refinement profiles of synchrotron powder diffraction data for $La_2O_2Cu_{0.66}Cd_{0.66}Se_2$ using the structural model proposed in Figure 7a, both without and with stacking faults. The correct model contains ~0.16% *pa* stacking faults. A $\sqrt{I}$ scale is used to emphasize the weaker supercell reflections.

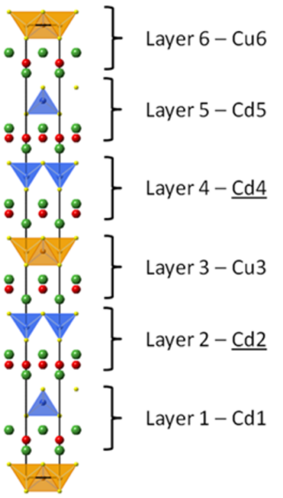

$$\begin{array}{cc} & \text{from layer } m \\ \text{to layer } n & \begin{pmatrix} 0 & 0 & pb & pa & 0 & 1-pa-pb \\ 1-pa & 0 & 0 & 0 & pa & 0 \\ 0 & 1-pa & 0 & 0 & 0 & pa \\ pa & 0 & 1-pa-pb & 0 & 0 & pb \\ 0 & pa & 0 & 1-pa & 0 & 0 \\ 0 & 0 & pa & 0 & 1-pa & 0 \end{pmatrix} \end{array}$$

Figure 9. Layer description and stacking probability matrix for x = 0.33. Each *pa* fault retains the Cd offset that would be adopted in an ideal stack.

stacking $(\text{Cd1}|\underline{\text{Cd2}}|\text{Cu3}|\underline{\text{Cd4}}|\text{Cd5}|\text{Cu6})_\infty$. A *pa* type fault can be introduced by an $m \rightarrow m+3$ transition and a *pb* fault by Cu3 → Cd1 or Cu6 → $\underline{\text{Cd4}}$. In this description a *pa* fault after a Cd layer retains the Cd offset pattern observed in $La_2O_2CdSe_2$ and a *pa* fault after a Cu layer leads to Cd's retaining the *xy* position they would have within a given layer in an unfaulted stack; by setting *pa* to an $m \rightarrow m$ transition for Cu layers the alternate fault in which Cd position is mirrored across a *pa*-induced Cu double layer can be explored.

The supercell was constructed by stacking 320 Cu and 640 Cd layers with internal geometries derived from the x = 0.25 refinement. The ideal thickness of each layer type along the *c* axis can be estimated from the *c* cell parameter in x = 0 (Cu) and x = 0.5 (Cd) series end members as 8.7975 Å and 9.3160 (= 18.6320/2) Å respectively. The thickness defines the displacement along *c* from one layer to the next. For rigid layers, the supercell should then have a *c* axis of 320 × 8.7975 Å + 640 × 9.3160 Å = 8777.44 Å, implying a subcell parameter of 9.1432 Å. Experimentally the subcell parameter is 9.1410(3) Å, so ideal thicknesses were automatically scaled during the refinement to account for this very small discrepancy. This supercell model gave a good fit to the diffraction data with an R_{wp} only marginally higher than a standard crystallographic model (4.1 vs 3.9% for 2–20° 2θ), despite having no refined structural parameters. Our peaks-buffer approach means that the pattern is simulated using 1530 *hkl* reflections rather than the 54 881 predicted for this supercell size and 2θ range. As expected, an identical R_{wp} is obtained for any unfaulted supercell containing 6*n* layers. A grid search was then performed with both *pa* and *pb* allowed to vary from 0 to 0.1 and 100 trial stacks tested for each *pa*/*pb* pair (approximately 15 h of computer time). Analysis of the R_{wp} surface (Figure 10) indicated a significant improvement in fit (R_{wp} = 2.78%) for structures with ~18 *pa* faults in the 960 layer stack and no *pb* faults, corresponding to a fault every ~490 Å or 54 layers. As shown in Figure 8d, this model reproduces the shape and intensities of weak supercell reflections extremely well, with only one additional structural parameter (*pa* value). Refinement of parameters defining the relative thickness of Cu/Cd layers gave essentially no change in R_{wp} and refined values of 8.806/9.307 Å. We also investigated models with imposed correlation lengths between faults but found that the best fits had uncorrelated faults. In addition to the "extra layer" *pa* model, we investigated a similar "missing layer" *pc* fault. We find that similar fits to the data are possible with either fault type, but that their sum remains constant.

Rietveld fits for the x = 0.375 composition are included later in Figure 12. The powder diffraction data are essentially consistent with the structural model shown in Figure 7b, which contains blocks of 3 Cd's, within which the structural arrangement is the same as in $La_2O_2CdSe_2$, followed by a Cu layer. This model, however, significantly overestimates the intensity of the weak 002 and 003 reflections at ~2 and ~3° 2θ as well as, for example, the 01*l* $l \neq 2n$ reflections. A *pa*/*pb* grid search similar to that for the x = 0.33 sample was investigated

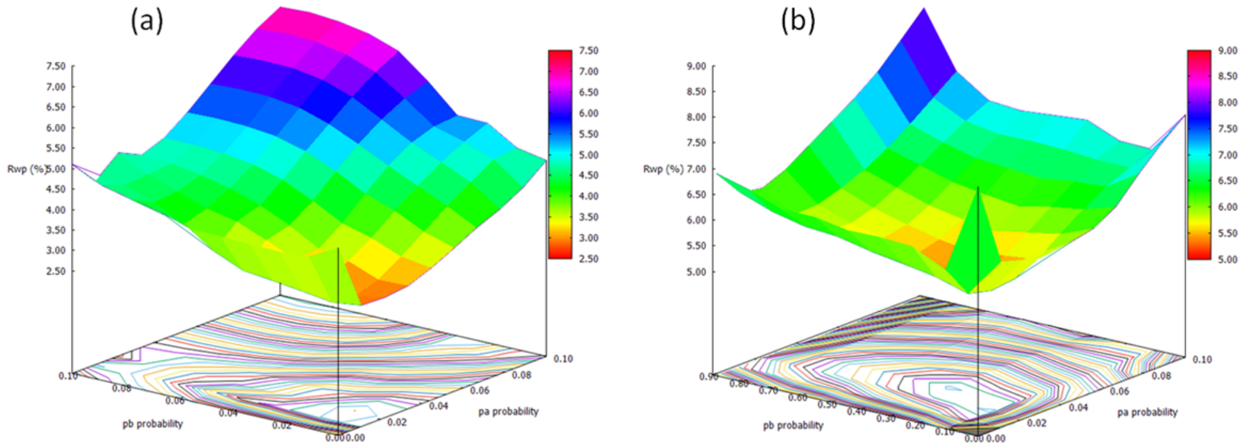

Figure 10. Dependence of R_{wp} on *pa* and *pb* for the $x = 0.33$ and $x = 0.167$ systems. Note different *pb* scale in b.

and a significant reduction in R_{wp} (5.81 to 2.78%, 2−20° 2θ) was achieved with approximately 25 *pa* faults. Introduction of *pb* faults caused an increase in R_{wp}. Refinement of the Cu/Cd slab thickness gave 8.861/9.248 Å, close to expected values.

Inspection of the powder data for $x = 0.4$ and $x = 0.45$ suggests similar basic structures with a (Cu|Cd|Cd|Cd|Cd)$_\infty$ repeat for $x = 0.4$, and similar *pa* type faults. The weak intensity of the superstructure peaks and the likelihood of partial phase separation precludes detailed analysis of the stacking faults. For $x = 0.45$, we see evidence for partial phase segregation to $x = 0.4$ and $x = 0.5$ compositions.

Cu-Rich Samples: x = 0.167, 0.125, 0.1, 0.05 (2Cu/1Cd, 3Cu/1Cd, 4Cu/1Cd, 9Cu/1Cd). From powder diffraction data we can identify 3 new discrete structure types for Cu-layer-rich compositions. The basic structure types found are depicted in Figure 11, though we again see marked supercell peak broadening and significant peak asymmetry. For $x = 0.167$ the supercell reflections are well fitted with $pa \approx 0.013$ suggesting a similar number of layer-repeat faults to the Cd-rich phases. There are also a significant number of *pb*-type faults ($pb \approx 0.25$) corresponding to 80 faults in the 960 layer stack, or a fault every 55 Å or 6 layers. The dependence of R_{wp} on *pa* and *pb* is given in Figure 10b. As the number of Cu layers is increased, the proportion of *pb*-type faults increases. At $x = 0.125$ (Cu|Cu|Cu|Cd) *pb* is ≈ 0.43 implying an almost-random choice for the position of the Cd layers. This leads to the triangular or Warren-like peak shape seen for the 10*l*-related peaks from ∼8.9° 2θ, shown in Figure 12. This sample also contains a significant number of *pa* type defects ($pa \approx 0.06$). Without these defects 00*l* reflections have too high a peak height. In a conventional crystallographic refinement using an average model this effect is partially "mopped up" by the thickness of Cd and Cu layers distorting.

For $x = 0.1$, we find $pb = 0.5$ gives the best fit to the data (Figure 11e) implying full disorder of the Cd layers. For $x = 0.05$ (targeted to be 9Cu/1Cd), phase separation is observed, into $x = 0.05$ and $x = 0$ compositions.

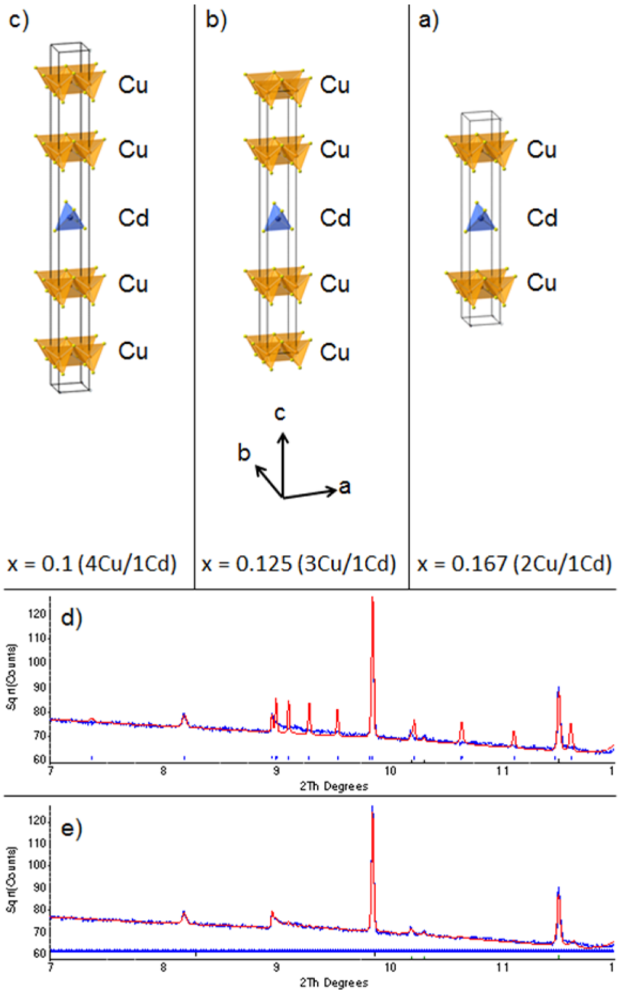

Figure 11. Structural models for (a) $La_2O_2Cu_{1.33}Cd_{0.33}Se_2$ (2Cu/1Cd), (b) $La_2O_2Cu_{1.50}Cd_{0.25}Se_2$ (3Cu/1Cd), and (c) $La_2O_2Cu_{1.60}Cd_{0.20}Se_2$ (4Cu/1Cd), all space group *P*-4*m*2. Cu^{1+} cations are shown in orange, Cd^{2+} cations in blue and Se^{2-} anions in yellow. $[La_2O_2]^{2+}$ layers are omitted for clarity. (d) and (e) show the Rietveld fit for $x = 0.1$ with no faults and 0.05/0.50 *pa*/*pb* faults, respectively. The 2θ 8.2° peak has $I \approx 0.4\%$ of the strongest reflection.

■ DISCUSSION

Our previous work on single-metal layered oxychalcogenides has shown that the combination of a rigid oxide layer and a more flexible chalcogenide layer can lead to structures with remarkable complexity and large superstructures in the *ab* plane.[14,15] In this work, we have shown that a similar level of complexity can be built into these materials along the stacking direction by using two metals, giving rise to the range of materials from 4Cd/1Cu to 1Cd/4Cu shown schematically in Figure 2. Although we use a conventional description in this

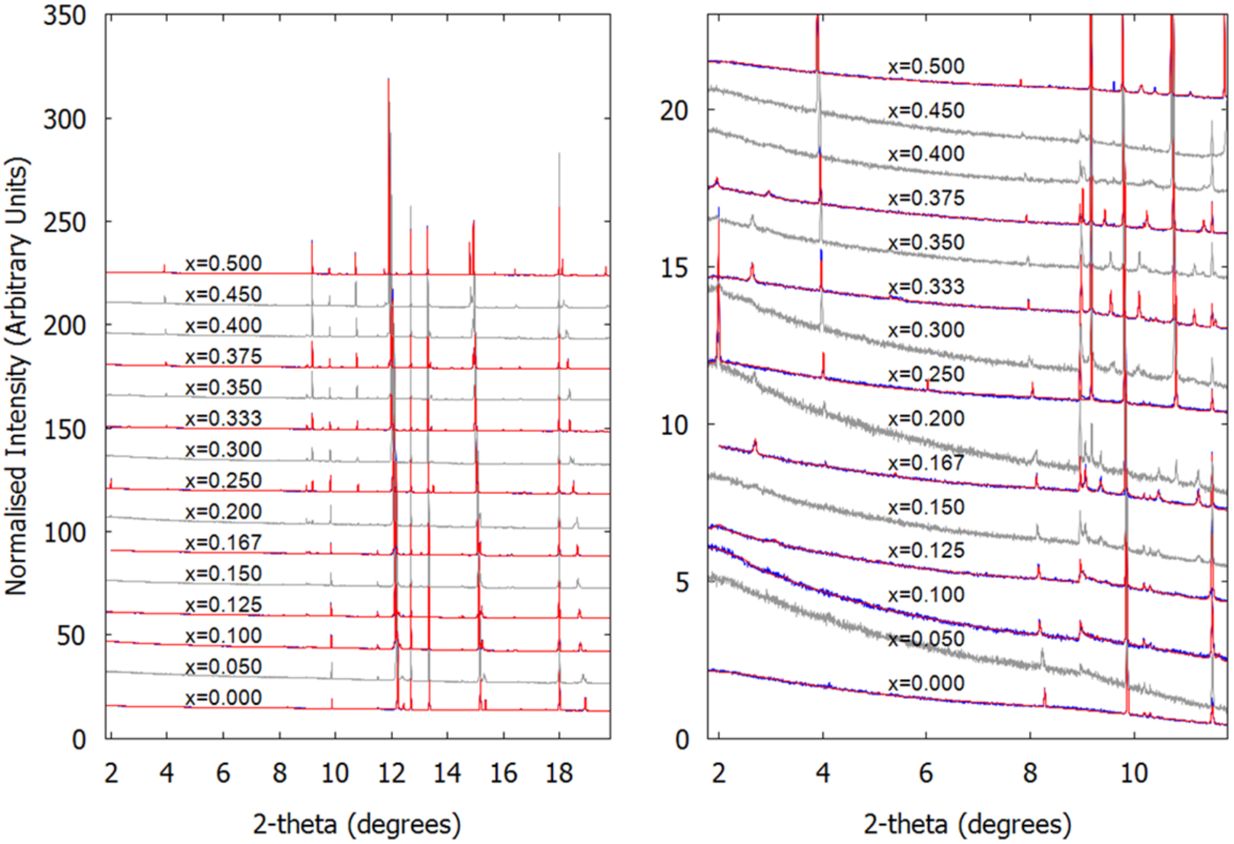

Figure 12. Rietveld fits for all compositions studied using the stacking approach. Left hand panel shows all data normalized on a 0−100 scale and offset vertically by 20 units for presentation. Right hand panel shows data over a low 2θ range to emphasize the weak superstructure reflections, which reveal metal ordering. Data sets are offset by 2 units along the *y*-axis. The differing backgrounds reflect different capillary packings. Rietveld fits of x = 0.167 and 0.125 are averages of 100 unique stacks.

work, these can all be described in terms of a superspace group $P4/nmm(00g)s00s$ [129.4]. The tendency to adopt ordered superstructures of this type is initially surprising, but again has its origin in the rigidity of the oxide layers in the *ab* plane. This rigidity forces two fixed Se−Se dimensions on the MSe_4 tetrahedra, and the planar layers means that they can only adjust to coordinate a given transition metal by elongation along their S_4 axis (parallel to *c*). Simple bond valence arguments[75,76] for a Cu^{1+} or Cd^{2+} in this environment imply Se−Se layer distances of ∼3.0 and ∼3.4 Å respectively. This large difference in geometry provides a strong driving force for segregation of Cu and Cd into separate layers.

Both our crystallographic models and stacking fault analyses show an initially counterintuitive arrangement of Cd sites in $CdSe_2$ layers separated by a Cu_2Se_2 block. In pure $La_2O_2CdSe_2$ the Cd ordering pattern can be derived from the parent Cu structure in terms of a Z_4^- ordering mode which leads to a checkerboard ordering within layers and adjacent layers with Cd positions offset by (1/2, 1/2) in the *ab* plane such that layers repeat in an ABAB sequence along *c*. This arrangement would be expected purely on electrostatic grounds and is retained within the Cd blocks of all our materials. However, the actual structure of $La_2O_2CuCd_{0.5}Se_2$ shown in Figure 6, right, shows that Cd positions are mirrored across the single Cu_2Se_2 layers in the Cd-rich materials. As such, the Cd A(B)A stacking sequence [where (B) indicates the effective position of the Cu layer] is retained. We also find that the *pa* stacking fault for the x = 0.33 and x = 0.375 samples is best modeled such that Cd sites alternate across a double layer, again retaining the A(B)(A)B sequence through the fault. One possible explanation for this is that the *pa* fault occurs within column-like domains in a crystallite. The Cd ions immediately following a local double-Cu layer would then be in registry with other Cd sites within that layer following this type of fault. The only structure in which the ABAB sequence is not followed is the x = 0.166 2Cu/1Cd composition. Because the *pb* type disorder is high in the Cu-rich sequences, our observations are consistent with Cd preferring a mirrored configuration across multiple Cu layers.

The powder diffraction data show that there is significant long-range order along the *c*-axis of these materials, with a relatively low probability of faults (*pa*) in the Cu/Cd sequence. There is also a strong tendency for Cd sites to adopt ordered positions in the *ab* plane in Cd-rich materials but that this tendency is reduced as the $CdSe_2$ layers become separated by more than 1 Cu_2Se_2 layers. Stacking fault probabilities *pa* and *pb* are given for all compositions in Figure 2. The different types of faults lead to the characteristic changes in superstructure peak shapes and intensities across the series shown in Figure 12.

■ CONCLUSIONS

In conclusion, we show that we can take the design principle of combining rigid oxide blocks with more flexible chalcogenide blocks learnt from the 2D $La_2O_2MSe_2$ infinitely flexible materials, and use them to produce cation-ordered materials over a large length scale in the third dimension. This has allowed us to produce materials with stacks of electronically interesting Cu_2Se_2 layers where we can systematically change the number of adjacent layers and/or the separation between them in a controlled fashion. This gives access to a large new oxychalcogenide family, which can potentially be doped to give p-type conductors related to the important LaOCuSe and BiOCuSe families. By using different metal chalcogenide layers, we have the possibility to combine electronic and magnetically active layers in a controllable structural family.

We also show how materials with low- and high-probability stacking faults can be properly analyzed within the Rietveld method for the first time. This allows us to simultaneously extract structural (by refining atomic coordinates) and microstructural (by analyzing stacking fault probabilities) information on our samples. The ability to correctly fit complex peak shapes with a small number of structurally meaningful parameters means that reflection intensities are correctly modeled, which is essential for accurate structural information or accurate quantitative analysis. The method we describe is entirely general and will be applicable to the wide range of materials that exhibit stacking faults. For example, we see important applications in battery materials such as Li_xMO_2,[33−36] $Na_xFe_{1/2}Mn_{1/2}O_2$,[32] Li_2FeSiO_4,[31] and MnO_2[30] where stacking faults are prevalent. Stacking fault Rietveld refinement will allow accurate cation distributions, detailed structural information, and quantitative analysis of in operando systems needed for full understanding of their chemistry. Similar faulting precludes detailed structural studies of a range of important zeolites.[37−44] Other areas likely to benefit include materials with low temperature topotactic transformations,[77] intercalation/ion-exchange hosts, a variety of layered minerals,[78] and understanding the details and implications of hexagonal/cubic intergrowths in different forms of ice.[50,51] Similar analysis will also be possible for layered magnetic systems, which often order in 2D or over short length scales prior to full 3D ordering.

■ ASSOCIATED CONTENT

Ⓢ Supporting Information

The Supporting Information is available free of charge on the ACS Publications website at DOI: 10.1021/acs.chemmater.6b00924.

> Table of sample colors, table of wt % of phases formed, graph showing the dependence of unit-cell parameters on composition, graph showing the thickness of Se−Cu−Se and Se−Cd−Se layers from conventional Rietveld refinement, table of crystallographic information from conventional refinement, graph showing full width at half-maximum of individual reflections in $x = 0.33$ sample, tables showing dependence of R_{wp} on *pa* and *pb* for $x = 0.33$, 0.167, and 0.125 compositions, scatter plot showing R_{wp} for stacks with different numbers of *pa*-type and *pb*-type faults for $x = 0.33$, 0.167, and 0.125 compositions (PDF)
> crystallographic information file for $x = 0.25$ (CIF)
> crystallographic information file for $x = 0.167$ (CIF)
> crystallographic information file for $x = 0.33$ (CIF)
> Annotated TOPAS input file for refinement of 3b (TXT)
> Data file for refinement of 3b (TXT)

■ AUTHOR INFORMATION

Corresponding Author

*E-mail: john.evans@durham.ac.uk.

Present Addresses

‡C.-H.W. is currently at School of Chemistry, The University of Sydney, NSW 2006 Australia
⊥H.E.J. is currently at University of Edinburgh, Joseph Black Building, David Brewster Road, Edinburgh, Scotland EH9 3FJ

Notes

The authors declare no competing financial interest.

■ ACKNOWLEDGMENTS

We thank EPSRC for funding (EP/J011533/1). Powder diffraction data were collected on the Powder Diffraction beamline at the Australian synchrotron. We thank Ivana Evans, Matthew Tate, Nicola Scarlett, and Garry McIntyre for assistance with data collections. JSOE would like to thank ANSTO for a visiting position during which part of this research was performed.

■ REFERENCES

(1) Kamihara, Y.; Watanabe, T.; Hirano, M.; Hosono, H. Iron-Based Layered Superconductor La$[O_{1-x}F_x]$FeAs ($x = 0.05−0.12$) with T_c = 26 K. *J. Am. Chem. Soc.* **2008**, *130* (11), 3296−3297.

(2) Hosono, H.; Kuroki, K. Iron-Based Superconductors: Current Status of Materials and Pairing Mechanism. *Phys. C (Amsterdam, Neth.)* **2015**, *514*, 399−422.

(3) Phelan, W. A.; Wallace, D. C.; Arpino, K. E.; Neilson, J. R.; Livi, K. J.; Seabourne, C. R.; Scott, A. J.; McQueen, T. M. Stacking Variants and Superconductivity in the Bi-O-S System. *J. Am. Chem. Soc.* **2013**, *135* (14), 5372−5374.

(4) Singh, S. K.; Kumar, A.; Gahtori, B.; Shruti; Sharma, G.; Patnaik, S.; Awana, V. P. S. Bulk Superconductivity in Bismuth Oxysulfide $Bi_4O_4S_3$. *J. Am. Chem. Soc.* **2012**, *134* (40), 16504−16507.

(5) Zhao, L.; Berardan, D.; Pei, Y.; Byl, C.; Pinsard-Gaudart, L.; Dragoe, N. $Bi_{-x}Sr_x$CuSeO Oxyselenides as Promising Thermoelectric Materials. *Appl. Phys. Lett.* **2010**, *97*, 092118−092121.

(6) Luu, S. D.; Vaqueiro, P. Synthesis, Structural Characterisation and Thermoelectric Properties of $Bi_{1−x}Pb_x$OCuSe. *J. Mater. Chem. A* **2013**, *1* (39), 12270−12275.

(7) Vaqueiro, P.; Al Orabi, R.; Luu, S.; Guélou, G.; Powell, A.; Smith, R.; Song, J.-P.; Wee, D.; Fornari, M. The Role of Copper in the Thermal Conductivity of Thermoelectric Oxychalcogenides: Do Lone Pairs Matter? *Phys. Chem. Chem. Phys.* **2015**, *17* (47), 31735−31740.

(8) Liu, Y.; Zhao, L.-D.; Liu, Y.; Lan, J.; Xu, W.; Li, F.; Zhang, B.-P.; Berardan, D.; Dragoe, N.; Lin, Y.-H.; Nan, C.-W.; Li, J.-F.; Zhu, H. Remarkable Enhancement in Thermoelectric Performance of BiCuSeO by Cu Deficiencies. *J. Am. Chem. Soc.* **2011**, *133* (50), 20112−20115.

(9) Bang, J.; Abboudi, M.; Abrams, B.; Holloway, P. H. Combustion Synthesis of Eu-, Tb- and Tm- Doped Ln_2O_2S (Ln = Y, La, Gd) Phosphors. *J. Lumin.* **2004**, *106* (3−4), 177−185.

(10) Clarke, S. J.; Denis, S. G.; Rutt, O. J.; Hill, T. L.; Hayward, M. A.; Hyett, G.; Gál, Z. A. Sodium Intercalation into the $n = 2$ Ruddlesden−Popper Type Host $Y_2Ti_2O_5S_2$: Synthesis, Structure, and Properties of α-$Na_xY_2Ti_2O_5S_2$ ($0 < x \leq 1$). *Chem. Mater.* **2003**, *15* (26), 5065−5072.

(11) Hyett, G.; Rutt, O. J.; Gal, Z. A.; Denis, S. G.; Hayward, M. A.; Clarke, S. J. Electronically Driven Structural Distortions in Lithium Intercalates of the $n = 2$ Ruddlesden-Popper-Type Host $Y_2Ti_2O_5S_2$: Synthesis, Structure, and Properties of $Li_xY_2Ti_2O_5S_2$ ($0 < x < 2$). *J. Am. Chem. Soc.* **2004**, *126* (7), 1980−1991.

(12) Indris, S.; Cabana, J.; Rutt, O. J.; Clarke, S. J.; Grey, C. P. Layered Oxysulfides $Sr_2MnO_2Cu_{2m-0.5}S_{m+1}$ (m = 1, 2, and 3) as Insertion Hosts for Li Ion Batteries. *J. Am. Chem. Soc.* **2006**, *128* (41), 13354−13355.

(13) McCabe, E. E.; Free, D. G.; Evans, J. S. O. A New Iron Oxyselenide $Ce_2O_2FeSe_2$: Synthesis and Characterisation. *Chem. Commun.* **2011**, *47* (4), 1261−1263.

(14) Wang, C.-H.; Ainsworth, C. M.; Gui, D.-Y.; McCabe, E. E.; Tucker, M. G.; Evans, I. R.; Evans, J. S. O. Infinitely Adaptive Transition Metal Oxychalcogenides: The Modulated Structures of $Ce_2O_2MnSe_2$ and $(Ce_{0.78}La_{0.22})_2O_2MnSe_2$. *Chem. Mater.* **2015**, *27* (8), 3121−3134.

(15) Ainsworth, C. M.; Wang, C.-H.; Johnston, H. E.; McCabe, E. E.; Tucker, M. G.; Brand, H. E. A.; Evans, J. S. O. Infinitely Adaptive Transition-Metal Ordering in $Ln_2O_2MSe_2$-Type Oxychalcogenides. *Inorg. Chem.* **2015**, *54* (15), 7230−7238.

(16) Hiramatsu, H.; Yanagi, H.; Kamiya, T.; Ueda, K.; Hirano, M.; Hosono, H. Crystal Structures, Optoelectronic Properties, and Electronic Structures of Layered Oxychalcogenides MCuOCh (M = Bi, La; Ch = S, Se, Te): Effects of Electronic Configurations of M^{3+} Ions. *Chem. Mater.* **2008**, *20* (1), 326−334.

(17) Ueda, K.; Takafuji, K.; Hiramatsu, H.; Ohta, H.; Kamiya, T.; Hirano, M.; Hosono, H. Electrical and Optical Properties and Electronic Structures of LnCuOS (Ln = La ∼ Nd). *Chem. Mater.* **2003**, *15* (19), 3692−3695.

(18) Hiramatsu, H.; Kamiya, T.; Tohei, T.; Ikenaga, E.; Mizoguchi, T.; Ikuhara, Y.; Kobayashi, K.; Hosono, H. Origins of Hole Doping and Relevant Optoelectronic Properties of Wide Gap p-Type Semiconductor, LaCuOSe. *J. Am. Chem. Soc.* **2010**, *132* (42), 15060−15067.

(19) Vajenine, G. V.; Hoffmann, R. Compounds Containing Copper-Sulfur Layers: Electronic Structure, Conductivity, and Stability. *Inorg. Chem.* **1996**, *35* (2), 451−457.

(20) Ueda, K.; Inoue, S.; Hirose, S.; Kawazoe, H.; Hosono, H. Transparent p-Type Semiconductor: LaCuOS Layered Oxysulfide. *Appl. Phys. Lett.* **2000**, *77* (17), 2701−2703.

(21) Hiramatsu, H.; Ueda, K.; Ohta, H.; Kamiya, T.; Hirano, M.; Hosono, H. Excitonic Blue Luminescence from p-LaCuOSe/*n*-$InGaZn_5O_8$ Light-Emitting Diode at Room Temperature. *Appl. Phys. Lett.* **2005**, *87* (21), 211107.

(22) Ijjaali, I.; Mitchell, K.; Haynes, C. L.; McFarland, A. D.; Van Duyne, R. P.; Ibers, J. A. Synthesis, Crystal Structure, and Optical Properties of $CeMn_{0.5}OSe$. *J. Solid State Chem.* **2003**, *176* (1), 170−174.

(23) Hiramatsu, H.; Ueda, K.; Kamiya, T.; Ohta, H.; Hirano, M.; Hosono, H. Synthesis of Single-Phase Layered Oxychalcogenide $La_2CdO_2Se_2$: Crystal Structure, Optical and Electrical Properties. *J. Mater. Chem.* **2004**, *14* (19), 2946−2950.

(24) Tuxworth, A. J.; McCabe, E. E.; Free, D. G.; Clark, S. J.; Evans, J. S. O. Structural Characterization and Physical Properties of the New Transition Metal Oxyselenide $La_2O_2ZnSe_2$. *Inorg. Chem.* **2013**, *52* (4), 2078−2085.

(25) Ainsworth, C. M.; Wang, C. H.; Tucker, M. G.; Evans, J. S. O. Synthesis, Structural Characterization, and Physical Properties of the New Transition Metal Oxyselenide $Ce_2O_2ZnSe_2$. *Inorg. Chem.* **2015**, *54* (4), 1563−1571.

(26) Peschke, S.; Nitsche, F.; Johrendt, D. Flux Synthesis, Modulated Crystal Structures, and Physical Properties of $REMn_{0.5}SeO$ (RE = La, Ce). *Z. Anorg. Allg. Chem.* **2015**, *641* (3−4), 529−536.

(27) Nitsche, F.; Niklaus, R.; Johrendt, D. New Polymorphs of $RE_2FeSe_2O_2$ (RE = La, Ce). *Z. Anorg. Allg. Chem.* **2014**, *640* (14), 2897−2902.

(28) Treacy, M. M. J.; Newsam, J. M.; Deem, M. W. A General Recursion Method for Calculating Diffracted Intensities from Crystals Containing Planar Faults. *Proc. R. Soc. London, Ser. A* **1991**, *433* (1889), 499−520.

(29) Leoni, M. Diffraction Analysis of Layer Disorder. *Z. Kristallogr.* **2008**, *223* (9), 561−568.

(30) Chabre, Y.; Pannetier, J. Structural and Electrochemical Properties of the Proton Gamma-MnO_2 system. *Prog. Solid State Chem.* **1995**, *23* (1), 1−130.

(31) Boulineau, A.; Sirisopanaporn, C.; Dominko, R.; Armstrong, A. R.; Bruce, P. G.; Masquelier, C. Polymorphism and Structural Defects in Li_2FeSiO_4. *Dalton Trans.* **2010**, *39* (27), 6310−6316.

(32) Yabuuchi, N.; Kajiyama, M.; Iwatate, J.; Nishikawa, H.; Hitomi, S.; Okuyama, R.; Usui, R.; Yamada, Y.; Komaba, S. P2-type Na_{-x} $Fe_{1/2}Mn_{1/2}$ O^{-2} made from Earth-Abundant Elements for Rechargeable Na Batteries. *Nat. Mater.* **2012**, *11* (6), 512−517.

(33) Lu, Z. H.; Dahn, J. R. In Situ X-Ray Diffraction Study of P2-$Na_{-2/3}$ $Ni_{1/3}Mn_{2/3}$ O^{-2}. *J. Electrochem. Soc.* **2001**, *148* (11), A1225−A1229.

(34) Bréger, J.; Jiang, M.; Dupré, N.; Meng, Y. S.; Shao-Horn, Y.; Ceder, G.; Grey, C. P. High-Resolution X-Ray Diffraction, DIFFaX, NMR and First Principles Study of Disorder in the Li_2MnO_3−$Li[Ni_{1/2}Mn_{1/2}]O_2$ Solid Solution. *J. Solid State Chem.* **2005**, *178* (9), 2575−2585.

(35) Croguennec, L.; Deniard, P.; Brec, R.; Lecerf, A. Nature of the Stacking Faults in Orthorhombic $LiMnO_2$. *J. Mater. Chem.* **1997**, *7* (3), 511−516.

(36) Boulineau, A.; Croguennec, L.; Delmas, C.; Weill, F. Structure of Li_2MnO_3 with Different Degrees of Defects. *Solid State Ionics* **2010**, *180* (40), 1652−1659.

(37) Anderson, M. W.; Terasaki, O.; Ohsuna, T.; Philippou, A.; Mackay, S. P.; Ferreira, A.; Rocha, J.; Lidin, S. Structure of the Microporous Titanosilicate ETS-10. *Nature* **1994**, *367* (6461), 347−351.

(38) Freyhardt, C. C.; Tsapatsis, M.; Lobo, R. F.; Balkus, K. J.; Davis, M. E. A High-Silica Zeolite with a 14-Tetrahedral-Atom Pore Opening. *Nature* **1996**, *381* (6580), 295−298.

(39) Anderson, M. W.; Terasaki, O.; Ohsuna, T.; Malley, P. J. O.; Philippou, A.; Mackay, S. P.; Ferreira, A.; Rocha, J.; Lidin, S. Microporous Titanosilicate ETS-10 - A Structural Survey. *Philos. Mag. B* **1995**, *71* (5), 813−841.

(40) Lobo, R. F.; Pan, M.; Chan, I.; Li, H. X.; Medrud, R. C.; Zones, S. I.; Crozier, P. A.; Davis, M. E. SSZ-26 and SSZ-33 - 2 Molecular-Sieves with Intersecting 10-Ring and 12-Ring Pores. *Science* **1993**, *262* (5139), 1543−1546.

(41) Lobo, R. F.; Tsapatsis, M.; Freyhardt, C. C.; Khodabandeh, S.; Wagner, P.; Chen, C. Y.; Balkus, K. J.; Zones, S. I.; Davis, M. E. Characterization of the Extra-Large-Pore Zeolite UTD-1. *J. Am. Chem. Soc.* **1997**, *119* (36), 8474−8484.

(42) Juttu, G. G.; Lobo, R. F. Characterization and Catalytic Properties of MCM-56 and MCM-22 Zeolites. *Microporous Mesoporous Mater.* **2000**, *40* (1−3), 9−23.

(43) Lobo, R. F.; Tsapatsis, M.; Freyhardt, C. C.; Chan, I.; Chen, C. Y.; Zones, S. I.; Davis, M. E. A Model for the Structure of the Large-Pore Zeolite SSZ-31. *J. Am. Chem. Soc.* **1997**, *119* (16), 3732−3744.

(44) Willhammar, T.; Sun, J.; Wan, W.; Oleynikov, P.; Zhang, D.; Zou, X.; Moliner, M.; Gonzalez, J.; Martínez, C.; Rey, F.; Corma, A. Structure and Catalytic Properties of the Most Complex Intergrown Zeolite ITQ-39 Determined by Electron Crystallography. *Nat. Chem.* **2012**, *4* (3), 188−194.

(45) Balogh, L.; Ungar, T.; Zhao, Y.; Zhu, Y. T.; Horita, Z.; Xu, C.; Langdon, T. G. Influence of Stacking-Fault Energy on Microstructural Characteristics of Ultrafine-Grain Copper and Copper-Zinc Alloys. *Acta Mater.* **2008**, *56* (4), 809−820.

(46) Sebastian, M. T.; Krishna, P. *Random, Non-random, and Periodic Faulting in Crystals*; Gordon and Breach Science: Philadelphia, 1994.

(47) Ufer, K.; Kleeberg, R.; Bergmann, J.; Dohrmann, R. Rietveld Refinement of Disordered Illite-Smectite Mixed-Layer Structures by a Recursive Algorithm. II: Powder-Pattern Refinement and Quantitative Phase Analysis. *Clays Clay Miner.* **2012**, *60* (5), 535−552.

(48) Ufer, K.; Kleeberg, R.; Bergmann, J.; Dohrmann, R. Rietveld Refinement of Disordered Illite-Smectite Mixed-Layer Structures by a Recursive Algorithm. I: One-Dimensional Patterns. *Clays Clay Miner.* **2012**, *60* (5), 507−534.

(49) Németh, P.; Garvie, L. A.; Aoki, T.; Dubrovinskaia, N.; Dubrovinsky, L.; Buseck, P. R. Lonsdaleite is Faulted and Twinned Cubic Diamond and does Not Exist as a Discrete Material. *Nat. Commun.* **2014**, *5*, 5447.

(50) Salzmann, C. G.; Murray, B. J.; Shephard, J. J. Extent of Stacking Disorder in Diamond. *Diamond Relat. Mater.* **2015**, *59*, 69−72.

(51) Malkin, T. L.; Murray, B. J.; Salzmann, C. G.; Molinero, V.; Pickering, S. J.; Whale, T. F. Stacking Disorder in Ice I. *Phys. Chem. Chem. Phys.* **2015**, *17* (1), 60−76.

(52) Fogg, A. M.; Evans, J. S. O.; O'Hare, D. Crystal Structure of Beta-MNX (M = Zr, Hf, X = Cl, Br). *Chem. Commun.* **1998**, *20*, 2269–2270.

(53) Stampfl, C.; Van de Walle, C. G. Energetics and Electronic Structure of Stacking Faults in AlN, GaN, and InN. *Phys. Rev. B: Condens. Matter Mater. Phys.* **1998**, *57* (24), R15052–R15055.

(54) Liu, R.; Bell, A.; Ponce, F. A.; Chen, C. Q.; Yang, J. W.; Khan, M. A. Luminescence from Stacking Faults in Gallium Nitride. *Appl. Phys. Lett.* **2005**, *86* (2), 021908.

(55) Anselmi-Tamburini, U.; Ohyanagi, M.; Munir, Z. A. Modeling Studies of the Effect of Twins on the X-Ray Diffraction Patterns of Boron Carbide. *Chem. Mater.* **2004**, *16* (22), 4347–4351.

(56) Anselmi-Tamburini, U.; Munir, Z. A.; Kodera, Y.; Imai, T.; Ohyanagi, M. Influence of Synthesis Temperature on the Defect Structure of Boron Carbide: Experimental and Modeling Studies. *J. Am. Ceram. Soc.* **2005**, *88* (6), 1382–1387.

(57) Palosz, B.; Stelmakh, S.; Gierlotka, S. Refinement of Polycrystalline Disordered Cubic Silicon-Carbide by Structure Modeling and X-Ray-Diffraction Simulation. *Z. Kristallogr. - Cryst. Mater.* **1995**, *210* (10), 731–740.

(58) Nguyen, P.; Sleight, A.; Roberts, N.; Warren, W. Modeling of Extended Defects in the Vanadium Phosphate Catalyst for Butane Oxidation, $(VO)_2P_2O_7$. *J. Solid State Chem.* **1996**, *122* (2), 259–265.

(59) Rajamathi, M.; Vishnu Kamath, P.; Seshadri, R. Polymorphism in Nickel Hydroxide: Role of Interstratification. *J. Mater. Chem.* **2000**, *10* (2), 503–506.

(60) Rajamathi, M.; Kamath, P. V.; Seshadri, R. Chemical Synthesis of Alpha-Cobalt Hydroxide. *Mater. Res. Bull.* **2000**, *35* (2), 271–278.

(61) Jayashree, R. S.; Kamath, P. V.; Subbanna, G. N. The Effect of Crystallinity on the Reversible Discharge Capacity of Nickel Hydroxide. *J. Electrochem. Soc.* **2000**, *147* (6), 2029–2032.

(62) Radha, A. V.; Kamath, P. V.; Shivakumara, C. Conservation of Order, Disorder, and "Crystallinity" during Anion-Exchange Reactions among Layered Double Hydroxides (LDHs) of Zn with Al. *J. Phys. Chem. B* **2007**, *111* (13), 3411–3418.

(63) Coelho, A. A. Indexing of Powder Diffraction Patterns by Iterative Use of Singular Value Decomposition. *J. Appl. Crystallogr.* **2003**, *36*, 86–95.

(64) Coelho, A. A. *TOPAS Academic: General Profile and Structure Analysis Software for Powder Diffraction Data*, 5th ed.; Bruker AXS: Karlsruhe, Germany, 2012.

(65) Coelho, A. A.; Evans, J. S. O.; Evans, I. R.; Kern, A.; Parsons, S. The TOPAS Symbolic Computation System. *Powder Diffr.* **2011**, *26*, S22–S25.

(66) Warren, B. E. X-Ray Diffraction in Random Layer Lattices. *Phys. Rev.* **1941**, *59* (9), 693–698.

(67) Proffen, T.; Neder, R. B. *Diffuse Scattering and Defect Structure Simulations: A Cook Book Using the Program DISCUS*; Oxford University Press: Oxford, U.K., 2008.

(68) Leoni, M.; Gualtieri, A. F.; Roveri, N. Simultaneous Refinement of Structure and Microstructure of Layered Materials. *J. Appl. Crystallogr.* **2004**, *37*, 166–173.

(69) Casas-Cabanas, M.; Rodriguez-Carvajal, J.; Canales-Vazquez, J.; Laligant, Y.; Lacorre, P.; Palacin, M. R. Microstructural characterisation of battery materials using powder diffraction data: DIFFaX, FAULTS and SH-FullProf approaches. *J. Power Sources* **2007**, *174* (2), 414–420.

(70) Ufer, K.; Roth, G.; Kleeberg, R.; Stanjek, H.; Dohrmann, R.; Bergmann, J. Description of X-Ray Powder Pattern of Turbostratically Disordered Layer Structures with a Rietveld Compatible Approach. *Z. Kristallogr. - Cryst. Mater.* **2004**, *219* (9), 519–527.

(71) Wang, X. D.; Li, J.; Hart, R. D.; van Riessen, A.; McDonald, R. Quantitative X-Ray Diffraction Phase Analysis of Poorly Ordered Nontronite Clay in Nickel Laterites. *J. Appl. Crystallogr.* **2011**, *44*, 902–910.

(72) Bette, S.; Dinnebier, R. E.; Freyer, D. Structure Solution and Refinement of Stacking-Faulted NiCl(OH). *J. Appl. Crystallogr.* **2015**, *48*, 1706–1718.

(73) Shannon, R. Revised Effective Ionic Radii and Systematic Studies of Interatomic Distances in Halides and Chalcogenides. *Acta Crystallogr., Sect. A: Cryst. Phys., Diffr., Theor. Gen. Crystallogr.* **1976**, *32* (5), 751–767.

(74) Her, J.-H.; Stephens, P. W.; Gao, Y.; Soloveichik, G. L.; Rijssenbeek, J.; Andrus, M.; Zhao, J.-C. Structure of Unsolvated Magnesium Borohydride $Mg(BH_4)_2$. *Acta Crystallogr., Sect. B: Struct. Sci.* **2007**, *63*, 561–568.

(75) Brese, N. E.; O'Keeffe, M. Bond-Valence Parameters for Solids. *Acta Crystallogr., Sect. B: Struct. Sci.* **1991**, *47* (2), 192–197.

(76) Brown, I. D. Recent Developments in the Methods and Applications of the Bond Valence Model. *Chem. Rev.* **2009**, *109* (12), 6858–6919.

(77) Hayward, M. A.; Green, M. A.; Rosseinsky, M. J.; Sloan, J. Sodium Hydride as a Powerful Reducing Agent for Topotactic Oxide Deintercalation: Synthesis and Characterization of the Nickel(I) Oxide $LaNiO_2$. *J. Am. Chem. Soc.* **1999**, *121* (38), 8843–8854.

(78) Bellotto, M.; Rebours, B.; Clause, O.; Lynch, J.; Bazin, D.; Elkaim, E. A Reexamination of Hydrotalcite Crystal Chemistry. *J. Phys. Chem.* **1996**, *100* (20), 8527–8534.

JOURNAL OF
APPLIED
CRYSTALLOGRAPHY

ISSN 1600-5767

Received 2 June 2016
Accepted 12 August 2016

Edited by Th. Proffen, Oak Ridge National Laboratory, USA

Keywords: stacking faults; Rietveld refinement; crystallography; *TOPAS* software.

Averaging the intensity of many-layered structures for accurate stacking-fault analysis using Rietveld refinement

Alan A. Coelho,[a]* John S. O. Evans[b] and James W. Lewis[b]

[a]72 Cedar Street, Wynnum, Brisbane, Queensland 4178, Australia, and [b]Department of Chemistry, University Science Site, Durham University, South Road, Durham DH1 3LE, England. *Correspondence e-mail: alancoelho@bigpond.com

Many technologically important synthetic and natural materials display stacking faults which lead to complex peak broadenings, asymmetries and shifts in their powder diffraction patterns. The patterns can be described using an enlarged unit cell (called a supercell) containing an explicit description of the layers. Since the supercell can contain hundreds of thousands of atoms with hundreds of thousands of *hkl* reflections, a Rietveld approach has been too computationally demanding for all but the simplest systems. This article describes the implementation of the speed-ups necessary to allow Rietveld refinement in the computer program *TOPAS* Version 6 (Bruker AXS, Karlsruhe, Germany). Techniques implemented include: a peaks buffer that allows hundreds of thousands of *hkl*-dependent peak shapes to be automatically approximated by a few hundred peaks; an averaging process for hundreds of large supercells with minimum impact on computational time; a smoothing technique that allows for the use of small supercells which approximate supercells ten to 20 times larger; and efficient algorithms for stacking sequence generation. The result is Rietveld refinement of supercells operating at speeds several thousand times faster than traditional Rietveld refinements. This allows quantitative and simultaneous analysis of structure and microstructure in complex stacking-faulted samples.

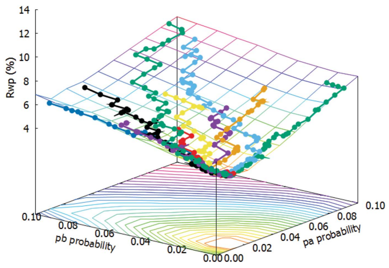

1. Introduction

Quantitative Rietveld analysis of layered structures exhibiting stacking vector faulting is becoming more common as computers become more powerful and the analytical software more accommodating. The supercell approach (Ufer *et al.*, 2004; Wang *et al.*, 2012; Lutterotti *et al.*, 2010) uses multiple layers in an enlarged unit cell in order to simulate faulted layered structures; it was used alongside recursive *DIFFaX* simulations (Treacy *et al.*, 1991) using *TOPAS* Version 5 by Bette *et al.* (2015). In that work many stacking sequences relating to the structure of NiCl(OH) were trialled, with each run taking days of computing time. The present work addresses the time-consuming computational aspects of the supercell approach and is an extension of the work by Ainsworth *et al.* (2016). Bottlenecks associated with unit cells comprising thousands of atoms resulting in hundreds of thousands of reflections are tackled. In particular the 3 h 1000 repeat Rietveld refinements performed by Ainsworth *et al.* (2016) for averaging of supercells can now be performed in under 1 min.

Rietveld refinement (Rietveld, 1969; Young, 1993) can be broken down into a number of steps: (i) calculation of structure factors, (ii) calculating peaks with intensities obtained from the structure factors, (iii) forming a diffraction pattern using the calculated peaks and (iv) calculating derivatives for parameters that are refined. We address the challenges associated with each of these steps and then exemplify the computational speed gains possible.

2. Calculating structure factors

The structure factor for a particular *hkl* of a structure that can be described in terms of stacked layers is the complex quantity

$$F_{\mathrm{str},hkl} = \sum_L \sum_v \sum_a O_{L,a} T_{L,a} (f_{o,L,a} + f'_{L,a} + i f''_{L,a}) \times \exp\{2\pi i[\mathbf{h}\cdot(\mathbf{r}_{L,a} + \mathbf{v}_{L,v})]\}, \qquad (1)$$

where the subscript L corresponds to the different layer types, v to stacking vectors of layer L and a to the atoms in layer L. $\mathbf{r}_{L,a}$ corresponds to the atom vector position in fractional coordinates, $T_{L,a}$ the temperature factor, $O_{L,a}$ the site occupancy, $f_{o,L,a}$ the atomic scattering factor, $f'_{L,a}$ and $f''_{L,a}$ the anomalous dispersion coefficients, $\mathbf{h}$ the *hkl* vector $\{h, k, l\}$, and $\mathbf{v}_{L,v}$ the stacking vector $\mathbf{v}$ of each layer in fractional coordinates. The stacking vector part of equation (1) can be taken out of the innermost summation, as shown in equation (2), allowing the stacking vector summation to be performed independently of the layer summation:

$$F_{\mathrm{str},hkl} = \sum_L \left\{ \sum_v \exp[2\pi i(\mathbf{h}\cdot\mathbf{v}_{L,v})] \right\} \mathrm{Layer}_{L,hkl},$$

where

$$\mathrm{Layer}_{L,hkl} = \sum_a \mathrm{Atom}_{L,a}$$

and

$$\mathrm{Atom}_{L,a} = O_{L,a} T_{L,a} (f_{o,L,a} + f'_{L,a} + i f''_{L,a}) \exp[2\pi i(\mathbf{h}\cdot\mathbf{r}_{L,a})]. \qquad (2)$$

In many cases the number of unique x and y coordinates N_{uxy} amongst the stacking vectors $\{\mathbf{v}_{L,v,x}, \mathbf{v}_{L,v,y}\}$ is small, and equation (2) can be rearranged to reflect this as shown in equation (3) where the summation over vxy corresponds to stacking vectors with unique $\{\mathbf{v}_{L,v,x}, \mathbf{v}_{L,v,y}\}$ and the summation over u corresponds to $\mathbf{v}_{L,v,z}$ values that all have the same $\{\mathbf{v}_{L,v,x}, \mathbf{v}_{L,v,y}\}$. The resulting $V_{L,hkl}$ is a complex quantity derived from all the stacking vectors as applied to layer L. Performing the summation of equation (2) using equation (3) can speed up the calculation of $F_{\mathrm{str},hkl}$ by a factor of 15–20:

$$F_{\mathrm{str},hkl} = \sum_L V_{L,hkl} \mathrm{Layer}_{L,hkl}$$

where

$$V_{L,hkl} = \sum_{vxy} \exp[2\pi i(hv_{x,vxy} + kv_{y,vxy})] \sum_u \exp(2\pi i l v_{z,vxy,u}). \qquad (3)$$

For analyses where $\{\mathbf{v}_{L,v,x}, \mathbf{v}_{L,v,y}\}$ vectors are randomly offset, as in the work of Bette *et al.* (2015), then the speed gain using equation (3) is not possible.

3. Obtaining an average intensity from many similarly faulted crystals

To more accurately represent the probabilistic nature of stacking faults using supercells of finite size, an average intensity from many crystals (called structures from here on) can be used. One could perform this averaging from N_{str} separate pattern calculations, where N_{str} corresponds to the number of structures used, which would require an N_{str}-fold increase in computational time. The process can, however, be performed by averaging the intensities as described in equation (4) and then calculating one pattern instead of N_{str} patterns:

$$I_{\mathrm{avg},hkl} = (1/N_{\mathrm{str}}) \sum_{\mathrm{str}} \left|F_{\mathrm{str},hkl}\right|^2. \qquad (4)$$

For structures comprising layer types of various thicknesses, the thickness of each structure will vary because of faulting. A finite and small N_v would then give N_{str} slightly different lattice parameters. Efficient use of equation (4), however, requires the use of a single set of lattice parameters for all structures; for stacking along the c axis this means using an average c lattice parameter c_{avg}. This allows the use of the same set of *hkl* reflections and the same calculated peak shapes in the Rietveld calculations, and means that summing the calculated peaks onto the calculated pattern is performed once and not N_{str} times. The neglected smoothing due to a differing lattice parameter can be approximated in a smoothing function described below.

The speed at which $I_{\mathrm{avg},hkl}$ can be calculated for 100 structures in the generation of a typical powder pattern is only two to three times slower than I_{hkl} for a single structure; this is demonstrated below. In the theoretical recursive method of Treacy *et al.* (1991) the intensity for a particular faulting probability is treated statistically. The present work achieves a similar effect numerically using $I_{\mathrm{avg},hkl}$.

From equations (3) and (4) the computational effort, $O(I_{\mathrm{avg},hkl})$, required to calculate $I_{\mathrm{avg},hkl}$ scales as equation (5):

$$O(I_{\mathrm{avg},hkl}) = N_{\mathrm{str}}(N_v l_{\mathrm{max}} + N_{uxy} N_{hkl}). \qquad (5)$$

l_{max} corresponds to the maximum l value encountered in the calculation of $V_{L,hkl}$ in equation (3).

4. Generating stacking sequences

In the generation of the stacking sequences from a particular stacking probability matrix, it is advantageous to have $I_{\mathrm{avg},hkl}$ changing as little as possible. This allows the goodness of fit of multiple Rietveld refinements to be compared as a function of the parameters of the stacking probability matrix. Indeed, the change in the goodness of fit can be determined as a function of the probability parameters and optimization performed in order to determine best-fit values.

Stacking sequences are generated from a stacking probability matrix of the type used in the *DIFFaX* package [Treacy *et al.* (1991); see for example Fig. 9 of Ainsworth *et al.* (2016)]. In an initial step the probability matrix is used to generate $N_{\mathrm{avg}} N_{\mathrm{str}} N_v$ layers, and from this prediction run the number of

```
1) For each structure generate $N_v$ layers based on the probability matrix and form
   a single summation over all structures to produce the summation matrix $\mathbf{S}_{gen}$ of
   layer i to j transitions.

2) Terminate the generation of $\mathbf{S}_{gen}$ when the following is obeyed for each of its
   elements:

   $\left|\mathbf{S}_{pred,i,j} - \mathbf{S}_{gen,i,j}\right| < q\,\mathbf{S}^{1/2}_{pred,i,j}$

   where the subscripts i and j are over the elements of S and q = 0.5.

3) Chose one of the generated structures at random.

4) Add a layer to the randomly chosen structure and keep the last $N_v$ layers.

5) Go to step (2).
```

Figure 1
Steps used in the generation of stacking sequences for all structures.

each layer i to j transition is determined and placed in a summation matrix $\mathbf{S}$, which is then divided by $N_{\rm avg}$ to give $\mathbf{S}_{\rm pred}$. $N_{\rm avg}$ is typically set to 100. Stacking sequences for each structure are then generated according to the steps shown in Fig. 1. This procedure ensures that the generated summation matrix $\mathbf{S}_{\rm gen}$ closely matches $\mathbf{S}_{\rm pred}$, which in turn matches the overall faulting expressed in the transition matrix. The overall time for generating sequences is small compared to the Rietveld calculations. On termination of the generation process an average c lattice parameter $c_{\rm avg}$ from the $N_{\rm str}$ structures is determined and subsequently used in the calculation of peak positions.

5. Smoothing ripples and correcting for differing layer thicknesses

For layer types with differing thicknesses the generation scheme in Fig. 1 will produce supercells of slightly varying thicknesses (varying c lattice parameters), resulting in smearing of the peaks. This smearing is not described by $I_{{\rm avg},hkl}$ (§3) owing to the use of a finite and single $c_{\rm avg}$ lattice parameter in the calculation of peak position. In addition, stacking-faulted diffraction patterns calculated from small-N_v supercells will contain ripples and oscillations from individual hkl reflections when the instrument, emission profile and sample aberrations are small. Using $I_{{\rm avg},hkl}$ reduces ripples caused by poor faulting statistics, but does not eliminate the ripples caused by small N_v. Ainsworth *et al.* (2016) therefore used a large supercell, $N_v = 5000$, to minimize both effects and generate a smooth pattern. Being able to reduce N_v whilst (i) reducing ripples and (ii) describing smearing due to the use of a single c lattice parameter without degrading the faulted pattern would be hugely beneficial; the number of reflections would be greatly reduced, resulting in much less computer memory allocation and far greater computational speed.

As N_v increases the number of peaks increase; in particular, stacking along the crystallographic c axis sees peaks inserted between the (h_1, k_1, l_1) and $(h_1, k_1, l_1 + 1)$ peaks where (h_1, k_1, l_1) are the Miller indices when $N_v = 1$. When the distance in 2θ from (h, k, l) to $(h, k, l + 1)$ is less than the step size of the data for all peaks, then the resulting diffraction pattern is smooth. For small N_v and sharp intrinsic peaks it is possible to produce a smooth pattern comparable to one created with a large N_v by inserting peaks, irrespective of N_v, from $2\theta_{h,k,l}$ to $2\theta_{h,k,l+1}$ with intensities ranging from $F^2_{h,k,l}$ to $F^2_{h,k,l+1}$. This introduction of peaks can be approximated by convoluting a right trapezoid of size ${\rm d}2\theta/{\rm d}l = (2\theta_{h,k,l} - 2\theta_{h,k,l+1})$ into each hkl reflection with intensities at its ends corresponding to $F^2_{h,k,l}$ and $F^2_{h,k,l+1}$. Similarly, a right trapezoid of size $(2\theta_{h,k,l-1} - 2\theta_{h,k,l})$ can be convoluted to insert peaks from $2\theta_{h,k,l-1}$ to $2\theta_{h,k,l}$. This twin right trapezoidal function can be approximated by a Gaussian centred at $2\theta_{h,k,l}$ and then shifted by the centroid shift of the twin trapezoid as shown in equation (6*a*).

Not all peaks should be broadened by ${\rm d}2\theta/{\rm d}l$. For example, if all layers have the same height, peaks with indices $(0, 0, nN_v)$ where n is an integer would not be broadened; nor would other categories of (h, k, nN_v) peaks depending on the faulting mechanism. When going from a no-faulting case to a faulting case, lattice points with unchanging perpendicular distances to a particular plane will have their corresponding peak remain sharp. One way of testing whether (h, k, l) should be broadened is by looking at the structure factors. If $F^2_{h,k,l-1}$ and $F^2_{h,k,l+1}$ are near zero and $F^2_{h,k,l}$ is large, then little to no broadening is expected. On the other hand if $F^2_{h,k,l-1}$, $F^2_{h,k,l}$ and $F^2_{h,k,l+1}$ are all of a similar intensity then ${\rm d}\theta/{\rm d}l$ broadening is expected. If we assume the broadening is dependent on $1 - F^2_{h,k,l}/(F^2_{h,k,l-1} + F^2_{h,k,l} + F^2_{h,k,l+1})$ we arrive at the broadening term $\Delta_{h,k,l}$ shown in equation (6*b*):

$$\text{Shift}_{h,k,l} = \left[\frac{(2\theta_{h,k,l-1} - 2\theta_{h,k,l})F^2_{h,k,l-1} + (2\theta_{h,k,l+1} - 2\theta_{h,k,l})F^2_{h,k,l+1}}{F^2_{h,k,l-1} + F^2_{h,k,l} + F^2_{h,k,l+1}}\right], \quad (6a)$$

$$\Delta_{h,k,l} = \tau {\rm d}2\theta/{\rm d}l\left(\frac{F^2_{h,k,l-1} + F^2_{h,k,l+1}}{F^2_{h,k,l-1} + F^2_{h,k,l} + F^2_{h,k,l+1}}\right). \quad (6b)$$

τ is a parameter that is varied in order to obtain the best fit during refinement. $\Delta_{h,k,l}$ is small when $F^2_{h,k,l-1}$ and $F^2_{h,k,l+1}$ are small and $F^2_{h,k,l}$ is large; it is large when $F^2_{h,k,l-1}$, $F^2_{h,k,l}$ and $F^2_{h,k,l+1}$ are of similar intensity. $\Delta_{h,k,l}$ corresponds to the FWHM in 2θ of a Gaussian function convoluted into each peak and $\text{Shift}_{h,k,l}$ is the shift applied to each convolution. Equations (6*a*) and (6*b*) represent a smoothing function that allows small supercells to approximate much larger supercells. In addition to reducing ripples due to a small N_v, it also approximates the smearing not seen when there are layer types of varying thicknesses and a single set of lattice parameters used.

This approach produces calculated patterns comparable to supercells ten to 20 times larger. Specifically for two cases a and b with $N_{v,a}$ and $N_{v,b}$ layers, the speed gain in terms of calculating $I_{\text{avg},hkl}$ using equation (5) is shown in equation (7):

$$\begin{aligned}\text{Gain} &= O_a(I_{\text{avg},hkl})/O_b(I_{\text{avg},hkl}) \\ &= N_{\text{str},a}(N_{v,a}l_{\max,a} + N_{uxy,a}N_{hkl,a}) \\ &\quad /[N_{\text{str},b}(N_{v,b}l_{\max,b} + N_{uxy,b}N_{hkl,b})],\end{aligned} \tag{7}$$

where $O(I_{\text{avg},hkl})$ is the computational effort to calculate $I_{\text{avg},hkl}$. For cases a and b to have similar faulting statistics then $N_{\text{str},a}N_{v,a} = N_{\text{str},b}N_{v,b}$. Noting also that $l_{\max,a}/l_{\max,b} = N_{v,a}/N_{v,b}$ and $N_{hkl,a}/N_{hkl,b} = N_{v,a}/N_{v,b}$, after substitution into equation (7) we get the speed gain shown in equation (8):

$$\text{Gain} = (N_{v,a}l_{\max,b} + N_{uxy,a}N_{hkl,a})/(N_{v,b}l_{\max,b} + N_{uxy,b}N_{hkl,b}). \tag{8}$$

For structures with small N_{uxy} equation (8) reduces to $\sim N_{v,a}/N_{v,b}$. If $\mathbf{v}_{L,v,x}$ and $\mathbf{v}_{L,v,y}$ were random values, then $N_{uxy,a}$ and $N_{uxy,b}$ would become $N_{v,a}$ and $N_{v,b}$ for systems a and b, respectively. The speed gain would then be exactly $N_{v,a}/N_{v,b}$.

6. Calculating derivatives of structural parameters

Derivatives of $I_{\text{avg},hkl}$ with respect to stacking vector coordinates, atomic coordinates, occupancies, atomic scattering factors, anomalous dispersion coefficients or temperature factors are all necessary in order to refine on the corresponding parameters in a nonlinear least-squares sense. Excluding the stacking vector coordinates, these derivatives can all be calculated using a layer-dependent $N_{\text{str}} \times N_{hkl}$ matrix calculated for each nonlinear least-squares iteration. Consider the case of calculating the derivative with respect to the fractional atomic coordinate $r_{L,a,x}$ for atom a of layer L. From equation (3) we have

$$\partial I_{\text{avg},hkl}/\partial r_{L,a,x} = 2F_{\text{str},hkl}V_{L,hkl}\text{Atom}_{L,a}2\pi ih. \tag{9}$$

In each derivative the quantity $2F_{\text{str},hkl}V_{L,hkl}$ is used. Both $F_{\text{str},hkl}$ and $V_{L,hkl}$ are used during the calculation of $I_{\text{avg},hkl}$ and hence do not need recalculating for the derivatives. Thus, once $I_{\text{avg},hkl}$ is calculated, determining the derivatives for a structural parameter for a multi-structure refinement takes the same computational effort as for a single-structure refinement. For the stacking vector coordinates, the derivative from equation (3) for the x coordinate of stacking vector v becomes

$$\partial I_{\text{avg},hkl}/\partial v_{L,x} = 2F_{\text{str},hkl}\text{Layer}_{L,hkl}\exp[2\pi i(\mathbf{h}\cdot\mathbf{v}_L)]2\pi ih. \tag{10}$$

Again, both $F_{\text{str},hkl}$ and $\text{Layer}_{L,hkl}$ are calculated during the calculation of $I_{\text{avg},hkl}$ and hence do not need recalculation for stacking vector coordinate derivatives. Even though these derivatives can be calculated in a fast manner, coordinates of the stacking vectors are typically not refined independently as the quality of the data does not support using thousands of such parameters. Instead, thicknesses of layer types might be refined, resulting in fewer than a dozen or so independent parameters.

7. Computational effort as compared to traditional Rietveld refinement

Rietveld refinement without the use of stacking vectors requires the explicit definition of atoms in each stacked layer. We can consider the computational effort using a traditional approach [*e.g.* *TOPAS* Version 4 (Bruker, 2009)] for averaging N_{str} = 100 structures each with N_v = 960 layers using the $\text{La}_2\text{O}_2\text{Cu}_{0.667}\text{Cd}_{0.667}\text{Se}_2$ example investigated by Ainsworth *et al.* (2016). Each structure has N_{hkl} = 54 881 *hkl* reflections and six layer types $N_L = 6$, with four layers having seven atoms per layer and two layers having eight atoms per layer. Each peak shape generated requires $N_{\text{ops\_per\_pk}} \simeq 2000$ operations and each summation of the peak shape to the calculated pattern requires $N_{\text{pk\_shape\_sum}} \simeq 150$ operations. The value of $N_{\text{ops\_per\_pk}} \simeq 2000$ corresponds to a pseudo-Voigt peak shape convoluted with one emission profile line with the instrument aberrations of axial divergence and a receiving slit width (Cheary & Coelho, 1992). The computational effort required to calculate $I_{\text{avg},hkl}$, $O(I_{\text{avg},hkl})$, and to calculate the peaks, $O(\text{Peaks})$, approximately scales according to equation (11) with all numbers originating from the program itself:

$$\begin{aligned}O(I_{\text{avg},hkl}) &= N_{\text{str}}N_{hkl}\Big(\sum_L N_{L,\text{atoms}}\Big)N_v/N_L \\ &= 100 \times 54881 \times 44 \times 960/6 = 3.86 \times 10^{10}, \\ O(\text{Peaks}) &= N_{hkl}(N_{\text{ops\_per\_pk}} + N_{\text{pk\_shape\_sum}}) \\ &= 54481 \times (2000 + 150) = 1.17 \times 10^8.\end{aligned} \tag{11}$$

The same calculation in *TOPAS* Version 6 with the stacking implementations discussed above reduces to the scaling shown in equation (12):

$$\begin{aligned}O(I_{\text{avg},hkl}) &= N_{hkl}\Big(\sum_L N_{L,\text{atoms}}\Big) + 2N_{hkl}\Big(\sum_L N_{L,\text{atoms}}\Big) + N_L(l_{\max} + N_{hkl}) \\ &= 54881 \times 44 + 2 \times 44 \times 54881 + 6 \times (4915 + 54881) \\ &= 7.60 \times 10^6 \\ O(\text{Peaks}) &= N_{\text{pks\_buf}}N_{\text{ops\_per\_pk}} + N_{\text{pks\_summed}}N_{\text{pk\_shape\_sum}} \\ &= 1348 \times 2000 + 11000 \times 150 = 4.34 \times 10^6.\end{aligned} \tag{12}$$

$N_{hkl}(\sum_L N_{L,\text{atoms}})$ corresponds to $\sum_L \text{Layer}_{L,hkl}$ in equation (2), which relates to the calculation of the structure factors for the six different layers. $l_{\max}$ corresponds to the maximum l value encountered in the calculation of $V_{L,hkl}$ in equation (3).

For *hkl*-dependent peak broadening traditional Rietveld programs, for example *TOPAS* Version 5 (Coelho, 2015) and earlier, would require the calculation of $N_{\text{str}}N_{hkl} = 2.5 \times 10^8$ peaks. *TOPAS* Version 6 uses a peaks buffer that is *hkl* dependent (Ainsworth *et al.*, 2016) to greatly reduce the number of peaks calculated. In this example it generates $N_{\text{pks\_buf}}$ = 3474 peaks which is used by the N_{str} structures. Summing the peaks from the peaks buffer to form the calculated pattern is also a process that can be streamlined such that peaks of a similar shape that lie between adjacent data points have their intensities appropriated to the adjacent data points. In this manner the number of peaks summed onto the calculated pattern is typically less than the number of data points in the pattern; in the present example $N_{\text{pks\_summed}} \simeq$ 11 000 as opposed to the number of reflections which is 54 881.

Table 1
Average and standard deviation of R_{wp} over 30 refinements each on *DIFFaX*-simulated diamond data for pa = 0.7 for various N_{str} and N_v values.

Refinement range 10–150° 2θ. The smoothing function was applied to all refinements except for the cases with N_v = 5000.

N_{str}	1	1	200	1000	500	200	10000	5000	200
N_v	200	5000	200	100	200	500	100	200	5000
$N_{str} \times N_v$	200	5000	40000	100000			1000000		
N_{hkl}	9474	236902	9474	2361	9474	23611	4724	9474	236902
N_{pks_buf}	2532	2760	2532	1122	2532	5305	1122	2532	2760
Average R_{wp} (%)	2.90	1.28	0.509	0.498	0.489	0.483	0.471	0.458	0.465
Standard deviation R_{wp} (%)	0.53	0.17	0.040	0.020	0.025	0.027	0.007	0.006	0.006

Both equations (11) and (12) are approximate in regards to computing time as each operation can amount to four to ten floating-point operations with the actual time taken being hardware dependent; they do, however, give an idea of the magnitude of the computation, especially when comparing the values between equations (11) and (12). For derivatives the computational effort is dependent on which parameters are refined. The number of operations for calculating a peak shape derivative scales by $O(\text{Peaks})$; for structural parameters it scales by N_{hkl} [see equation (9)] and $O(N_{pks\_summed}\, N_{pk\_shape\_sum})$. Thus even though $O(N_{pks\_summed}\, N_{pk\_shape\_sum})$ is relatively small compared to $I_{avg,hkl}$ of equation (12), it can become significant when many structural parameters are refined.

The resulting computational speed-up of equation (12) compared to traditional Rietveld refinement [equation (11)] is of the order of 10^4; this would further increase for structures with more atoms in each layer, or for cases where more complex peak shapes are used.

8. Test data

Fig. 2 shows the current implementation fitting data generated with the test input file `dia.dat` for stacking-faulted diamond distributed with the *DIFFaX* suite (Treacy *et al.*, 1991) with a 0.7 probability (pa) for N_v = 200 and for the cases of N_{str} = 1 and N_{str} = 200. The much improved fit for N_{str} = 200 (Fig. 2*b*), R_{wp} = 0.51% as opposed to R_{wp} = 3.74%, is due to the averaging procedure of equation (4) and the smoothing function of equations (6*a*) and (6*b*). No weighting was given to the data during refinement and the formula used to calculate R_{wp} is shown in equation (13), where Y_o and Y_c correspond to observed (here *DIFFaX*-simulated) and calculated intensities:

$$R_{wp} = 100\left[\frac{\sum_{m=1}^{N_{data}}(Y_{o,m} - Y_{c,m})^2}{\sum_{m=1}^{N_{data}}(Y_{o,m})^2}\right]^{1/2}. \qquad (13)$$

The time taken to perform the first eight iterations for N_{str} = 1 is 1.92 s; for N_{str} = 200 it is 1.99 s. Refinement times, however, depend on what is being refined as various calculated data are saved during refinement and calculated only once. It is therefore more relevant to consider the time taken to calculate the pattern itself; for ten pattern calculations the time for N_{str} = 1 is 0.67 s; for N_{str} = 200 it is 1.26 s; or it is around twice as slow for 200 times more structure-factor calculations. Working with the same *DIFFaX* data of Fig. 2, Ainsworth *et al.* (2016) used N_v = 5000 stacking vectors but with N_{str} = 1. Using the input file of Fig. 3 but with these parameters (N_{hkl} = 236 902, N_{pks_buf} = 2760) results in an R_{wp} of 1.28% and a time to calculate the pattern ten times of 6.8 s. This demonstrates the great benefit of averaging in both computing time and accuracy.

To explore the influence of N_{str} and N_v the simulated data were initially fitted with N_{str} = 200 and N_v = 5000 and without the use of the smoothing function; five peak shape parameters, a zero error and one Rietveld scale parameter were initially refined. These large N_{str} and N_v values result in a low R_{wp} of 0.465% as shown in Table 1. The peak shape parameters and zero error were then fixed and the smoothing function of equations (6*a*) and (6*b*) included in refinements using

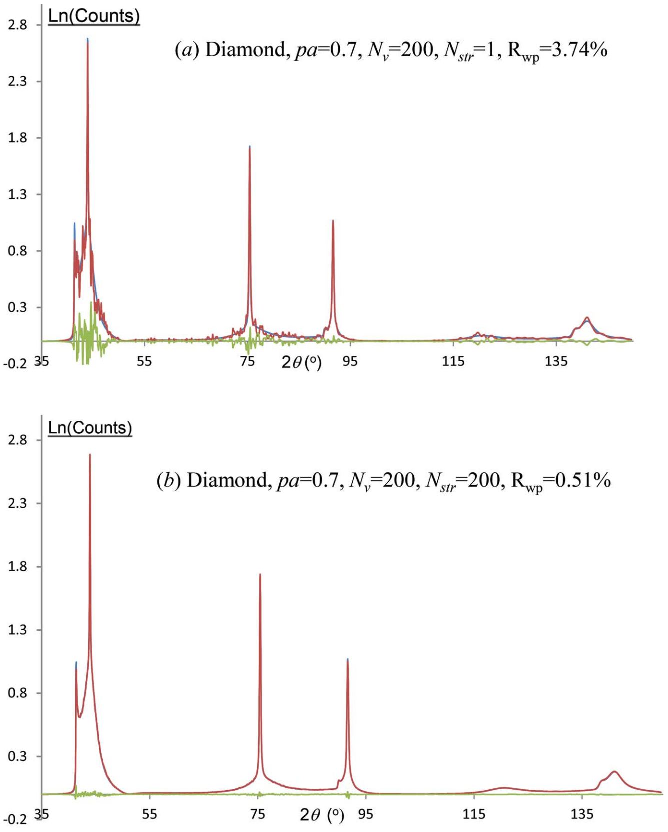

Figure 2
Fit to simulated diamond data from *DIFFaX* for the cases of (*a*) N_{str} = 1 and (*b*) N_{str} = 200. In both cases N_{hkl} = 9474 and N_{pks_buf} = 2532 peaks. Red, blue and grey lines correspond to calculated, *DIFFaX* simulation and difference plots, respectively.

Table 2
Fractional atomic coordinates used to generate test patterns.

All sites occupied with carbon atoms with an occupancy of 1.

Layer	Atom	x	y	z	$B_{\rm eq}$ (Å^2)
1	C	−1/3	−1/6	−0.125	1
1	C	1/3	1/6	0.125	1
2	C	1/3	1/6	−0.125	1
2	C	−1/3	−1/6	0.125	1

different $N_{\rm str}$ and N_v values; Table 1 shows the results. For equivalent faulting statistics ($N_{\rm str} \times N_v$ equal) the $R_{\rm wp}$ values are very similar. A reduction in $R_{\rm wp}$ is seen as $N_{\rm str} \times N_v$ increases. For $N_v \geq 100$ and for $N_{\rm str} \times N_v \geq 100\,000$ $R_{\rm wp}$ values are similar. The case of $N_{\rm str} = 200$, $N_v = 200$ has a marginally higher $R_{\rm wp} = 0.509\%$, but still with the excellent fit seen in Fig. 2(*b*). These data demonstrate that small supercells (low N_v) can approximate much larger supercells when averaging and the smoothing function of equations (6*a*) and (6*b*) are used.

To further test the $I_{\rm avg}$ procedure, the test structure described in Table 2 and Fig. 4 was used to generate a complex test pattern with $pa = 0.7$ and with two different layer heights of 5 and 6 Å ($\varepsilon = 1$ in Fig. 4), with the other five lattice parameters being $a = 3$, $b = 4$ Å, $\alpha = 90$, $\beta = 90$ and $\gamma = 95°$. For accuracy, a small step size of 0.01° 2θ was used and the peak shape comprised a Gaussian instrument function with an FWHM of twice the step size; this results in a pattern that is essentially the aberration function produced from stacking faults. The pattern was generated using a normal Rietveld calculation averaging 200 individual structures, each with a large supercell comprising $N_v = 2000$ layers and each with separate c lattice parameters corresponding to the overall heights of the stacked layers. Each unit cell therefore comprised $2000 \times 4 = 8000$ atoms for a total of 1 600 000 atomic sites in the calculation. The calculation was performed out to 40° 2θ which encompassed 28 325 reflections. This translates to an innermost loop for the calculation of structure factors that is executed $1\,600\,000 \times 28\,325 = 45\,176\,000\,000$ times; the pattern calculation time was long at 1828 s. Fitting to this test pattern using $I_{\rm avg}$ with $N_{\rm str} = 200$ and $N_v = 2000$ (identical faulting statistics to the generation procedure) produces the good fit shown in Fig. 5 where $R_{\rm wp} = 3.27\,(20)\%$; the calculation time for the first iteration was only 1.2 s. The nonzero $R_{\rm wp}$ is due to the faulting statistics represented by the transition probability matrix and remaining minor ripples in the (instrument/sample unbroadened) test pattern. Setting $N_v = 400$ and using the smoothing function of equations (6*a*) and (6*b*) results in $R_{\rm wp} = 4.08\,(25)\%$ and a tenfold faster calculation of 0.12 s. Thus $I_{\rm avg}$ correctly describes the Rietveld-generated pattern with two layer heights in an extremely fast manner when a relatively small N_v is used together with the smoothing function.

To further show the benefits of the smoothing function of equations (6*a*) and (6*b*) the same structure but with $\alpha = 75$, $\beta = 85$ and $\gamma = 95°$ was used to generate a test pattern out to 150° 2θ; no smoothing function was used and the

```
xdd diffax_dia.xye
  LP_Factor(0) bkg 1
  start_X 10 finish_X 149.6
  rebin_with_dx_of 0.01
  lam ymin_on_ymax 0.0001 la 1 lo 1.5405754 lh  1e-5
  Zero_Error(@, 0.0025)
  weighting 1
  str
     space_group P1
     a 2.518156 b 2.518156 c = Get(generated_c); ga 120
     prm !pa 0.7 prm !h 2.05870
     prm s 1 min 1e-15 scale = s 1e-6 / (Nv Nstr);
     generate_stack_sequences {
        number_of_sequences Nstr 200
        number_of_stacks_per_sequence Nv 5000
        Transition(A, h)
           to A = pa;   a_add =  2/3; b_add =  1/3;
           to B = 1-pa; a_add =  0;   b_add =  0;
         Transition(B, h)
           to A = 1-pa; a_add =  0;   b_add =  0;
           to B = pa;   a_add = -2/3; b_add = -1/3;
     }
     site C1 x =-1/3; y =-1/6; z = -0.125/Nv; occ C 1 beq 1 layer A
     site C2 x = 1/3; y = 1/6; z =  0.125/Nv; occ C 1 beq 1 layer A
     site C3 x = 1/3; y = 1/6; z = -0.125/Nv; occ C 1 beq 1 layer B
     site C4 x =-1/3; y =-1/6; z =  0.125/Nv; occ C 1 beq 1 layer B
     peak_buffer_based_on = Xo; peak_buffer_based_on_tol 0.1
     TCHZ_Peak_Type(@,0.01,@,-0.01,@,0.01,,0,@,0.1,@,0.01) 'Instrument function
```

Figure 3
Input file used for fitting to *DIFFaX* diamond data for $N_{\rm str} = 200$ and $N_v = 5000$.

From layer 1

To layer 1 with a probability of *pa* and shifted by the vector {2/3,1/3,c/N_v}

To layer 2 with a probability of 1-*pa* and shifted by the vector {0,0,c/N_v}

From layer 2

To layer 1 with a probability of 1-*pa* and shifted by the vector {2/3,0,$(c+\varepsilon)/N_v$}

To layer 2 with a probability of *pa* and shifted by the vector {2/3,2/3,$(c+\varepsilon)/N_v$}

Figure 4
Transition matrix and stacking vectors used to generate test patterns. Shifts in the *ab* plane are expressed in fractional coordinates, those along the stacking direction in Å.

pattern was again generated using $I_{\rm avg}$ with $N_{\rm str} = 200$ and $N_\nu = 2000$. Fitting to this test pattern with the same faulting statistics (equal $N_{\rm str} \times N_\nu$) we put $N_{\rm str} = 2000$ and $N_\nu = 200$. Fig. 6(*a*) shows the poor fit when the smoothing function is not used. Fig. 6(*b*) shows the fit when the smoothing function is used, resulting in $R_{\rm wp} = 1.77$ (13)% out to 150° 2θ. Setting $N_{\rm str} = 200$ gives an $R_{\rm wp} = 1.82$ (5)%. Thus, the smoothing function with a small supercell accurately describes much larger supercells for the complex case of varying layer heights.

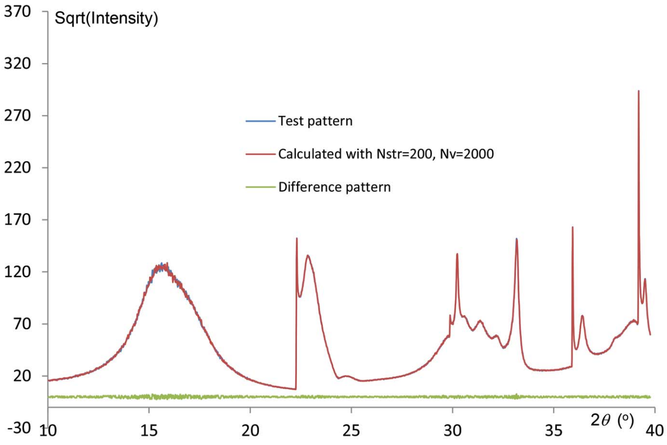

Figure 5
Fit to Rietveld-generated pattern comprising 200 structures each with 2000 layers and each with its own *c* lattice parameter determined from the different layer thicknesses and faulting. The calculated pattern used the $I_{\rm avg}$ implementation with a single *c* lattice parameter.

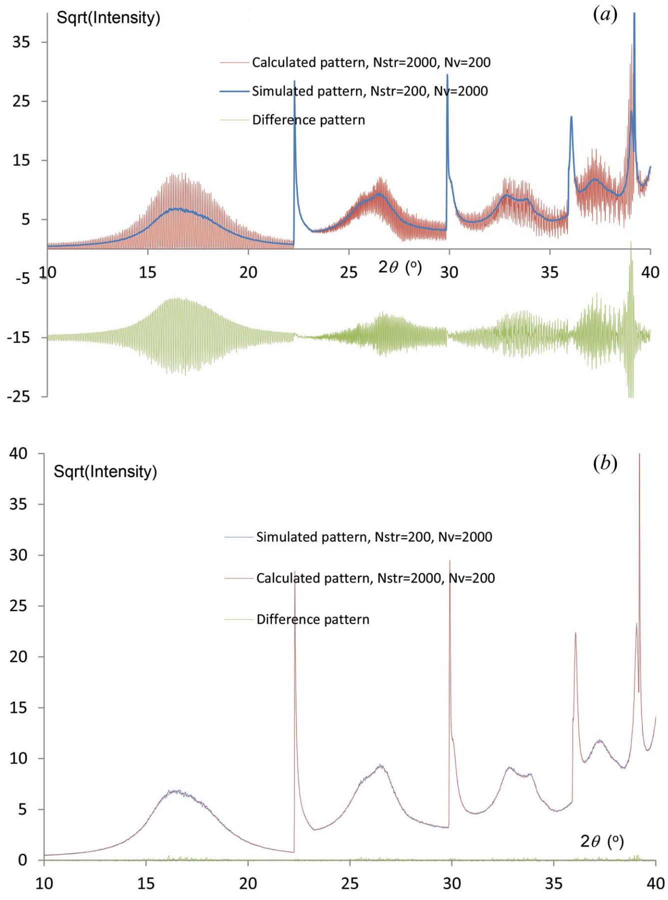

Figure 6
Fit to a simulated test pattern created with $N_\nu = 2000$ and no smoothing function using a calculated pattern created with $N_\nu = 200$ for the cases (*a*) with no smoothing function and (*b*) with the smoothing function.

Fig. 7 shows the fit to a simulated pattern of the $La_2O_2Cu_{0.667}Cd_{0.667}Se_2$ structure reported by Ainsworth *et al.* (2016) which comprised three layer types. The simulated pattern used a step size of 0.005° 2θ, peak shapes set to a Gaussian with an FWHM of 0.01° 2θ, $N_{\rm str} = 200$ and $N_\nu = 2000$, and no smoothing function. The calculated pattern for $N_{\rm str} = 2000$ and $N_\nu = 200$ with the smoothing function resulted in $R_{\rm wp} = 1.335$ (39)%; setting $N_{\rm str} = 200$ and $N_\nu = 200$ gives $R_{\rm wp} = 1.63$ (27)%. These $R_{\rm wp}$ values can be compared to 1.45% for $N_{\rm str} = 200$ and $N_\nu = 2000$ (same values as those used for the simulated pattern; nonzero $R_{\rm wp}$ due to the faulting statistics). Fig. 8 shows $R_{\rm wp}$ as a function of iteration time from Rietveld refinement using $I_{\rm avg}$, the smoothing function, $N_{\rm str} = 200$ and $N_\nu = 200$ for the $La_2O_2Cu_{0.667}Cd_{0.667}Se_2$ test pattern. The refinement range was set to 1.5–30° 2θ, resulting in 41 272 reflections. The refinement comprised 15 site coordinate

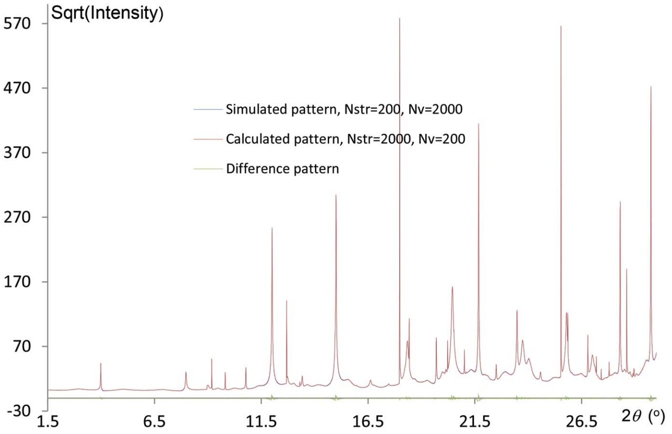

Figure 7
Fit to a simulated $La_2O_2Cu_{0.667}Cd_{0.667}Se_2$ test pattern created with *pa* = 0.3, $N_\nu = 2000$ and no smoothing function using a calculated pattern with $N_\nu = 200$ and with the smoothing function.

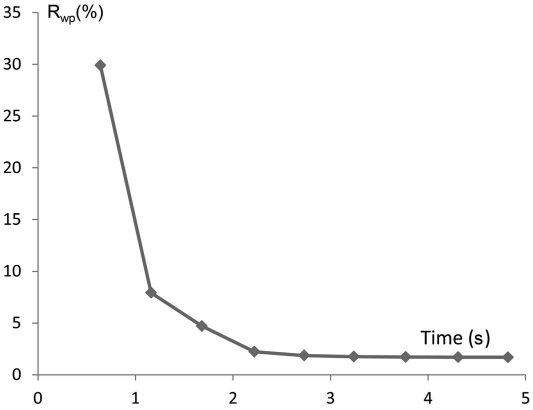

Figure 8
$R_{\rm wp}$ *versus* time from Rietveld refinement of a test $La_2O_2Cu_{0.667}Cd_{0.667}Se_2$ pattern. The refinement used $N_{\rm str} = 200$ and $N_\nu = 200$.

Table 3
Average and standard deviation of $R_{\rm wp}$ and $pa_{\rm gen}$ over 500 refinements for $La_2O_2Cu_{0.667}Cd_{0.667}Se_2$ [data from Ainsworth *et al.* (2016)] for various $N_{\rm str}$ and N_v values.

Refinement range 1.5–20° 2θ. The approximate relative time required for each of the 500 refinements is given.

$N_{\rm str}$	1	100	200	1	25	100	200
N_v	960	960	960	192	192	192	192
N_{hkl}	54877	54877	54877	10973	10973	10973	10973
$N_{\rm pks\_buf}$	3474	3474	3474	1326	1326	1326	1326
Average $R_{\rm wp}$ (%)	3.014	2.933	2.933	3.591	2.780	2.751	2.748
Standard deviation $R_{\rm wp}$ (%)	0.146	0.010	0.008	0.662	0.044	0.019	0.014
$pa_{\rm gen}$	0.0096	0.01103	0.01101	0.009	0.0109	0.01101	0.01101
Standard deviation $pa_{\rm gen}$	0.0014	0.00012	0.00008	0.006	0.0006	0.00025	0.00022
Time (s)	0.71	1.33	1.96	0.45	0.49	0.56	0.66

parameters, three layer height parameters, one lattice parameter, one Rietveld scale parameter and τ from the smoothing function of equation (6*b*). Layer height parameters were initially set to ~0.05 Å from their optimal values. Fig. 8 shows the fast convergence of these stacking vector parameters. The 5 s to refinement convergence is significant as it allows for hands-on real-time analysis of such data sets.

These test data suggest that large N_v supercells are not necessary to fit complex patterns. In addition, real data have considerable intrinsic broadening due to instrument, emission profile and specimen-type aberrations such as crystallite size and strain broadening. Thus, even though the smoothing function of equations (6*a*) and (6*b*) is important in allowing small-N_v fits to simulated test data with narrow intrinsic peaks, the need with real data is lower.

9. Real data analysis

We can further explore the speed and accuracy gains enabled by these developments using one of the data sets described by Ainsworth *et al.* (2016). We choose the $La_2O_2Cu_{0.667}Cd_{0.667}Se_2$ composition discussed above, which is a layered oxychalcogenide that can be described in terms of alternating fluorite-like $[La_2O_2]^{2+}$ slabs and either $[CdSe_2]^{2-}$ or $[Cu_2Se_2]^{2-}$ anti-fluorite-derived slabs. The ideal structure has a 2:1 ordered sequence of metal chalcogenide layers (Cd1|$\underline{\text{Cd2}}$|Cu3|$\underline{\text{Cd4}}$|Cd5|Cu6), where each underlined Cd layer is offset by (*a*/2, *b*/2). Two types of faults were investigated: a *pa*-type fault involving an additional layer of either metal to form local (Cu|Cu|Cd|Cd) or (Cu|Cd|Cd|Cd) sequences; and a *pb* fault involving Cd layers being offset by (*a*/2, *b*/2) either side of a Cu layer. In the original paper the dependence of $R_{\rm wp}$ on fault probabilities *pa* and *pb* was investigated using a model with six [LaOLaSe(Cu$_2$/Cd)Se] layers (three unique) stacked to form a supercell with 960 layers in total ($N_{\rm str}$ = 1, N_L = 6, N_v = 960).

Firstly, we investigate the stacking generation method as a function of the constant q described in step (2) of Fig. 1. Fig. 9(*a*) shows the frequency distribution of $R_{\rm wp}$ for 500 Rietveld refinements for the cases of q = 0.5 and $q = \infty$; in the latter case there is no constraint on the number of faults generated in the structures and the average $R_{\rm wp}$ is slightly larger than the value for q = 0.5. Fig. 9(*b*) shows corresponding generated *pa* values $pa_{\rm gen}$; a much narrower spread in $pa_{\rm gen}$ is found for q = 0.5 as expected. For this reason q = 0.5 is used in the analysis below.

Table 3 shows the influence of different values for $N_{\rm str}$ and N_v on $R_{\rm wp}$ and $pa_{\rm gen}$ using our averaging approach. Fig. 10 shows the influence of different $N_{\rm str}$ values for the $R_{\rm wp}$ surfaces obtained for N_v = 960 with *pa* and *pb* values between 0.0 and 0.1 with different procedures. Fig. 10(*a*) shows the surface of minimum $R_{\rm wp}$ values obtained from 100 $N_{\rm str}$ = 1 trial structures for each of 64 *pa*/*pb* combinations as reported in the original paper. The entire surface took around 15 h to calculate on an i7 3.4 GHz single-core desktop computer. Fig. 10(*b*) shows the equivalent $R_{\rm wp}$ surface determined using our averaging processes with $N_{\rm str}$ = 100, which took 160 s on the same computer. The speed gain is a combination of the smaller number of refinements required (64 *versus* 6400), the use of a more efficient algorithm to create constrained stacking sequences and other improvements to *TOPAS*. A more direct comparison of the speed gain from averaging can be obtained by comparing the time to perform 64 × 100 refinements with $N_{\rm str}$ = 1 (~8000 s) with that to carry out 64 $N_{\rm str}$ = 100 refinements (160 s). A speed gain of

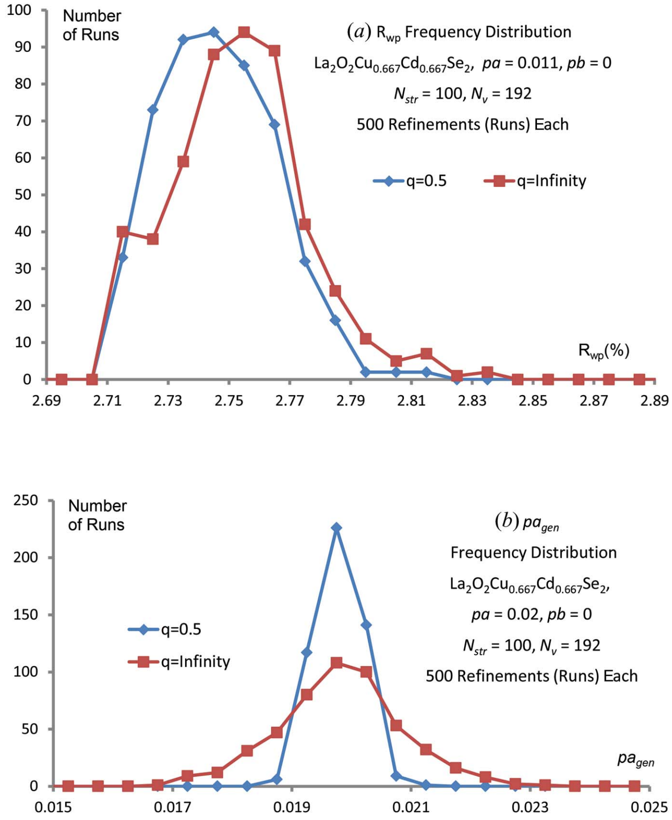

Figure 9
Frequency distribution from two sets of refinements, q = 0.5 and $q = \infty$, each comprising 500 refinements of $La_2O_2Cu_{0.667}Cd_{0.667}Se_2$ with $N_{\rm str}$ = 100 and N_v = 192 for (*a*) $R_{\rm wp}$ and for (*b*) $pa_{\rm gen}$.

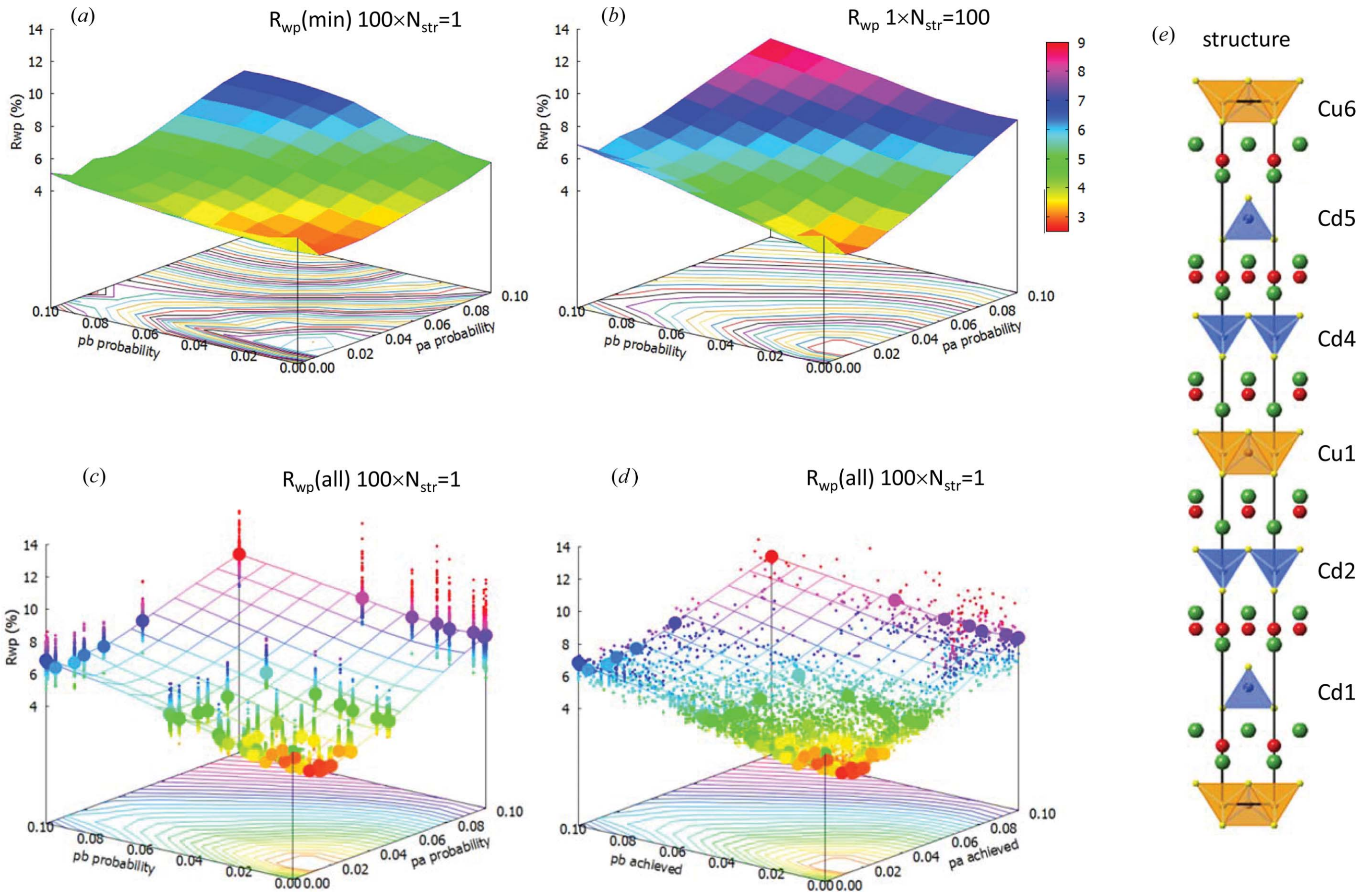

Figure 10
Three-dimensional plots showing R_{wp} values for refinements of different $La_2O_2Cu_{0.667}Cd_{0.667}Se_2$ stacking models. (*a*) The minimum R_{wp} value from 100 repeat refinements of models with $N_\nu = 960$ and $N_{str} = 1$ and different *pa*/*pb* values. (*b*) The R_{wp} value from single models with $N_\nu = 960$ and $N_{str} = 100$. (*c*) A plot of the 100 R_{wp} values for $N_{str} = 1$ (small points) and the single value for $N_{str} = 100$ (large points). (*d*) Same as (*c*) but with data plotted against the actual number of faults generated in each sequence. The same *z* range and colouring are used in each plot. Lines in (*c*) and (*d*) are to guide the eye. (*e*) The structure in terms of $[La_2O_2]^{2+}$ (green/red), $[CdSe_2]^{2-}$ (blue/yellow) and $[Cu_2Se_2]^{2-}$ (brown/yellow) slabs.

around 50-fold is observed, as expected from the discussion above. Using the convolution approach of §5 an equivalent surface can be calculated for $N_\nu = 96$ in around 20 s.

The averaging process with $N_{str} = 100$ also leads to a much better defined minimum in the R_{wp} surface, as shown by the contour levels and minimum–maximum R_{wp} ranges in Figs. 10(*a*) and 10(*b*) (2.80–7.02% and 2.71–8.59%, respectively). The flatter surface in Fig. 10(*a*) arises from the range of R_{wp} values encountered for different individual $N_{str} = 1$ sequences. Fig. 10(*c*) shows this effect by superimposing the single R_{wp} value from the $N_{str} = 100$ refinement (large points and surface mesh) with the 100 R_{wp} values from $N_{str} = 1$ refinements (small points). For each set *pa*/*pb* combination we see a vertical 'rod' of R_{wp} values reflecting the random nature of the individual stacking sequences generated in each structure. Close to the overall R_{wp} minimum the $N_{str} = 100$ refinements lie at the minimum of these rods. For larger *pa*/*pb* values some $N_{str} = 1$ refinements show a lower R_{wp}, but this is due to individual structures having fewer faults than the expectation value. Fig. 10(*d*) shows an equivalent plot to Fig. 10(*c*), but with R_{wp} values for the $N_{str} = 1$ refinements plotted against the actual number of faults present in each stack. On this plot $N_{str} = 100$ models lie essentially on the minimum-R_{wp} surface. This plot also shows that $N_{str} = 1$ R_{wp}

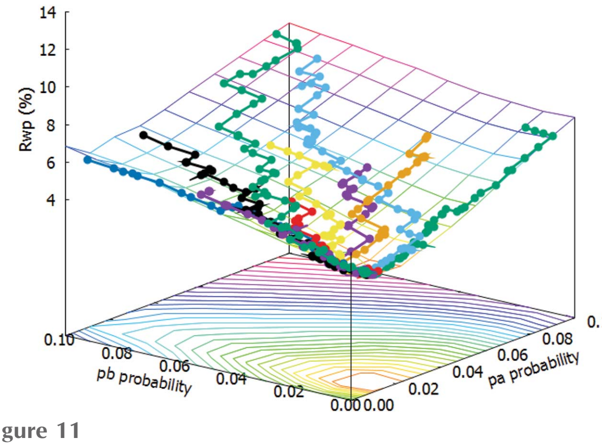

Figure 11
Minimization pathway using a simple downhill algorithm. Minimization pathways from ten different random starting points shown on an equivalent surface to that of Fig. 10(*b*).

values have significant scatter; around the $R_{\rm wp}$ minimum individual $R_{\rm wp}$ values can be up to 1% higher than the lowest value.

As expected from the smooth $R_{\rm wp}$ surfaces in Fig. 10, it is relatively straightforward to directly optimize values of *pa* and *pb*. There are a number of ways of doing this based on Monte Carlo or simulated annealing type approaches (*e.g.* Bette, 2015). Here a straightforward downhill or greedy algorithm is effective. Fig. 11 shows typical minimization pathways for this problem. Each minimization was complete in a few minutes of computer time.

10. Conclusion

In conclusion we show how the use of efficient algorithms for calculating structure factors, efficient pattern averaging, speed-ups in powder pattern calculation using a peaks buffer, a smoothing procedure that allows for the use of much smaller supercells and efficient stacking algorithms lead to massive speed gains in the Rietveld analysis of stacking-faulted structures. Real speed gains of the order of 10^4 have been obtained, allowing rapid combined structural and microstructural analysis of complex systems. These processes have been implemented in a general way in the computer program *TOPAS* Version 6, and we believe they will have wide applicability.

References

Ainsworth, C. M., Lewis, J. W., Wang, C., Coelho, A. A., Johnston, H. E., Brand, H. E. A. & Evans, J. S. O. (2016). *Chem. Mater.* **28**, 3184–3195.

Bette, S., Dinnebier, R. E. & Freyer, D. (2015). *J. Appl. Cryst.* **48**, 1706–1718.

Bruker (2009). *DIFFRACplus TOPAS4.2*. Technical Reference Manual. Bruker AXS, Karlsruhe, Germany.

Bruker (2015). *TOPAS*. Version 6.0. Bruker AXS, Karlsruhe, Germany.

Cheary, R. W. & Coelho, A. (1992). *J. Appl. Cryst.* **25**, 109–121.

Coelho, A. A. (2015). *TOPAS Academic*. Version 5. http://www.topas-academic.net.

Lutterotti, L., Voltolini, M., Wenk, H. R., Bandyopadhyay, K. & Vanorio, T. (2010). *Am. Mineral.* **95**, 98–103.

Rietveld, H. M. (1969). *J. Appl. Cryst.* **2**, 65–71.

Treacy, M. M. J., Newsam, J. M. & Deem, M. W. (1991). *Proc. R. Soc. A Math. Phys. Eng. Sci.* **433**, 499–520.

Ufer, K., Roth, G., Kleeberg, R., Stanjek, H., Dohrmann, R. & Bergmann, J. (2004). *Z. Kristallogr.* **219**, 519–527.

Wang, X., Hart, R. D., Li, J., McDonald, R. G. & van Riessen, A. (2012). *J. Appl. Cryst.* **45**, 1295–1302.

Young, R. A. (1993). Editor. *The Rietveld Method: Introduction to the Rietveld Method*, pp. 1–39, IUCr Monographs on Crystallography. Oxford University Press.